



Wydział Chemii

Piotr Wróbel

Rozprawa doktorska

Studies of interactions in solutions based on Molecular Dynamics
methods and simulated vibrational spectra

Badania oddziaływań w roztworach w oparciu o metody dynamiki molekularnej i
symulowane widma oscylacyjne

Praca wykonana w
Zakładzie Metod Obliczeniowych Chemii
pod kierunkiem
dra hab. Andrzeja Eilmesa

Kraków 2023

*Pragnę podziękować
dr. hab. Andrzejowi Eilmesowi
za poświęcony czas, opiekę naukową,
i pomoc w przygotowaniu niniejszej rozprawy,
dr. Piotrowi Kubisiakowi
za współpracę i pomoc w badaniach
oraz
Ilonie
za wsparcie*

Contents

List of publications being a part of the Thesis	8
List of other publications	9
List of active conference participations	10
Abstract	11
Streszczenie	13
List of abbreviations and symbols	15
1 Introduction	17
1.1 Interactions and vibrational spectra	17
1.2 Search for non-lithium electrolytes	20
1.3 Theoretical studies of electrolytes for metal-ion batteries	24
1.3.1 Lithium Ion Batteries	24
1.3.2 Beyond lithium	26
1.4 Vibrational spectra from MD simulations	28
1.5 Aim of this work	29
2 Theoretical methods	31
2.1 Molecular dynamics	31
2.1.1 Born-Oppenheimer approximation	31
2.1.2 Classical Molecular Dynamics	32
2.1.3 Ab initio Molecular Dynamics	34
2.1.4 Pseudopotentials	35
2.1.5 Plane waves	35
2.1.6 Thermostating	36
2.1.7 Structural properties	37
2.1.8 Infrared spectra from MD	39
2.2 Density Functional Theory	41
2.2.1 Kohn-Sham method	42
2.3 Density Functional based Tight-Binding	44

2.3.1	Slater-Koster parameters	46
2.3.2	Extended Tight Binding	47
2.4	Machine Learning	48
2.4.1	Neural Networks	48
2.5	Computational details	49
3	Structural data from MD simulations	51
3.1	NaFSI solutions in EMIM-FSI ionic liquid	51
3.1.1	System details	52
3.1.2	Results	52
3.2	EMIM-TFSI with NaTFSI or LiTFSI solutions	60
3.2.1	System details	60
3.2.2	Results	60
3.3	Magnesium chloride solutions in DME	64
3.3.1	System details	64
3.3.2	Results	65
3.4	Ethylene carbonate with Na/Li TFSI salt	74
3.4.1	System details	74
3.4.2	Results	74
3.5	NaFSI/TFSI solutions in ether solvents	80
3.5.1	System details	80
3.5.2	Results	80
3.6	EMIM-TFSI with water	87
3.6.1	System details	87
3.6.2	Results	87
4	IR spectra from AIMD simulations	92
4.1	NaFSI solutions in EMIM-FSI ionic liquid	92
4.2	Magnesium chloride solutions in DME	97
4.3	Ethylene carbonate with Na/Li TFSI salt	100
4.4	EMIM-TFSI with water	105
4.5	LiTFSI in water	111
5	Alternatives to AIMD	113
5.1	DFTB	113
5.1.1	Ethylene carbonate with Na/Li TFSI salt	113
5.1.2	EMIM-TFSI with water	118
5.2	Machine Learning	122
5.2.1	Ethylene carbonate	122
5.2.2	Water	123

6 Summary	125
6.1 Acknowledgements	126
List of Figures	127
List of Tables	131
Bibliography	132

List of publications being a part of the Thesis

- [I] P. Wróbel, P. Kubisiak, and A. Eilmes. “Interactions in Sodium Bis(fluorosulfonyl)imide/1-Ethyl-3-methylimidazolium Bis(fluorosulfonyl)imide Electrolytes for Na-Ion Batteries: Insights from Molecular Dynamics Simulations”. *J. Phys. Chem. C* 123 (2019), 14885–14894.
- [II] P. Kubisiak, P. Wróbel, and A. Eilmes. “Molecular Dynamics Investigation of Correlations in Ion Transport in MeTFSI/EMIM-TFSI (Me = Li, Na) Electrolytes”. *J. Phys. Chem. B* 124 (2020), 413–421.
- [III] P. Wróbel, P. Kubisiak, and A. Eilmes. “Quantum-Chemical and Molecular Dynamics Investigations of Magnesium Chloride Complexes in Dimehtoxyethane Solutions”. *ACS Omega* 5 (2020), 12842–12852.
- [IV] P. Wróbel, P. Kubisiak, and A. Eilmes. “MeTFSI (Me = Li, Na) Solvation in Ethylene Carbonate and Fluorinated Ethylene Carbonate: A Molecular Dynamics Study”. *J. Phys. Chem. B* 125 (2021), 1248–1258.
- [V] P. Wróbel, P. Kubisiak, and A. Eilmes. “NaFSI and NaTFSI Solutions in Ether Solvents from Monoglyme to Poly(ethylene oxide) - A Molecular Dynamics Study”. *J. Phys. Chem. B* 125 (2021), 10293–10303.
- [VI] P. Wróbel, P. Kubisiak, and A. Eilmes. “Hydrogen Bonding and Infrared Spectra of Ethyl-3-methylimidazolium Bis(trifluoromethylsulfonyl)imide / Water Mixtures: A View from Molecular Dynamics Simulations”. *J. Phys. Chem. B* 126 (2022), 10922–10932.

List of other publications

- [A] P. Kubisiak, P. Wróbel, and A. Eilmes. “How Temperature, Pressure, and Salt Concentration Affect Correlations in LiTFSI/EMIM-TFSI Electrolytes: A Molecular Dynamics Study”. *J. Phys. Chem. B* 125 (2021), 12292–12302.
- [B] A. Eilmes, P. Kubisiak, and P. Wróbel. “Explicit and Hybrid Solvent Models for Estimates of Parameters Relevant to the Reduction Potential of Ethylene Carbonate”. *Int. J. Mol. Sci.* 23 (2022), 15590.

List of active conference participations

1. Piotr Wróbel, Piotr Kubisiak, Andrzej Eilmes, Classical and ab initio molecular dynamics of NaFSI/EMIM-FSI electrolytes, Konferencja Użytkowników Komputerów Dużej Mocy 2019, 6-8.03.2019, Zakopane, Poland, poster
2. Piotr Wróbel, Piotr Kubisiak, Andrzej Eilmes, Ab initio molecular dynamics studies of Na-FSI/EMIM-FSI electrolyte, Lviv Chemical Readings 2019, 3-5.06.2019, Lviv, Ukraine, oral presentation
3. Piotr Wróbel, Piotr Kubisiak, Andrzej Eilmes, Computational Modeling of Magnesium Chloride Complexes in Dimethoxyethane Solutions, Current Trends in Theoretical Chemistry VIII, 1-5.09.2019, Kraków, Poland, poster
4. Piotr Wróbel, Piotr Kubisiak, Andrzej Eilmes, Classical and Ab Initio Molecular Dynamics of Magnesium Chloride Complexes in Dimethoxyethane Solutions, Konferencja Użytkowników Komputerów Dużej Mocy 2020, 23-24.11.2020, online, oral presentation
5. Piotr Wróbel, Piotr Kubisiak, Andrzej Eilmes, Molecular dynamics studies of NaTFSI/LiTFSI in ethylene carbonate and its derivatives, Lviv Chemical Readings 2021, 31.05-2.06.2021, Lviv, Ukraine, oral presentation
6. Piotr Wróbel, Piotr Kubisiak, Andrzej Eilmes, Modeling IR Spectra of Liquids from MD Simulations, Young Multis 2021, 5-7.07.2021, online, oral presentation
7. Piotr Wróbel, Piotr Kubisiak, Andrzej Eilmes, Molecular dynamics studies of NaTFSI/LiTFSI in ethylene carbonate and its derivatives, Konferencja Użytkowników Komputerów Dużej Mocy 2022, 7-8.04.2022, online, oral presentation
8. Piotr Wróbel, Piotr Kubisiak, Andrzej Eilmes, AIMD Simulations in Modeling IR Spectra of Liquids, 18th Central European Symposium on Theoretical Chemistry, 7-10.09.2022, Balatonszárszó, Hungary, oral presentation
9. Piotr Wróbel, Piotr Kubisiak, Andrzej Eilmes, IR Spectra of Liquids Modeling with MD Simulations, Modeling and Design of Molecular Materials 2022, 19-22.09.2022, Gdańsk, Poland, oral presentation
10. Piotr Wróbel, Piotr Kubisiak, Andrzej Eilmes, Ab Initio Molecular Dynamics Studies of Hydrogen Bonding and IR Spectra in EMIM-TFSI/H₂O Systems, Konferencja Użytkowników Komputerów Dużej Mocy 2023, 19-21.04.2023, Zakopane, Poland, oral presentation

Abstract

This work concentrates on studies of interactions in different systems, all in the liquid phase, by interpretation of Molecular Dynamics (MD) simulations. Investigated systems have recently been experimentally studied as potential electrolytes for novel batteries. Thus, in most cases there were some ions present in the liquid. In the majority of systems considered, both classical and ab initio (AIMD) MD approaches were used.

The analysis started with the structural properties in Chapter 3. One group of investigated systems were salt solutions in ionic liquids (ILs): NaFSI salt in EMIM-FSI IL and Na/LiTFSI salts in EMIM-TFSI IL. The effects of interactions on the internal structure of the system were studied mainly by radial distribution functions (RDFs) of selected atom pairs and the analysis of conformers and changes in their abundance for changing concentrations of the electrolyte. On the basis of RDFs, coordination preferences of metal ions were detected, and differences in coordination patterns for sodium and lithium were determined and compared to experimental values. Dynamics of the systems was studied via residence time autocorrelation functions showing that solvent exchange in the solvation shell of the cation becomes slower with increasing salt concentration and that the changes for Na^+ are faster than for Li^+ .

The other set of systems were electrolytes based on molecular liquids: solutions of magnesium salts in dimethoxyethane (DME) with different Mg:Cl ions ratio, Li/NaTFSI in ethylene carbonate (EC) and its fluorinated derivatives, and NaFSI/TFSI solutions in three ethereal solvents: monoglyme, tetraglyme, and poly(ethylene oxide) (PEO). In the case of Mg electrolytes structures of possible aggregates and their energies were determined. For systems with different initial distribution of ions, classical MD simulations provided insight into the aggregation process. The coordination numbers and differences between the coordination shells of different ions were studied for carbonate- and ether-based solutions. For the latter, preferences for different binding sites and the mobility of cations along PEO chains were examined.

The third class of systems were electrolytes with water: EMIM-TFSI/water mixtures and concentrated LiTFSI/water solutions. For EMIM-TFSI IL with changing concentration of water, the total number of hydrogen bonds was determined, as well as their distribution between different donors and acceptors.

AIMD was particularly useful for the determination of infrared (IR) spectra. The results obtained are described in Chapter 4. Usually, when compared to experiment, frequencies in the spectra calculated from simulations are systematically shifted. However, band shifts occurring when the composition of the system (e.g. salt concentration) changes are reproduced correctly. The interaction-induced shifts were clearly demonstrated for interactions of FSI^- anions with

sodium cations and for Li^+/Na^+ solvation in cyclic carbonates. The effect of HB formation on the IR spectra is also satisfactorily described, as can be seen for EMIM-TFSI/ H_2O and LiTFSI/ H_2O systems.

For a more detailed description of systems, a simple but successful approach was used. It was based on the calculation of Fourier transforms (FTs) of particular geometrical parameters, e.g. bond lengths or angles. Such FTs allowed to assign vibrations to bands visible in IR spectrum. It was also demonstrated that FTs help reveal effects of interactions; e.g. in NaTFSI/LiTFSI solutions in EC, two separated groups of frequencies were observed corresponding to solvent molecules interacting or non-interacting with metal cations. In addition, the averages of the FTs over all ions or molecules exhibited similar patterns of shifts in the positions of the maxima between systems with different compositions, as observed in the IR spectra.

AIMD simulations are computationally expensive, therefore, some cheaper approaches were described in Chapter 5. For two of the systems studied by AIMD additionally DFTB MD simulations were performed. For neat EC and its derivatives, the 3ob parametrization was able to reproduce shifts of the C=O band in the IR spectrum; however, the effect was weaker than in AIMD, and for the NaTFSI/EC electrolyte, it failed to reproduce appearance of a new band observed in AIMD. The GFN2-xTB approach was able to reproduce this effect for lithium electrolytes. A study carried out for bulk water showed that the quality of the results obtained strongly depends on the parameterization used and is the best when the parameters are developed for a particular system, although also the general-purpose GFN2-xTB approach yielded satisfactory reproduction of the spectrum. However, for IL- H_2O case even the GFN2-xTB approach was inaccurate in the description of HB. Thus, the DFTB method is a promising alternative to AIMD, but still needs the development of better parameters for this purpose.

Another approach computationally cheaper than AIMD were Machine Learning methods. For neat EC and for neat water, neural networks were trained to predict the potential energy, forces, and dipole moment for a given system geometry. It was possible to perform MD simulations for a small number of molecules, resulting spectra were comparable to AIMD results.

The results reported here demonstrated that AIMD is able not only to study the effects of interactions on the structure of electrolytes, but also to reproduce their manifestations in the IR spectra. Further development of methodology is necessary to exploit the potential of computationally less demanding approaches.

Streszczenie

Niniejsza praca skupiona jest na badaniach oddziaływań w układach w fazie ciekłej, poprzez interpretację wyników symulacji dynamiki molekularnej (MD). Badane układy stanowią niedawno badane eksperymentalnie potencjalne elektrolity do baterii nowej generacji. Stąd, zazwyczaj zawierały one jony. W większości rozważanych przypadków zastosowano zarówno klasyczną MD jak i dynamikę ab initio (AIMD).

Analizę rozpoczęto od właściwości strukturalnych w rozdziale 3. Jedną z grup badanych układów były roztwory soli w cieczach jonowych (IL): NaFSI w EMIM-FSI oraz Na/LiTFSI w EMIM-TFSI. Wpływ oddziaływań na wewnętrzną strukturę układu badano głównie za pomocą radialnych funkcji rozkładu (RDF) wybranych par atomów oraz analizy konformerów i zmian ich liczebności przy zmieniającym się stężeniu elektrolitu. Na podstawie RDF wykryto preferencje koordynacyjne jonów metali oraz określono różnice w strukturach koordynacyjnych dla sodu i litu, które porównano z wartościami eksperymentalnymi. Dynamikę układów badano za pomocą funkcji autokorelacji czasu oddziaływanego, wykazując, że wymiana rozpuszczalnika w powłoce solwatacyjnej kationu staje się wolniejsza wraz ze wzrostem stężenia soli oraz że zmiany dla Na^+ są szybsze niż dla Li^+ .

Drugi zestaw układów stanowiły elektrolity oparte na cieczach molekularnych: roztwory soli magnezu w dimetoksyetytanie (DME) różniące się stosunkiem jonów Mg:Cl, Li/NaTFSI w węglaniu etylenu (EC) i jego fluorowanych pochodnych oraz roztwory NaFSI/TFSI w trzech rozpuszczalnikach eterowych: monoglimie, tetraglimie i poli(tlenku etylenu) (PEO). W przypadku elektrolitów magnezowych wyznaczono struktury możliwych agregatów oraz ich energie. Dla układów o różnym początkowym rozkładzie jonów klasyczne symulacje MD zapewniły wgląd w proces agregacji. Określono liczby koordynacyjne i różnice między sferami koordynacyjnymi różnych jonów dla roztworów na bazie węglanów i eterów. W przypadku tych ostatnich zbadano preferencje dla różnych miejsc wiązania oraz ruchliwość kationów wzdłuż łańcuchów PEO.

Trzecią klasę układów stanowiły elektrolity z wodą: mieszaniny EMIM-TFSI/woda oraz stężone roztwory LiTFSI/woda. Dla EMIM-TFSI ze zmieniającym się stężeniem wody wyznaczono całkowitą liczbę wiązań wodorowych oraz ich rozkład pomiędzy różnymi donorami i akceptorami.

AIMD była szczególnie przydatna do wyznaczania widm w podczerwieni (IR). Otrzymane wyniki opisano w rozdziale 4. Zwykle w porównaniu z eksperymentem częstotliwości w widmach obliczonych na podstawie symulacji są systematycznie przesunięte. Jednak przesunięcia pasm występujące, gdy zmienia się skład układu (np. stężenie soli) są odtwarzane poprawnie. Przesunięcia wywołane przez oddziaływanie zostały wyraźnie zaobserwowane dla oddziaływań

anionów FSI^- z kationami sodu oraz dla solwatacji Li^+/Na^+ w cyklicznych węglanach. Wpływ tworzenia wiązań wodorowych na widma IR jest również zadowalająco opisany, co można zaobserwować dla układów EMIM-TFSI/ H_2O i LiTFSI/ H_2O .

W celu uzyskania bardziej szczegółowego opisu drgań w badanych układach zastosowano proste, ale skuteczne podejście. Polegało ono na obliczeniu transformat Fouriera (FT) poszczególnych parametrów geometrycznych, m.in. długości wiązań lub kątów. Takie FT pozwoliły przypisać drgania pasmom widocznym w widmie IR. Wykazano również, że FT pomagają ujawnić efekty oddziaływań, np. w roztworach NaTFSI/LiTFSI w EC zaobserwowano dwie odrębne grupy częstotliwości odpowiadające cząsteczkom rozpuszczalnika oddziałującym lub nieoddziałującym z kationami metali. Ponadto średnie FT dla wszystkich jonów lub cząsteczek wykazywały podobne wzorce przesunięć pozycji maksimów między układami o różnych składach, jak zaobserwowano w widmach IR.

Symulacje AIMD są kosztowne obliczeniowo, dlatego niektóre tańsze podejścia zostały opisane w rozdziale 5. Dla dwóch układów badanych za pomocą AIMD wykonano dodatkowo symulacje metodą DFTB. Dla czystego EC i jego pochodnych parametryzacja 3ob była w stanie odtworzyć przesunięcia pasma C=O w widmie IR, jednak efekt był słabszy niż w AIMD, a dla elektrolitu NaTFSI/EC nie udało się odtworzyć pojawienia się nowego pasma obserwowanego w AIMD. Wariant GFN2-xTB umożliwił odtworzenie tego efektu dla elektrolitów litowych. Badanie przeprowadzone dla wody wykazało, że jakość uzyskanych wyników silnie zależy od zastosowanej parametryzacji i jest najlepsza, gdy parametry są opracowywane dla konkretnego układu, chociaż również ogólne podejście GFN2-xTB dało zadowalające odwzorowanie widma. Jednak w przypadku układów ciecz jonowa- H_2O nawet podejście GFN2-xTB było niedokładne w opisie wiązań wodorowych. Zatem metoda DFTB jest obiecującą alternatywą dla AIMD, ale wciąż wymaga opracowania lepszych parametrów do tego celu.

Innym podejściem, tańszym obliczeniowo niż AIMD, były metody uczenia maszynowego. Dla czystego EC i czystej wody sieci neuronowe zostały wytrenowane w przewidywaniu energii potencjalnej, sił i momentu dipolowego dla danej geometrii układu. Możliwe było przeprowadzenie symulacji MD dla niewielkiej liczby cząsteczek, otrzymane widma były porównywalne z wynikami AIMD.

Przedstawione tu wyniki wykazały, że AIMD jest w stanie nie tylko badać wpływ oddziaływań na strukturę elektrolitów, ale także odtwarzać ich przejawy w widmach IR. Dalszy rozwój metodologii jest konieczny, aby wykorzystać potencjał podejść mniej wymagających obliczeniowo.

List of abbreviations and symbols

AF	autocorrelation function
AI	artificial intelligence
AIMD	ab initio molecular dynamics
BMIM	1-butyl-3-methylimidazolium
BOMD	Born-Oppenheimer molecular dynamics
CDF	combined distribution function
CPMD	Car-Parinello molecular dynamics
DFT	Density Functional Theory
DFTB	Density Functional based Tight-Binding
DFTB3	third order Density Functional based Tight-Binding
DMC	dimethyl carbonate
DME	dimethoxyethane
DP-FF	polarizable force field with Drude particles
EC	ethylene carbonate
EMIM	1-ethyl-3-methylimidazolium
FF	force field
FSI	bis(fluorosulfonyl)imide anion
FT	Fourier transform
GFN-xTB	Geometry, Frequency, Noncovalent extended Tight-Binding
GGA	Generalised Gradient Approximation
h	Planck constant
\hbar	reduced Planck constant
HB	hydrogen bond
HF	Hartree-Fock
IL	ionic liquid
IR	infrared
LDA	Local Density Approximation
LIB	lithium-ion battery
MD	molecular dynamics
ML	Machine Learning
MP2	second order Møller-Plesset perturbation theory
NN	neural network
NP-FF	nonpolarizable force field
PBC	periodic boundary conditions
PC	propylene carbonate
PCM	polarizable continuum model
PES	potential energy surface
PFF	polarizable force field
PEO	poly(ethylene oxide)
QC	quantum chemical

RDF	radial distribution function
SCC	self consistent charge
SDF	spatial distribution function
SEI	solid electrolyte interphase
TFSI	bis(trifluoromethylsulfonyl)imide anion
TOTO	2,5,8,11-tetraoxatridecan-13-oate
xTB	extended tight binding

Chapter 1

Introduction

This chapter presents the background to the matter of this thesis. It starts with a description of interactions through vibrational spectroscopy, and then proceeds to related experimental work on the topic of search for novel electrolytes for metal-ion batteries. Next, the current state of research in theoretical studies of such electrolytes and the computations of vibrational spectra from ab initio molecular dynamics (AIMD) are briefly described. Finally, the aim of the thesis is presented.

1.1 Interactions and vibrational spectra

Spectroscopy is the field of science which studies the interactions between electromagnetic radiation and matter [1]. In general, processes of interest could be divided into two groups: absorption or emission of the radiation. The vibrational spectrum is related to changes in vibrational energy states during interaction of the studied system with radiation. It is observed in the energy range corresponding to the differences between the vibrational energy levels, commonly expressed in units of cm^{-1} , i.e. between 10 and 12 000 cm^{-1} . The basic techniques in vibrational spectroscopy are infrared (IR) spectroscopy and Raman spectroscopy.

Selection rules for vibrational spectroscopy are the following:

- the energy of the photon must match the difference between two vibrational states:

$$\Delta E = h\nu \tag{1.1}$$

- non-zero change of the vibrational quantum number v : $\Delta v = \pm 1, \pm 2, \pm 3, \dots$
- non-zero intensity I of the band, for IR spectroscopy intensity I_{IR} is proportional to change of the dipole moment during changing normal coordinate:

$$I_{\text{IR}} \sim \left| \left(\frac{d\mu}{dq} \right)_{q=q_e} \right|^2, \tag{1.2}$$

while for the Raman spectroscopy it is related to polarizability:

$$I_{\text{Raman}} \sim \left| \left(\frac{d\alpha}{dq} \right)_{q=q_e} \right|^2, \quad (1.3)$$

where q_e stands for the equilibrium position of the normal coordinate q .

The potential energy of a vibration U , could be expressed as Taylor series around the equilibrium position q_e :

$$U(q) = U(q_e) + \frac{1}{2}\kappa(q - q_e)^2 + \mathcal{O}(q^3), \quad (1.4)$$

where κ stands for the force constant of the vibration and is defined as follows:

$$\kappa = \left(\frac{\partial^2 U}{\partial q^2} \right)_{q=q_e}. \quad (1.5)$$

Retaining only terms up to q^2 in the equation 1.4 corresponds to a commonly used harmonic oscillator approximation. For a vibration, the κ value characterizes the strength of the oscillator, e.g., the strength of the particular bond. It can be calculated by standard quantum chemical methods by determining the second derivatives of the energy. In the harmonic oscillator approximation, it is related to the vibration frequency ν by the formula:

$$\nu = \frac{1}{2\pi} \sqrt{\frac{\kappa}{\mu_{\text{red}}}}, \quad (1.6)$$

where μ_{red} is the reduced mass of the oscillating system.

Many types of chemical bonds have visible bands in the IR spectrum in a specific range of frequency, e.g. C=O stretching vibration usually appears between 1600 and 1750 cm⁻¹ [2]. For this reason, IR spectroscopy is commonly used especially in organic chemistry, to identify functional groups present in the studied sample [3].

Interactions influence the potential energy surfaces, therefore, vibrational spectroscopies (IR or Raman) could be used to detect and to study interactions in the system. The blue shift or the red shift of a particular band with change of some conditions may suggest an increase or decrease of the bond strength. Appearance of a new band could be a result of new intermolecular interaction, e.g. when comparing the spectrum of neat solvent and a salt solution. It is a common situation when hydrogen bonds (HBs) are present. For example, an effect of competition between molecules could be observed, e.g. when hydrogen bonding is possible both as a solvent-solvent or solvent-solute substance interaction. It should be noted that complexes formed by these interactions must have a long enough lifetime to be observed in the IR spectrum, i.e. this lifetime is larger than the period of interacting electromagnetic wave, which for IR is equal about 10⁻¹³ s [1].

In the literature, there are many examples of studies of interaction through vibrational spectroscopy. One class of them is related to the strength of interactions. For example, IR spectra were used to study the solvent effect in nitriles [5], or for ionic liquids (ILs), which are a part of interest in this work, like for monitoring the state of protonation of the anion [6] or the strength

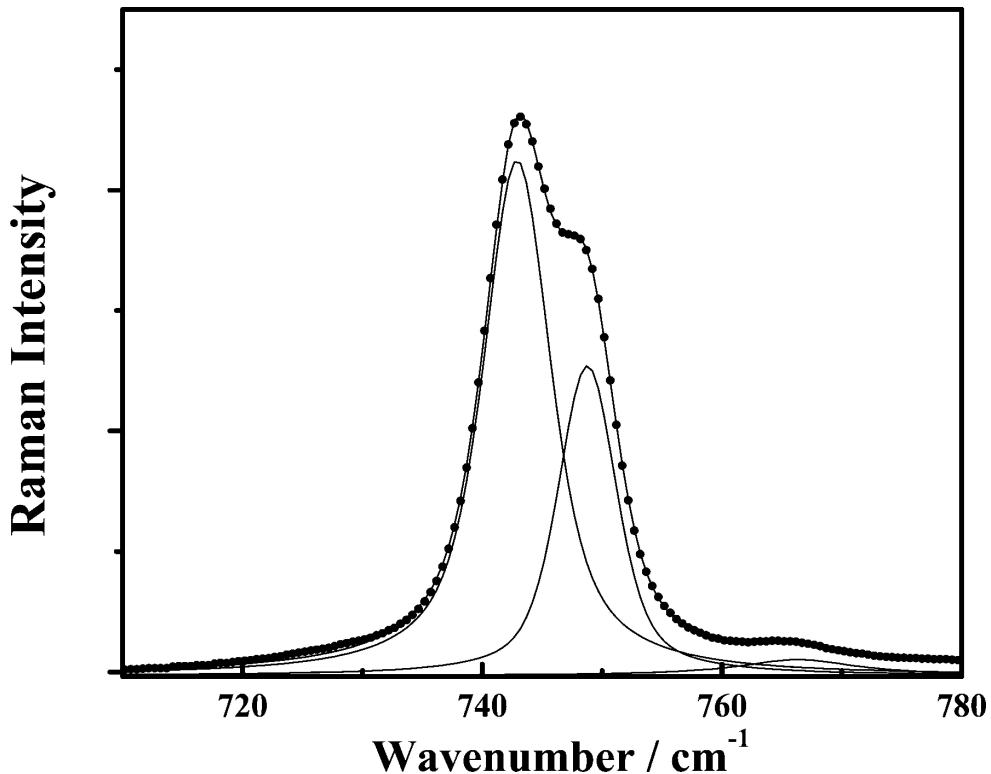


Figure 1.1: Raman spectrum of EMIM-TFSI solution with dissolved LiTFSI. Dotted line is the experimental spectrum and the solid lines are the deconvoluted bands for free TFSI^- (744 cm^{-1}), bound TFSI^- (750 cm^{-1}) and EMIM^+ (766 cm^{-1}) [4]

of interactions between ions in ILs based on imidazolium derivatives [7]. Such spectra are able to study changes in the chemical environment. Due to their sensitivity to these differences, some molecules containing interaction-sensitive groups are proposed as probes. For example, in the ILs mentioned, benzonitrile was used as a probe of the chemical environment due to the high sensitivity of the CN stretching vibration in the nitrile group [8]. Similarly, the thiocyanate group has been presented as an analogous probe for proteins [9]. The study of interactions by vibrational spectroscopy is also used for biological systems, for example, to examine interactions between carbohydrates and dried proteins [10], between alginate and chitosan biopolymers [11] or adsorption abilities of humic acid on different nanosized media [12].

Another class of works utilizes vibrational spectra in verification of hypotheses about system structures. Symmetry-related selection rules for vibrational spectra allowed the identification of stable conformers, their populations, and their thermal dependence in systems studied in this work such as 1,2-dimethoxyethane [13], 1-ethyl-3-methylimidazolium bis(fluorosulfonyl) imide (EMIM-FSI) [14] or glymes [15]. For other systems, this symmetry effect was used to identify structures of benzenesulfonate complexes [16], propose structure of poly(L-lactic acid) crystals [17] or to determine the structure of cathinone derivatives complexes [18].

Vibrational spectroscopy is also a sensitive tool to study hydrogen bonds (HBs) [19]. There are some articles describing HBs in ILs, which are most of the systems studied in this work. IR spectroscopy, along with other experimental methods, was used for determination of HB strength in a set of ILs [20, 21]. Other work described the low-frequency part of the spectrum for ILs contaminated with water [22]. Raman spectra were used to study the formation of HB

in ILs by monitoring shifts of the C=O, C=C and NH₂ stretching modes [23]. Such studies are not limited to ILs; for example, research on HB formation was done for N-methylacetamide mixtures with water [24] as well as for mixtures of water and heavy water [25].

In further parts, this work concentrates on liquid systems that could be used as electrolytes for batteries, which were also studied by vibrational spectroscopy. Since the technology of lithium-based batteries is known for a long time, there are many works that describe the properties of such systems. Raman spectra were used for the identification of Li⁺ coordination in LiClO₄ solutions in ethylene carbonate (EC) and its derivatives [26, 27] and it was observed that the bands related mainly to C=O stretching and ring deformation are influenced by increasing the concentration of the salt. In the systems based on gamma-butyrolactone and dimethylformamide, Li⁺ coordination to carbonyl group was proved by IR measurements [28]. For a system based on ionic liquid — ethyl-3-methylimidazolium bis(trifluoromethanesulfonyl) imide (EMIM-TFSI), analysis of intensity changes revealed that the lithium cation has coordination number equal 4 and is coordinated by oxygen atoms from two TFSI⁻ anions [4]. A sample spectrum and its deconvolution is shown in the Figure 1.1: a new band corresponding to the TFSI⁻ anions interacting with the Li⁺ cations is readily visible. Analogous results were obtained for systems with different imidazolium derivative as cation [29], systems based on LiBF₄ [30] or LiPF₆ [31] salt, systems with polyester-based polymer [32] or LiTFSI solutions in different solvents [33]. Another work shows that in concentrated LiTFSI solutions in ionic liquids, the lithium coordination number becomes less than 2 and aggregate formation is possible [34, 35]. IR spectroscopy was used to study the changes in the lithium ion coordination scheme at different temperatures [36].

Vibrational spectroscopy was also utilized to study interactions in novel electrolytes for metal-ion batteries, i.e. those based on other cations than lithium — usually sodium. Similarly to lithium-based electrolytes, systems containing polymers such as poly(ethylene oxide) (PEO) were studied, and Raman spectroscopy results indicated that in the system containing NaFSI salt more anions are coordinated to the cation compared to the electrolyte with NaTFSI salt [37]. For systems based on ionic liquids, the dependence of band positions in the Raman spectrum on NaTFSI concentration has been determined [38]. A similar study was performed for glyme-based systems [39].

1.2 Search for non-lithium electrolytes

Nowadays, the demand for power storage systems is increasing, mainly due to the growth of the mobile devices and the electric cars market [40]. One of the most popular types of energy source in everyday use are lithium-ion batteries (LIBs), widely used in portable electronics, such as notebooks, smartphones, etc. [41]. This is due to the relatively high standard potential of the Li/Li⁺ pair and the low lithium density. Early research showed that the presence of metallic lithium in the battery can cause explosions, so the standard LIB used graphite as the anode and cobaltium oxide as the cathode [42]. In recent years, some improved electrode materials for LIBs were developed [43]. As an electrolyte in such batteries, LiPF₆ solution in a mixture of ethylene carbonate (EC) and dimethyl carbonate (DMC) or lithium salts solutions in ionic liquids are

Table 1.1: Abundance of example elements in the earth crust [46]

Element	Abundance in earth crust [ppm]	
	Upper	Lower
Na	25670	21200
Mg	13510	31550
V	53	149
Zn	52	79
La	32.3	26.8
Nd	25.9	28.1
Li	22	13
Nb	26	11.3
Ga	14	17

commonly used [44]. Systems based on poly(ethylene oxide) (PEO) were also studied, due to their safety, ease of fabrication, and low cost [45].

Despite the efficiency of LIBs in energy storage, there exists a possible danger to their widespread use, due to the limited abundance of lithium in earth crust [46]. The abundance of sample elements is presented in Table 1.1. What can be observed is the fact that lithium is not so widespread and its content in earth crust is of the same order of magnitude as for elements usually considered as rare, like neodymium or gadolinium. Furthermore, its deposits are mainly located in countries in Africa and South America as well as China and Russia, which may cause political problems with stability of deliveries [47]. However, there are also opinions that lithium shortage is not a serious threat [48].

The problems mentioned with lithium supplies are one of the reasons why since early 2010s a large effort is put into research of alternative batteries using elements which are quite common and widespread, such as sodium [49–53] or magnesium [54–62]. An additional advantage of this approach is that sodium-based systems are friendly to the environment [63].

Due to similar chemical properties of sodium and lithium, materials used in LIBs were also studied for sodium-ion batteries, nevertheless, there were some differences in properties because of larger size and different bonding characteristics of sodium compared to lithium [64]. In sodium-based batteries technology, pyrolyzed carbon compounds, derivatives of titanium oxide [49], transition metal sulfides [53], tin-antimonium alloys [50] were considered as anodes and doped oxides of cobalt, vanadium or manganese, transition metal phosphates, fluorides [49], sulfides [50] and hexacyanoferates [53] were proposed as catode materials. For magnesium-based batteries, pure magnesium [54] (although with complications related to the formation of the passivation layer [65]), alloys of bismuth and antimony [66] or tin [67] were considered as anodes, while catodes were mostly based on transition metal oxides such as cobalt [68], vanadium [69], manganese [70], ruthenium [71] or molybdenum [72]. Unlike LiPF₆ dissolved in a mixture of EC and DMC, which is a standard electrolyte for LIBs, the case of an optimal electrolyte for non-lithium batteries is still a subject of research. Such system, to be applicable for use in batteries, should fulfill some requirements [52]:

- chemical stability — no side chemical reactions during cell utilization,
- electrochemical stability — its components should have HOMO-LUMO gap large enough to not undergo redox processes during cell utilization,
- thermal stability — it should be liquid or gel and do not decompose in the working temperature range,
- insensitive to contamination of water,
- be a good ionic conductor and electronic insulator,
- non-toxic, cheap in production, environment-friendly.

The electrochemical stability condition limits the choice of the anion for the salt dissolved in the electrolyte, among them are anions that are also commonly used in lithium cells, such as BF_4^- , ClO_4^- , $[\text{N}(\text{FSO}_2)_2]^-$ (FSI) or $[\text{N}(\text{CF}_3\text{SO}_2)_2]^-$ (TFSI) [52]. The last two are very valuable because NaFSI and NaTFSI are nontoxic, thermally stable, and their solutions have reasonable values of conductivity [73, 74]. For magnesium-based electrolytes, very popular is the use of MgCl_2 [60] (due to its low cost) or magnesium aluminium chloride complexes [59].

Protic solvents are excluded because of the condition of electrochemical stability. One class of compounds studied are organic solvents and their mixtures with compositions aiming at improving stability and lowering viscosity. Among them are cyclic (EC) or linear (DMC) carbonates [75], nitriles [76], esters and ethers such as glymes [77–79], imidazolium derivatives [80] and polymer systems based on poly(ethylene oxide) (PEO) [81–83]. Furthermore, fluorinated derivatives of solvents, e.g., EC fluorinated derivatives, were investigated due to their ability to lower the flammability of the electrolyte and improve its electrochemical stability [84–87]. From these solvents, one of the best mixtures was EC with propylene carbonate (PC) and either DMC or dimethoxyethane (DME) [88, 89]. It was also shown that the change in electrolyte properties can be made by using a salt mixture, such as MgCl_2 and AlCl_3 [59]. Another example are $\text{Mg}(\text{TFSI})_2$ solutions in DME, where an addition of chloride anions in the form of MgCl_2 [90] improved its performance.

Another class of solvents considered are ionic liquids (ILs). In general, they are organic salts which are molten at ambient temperature. They are chemically and electrochemically stable [91], have a wide range of liquid state and very low vapor pressure, making them safe due to their nonflammability [92]. ILs are composed entirely of ions; therefore, electrostatic interactions dominate their properties. In ILs, a wide choice of anions can be used, the systems most frequently studied are based on FSI^- and TFSI^- or simpler anions such as chlorides, bromides, iodides, nitrates, acetates, phosphates, tetrafluoroborates and hexafluorophosphates [93]. The proper choice of IL cation could improve the performance of the electrolyte; the most popular in recent studies are cations based on imidazolium (like 1-ethyl-3-methylimidazolium, briefly EMIM) or pyrrolidinium [38, 68, 71, 74, 94–102]. The usage of ILs is not limited to electrolytes, as they were also used as CO_2 absorbents [103], catalysts in organic and inorganic synthesis,

solvents for enzymes or lubricants [104]. A common experimental problem with ILs is that they are usually contaminated with water [105].

Research on "beyond lithium" chemistries is quite intense and several potentially interesting systems were found - some of the developed sodium-based electrolytes are better in terms of conductivity than lithium-based analogs [73]. Another alternative studied (although not as intensively as sodium or magnesium electrolytes) were systems based on zinc [94, 106, 107] or aluminum [108–110].

Experimental research on electrolyte properties is conducted both at the local level - solvation shells and electrode/electrolyte interfaces - and at the macroscopic level, including density, viscosity, and ionic conductivity. Impedance spectroscopy with NMR spectroscopy are used for studying ion transport. For testing electrochemical stability, cyclic voltammetry is usually applied. Safety features, such as temperature stability, vapor pressures or ignition temperatures, are studied with thermogravimetric analysis, differential scanning calorimetry, or accelerating rate calorimetry [52]. Other examples of such research include structure determination by rentgenographic methods [111], neutron diffraction [112] or spectroscopy [113, 114]. An example of such Raman spectrum is shown in Figure 1.2.

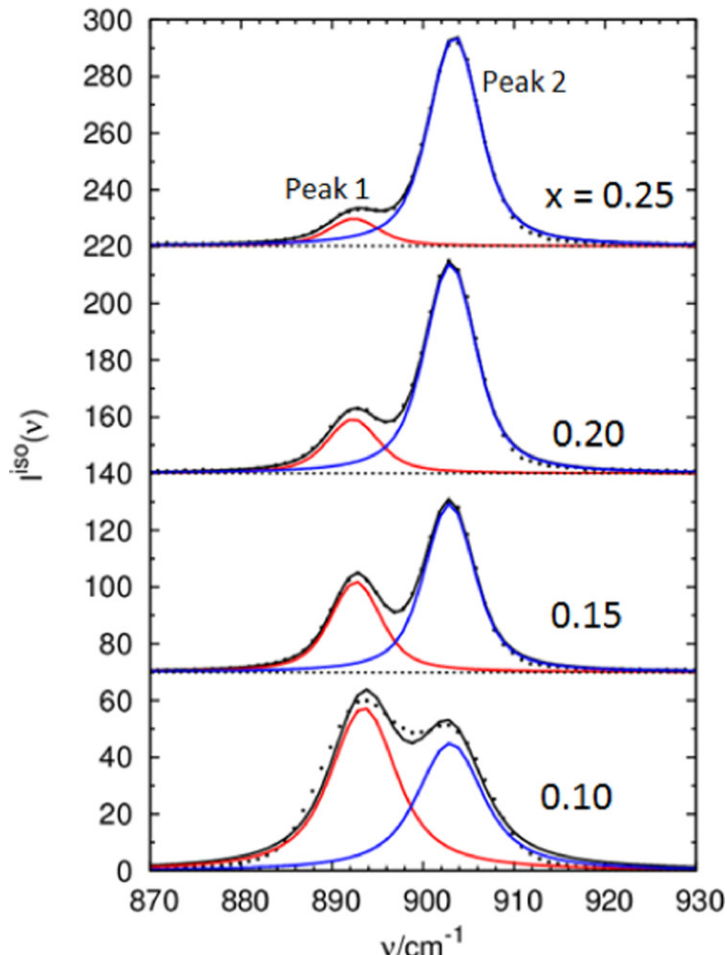


Figure 1.2: Raman spectra of $(\text{LiTFSI})_x \text{EC}_{1-x}$ with different molar fraction x of lithium salt, with deconvoluted bands for free and coordinated EC [112]

1.3 Theoretical studies of electrolytes for metal-ion batteries

In parallel to experimental works, research on electrolytes was supported by numerous computational studies. Recent reviews provide general information about the theoretical modeling of electrolytes for LIBs [115] and non-lithium ionic batteries [116]. In this chapter some selected examples will be described in more detail.

1.3.1 Lithium Ion Batteries

The first big group of studies involve quantum chemical (QC) methods. For systems based on organic carbonates, calculations for Li^+ -solvent pairs in the gas phase were performed with Density Functional Theory (DFT) methods. They indicated the preferred lithium coordination number in the complex with EC [117, 118] and optimized structures of complexes with EC and PC [119]. A similar study was carried out for LiClO_4 solutions in EC and PC [120]. For these systems theoretical Raman spectra obtained from DFT calculations in the gas phase were also used to determine the extent of cation-solvent interactions in the solvation shell [121]. Other DFT calculations performed for systems with LiPF_6 dissolved in a series of organic carbonates identified EC as the solvent with the strongest coordination ability for both the cation and the anion [122]. In a study investigating associates of carbonates and lithium ions, the analysis of intermolecular O-Li-O interactions [123], led to the conclusion that the Li-O interaction behaves as ionic. The simplest computational methods investigate systems in vacuum. Nevertheless, for proper modeling of the electrolytes and solutions, inclusion of solvent effects is necessary. The cost-effective method is to apply an implicit solvent method, e.g. the Polarizable Continuum Model (PCM). The use of continuum solvation models for interactions in electrolytes was studied in several works [124–126]. Example of obtained complexes for LiClO_4 in diglyme are presented in Figure 1.3. More advanced modeling may involve explicit solvent model or hybrid (continuous-explicit) approaches [127, 128]. DFT with implicit solvent methods were used for determination of oxidative [129] or reductive [130, 131] solvent decomposition mechanisms. Electronic structure calculations for several lithium salts were performed at the DFT level with the PCM approach [125]. Another study shows DFT results for the binding energy between lithium cations and glymes with increasing chain length [132].

QC calculations were also applied to study the ILs and salt solutions in ILs. Three systems of big cation-anion clusters for EMIM- BF_4^- , EMIM- PF_6^- and EMIM-TFSI were modeled by DFT [133]. Another work involved DFT calculations for ionic aggregates responsible for the conductivity of the electrolyte [134]. DFT was also used to determine the electrochemical stability window for ILs based on imidazolium derivatives [135]. IR spectra obtained from DFT calculations helped to analyze the changes of TFSI^- anion vibrations resulting from the interaction with lithium [34].

QC methodology was shown a useful tool to model small molecules or aggregates. However, to properly describe condensed-phase systems, such as solutions, implicit methods like PCM are

insufficient. For that purpose, molecular dynamics (MD) methods are used because they allow to explicitly describe solvent effects, to study the structure changes over time and to calculate important parameters of electrolytes: viscosity, diffusion coefficients, and conductivity. For ILs, in which electrostatic interactions are crucial, in classical force field (FF) MD one of the issues is including polarizability in the FF. Classical FFs such as OPLS [136] or Lopes/Pádua [137] are non-polarizable, that is, do not include induced dipole moments in the evaluation of the electrostatic contribution to energy. However, it was shown that polarization effects are significant for electrolytes [138, 139], and become particularly important for ILs [140, 141]. The two main approaches to model polarization are to explicitly calculate induced dipoles (such as in the FF APPLE&P [142]) or to effectively simulate them via Drude oscillators [143]. The latter method was used to develop a polarizable version of Lopes/Pádua FF for ILs [144]. Another possible method to include polarization is the scaling of the charges of ionized groups [145]. In general, in polarizable FFs, calculated viscosity is smaller and conductivity larger than in non-polarizable FF, respectively [144]. The constantly growing computational power of modern computers leads to increased applications of ab initio molecular dynamics (AIMD) [146–148].

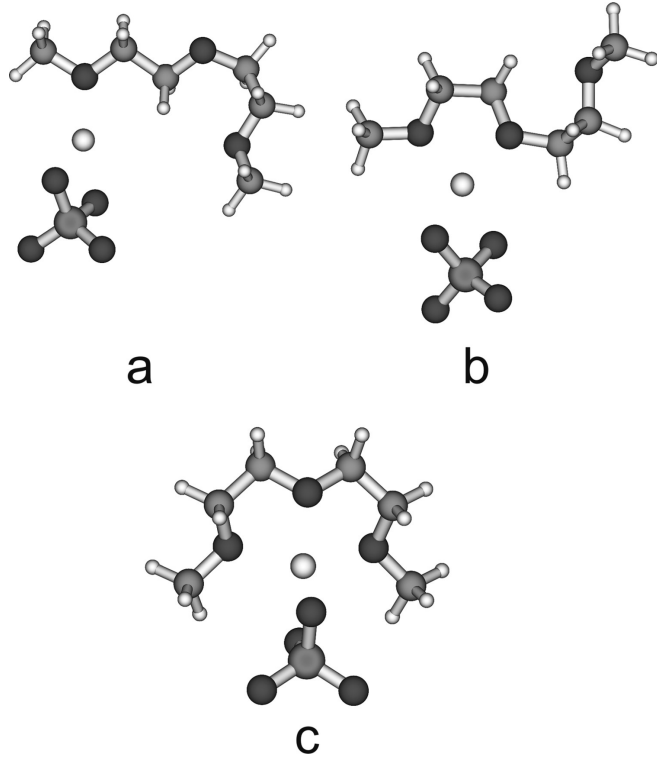


Figure 1.3: Structures of diglyme- LiClO_4 complexes calculated with DFT methods [126]

MD simulations were conducted for several systems relevant to LIB electrolytes. MD with polarizable force field (PFF) was performed for solid electrolyte interphase components (SEI). The results of these MD simulations allowed to determine the coordination numbers of lithium cations and calculate the conductivities of the systems [149, 150]. A similar study on the charge transport mechanism was performed for LiTFSI in PEO [151, 152] or salts with PF_6^- anion and cations based on imidazolium derivatives dissolved in PEO [153]. Other research examined the influence of the Lewis acid centers (boron or aluminum) in the electrolyte containing PEO and LiClO_4 on structural properties, as well as on diffusion coefficients and conductivity [154].

An approach using both QC and MD results was used to model the cation solvation shell and to predict the transport properties in liquid solutions of LiPF₆ in EC and its derivatives [118, 155, 156]. For pure, binary and ternary mixtures of PC, EC, and DMC classical MD confirmed the results of QC calculations that complexes with four solvent molecules around the lithium cation are the most stable and also revealed the existence of structural heterogeneities beyond the first coordination shell [157]. MD was also used to model the structure of the near-electrode layer depending on the electrode potential [158]. In addition, AIMD were used in lithium-based electrolyte studies, for example to determine the structural properties of LiPF₆ dissolved in carbonate solvents and to establish the relation between the structure of the liquid and the experimental Raman spectrum [159]. In other research, MD simulations were used to detect the mechanism of lithium ion transport in two ILs and to compare their performance in terms of conductivity [160]. To improve the results of classical MD, some specific PFFs for IL modeling were developed [161–165].

ILs were studied by MD methods not only as solvents but also as neat liquids. Classical MD was used to determine the shape of the EMIM-TFSI droplet formed in the presence of the applied electric field [166]. It was also used in determining the structure of the IL based on radial distribution functions (RDFs) and for comparison with experimental data for a set of different ILs with cations based on imidazolium or aliphatic amines and anions including acetates, TFSI⁻ and PF₆⁻ [167]. A similar study was performed for ILs based on amino acid anions [168]. Other research concentrated on studying the properties of the surface between two mixtures: one consisting of water and IL and the second consisting of nonane and IL [169]. AIMD was utilized to determine the structural properties of EMIM-SCN and EMIM-Cl ILs [170]. In particular, AIMD was used to study hydrogen bonds (HBs) in gas phase and crystalline alkylammonium based ILs [171]. In another study, the structural and dynamical properties of imidazolium based ILs were studied by classical MD and compared with AIMD [172].

The issue of applicability of the mentioned computational methods for modeling of IL systems was also discussed. Comparison between the results obtained from MP2 and from a set of different DFT functionals [173, 174] showed that only new generations functionals such as M05-2X or KMLYP give results close to the MP2 reference. However, including the Grimme's dispersion correction [175] improves the quality of the results, probably because of the cancellation of errors [176]. For some IL systems, DFTB was presented as a reasonable method to speed-up calculations with acceptable loss of accuracy [177].

1.3.2 Beyond lithium

The biggest number of research results devoted to "beyond lithium" systems was published for liquid sodium-based electrolytes; the theoretical approaches used are basically the same as for lithium counterparts. The reduction reactions of popular carbonate solvents (EC, PC) and fluorinated EC were studied using DFT methods [178, 179]. Other works utilized DFT for studying cation-anion interaction for both lithium and sodium cations with anions among which were FSI⁻, F⁻, BF₄⁻ and shown that for sodium the strength of the interaction is lower

than for lithium [180, 181]. A similar behavior was observed for sodium salt with 2,5,8,11-tetraoxatridecan-13-oate (TOTO) [141], which in addition is an IL itself. For nitrile-based sodium salts, DFT was used to calculate ion-ion interaction energies and anion oxidation potentials [182]. Other theoretical works describe the calculation of the solvation energy by DFT for about 30 common solvents for sodium batteries [183, 184]. Different approaches to solvation effects were presented in [185], in which the structures for the DFT calculations were extracted from MD simulations. Another work focusing on the determination of the interaction strength describes the comparison of lithium and sodium complexes with crown ethers [186]. DFT study of NaTFSI in imidazolium-based ILs with TFSI⁻ anion showed that coordination numbers for sodium are close to 3, what is bigger than typical value of 2 obtained for the lithium analog [38]. Glyme-based systems were also studied with the use of DFT, in [187] the oxidative stability of pentaglyme and its complex with NaTFSI was determined with the Hartree-Fock method and compared with results for different cations (Li and K) [188]. MP2 method was used to study the interaction energies in a series of glymes from monoglyme to pentaglyme [189–191]. Similarly as for the lithium-based systems, polymer electrolytes were also studied. Starting with small models, the geometries of complexes between sodium and oligoglymes simulating parts of PEO were determined with HF or DFT methods [192–194]. Other works extended this approach and also included the influence of the presence of anion in the system to determine the dependence of vibrational frequencies on the local electronic structure [195–198]. DFT methods were also utilized to study the properties of magnesium-based systems. Such works involve determination of structures of Mg-Cl complexes in tetrahydrofuran and glymes [199], studies of the stability of complexes with different anions and solvents — DMSO [200] and glymes [201]. Using DFT methodology, the thermal and electrochemical stability of complex between Mg(TFSI)₂ and tetraglyme were studied [189]. The reductive stability of the complexes for Mg (TFSI)₂ in diglyme was studied by DFT methods [202]. Another usage of DFT methods included determination of bond dissociation energies, electrochemical stability window, and hydrolytic enthalpy for various mutations of the TFSI anion salts [203].

Likewise lithium-based electrolytes, also for systems with sodium or magnesium DFT was used in studying the spectroscopic properties of these systems. For several carbonate solvents, including EC, PC, DMC, and DME, shifts of the Raman active ring breathing vibration and of the IR active C=O stretching vibration were reproduced [185, 204, 205]. The calculated values of the frequency shifts were lower than for the lithium analogs, due to the lower interaction energy, and were in the range between 5 and 50 cm⁻¹. Another example are DFT calculations of Raman spectral data for the tetraglyme and pentaglyme with NaTFSI [206]. The calculated structural data for systems with Mg(TFSI)₂ and di- or triglyme were related to the experimentally measured IR spectrum [207].

Sodium-based electrolytes were also studied by MD simulations. Several of these works focused on the determination of the coordination numbers of sodium cations in different solvents, carbonates [208, 209], acetonitrile [210, 211] (including complexes with crown ethers [212]) and DMSO [213]. They showed that the coordination numbers for Na⁺ are usually in the range of 5-7, except for linear carbonates, where they are lower and close to 3. Another study

examined the properties of the SEI formation of NaPF_6 in neat PC and its mixtures with fluorinated EC [214]. MD studies for ILs with Na salts were also published. For the Na-TOTO system, preference in coordination of Na^+ cations to carboxylate oxygens rather than ether oxygens was shown. The calculated conductivity is underestimated, which is explained as a consequence of the use of the nonpolarizable FF [141]. In another work, AIMD was used to verify radial distribution functions (RDFs) obtained with classical MD in nonpolarizable FF for NaTFSI in pyrrolidinium based IL and it showed good agreement between the results of these two approaches [215]. MD was also used to study aggregates forming in high concentrations of NaFSI in ILs and their charge transport properties [102, 216]. For diglyme system with sodium salt, AIMD simulation was used for the development of the FF and later classical MD simulations were used to determine the structures of sodium aggregates [39]. PEO based systems in early works were approximated by olygoglymes, e.g. tetruglyme [217]. More complicated models use multiple longer polymer chains [218] but had some problems with the reproduction of experimental data, which was corrected by adding harmonic springs between the cations and the oxygen ether atoms [219] and further by including polarizability in the FF [220]. Other models introduce ionomers - polymer chains bound to the anion of the dissolved salt, such systems were simulated with PEO as a polymer to study transport properties. [221–224]. MD was also used for magnesium-based electrolytes: for example, for the determination of coordination numbers for different Mg salts in DMSO and glymes [200], transport properties for a series of salts based on TFSI^- derivatives [203], influence of ion complexation and aggregate formation on diffusion coefficients [225, 226].

1.4 Vibrational spectra from MD simulations

The simplest way to model the vibrational spectrum of the system is to perform a vibrational analysis based on the eigenvalues of the Hessian matrix (the matrix of second derivatives of the potential energy). However, this analysis is valid at the fixed geometry of the system (at stationary points of the potential energy surface) and can include solvent effects only by the implicit models like PCM or through explicit including of the presence of some of the solvent molecules. Thus, for the case of liquid systems, to properly include effects of changing coordination, different conformations or appearance of hydrogen bonding and long distance effects, MD simulations need to be performed [227]. The vibrational spectrum can be obtained from a MD trajectory by calculation of the appropriate autocorrelation function (AF): AF of the velocities for the power spectrum, AF of the dipole moment for the IR spectrum, and AF of the polarizability for the Raman spectrum [228]. To gain results of a desirable accuracy, the AIMD approach is preferable, because of problems with classical FFs to reproduce vibrational frequencies, especially in the case when HBs play a significant role.

AIMD was used successfully in the reproduction of experimental IR spectra. One example are systems with ILs consisting of EMIM cations and cyanamide-based anions [231]. This approach was able to correctly show the existence of Fermi resonance on the spectrum of dicyanamide. For a different system of droplets of EMIM acetate hydrogen bonding dynamics was investigated and

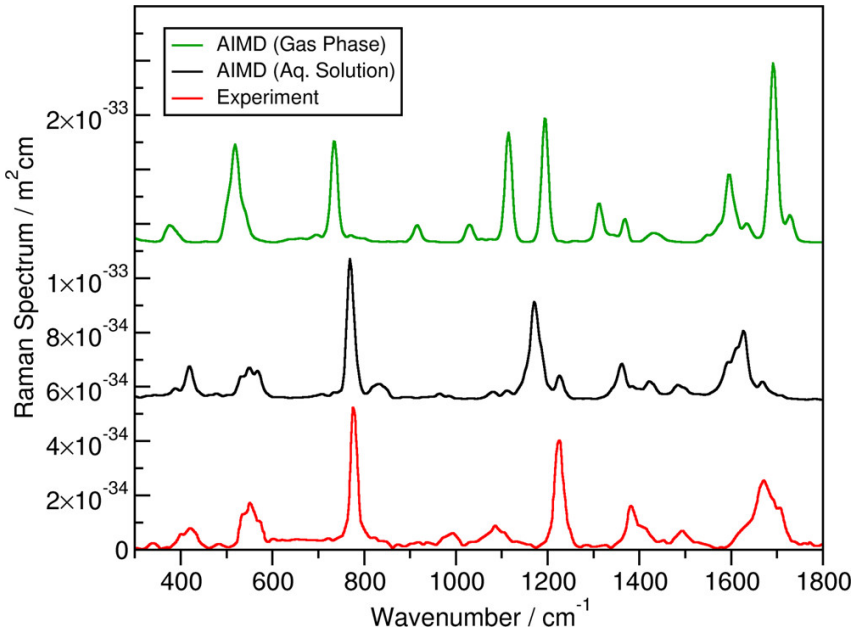


Figure 1.4: Raman spectrum of uracil calculated from AIMD simulation in gas phase and in aqueous solution [229] compared with experimental spectrum [230]

the calculated power spectra were in good agreement with the experimental data [232]. Similar results were obtained for a series of ILs based on cholinium [233]. Other examples of the usage of the AIMD in prediction of vibrational spectra include studies on the IR spectra of iron(II) polypyridyl complexes [234], resonance Raman spectra of uracil solution in water (with the use of time dependent DFT) [229] and the C-H region in IR and Raman spectrum of dimethyl sulfoxide [235]. Example of a spectrum calculated from AIMD is presented in Figure 1.4. One of recent articles mentions studies of spectral changes caused by interaction between lithium salt and solvent in EMIM-BF₄ and PC [236].

Usually, Born-Oppenheimer MD with DFT methods for obtaining wavefunctions for every time step of the simulation are used. Other approaches were also successful in this field. Car-Parinello MD (CPMD) [237] was used for calculation of spectra of imidazolium based IL mixture with CO₂ [238] as well as for Raman spectra of the cluster of ethyl ammonium nitrate [239]. A semi-empirical method, DFTB, was used in analysis of the HBs in ethylammonium nitrate by studying theoretical IR spectra [240] or for sodium salts in water [241].

1.5 Aim of this work

This work concentrates on studying the relationship between interactions in solutions (mostly electrolytes) and the structure of the system or its IR spectrum. In particular, its aim is to examine whether AIMD is able to reproduce effects of such interactions on vibrational spectra observed experimentally. Furthermore, an analysis of correlations between the calculated spectrum of the whole system and the local environment of molecules is done. In contrast to most of the works mentioned in Section 1.4, here changes in IR spectrum with changing composition of a particular system are studied.

As AIMD is rather computationally expensive, the quality of results obtained by simplified methods was also studied. These methods were DFTB and a novel approach with utilization of neural networks.

To summarize, the main aims could be briefly divided into the following points:

- studying the structure (preferred complexes, coordination numbers, hydrogen bonds) and the dynamics (stability of aggregates, residence times) of electrolytes and liquids,
- obtaining theoretical IR spectra from AIMD simulations, comparing them with experimental data, and assignment of spectral features to effects of interactions in the solution,
- finding and analysing correlations between position of bands in the IR spectrum and the chemical environment of molecules or ions,
- testing the applicability of approaches computationally cheaper than AIMD, such as Density Functional based Tight-Binding (DFTB) or Machine Learning (ML) of interatomic potentials.

Theoretical methods used in this thesis will be presented in Chapter 2. Results will be described and discussed in Chapters 3-5.

Chapter 2

Theoretical methods

This chapter describes theoretical methods used in the research presented in subsequent chapters. It starts with description of Molecular Dynamics (MD) and then goes through particular methods used in the ab initio variant of MD, the Density Functional Theory and simplified approaches: Density Functional based Tight-Binding and Machine Learning.

2.1 Molecular dynamics

To include dynamic effects such as the change in coordination or ionic transport present in the systems considered in this work, a method for obtaining a simulation of atomic movement in a given period of time is needed. For such purpose usually MD is used.

2.1.1 Born-Oppenheimer approximation

Atomic nuclei are about 2000 times heavier than electrons what leads to the conclusion that the motion of the latter is much faster than the former. Thus, this gives a reason for the assumption that for a description of nuclei dynamics, the averaged effect of electronic movements is sufficient.

In a molecular system consisting of M atomic nuclei with masses M_α , charges Z_α and spins $\{\vec{\Sigma}_\alpha\}$, located at positions $\{\vec{R}_\alpha\}$ (noted as combination $\vec{Q} = \{\vec{R}_\alpha, \vec{\Sigma}_\alpha\}$) and N electrons with spins $\{\vec{\sigma}_i\}$ at positions $\{\vec{r}_i\}$ (noted as $\vec{q} = \{\vec{r}_i, \vec{\sigma}_i\}$), the probability distribution $P(\vec{Q}, \vec{q})$ of \vec{Q} and \vec{q} , could be expressed in terms of the probability distribution $\pi(\vec{Q})$ for \vec{Q} :

$$P(\vec{Q}, \vec{q}) = \pi(\vec{Q}) \frac{P(\vec{Q}, \vec{q})}{\pi(\vec{Q})} = \pi(\vec{Q}) p(\vec{q}|\vec{Q}), \quad (2.1)$$

where $p(\vec{q}|\vec{Q})$ is the conditional probability of \vec{q} at \vec{Q} . Since the probability $P(\vec{Q}, \vec{q})$ is the square of modulus of the wavefunction $\Psi(\vec{Q}, \vec{q})$ of the system:

$$P(\vec{Q}, \vec{q}) = |\Psi(\vec{Q}, \vec{q})|^2, \quad (2.2)$$

this function could be approximated by the product of nuclear function χ and electronic func-

tion φ :

$$\Psi(\vec{Q}, \vec{q}) \approx \chi(\vec{Q})\varphi(\vec{q}; \vec{Q}). \quad (2.3)$$

The Hamiltonian of the system has the following form:

$$\hat{H} = \hat{T}_n(\vec{Q}) + \left[\hat{T}_e(\vec{q}) + \hat{V}_{ne}(\vec{q}, \vec{Q}) + \hat{V}_{ee}(\vec{q}) + \hat{V}_{nn}(\vec{Q}) \right] = \hat{T}_n(\vec{Q}) + \hat{H}_e(\vec{q}, \vec{Q}), \quad (2.4)$$

where $\hat{T}_n(\vec{Q})$ is the kinetic energy of nuclei, $\hat{T}_e(\vec{q})$ is the kinetic energy of electrons, $\hat{V}_{ne}(\vec{q}, \vec{Q})$ is the attraction potential energy between nuclei and electrons, $\hat{V}_{ee}(\vec{q})$ is the repulsion energy between electrons, $\hat{V}_{nn}(\vec{Q})$ is the repulsion energy between nuclei and $\hat{H}_e(\vec{q}, \vec{Q})$ is the electronic part of the Hamiltonian (it contains $\hat{V}_{nn}(\vec{Q})$ due to the fact, that this term is constant for fixed values of \vec{Q}).

The crude Born-Oppenheimer approximation assumes that the expected value of \hat{T}_n acting on the φ function is 0. After insertion of equation 2.3 into the Schrödinger equation and integration over the \vec{q} values, the effective Schrödinger equation for $\chi(\vec{Q})$ is obtained:

$$\left[\hat{T}_n(\vec{Q}) + U_e(\vec{Q}) \right] \chi(\vec{Q}) = E \chi(\vec{Q}), \quad (2.5)$$

where $U_e(\vec{Q})$ is the expectation value of the electronic Hamiltonian \hat{H}_e :

$$U_e(\vec{Q}) = \langle \varphi(\vec{q}; \vec{Q}) | \hat{H}_e(\vec{q}, \vec{Q}) | \varphi(\vec{q}; \vec{Q}) \rangle_{\vec{q}}, \quad (2.6)$$

called the Potential Energy Surface (PES) [242].

2.1.2 Classical Molecular Dynamics

Molecular Dynamics (MD) methods are based on the Born-Oppenheimer approximation. Classical MD simplifies the problem given by the equation 2.5 even more: here the Schrödinger equation is not used at all, and the atomic nuclei are treated as classical objects moving in the potential field $V(\vec{Q})$. Forces acting on them are calculated using the equation:

$$\vec{F}_\alpha = -\nabla_\alpha V(\vec{Q}), \quad (2.7)$$

and then, according to the Newton's second law of dynamics accelerarions acting on the nuclei are determined:

$$M_\alpha \vec{R}_\alpha = \vec{F}_\alpha. \quad (2.8)$$

Perfomation of a simulation of evolution of a system over time is in fact, a problem of solving differential equations with given initial conditions with the use of numerical methods. Thus, time becomes discrete and during an arbitrarily chosen timestep Δt the forces acting on the nuclei are constant. As a starting point one needs also to know the initial positions and velocities of atoms; the former are defined by the starting geometry, while the latter are usually randomly chosen from the Maxwell-Boltzmann distribution for a specified value of the system's

temperature [243].

Different classical MD approaches use different functions $V(\vec{Q})$ to calculate the potential energy of the system for given nucleus positions. The functional form of $V(\vec{Q})$, together with parameters, is called the Force Field (FF).

Typical FFs contain terms describing the "bonded interactions" (such as changes of bond lengths, angles, dihedrals, as well as improper dihedrals) and the "non-bonded interactions" (electrostatic and van der Waals interactions). In non-polarizable FFs, the electrostatic part is the energy of permanent electric charges interactions in the system. Polarizable FFs additionally contain terms with interactions between induced dipoles (or higher multipoles). The parameters for FFs are obtained from QC calculations or by fitting them to reproduce experimental data.

An example of polarizable FF is the APPLE&P FF [138, 139, 142] developed for simulations of electrolytes and ionic liquids (ILs). In this FF the potential energy is defined as a following sum:

$$U_e(\vec{Q}) = U^{\text{NB}}(\vec{Q}) + \sum_{\text{bonds}} U^{\text{BEND}}(\theta_{ijk}) + \sum_{\text{dihedrals}} U^{\text{DIHEDRAL}}(\varphi_{ijkl}) + \sum_{\text{improper dih.}} U^{\text{IMP}}(\varphi_{ijkl}^{\text{imp}}), \quad (2.9)$$

where the sums include bonds, dihedrals, improper dihedrals (used for forcing planar structure) and nonbonded energy $U^{\text{NB}}(\vec{Q})$. These terms are expressed as follows:

$$U^{\text{BEND}}(\theta_{ijk}) = \frac{1}{2} k_{\alpha\beta\gamma}^{\text{BEND}} (\theta_{ijk} - \theta_{ijk}^0)^2, \quad (2.10)$$

$$U^{\text{DIHEDRAL}}(\varphi_{ijkl}) = \sum_t \frac{1}{2} k_{\alpha\beta\gamma,t}^{\text{DIHEDRAL}} [1 - \cos(t\varphi_{ijkl})], \quad (2.11)$$

$$U^{\text{IMP}}(\varphi_{ijkl}^{\text{imp}}) = \frac{1}{2} k_{\alpha\beta\gamma\delta}^{\text{IMP}} (\varphi_{ijkl}^{\text{imp}})^2, \quad (2.12)$$

where θ_{ijk} and θ_{ijk}^0 are bending angles (instantaneous and equilibrium) for atoms i , j and k , φ_{ijkl} is the dihedral angle for atoms i , j , k and l and $\varphi_{ijkl}^{\text{imp}}$ is the out-of-plane bending angle for atoms i , j , k and l where sp^2 center is at atom j . The values of $k_{\alpha\beta\gamma}^{\text{BEND}}$, $k_{\alpha\beta\gamma\delta}^{\text{DIHEDRAL}}$ and $k_{\alpha\beta\gamma\delta}^{\text{IMP}}$ denote the force constants for these interactions and the indices α , β , γ and δ denote the atom type for i , j , k and l . The term $U^{\text{NB}}(\vec{q})$ stands for the potential of non-bonded interactions and is expressed as:

$$U^{\text{NB}}(\vec{Q}) = U^{\text{RD}}(\vec{Q}) + U^{\text{coul}}(\vec{Q}) + U^{\text{pol}}(\vec{Q}), \quad (2.13)$$

where $U^{\text{RD}}(\vec{Q})$ stands for two-body dispersion energy, $U^{\text{coul}}(\vec{Q})$ for the Coulomb energy between fixed charges and $U^{\text{pol}}(\vec{Q})$ for the polarization energy appearing from the interaction between induced dipoles. The last term is calculated in a self-consistent determination of the induced dipoles in the potential field of all other charges and dipoles in the system.

Another approach to include polarizability in MD is to use Drude oscillators [143]. In this method, the polarizability α of a given atom with partial charge q is modeled by adding to this atom a so-called Drude particle with charge q_D . This particle is harmonically bound to the atom

with a force constant k_D . Parameters of Drude particle are chosen in a way to fulfill:

$$\alpha = \frac{q_D^2}{k_D}. \quad (2.14)$$

Usually, the force constant k_D is chosen in a way that the displacement \vec{d} between the Drude particle and the given atom is smaller than any interatomic distance in the system. With this condition, the pair atom-Drude particle behaves like an induced dipole. The partial charge of an atom is changed to $q - q_D$ to conserve the entire charge of the system. In this approach, the potential energy $U_e(\vec{Q}, \vec{d})$ has the following form:

$$U_e(\vec{Q}) = U_{\text{self}}(\vec{d}) + U_{\text{bond}}(\vec{Q}) + U_{\text{elec}}(\vec{Q}, \vec{d}) + U_{\text{LJ}}(\vec{Q}), \quad (2.15)$$

where $U_{\text{self}}(\vec{d})$ is the atom-Drude harmonic bonds energy, $U_{\text{bond}}(\vec{Q})$ is the energy of bonded interactions, $U_{\text{elec}}(\vec{Q}, \vec{d})$ corresponds to all Coulombic interactions (atom-atom, atom-Drude, Drude-Drude) and $U_{\text{LJ}}(\vec{Q})$ is the Lennard-Jones potential.

The quality of the results obtained from the FF-based MD is highly dependent on the FF used (its form and parameters). General FF parameterizations (e.g., UFF [244]) yield only limited accuracy. In practice, the parameters of the FF need to be tailored for a class of compounds or even for a particular system (especially if specific interactions have to be modeled). Therefore, the application of classical MD to new systems is usually not straightforward and often requires FF optimization.

Classical MD has been implemented in several software packages such as Tinker [245], NAMD [246], GROMACS [247], AMBER [248], CHARMM [249], and LAMMPS [250].

2.1.3 Ab initio Molecular Dynamics

In the ab initio MD (AIMD) approach, FF is not used. Instead, at least once during the simulation, the electronic Schrödinger equation (equation 2.6) is solved and from obtained wavefunctions/electronic density the potential acting on atomic nuclei is determined:

$$M_\alpha \vec{\dot{R}}_\alpha = -\nabla_\alpha \min_{\varphi} \langle \varphi(\vec{q}; \vec{Q}) | \hat{H}_e | \varphi(\vec{q}; \vec{Q}) \rangle. \quad (2.16)$$

For solving this equation, quantum chemical methods are used, usually these based on the Density Functional Theory (DFT). Without the need to develop the FF, AIMD is in principle applicable to any chemical system. The quality of the results depends on the level of theory (QC method, basis set) used to calculate the PES. Therefore, AIMD can properly take into account specific interactions, such as hydrogen bonding, provided that an appropriate QC method is used.

Two main approaches are Car-Parinello MD and Born-Oppenheimer MD [251] (BOMD). In the former, the equation 2.6 is solved once at the beginning of the simulation and then is changed by a law similar to Newton's second law, whereas in the latter the electronic wavefunctions are determined for every time step of the simulation. Calculation of the IR spectrum from

MD simulations requires accuracy beyond that typically provided by classical FF-based MD. Therefore, in this work, BOMD was used for this purpose.

AIMD is available to perform in some computational packets, for example, CPMD [252], CP2K [253], or Quantum Espresso [254, 255].

2.1.4 Pseudopotentials

In studying interactions, usually the valence electrons are important, and inner shell electrons are inert. Thus, to speed up AIMD simulations, commonly so-called pseudopotentials are used that replace the behavior of the inner shell electrons. In this work, the pseudopotential family developed by Goedecker et. al. [256–258] are used. These pseudopotentials are generally divided into two parts for every element: the local and non-local one. For example, for hydrogen atom and PBE [259–262] functional, there is only the local part in a form:

$$V_{\text{loc}}(r) = -\frac{1}{r} \text{erf}\left(\frac{r}{\sqrt{2}r_{\text{loc}}}\right) e^{-\frac{1}{2}\left(\frac{r}{r_{\text{loc}}}\right)^2} \left(C_1 + C_2 \left(\frac{r}{r_{\text{loc}}}\right)^2\right), \quad (2.17)$$

where r_{loc} is the range of Gaussian ionic charge distribution and equal here 0.2 Bohr and C_1 and C_2 are coefficients, equal in this case -4.17890044 and 0.72446331 respectively [258].

Non-local form includes sum of Gaussian-type projectors products:

$$V_{\text{non-loc}}(\vec{r}, \vec{r}') = \sum_{lm} \sum_{ij} p_i^{lm}(\vec{r}) h_{ij}^l p_j^{lm*}(\vec{r}'), \quad (2.18)$$

where Gaussian-type projectors $p_i^{lm}(\vec{r})$ have the following form:

$$p_i^{lm}(\vec{r}) = N_i^l Y^{lm}(\hat{r}) r^{l+2i-2} e^{-\frac{1}{2}\left(\frac{r}{r_l}\right)^2}, \quad (2.19)$$

where N_i^l is the normalization constant, Y^{lm} is the spherical harmonic for quantum numbers l and m and r_l with h_{ij}^l are the parameters for given parts of the pseudopotential. For example, for boron and PBE functional atom only $l = 1$ is included with one term for each m :

$$V_{\text{non-loc}}(\vec{r}, \vec{r}') = \sum_{m \in \{-1, 0, 1\}} p_1^{1m}(\vec{r}) h_{11}^1 p_1^{1m*}(\vec{r}'), \quad (2.20)$$

with h_{11}^1 equal 6.29728018 and r_1 is equal 0.37132046 Bohr.

2.1.5 Plane waves

In MD simulations of condensed phase (e.g. liquids), usually the periodic boundary conditions (PBC) are applied. In such cases, it is convenient to express the wavefunctions in AIMD as plane waves. When a simulation cell is defined by vectors \vec{a}_1 , \vec{a}_2 and \vec{a}_3 , for vector $\vec{L} = h\vec{a}_1 + k\vec{a}_2 + l\vec{a}_3$

with $h, k, l \in \mathbb{Z}$, the wavefunctions ϕ satisfy the condition:

$$\phi(\vec{r}) = \phi(\vec{r} + \vec{L}). \quad (2.21)$$

With defining the reciprocal lattice with basis vectors \vec{b}_1, \vec{b}_2 and \vec{b}_3 :

$$\vec{a}_i \cdot \vec{b}_j = 2\pi\delta_{ij}, \quad (2.22)$$

and the basis of orthonormal plane waves $f_{\vec{G}}$:

$$f_{\vec{G}}(\vec{r}) = \frac{1}{\sqrt{\Omega}} e^{i\vec{G}\cdot\vec{r}}, \quad (2.23)$$

$$\vec{G} = p\vec{b}_1 + q\vec{b}_2 + r\vec{b}_3, \quad p, q, r \in \mathbb{Z}, \quad (2.24)$$

where Ω is the volume of the simulation box, any periodic function with the same period as the simulation box could be expressed as a linear combination:

$$\phi(\vec{r}) = \frac{1}{\sqrt{\Omega}} \sum_{\vec{G}} \phi(\vec{G}) e^{i\vec{G}\cdot\vec{r}}. \quad (2.25)$$

In the periodic potential $V(\vec{r}) = V(\vec{r} + \vec{L})$, the Bloch theorem states that, electronic wavefunctions have the form:

$$\phi(\vec{r}) = e^{i\vec{k}\cdot\vec{r}} u(\vec{r}), \quad (2.26)$$

where \vec{k} is a vector from the first Brillouin zone of the reciprocal lattice, and $u(\vec{r})$ is a function with the same periodicity as the lattice. Using equation 2.25, the wavefunction could be expressed as:

$$\phi(\vec{r}) = \frac{1}{\sqrt{\Omega}} \sum_{\vec{G}} c(\vec{G}) e^{i(\vec{G} + \vec{k})\cdot\vec{r}}. \quad (2.27)$$

For practical reasons, the basis is limited by arbitrarily cutoff E_{cut} , and contains only functions satysfying:

$$\frac{1}{2} |\vec{k} + \vec{G}| \leq E_{\text{cut}}. \quad (2.28)$$

2.1.6 Thermostating

One of typical set-ups in MD are the simulations at an arbitrarily set value of the system temperature. However, equation 2.16 has no term controlling this quantity, what may cause that at some point system atoms reach points at the PES with high differences in energy and increase rapidly their velocities. This leads to an increase in the temperature and might end in the disintegration of the simulated system.

To avoid such problems, thermostats were developed. In the simplest case, the velocities are rescaled in specified time intervals to keep the set temperature [263]. The more sophisticated method, used for the purpose of this work, is the Nosé-Hoover thermostat [251, 264–266]. Here,

additional fictitious positions η_i and velocities ν_{η_i} are added into the system acting as a thermal bath, in number called the chain length K . In this approach, the equation 2.16 is modified by adding a new term [267–269]:

$$M_\alpha \vec{R}_\alpha = -\nabla_\alpha \min_{\varphi} \langle \varphi(\vec{q}; \vec{Q}) | \hat{H}_e | \varphi(\vec{q}; \vec{Q}) \rangle - \nu_{\eta_1} M_\alpha \vec{R}_\alpha, \quad (2.29)$$

where additional degrees of freedom satisfy the chain of equations:

$$Q_1 \dot{\nu}_{\eta_1} = \left(\sum_{\alpha=1}^M M_\alpha \vec{R}_\alpha^2 - g k_B T \right) - \nu_{\eta_2} Q_1 \nu_{\eta_1}, \quad (2.30)$$

$$Q_j \dot{\nu}_{\eta_j} = \left(Q_{j-1} \nu_{\eta_{j-1}}^2 - k_B T \right) - \nu_{\eta_{j+1}} Q_j \nu_{\eta_j}, \quad (2.31)$$

$$Q_K \dot{\nu}_{\eta_K} = \left(Q_{K-1} \nu_{\eta_{K-1}}^2 - k_B T \right), \quad (2.32)$$

$$\dot{\eta}_j = \nu_{\eta_j}, \quad (2.33)$$

where g is the number of nuclear degrees of freedom, k_B the Boltzmann constant, T given temperature and Q_j are the fictitious masses of thermostat defined by a relation:

$$Q_1 = \frac{M k_B T}{\omega_{th}^2}, \quad (2.34)$$

$$Q_j = \frac{k_B T}{\omega_{th}^2}, \quad j \neq 1, \quad (2.35)$$

where ω_{th} is the thermostat frequency chosen as a typical phonon or vibrational frequency in given system (usually between 2000 and 4000 cm⁻¹). The fictitious velocity ν_{η_1} in the equation 2.29, acts as a dynamical friction coefficient decelerating or accelerating atoms depending on their current velocity [264].

2.1.7 Structural properties

In the canonical statistical ensemble (NVT) with N particles in constant volume V and constant temperature T , the partition function Z_N has the following form:

$$Z_N = \int \dots \int e^{-\frac{U_N}{k_B T}} d^3 \vec{r}_1 \dots d^3 \vec{r}_N, \quad (2.36)$$

where U_B stands for the potential energy of the system.

For a set of identical particles, the probability of finding any particle of the first kind at \vec{r}_1 and any particle of second kind at \vec{r}_2 is equal:

$$\rho^{(2)}(\vec{r}_1, \dots, \vec{r}_N) = \frac{N!}{Z_N (N-2)!} \int \dots \int e^{-\frac{U_N}{k_B T}} d^3 \vec{r}_3 \dots d^3 \vec{r}_N, \quad (2.37)$$

for a liquid system of non-interacting particles this quantity is equal to the square of the system's

density ρ . Interactions between particles affect this probability, in this case equation 2.37 is modified by introducing the radial pair distribution function (RDF) $g(r_{12})$:

$$\rho^{(2)}(\vec{r}_1, \dots, \vec{r}_N) = \rho^2 g(r_{12}) = \left(\frac{N}{V}\right)^2 g(r_{12}), \quad (2.38)$$

thus:

$$g(r_{12}) = \frac{V^2 N!}{Z_N N^2 (N-2)!} \int \dots \int e^{-\frac{U_N}{k_B T}} d^3 \vec{r}_3 \dots d^3 \vec{r}_N. \quad (2.39)$$

This function is normalized:

$$\lim_{r_{12} \rightarrow \infty} g(r_{12}) = 1. \quad (2.40)$$

The pair number n_p dependence on the distance, which is used in this work to calculate coordination numbers, is calculated as the following integral [270]:

$$n_p(r) = 4\pi \rho^2 \int_0^r r_{12}^2 g(r_{12}) dr_{12}. \quad (2.41)$$

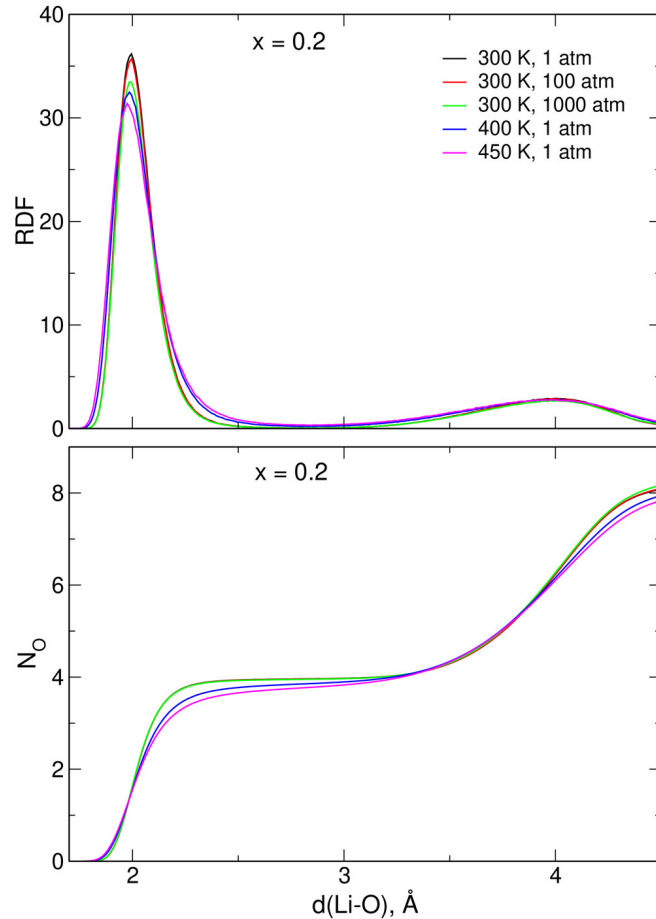


Figure 2.1: Example RDF (top) and integrated RDF (bottom) for Li-O pairs in LiTFSI solution in EMIM-TFSI IL with molar fraction of the salt equal 0.2 in different temperatures and pressures [A]

For data obtained from MD simulation, RDFs are usually obtained by calculating and nor-

malizing a histogram of interatomic distances between specified pair of atoms [271]. An example of such relations is presented in Figure 2.1.

Another class of particle density histograms are spatial distribution functions (SDFs). In the TRAVIS [272, 273] tool used in this work for obtaining such relations, it is calculated by defining a local coordinate system based on arbitrarily chosen three points of given molecule and afterwards, computing the average particle density of some other molecules/atoms around the molecule of choice. Results are volumetric data, thus only isosurfaces are plotted. Such functions were used for the analysis in section 3.6.

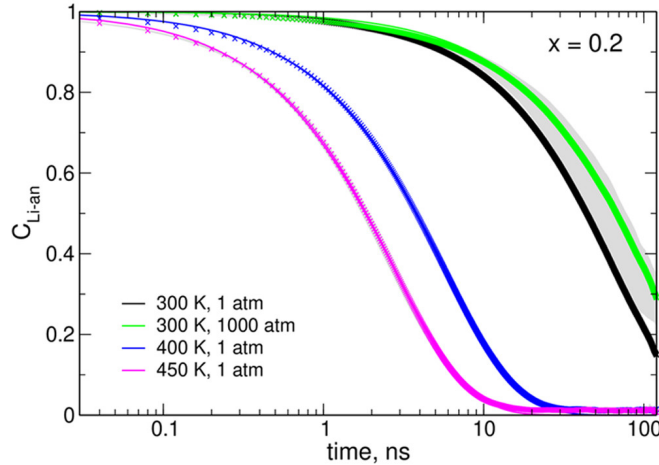


Figure 2.2: Lithium-TFSI[−] residence time autocorrelation functions (symbols) and exponential fits to the data (lines), in LiTFSI solution in EMIM-TFSI IL with molar fraction of the salt equal 0.2 and different temperatures and pressures [A]

For qualitative analysis of the stability of interactions between objects (atoms or molecules) A and B (dynamics of the exchange of B in the solvation shell of A), at this work residence time autocorrelation functions $C_{A-B}(t)$ are calculated as:

$$C_{A-B}(t) = \frac{\langle H_{ij}(t)H_{ij}(0) \rangle}{\langle H_{ij}(0)H_{ij}(0) \rangle}, \quad (2.42)$$

where $H_{ij}(t) = 1$, if at time t the distance between the i-th atom A and the j-th atom B is lower than a threshold distance d_{thr} or $H_{ij}(t) = 0$ otherwise. Angle brackets indicate averaging over every possible A-B pair and over all possible choices of $t = 0$ within the simulation. Usually, to the obtained $C_{A-B}(t)$ relation, a stretched exponential function in form $e^{-\left(\frac{t}{t_r}\right)^\alpha}$ is fitted, where t_r is called the residence time. An example of such calculated functions are presented in Figure 2.2.

2.1.8 Infrared spectra from MD

From equation 1.2 it follows that the intensity in the IR spectrum is proportional to the change in dipole moment associated with a given vibration. Therefore, to calculate this spectrum from the MD simulation, at every timestep the dipole moment $\vec{\mu}$ of the whole system is calculated. From the autocorrelation function of $\vec{\mu}$, the band shape function $I(\nu)$ is calculated as the following

Fourier transform [274, 275]:

$$I(\nu) = \frac{1}{2\pi} \int_{-\infty}^{+\infty} \langle \vec{\mu}(0) \cdot \vec{\mu}(t) \rangle e^{-2\pi i \nu t} dt. \quad (2.43)$$

Then this function is used for calculation of the absorption coefficient $\alpha(\nu)$ [274, 276]:

$$\alpha(\nu) = \left(\frac{16\pi^4 \nu}{3\Omega h c n(\nu)} \right) \left(1 - e^{-\frac{h\nu}{k_B T}} \right) Q(\nu) I(\nu), \quad (2.44)$$

where h - Planck constant, k_B - Boltzmann constant, T - the temperature of the system, $n(\nu)$ - refraction index, c - velocity of light, Ω - simulation box volume and $Q(\nu)$ - correction function. In this work, the harmonic correction function is used [276, 277]:

$$Q(\nu) = \frac{\frac{h\nu}{k_B T}}{1 - e^{-\frac{h\nu}{k_B T}}}. \quad (2.45)$$

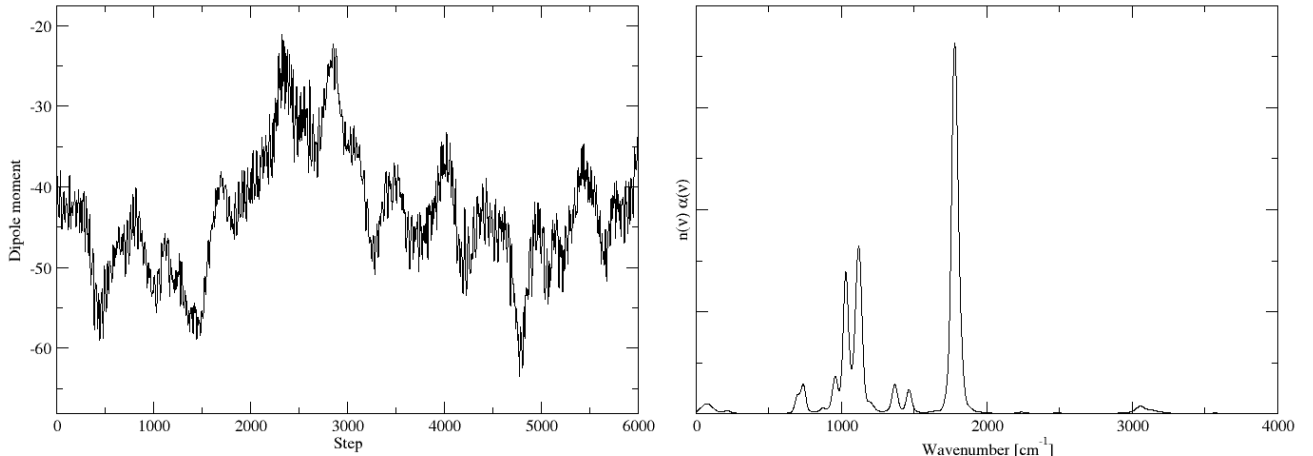


Figure 2.3: Example of dipole moment dependence on time of the simulation (left) and obtained from it IR spectrum (right) for the system with ethylene carbonate

In general, the value of $n(\nu)$ and its dependence on the frequency is unknown; therefore, the IR spectra obtained from MD simulations are usually presented as the dependence of the product $\alpha(\nu)n(\nu)$ on the frequency ν . An example of changes in the dipole moment over the simulation time and the obtained IR spectrum is shown in Figure 2.3.

To obtain the contribution of a particular oscillation (change of bond length or of valence angle) to the IR spectrum, one needs to know the partial charges on the atoms involved in this vibration. In AIMD these may be obtained with the use of Wannier functions. They are, in general, the localized variant of the Bloch functions described by equation 2.25 [278]. The use of these functions requires additional computational cost and, in the case of research described in this work, there were problems with the stability of this approach for ILs. Thus, a simpler analysis based on calculations of Fourier transforms (FTs) of particular geometric parameters such as bond lengths or angles is utilized for described systems. An example is presented in Figure 2.4. Here, it could be observed, that S-F stretching has a contribution to modes near

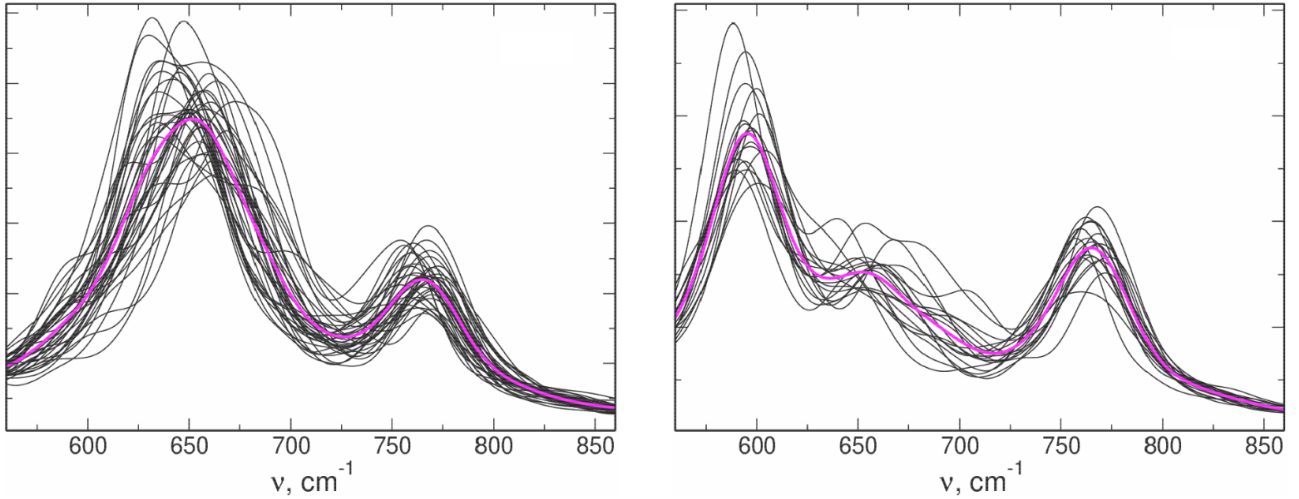


Figure 2.4: Fourier transforms of the S-F bond length and S-N-S angles of FSI^- anions in the EMIM-FSI ionic liquid. Magenta line is the average $[\mathbf{I}]$

650 and 770 cm^{-1} and changes of the S-N-S angle contribute mainly to modes near 600 and 770 cm^{-1} . Oscillation frequencies are different for distinct molecules and it is possible to study correlations between these frequencies and the local environment of molecules. It is worth noting that this approach gives only frequencies of vibrations without their intensities as it does not consider changes of dipole moment. One of the advantages of this method is that it can be easily applied a posteriori to a recorded MD trajectory of any kind.

2.2 Density Functional Theory

The electron density for N electron system described by the wavefunction Ψ is defined as:

$$\rho(\vec{r}) = \langle \Psi | \sum_{i=1}^N \delta(\vec{r}_i - \vec{r}) | \Psi \rangle, \quad (2.46)$$

and is an observable possible for measurement in the diffraction experiment.

With knowledge of the $\rho(\vec{r})$ it is possible to determine the positions of atomic nuclei, because radial electron density $\rho_{\text{rad}}(r)$:

$$\rho_{\text{rad}}(r) = \frac{1}{4\pi} \int_0^\pi \int_0^{2\pi} \rho(\vec{r}) d\vartheta d\varphi, \quad (2.47)$$

satisfies the nuclear cusp condition:

$$\lim_{r_\alpha \rightarrow 0} \left[\left(\frac{\partial}{\partial r_\alpha} + 2Z_\alpha \right) \rho(r_\alpha) \right] = 0, \quad (2.48)$$

$$r_\alpha = |\vec{r} - \vec{R}_\alpha|, \quad (2.49)$$

where Z_α is the charge of the nucleus at the position \vec{R}_α .

It was realized that it is possible to use formalism based on utilizing electron density instead of wavefunctions, which is consistent with quantum mechanics. The first Hohenberg-Kohn theorem states that [279]:

Theorem 1 *The external potential ν is uniquely determined to an additive constant by the non-degenerated ground state density ρ_0 .*

So, the mapping from potential ν to wavefunction Ψ and then to density ρ is reversible.

The second theorem provides the variational principle [279]:

Theorem 2 *The exact electronic energy $E[\rho]$ is the lower bound for energies $E_\nu[\rho']$ obtained for any probe ρ' density (reproducing the ν).*

These theorems are the fundamentals of the Density Functional Theory (DFT) which is an alternative to quantum mechanics based on wavefunctions.

The nuclear-electron potential energy in equation 2.4 can be defined as:

$$\hat{V}_{ne} = - \sum_{i=1}^N \sum_{\alpha=1}^M \frac{Z_\alpha}{|\vec{R}_\alpha - \vec{r}_i|} = \sum_{i=1}^N \nu_i, \quad (2.50)$$

and its average energy expressed in terms of $\rho(\vec{r})$:

$$\langle \Psi | \hat{V}_{ne} | \Psi \rangle = \langle \Psi | \sum_{i=1}^N \nu_i | \Psi \rangle = \int_{\mathbb{R}^3} \nu(\vec{r}) \rho(\vec{r}) d^3 \vec{r}. \quad (2.51)$$

According to the variational principle, the energy E_0 could be expressed as:

$$E_0 = \min_{\rho} \left[\int_{\mathbb{R}^3} \nu(\vec{r}) \rho(\vec{r}) d^3 \vec{r} + F^{\text{HK}}[\rho] \right] = \min_{\rho} E_\nu^{\text{HK}}[\rho], \quad (2.52)$$

where $F^{\text{HK}}[\rho]$ is the universal functional:

$$F^{\text{HK}}[\rho] = \min_{\Psi \rightarrow \rho} \langle \Psi | \hat{T}_e + \hat{V}_{ee} | \Psi \rangle. \quad (2.53)$$

In general, it is only known that $F^{\text{HK}}[\rho]$ correctly reproducing the system's energy exists, but its exact form is unknown. Thus in practical calculations, different approximations of it are used [242].

2.2.1 Kohn-Sham method

In the system of N noninteracting electrons with the potential ν_0 enforcing that the density ρ is identical with the density of the real considered ground state, the eigenproblem of Hamiltonian becomes one-electron problem:

$$\left(-\frac{1}{2} \Delta + \hat{\nu}_0 \right) \phi_i = \varepsilon_i \phi_i, \quad (2.54)$$

where ϕ_i are the Kohn-Sham spinorbitals. The wavefunction of the whole system is defined as the Slater determinant of Kohn-Sham spinorbitals.

Introducing T_0 as the kinetic energy of noninteracting electrons, $J[\rho]$ as the classic energy of interaction of electron density with itself and $E_{xc}[\rho]$ as the functional containing all other contributions to the system's energy:

$$T_0 = -\frac{1}{2} \sum_{i=1}^N \langle \phi_i | \Delta_i | \phi_i \rangle, \quad (2.55)$$

$$J[\rho] = \frac{1}{2} \int_{\mathbb{R}^3} \int_{\mathbb{R}^3} \frac{\rho(\vec{r}_1)\rho(\vec{r}_2)}{|\vec{r}_1 - \vec{r}_2|} d^3\vec{r}_1 d^3\vec{r}_2, \quad (2.56)$$

the energy of the system can be written in form:

$$E_0 = T_0 + \int_{\mathbb{R}^3} \nu(\vec{r})\rho(\vec{r})d^3\vec{r} + J[\rho] + E_{xc}[\rho]. \quad (2.57)$$

By calculation of energy variation with varying the conjugated orbitals ϕ_i^* , setting it as zero and making an unitary transformation of the orbitals, Kohn-Sham equations are obtained:

$$\left[-\frac{1}{2}\Delta + \nu + \sum_{j=1}^N \hat{J}_j + \frac{\delta E_{xc}}{\delta \rho} \right] \phi_i = \varepsilon_i \phi_i, \quad (2.58)$$

with \hat{J}_j :

$$\hat{J}_j(\vec{r}_2) = \sum_{\sigma_1} \int_{\mathbb{R}^3} \frac{\phi_j^*(\vec{r}_1, \sigma_1) \phi_j(\vec{r}_1, \sigma_1)}{|\vec{r}_1 - \vec{r}_2|} d^3\vec{r}_1. \quad (2.59)$$

Using symbols:

$$\hat{\nu}_{\text{coulomb}} = \sum_{j=1}^N \hat{J}_j, \quad (2.60)$$

$$\hat{\nu}_{\text{xc}} = \frac{\delta E_{xc}}{\delta \rho}, \quad (2.61)$$

the Kohn-Sham equations could be rewritten in the following form:

$$\left[-\frac{1}{2}\Delta_i + \nu + \hat{\nu}_{\text{coulomb}} + \hat{\nu}_{\text{xc}} \right] \phi_i = \varepsilon_i \phi_i. \quad (2.62)$$

Due to the fact that the operators $\hat{\nu}_{\text{coulomb}}$ and $\hat{\nu}_{\text{xc}}$ depend on the orbitals ϕ_i , this equation is solved iteratively [242].

Since the development of the DFT, many different forms of E_{xc} functional have been published. They are organized in the so-called Jacob's ladder of functionals, consisting of 5 rungs. The first are functionals that include only the ρ (Local Density Approximation — LDA). The second take into consideration also its gradient $|\nabla\rho|$ (Generalized Gradient Approximation — GGA). The next rung are meta-GGA approaches where the square of gradient of ρ is also used.

Another step towards improved accuracy of results are hybrid (or hyper-GGA) functionals, where the results of the DFT functionals are mixed with exact results, e.g., in B3LYP where the Hartree-Fock exchange energy is used as the exact one [280–283]. The most accurate functionals are called generalized RPA and they also consider unoccupied Kohn-Sham orbitals. The PBE functional used in this work belongs to the GGA group [259–262].

The dispersion energy is not included in standard Kohn-Sham calculations, but its contribution to the energy can be approximated using Grimme's correction [175].

2.3 Density Functional based Tight-Binding

The total energy of a system in DFT is equal:

$$E[\rho] = \sum_{i=1}^N \langle \phi_i | \left(-\frac{1}{2} \Delta + \int_{\mathbb{R}^3} \nu \right) | \phi_i \rangle + J[\rho] + E_{xc}[\rho] + E_{nn}, \quad (2.63)$$

where E_{nn} is the interaction energy between atomic nuclei.

In a system where all of the atoms are free and neutral, the electron density is equal ρ_0 and differs from the true density ρ by a term $\delta\rho$. It is interpreted as ρ_0 is a density of the system without any charge transfer, while $\delta\rho$ represents charge fluctuation.

After expansion of $E[\rho]$ around ρ_0 to second order in $\delta\rho$:

$$\begin{aligned} E[\delta\rho] \approx & \sum_{i=1}^N \langle \phi_i | \left(-\frac{1}{2} \Delta + \nu + \hat{\nu}_{\text{coulomb}}[\rho_0] + \hat{\nu}_{\text{xc}}[\rho_0] \right) | \phi_i \rangle + \\ & + \frac{1}{2} \int_{\mathbb{R}^3} \int_{\mathbb{R}^3} \left(\frac{\delta^2 E_{xc}[\rho_0]}{\delta \rho_1 \delta \rho_2} + \frac{1}{|\vec{r}_1 - \vec{r}_2|} \right) \delta \rho_1 \delta \rho_2 d^3 \vec{r}_1 d^3 \vec{r}_2 + \\ & - \frac{1}{2} \int_{\mathbb{R}^3} \hat{\nu}_{\text{coulomb}}[\rho_0](\vec{r}) \rho_0(\vec{r}) d^3 \vec{r} + E_{xc}[\rho_0] + E_{nn} + \\ & - \int_{\mathbb{R}^3} \hat{\nu}_{\text{xc}}[\rho_0](\vec{r}) \rho_0(\vec{r}) d^3 \vec{r}. \end{aligned} \quad (2.64)$$

The first component of the sum in the equation 2.64 is called the band-structure energy E_{BS} :

$$E_{BS}[\delta\rho] = \sum_{i=1}^N \langle \phi_i | H[\rho_0] | \phi_i \rangle, \quad (2.65)$$

where the Hamiltonian $H[\rho_0]$ does not depend on the fluctuation $\delta\rho$. The second term in equation 2.64 is the energy from charge fluctuations $E_{\text{fluct}}[\delta\rho]$:

$$E_{\text{fluct}}[\delta\rho] = \frac{1}{2} \int_{\mathbb{R}^3} \int_{\mathbb{R}^3} \left(\frac{\delta^2 E_{xc}[\rho_0]}{\delta \rho_1 \delta \rho_2} + \frac{1}{|\vec{r}_1 - \vec{r}_2|} \right) \delta \rho_1 \delta \rho_2 d^3 \vec{r}_1 d^3 \vec{r}_2, \quad (2.66)$$

and the remaining terms are called repulsive energy E_{rep} :

$$E_{\text{rep}} = -\frac{1}{2} \int_{\mathbb{R}^3} \hat{\nu}_{\text{coulomb}}[\rho_0](\vec{r}) \rho_0(\vec{r}) d^3\vec{r} + E_{\text{xc}}[\rho_0] + E_{\text{nn}} - \int_{\mathbb{R}^3} \hat{\nu}_{\text{xc}}[\rho_0](\vec{r}) \rho_0(\vec{r}) d^3\vec{r}. \quad (2.67)$$

Thus:

$$E[\delta\rho] = E_{\text{BS}}[\delta\rho] + E_{\text{fluct}}[\delta\rho] + E_{\text{rep}}. \quad (2.68)$$

In the so-called zeroth-order DFTB, the E_{fluct} is neglected.

The last term can be approximated by:

$$E_{\text{rep}} = \sum_{I < J} V_{\text{rep}}^{IJ}(R_{IJ}), \quad (2.69)$$

where $V_{\text{rep}}^{IJ}(R_{IJ})$ is the repulsive function between atoms of type I and J .

Dividing the volume V into partial volumes V_I for every atom:

$$V = \sum_I V_I, \quad (2.70)$$

the difference in electron population Δq_I on atom I is approximately equal:

$$\Delta q_I \approx \int_{V_I} \delta\rho(\vec{r}) d^3\vec{r}. \quad (2.71)$$

By assuming that $\delta\rho_I(r)$ has a Gaussian profile with full width at half maximum equal f_I , the fluctuation term of the energy can be approximated by:

$$E_{\text{fluct}}[\delta\rho] \approx \frac{1}{2} \sum_{I,J} \gamma_{IJ}(R_{IJ}) \Delta q_I \Delta q_J, \quad (2.72)$$

where

$$\gamma_{IJ}(R_{IJ}) = \begin{cases} U_I, & I = J \\ \frac{\text{erf}(C_{IJ}R_{IJ})}{R_{IJ}}, & I \neq J \end{cases}, \quad (2.73)$$

where U_I is equal to the difference between ionization energy (IE) and electron affinity (EA):

$$U_I \approx IE_I - EA_I, \quad (2.74)$$

and the C_{IJ} :

$$C_{IJ} = \sqrt{\frac{4 \ln 2}{f_I^2 + f_J^2}}. \quad (2.75)$$

By expanding orbitals in the basis $\{\chi_\mu\}$:

$$\phi_i(\vec{r}) = \sum_\mu c_\mu^i \chi_\mu(\vec{r}), \quad (2.76)$$

the E_{BS} can be rewritten in the form:

$$E_{\text{BS}} = \sum_{i=0}^N \sum_{\mu\nu} c_{\mu}^{i*} c_{\nu}^i H_{\mu\nu}^0, \quad (2.77)$$

where $H_{\mu\nu}^0$ are parameters of this method.

By finding a minimum of energy given by equation 2.68 with the use of undetermined Lagrange coefficients ϵ_i , an equation analogous to the Kohn-Sham equation in the Density Functional based Tight-Binding (DFTB) is obtained:

$$\sum_{\nu} c_{\nu}^i (H_{\mu\nu} - \epsilon_i S_{\mu\nu}) = 0, \quad (2.78)$$

where $S_{\mu\nu} = \langle \chi_{\mu} | \chi_{\nu} \rangle$ represent elements of the overlap matrix and $H_{\mu\nu}$ is expressed as:

$$H_{\mu\nu} = H_{\mu\nu}^0 + \frac{1}{2} S_{\mu\nu} \sum_K (\gamma_{IK} + \gamma_{JK}) \Delta q_K, \quad \mu \in I, \nu \in J. \quad (2.79)$$

With defining charge fluctuation ζ_I as:

$$\zeta_I = \sum_K \gamma_{IK} \Delta q_K, \quad (2.80)$$

and introducing symbol:

$$h_{\mu\nu}^1 = \frac{1}{2} (\zeta_I + \zeta_J), \quad \mu \in I, \nu \in J, \quad (2.81)$$

equation 2.79 can be rewritten as follows:

$$H_{\mu\nu} = H_{\mu\nu}^0 + h_{\mu\nu}^1 S_{\mu\nu}, \quad (2.82)$$

what can be interpreted as that charge fluctuations shift the element $H_{\mu\nu}$ according to the averaged potentials around μ and ν orbitals [284].

As in the Kohn-Sham method, equation 2.78 is also solved iteratively: from initial guess the starting set of $\{\Delta q_I\}$ is used to obtain $H_{\mu\nu}$ and then $\{c_{\mu}^i\}$ which are used to obtain new values of $\{\Delta q_I\}$ [285, 286]. Thus, this approach is called the Self Consistent Charge (SCC) DFTB approach in opposite to the one neglecting the E_{fluct} term [287]. Including additionally the third order in $\delta\rho$ in equation 2.64 leads to the third-order DFTB method (DFTB3) [288].

DFTB method is available to use in some software packages, for example in CP2K [253] and in DFTB+ [289].

2.3.1 Slater-Koster parameters

DFTB method is semi-empirical one, thus it needs arbitrarily set parameters. In standard cases, these parameters are provided via the so-called Slater-Koster's files, which contain the elements of the Hamiltonian $H_{\mu\nu}^0$ as well as the elements of the overlap matrix $S_{\mu\nu}$ and spline representation

of the repulsive potential $V_{\text{rep}}^{\text{IJ}}(R_{\text{IJ}})$ for every possible element pair in the considered system.

Some sets of parameter with wide uses are available. Among them there are 3ob [290–293], ob2 [294] and mio [295] developed for biological systems and matsci for materials [296]. For specific systems tailored parametrizations were developed, e.g. water-matsci with corrections made to successfully reproduce RDFs for water systems [297].

2.3.2 Extended Tight Binding

The main disadvantage of using DFTB is the necessity of having parameters for every pair of elements present in the system. Thus, for a case with n elements, the number of parameter files is in the order of $\mathcal{O}(n^2)$. Development of own Slater-Koster files is complicated and time-consuming because it needs fitting of the repulsion potential. For the purpose of this work it was a serious problem, because some of the studied systems contained lithium ions, which are not present in any of the publicly available parameter sets.

Due to such limitations of the standard DFTB approach, Grimme et. al. developed the extended Tight Binding (xTB) method [298] in a way that avoids using pair-specific parameters. The main target quantities for xTB are structural properties like vibrational frequencies and noncovalent interactions with extension of the standardly used minimal basis set and keeping the minimal number of parameters. So, this xTB variant is called Geometry, Frequency, Noncovalent, extended Tight-Binding (GFN-xTB). It is applicable to all elements with atomic numbers up to 86, thus it is suitable for all systems studied in this work. It has two types of parameters - global and element-specific ones.

In the GFN-xTB approach, the energy is expressed as the following sum:

$$E = E_{\text{el}} + E_{\text{rep}} + E_{\text{disp}} + E_{\text{XB}}, \quad (2.83)$$

where E_{el} is the electronic energy calculated similarly as in the DFTB3 approach, E_{rep} is atom pairwise repulsion energy, E_{disp} is the dispersion energy and E_{XB} is the energy of halogen bonding.

The repulsion energy is represented by the potential:

$$E_{\text{rep}} = \sum_{A,B} \frac{Z_A^{\text{eff}} Z_B^{\text{eff}}}{R_{AB}} e^{-\sqrt{a_A a_B} (R_{AB})^{k_f}}, \quad (2.84)$$

where Z_A^{eff} and Z_B^{eff} are effective nuclear charges, k_f is a global parameter of this method, a_A and a_B are element specific parameters and R_{AB} is the distance between atoms A and B.

The dispersion energy E_{disp} is computed as in the D3 correction to DFT [175] without three-body terms.

Finally, the halogen bonding energy is represented as a modified Lennard-Jones potential:

$$E_{\text{XB}} = \sum_{\text{XB}} f_{\text{dmp}}^{\text{AXB}} k_X \frac{\left(1 + \left(\frac{R_{\text{cov},AX}}{R_{AX}}\right)^{12} - k_{X2} \left(\frac{R_{\text{cov},AX}}{R_{AX}}\right)^6\right)}{\left(\frac{R_{\text{cov},AX}}{R_{AX}}\right)^{12}}, \quad (2.85)$$

where $R_{\text{cov},AX}$ is the effective covalent distance, k_X and k_{X2} are global parameters, R_{AX} is the distance between halogen bonding acceptor A and the halogen atom X and $f_{\text{dmp}}^{\text{AXB}}$ is the damping function designed in the way that this correction vanishes for nonlinear arrangements of the atoms in a possible halogen bond (A acceptor, X halogen and B the atom bound to X):

$$f_{\text{dmp}}^{\text{AXB}} = \left(\frac{1}{2} - \frac{1}{4} \cos \theta_{\text{AXB}} \right)^6. \quad (2.86)$$

The extended version of the GFN-xTB method called GFN2-xTB was recently published [299]. Furthermore, the variant xTB designed for the calculation of ionization potentials IPEA-xTB was also developed [300].

2.4 Machine Learning

Machine Learning (ML) is a subfield of the more broad field of Artificial Intelligence (AI). In general, it concentrates on the problem of construction of computer programs which are able to learn some knowledge without explicitly programming them for this purpose [301]. The process of learning is defined as follows [302]:

"A computer program is said to learn from experience E with respect to some class of tasks T and performance measure P , if its performance at tasks in T , as measured by P , improves with experience E ."

This approach is different from the standard way to develop computer programs. As for the latter, the former starts with definition of the problem, but the rules of solving it are not explicitly set by the programmer, but instead they are implicitly extracted from initially known solutions for such problem called a training dataset. This process is referred as learning or training. It lasts until the efficiency measure P reaches the desired value. Usually from known data, some subset is extracted for model evaluation; this set is called the test dataset.

There are different ML models commonly used, starting from simple such as linear and logistic regression or classification based on k -nearest neighbors algorithm and ending in more sophisticated ones such as Support Vector Machines (SVMs) and Neural Networks (NNs) [301].

2.4.1 Neural Networks

Neural Networks (NNs) are models which structure is inspired by attempts to develop a mathematical description of information processing in biological systems. A standard NN consists of N layers of the so-called neurons, each having its inputs $\{x_i\}$ with weights $\{w_{ji}\}$ taken from the outputs of the neurons connected to its preceding layer and the outputs $\{a_j\}$ serving as inputs to connected next-layer neurons. In addition, a non-linear activation function h is defined, because without it, a set of layers could be replaced by a single layer with linear combinations of weights.

For j -th layer with D inputs its output a_j is defined as:

$$a_j = h \left(\sum_{i=1}^D w_{ji} x_i + w_{j0} \right). \quad (2.87)$$

NN training is performed using the error backpropagation algorithm [301, 303]. In general, at the first step, the output of the whole network is calculated, then, in the last layer, the derivative of the cost function P with respect to inputs to this layer are calculated. The weights of inputs w_i are then updated in an arbitrarily chosen approach, e.g. steepest gradient descent (SGD) algorithm:

$$w_{ji}^{n+1} = w_{ji}^n - \gamma \nabla P(\{w_{ji}\}), \quad (2.88)$$

where w_{ji}^{n+1} is the updated value of weight w_{ji}^n and γ is the so-called learning rate, usually chosen in range of 10^{-3} - 10^{-6} . After that, the steps of computation of derivatives and updating weights are continued for other layers. The whole process is repeated until convergence (based on arbitrarily defined conditions) is reached.

The use of NNs in computational chemistry is a novel approach, however it has some successful applications such as modeling PES, thermodynamical properties [304] or drug discovery [305]. An interesting utilization for the purpose of this work is NN application in the task of learning from results of QC method to correctly predict the potential energy and forces for given system geometry. In terms of the definition quoted in the introduction to this section, the results of the QC calculations are the experience E , the set of tasks T is to predict the value of energy and forces for the given geometry of the system, and the performance measure P could be the mean squared error between the prediction of the NN and the energy and forces calculated by QC for the same geometry. After the NN is trained, it allows to perform a MD simulation at a computational cost significantly lower than that of the QC method used to obtain data for training geometries.

At the moment some packages are available to learn the FF from known geometries of the given system, such as GPUMD [306], DeePMD-kit [307] or Schnetpack [308] used in this work.

2.5 Computational details

Quantum Chemical (QC) calculations were performed using Gaussian 09 [309]. For the research presented in this work, either the MP2 or DFT method with PBE functional [259–262] and Grimme’s D3 dispersion correction were utilized in the aug-cc-PVDZ basis.

The initial structures for MD simulations were prepared with Packmol [310].

Classical MD simulations were performed in NAMD v 2.12 [246]. Usually, two versions of FFs were used: polarizable, based on Drude particles [143], with parameters taken from APPLE&P [142] (marked further as DP-FF) and nonpolarizable, with parameters taken from Köddermann’s [311] and Lopes’ works [137] (marked further as NP-FF). For all systems studied, PBC were applied with electrostatic interactions taken into account using the particle mesh Ewald algorithm [312]. Simulations were performed in the NpT or NVT ensemble with Langevin

dynamics and modified Nosé-Hoover Langevin barostat [313, 314].

Ab initio MD simulations were performed in CP2K [253]. For all of them, DFT methods were used with the PBE functional [259–262], Grimme’s D3 dispersion correction [175], the replacement of core electrons with Goedecker’s pseudopotentials [256, 257], the molecularly optimized DZVP basis set and applying the Nosé-Hoover thermostat [264–269] in the NVT ensemble.

For practical reasons, connected with the high computational cost of calculating the polarizability tensor, this work concentrates only on IR spectra.

For the calculation of the theoretical IR spectra, the Fourier tool [315] from the CPMD-contributed tools was used with applying the harmonic thermal correction. For smoothing the obtained results, superposition of Gaussian curves with arbitrarily set σ (10 cm^{-1} unless specified differently) was used to plot the spectra.

System-specific details such as compositions of systems, temperature, pressure or length of obtained trajectories or exceptions to this general methodology are given in following chapters of this work describing individual cases.

Chapter 3

Structural data from MD simulations

This chapter presents the structural data obtained for studied systems, focusing on the structure of complexes, coordination numbers calculated from RDFs and stability of interactions assessed through residence time autocorrelation functions, as defined in Section 2.1.7.

Classical MD simulations were set-up and performed by one of co-authors of published papers, Dr. Piotr Kubisiak. The author of this Thesis contributed to the results of this chapter by conducting AIMD simulations, writing scripts and programs, and performing structural analysis of MD trajectories (classical and AIMD).

3.1 NaFSI solutions in EMIM-FSI ionic liquid

This section presents results for the solutions of NaFSI salt in the EMIM-FSI ionic liquid at different concentrations. Such electrolytes were experimentally investigated in [73, 74]. This part is an extension to studies which were the basis for the Master of Science thesis of the author of this work [316]. Most of the results described here were published in the paper [I].

Table 3.1: Compositions of $(\text{NaFSI})_x(\text{EMIM-FSI})_{1-x}$ systems

x	classical MD		
	Na^+	EMIM^+	FSI^-
0	0	175	175
0.1	19	171	190
0.2	40	160	200
0.3	66	154	220
0.4	94	141	235
0.5	129	129	258

x	ab initio MD		
	Na^+	EMIM^+	FSI^-
0	0	18	18
0.2	4	16	20
0.5	13	13	26

3.1.1 System details

MP2 method was used for the geometry optimizations of different conformers of FSI^- anion and Na^+FSI^- pairs in vacuum.

The compositions of the systems simulated in MD are presented in Table 3.1.

For classical MD pressure $p = 1 \text{ atm}$ and temperature $T = 298 \text{ K}$ were used. After 100-150 ns of equilibration trajectories for all systems were recorded for 1 μs in simulations using DP-FF and NP-FF with a time step of 1.0 fs.

AIMD was performed for selected concentrations of sodium salt. Initial structures were chosen from equilibrated NVT simulations in classical polarizable FF. Two systems with $x = 0$ and $x = 0.2$ were simulated, and three with $x = 0.5$. The temperature was set to 298 K. Time step equal 1.0 fs was used and 30 ps of the trajectory was recorded for each system.

3.1.2 Results

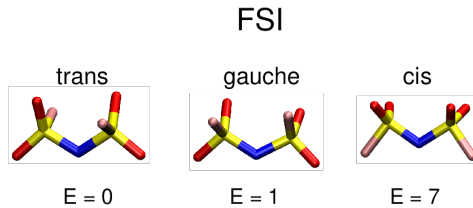


Figure 3.1: Conformers of the FSI^- anion with their relative energies in kcal/mol

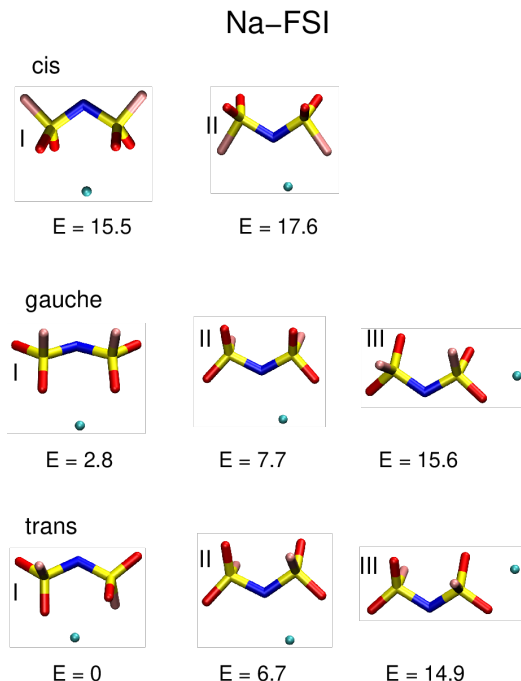


Figure 3.2: Conformers of the $\text{Na}-\text{FSI}$ pairs with their relative energies in kcal/mol

Three conformers of the FSI^- anion: cis, gauche and trans were optimized at the MP2 level of theory, their structures with relative energies in kcal/mol are presented in Figure 3.1. It is visible that the lowest energy is obtained for the trans conformer and is followed by gauche. The

energy difference between the cis and trans or gauche conformers is rather big and suggests that appearance of cis structure in the liquid is unlikely. The lowest energy for the trans structure stands in an agreement with experimental results obtained from Raman spectroscopy [14].

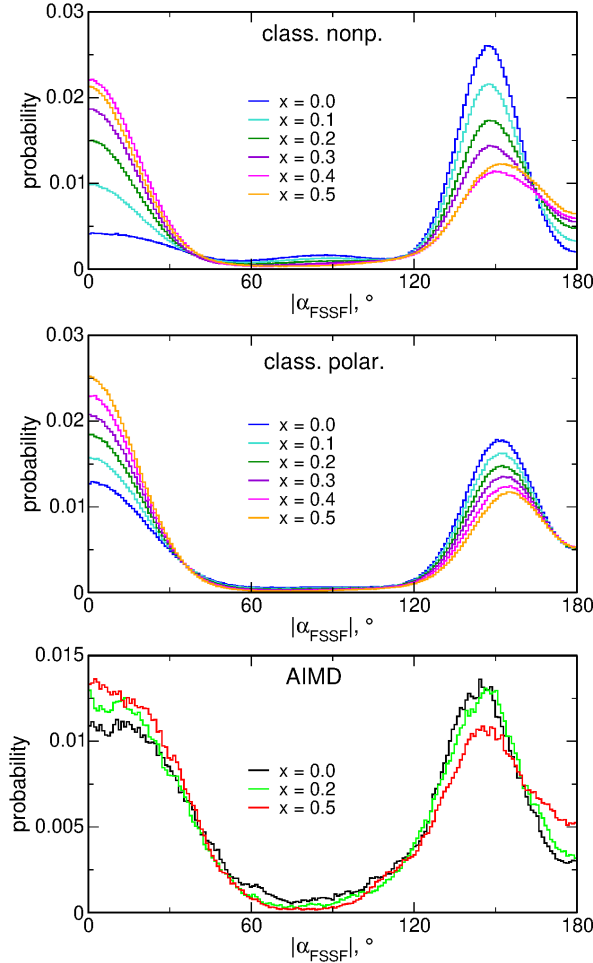


Figure 3.3: Histograms of the FSSF angle in simulated systems for classical and ab initio MD

Analogical analysis was performed for ion pairs Na^+FSI^- and its results are shown in Figure 3.2. For gauche and trans conformation of the anion, three types of geometries could be highlighted: (I) with sodium cation between two oxygen atoms, (II) with sodium cation interacting with nitrogen and one oxygen atom, and (III) with sodium cation located on the side of one of SO_2F groups. Types (I) and (II) are the most stable ones. For the cis conformation of the anion only two structures were found: one of type (I) and the second with different type - sodium cation is interacting with nitrogen and fluorine atoms.

MP2 calculations did not include solvent effects and considered only isolated anions/ion pairs in vacuum; however, they provide some intuition to further interpretation of results. Energy differences suggest that only trans and gauche conformers of FSI^- anion will dominate in solution, as well as the type (I) of complex geometries.

To analyze the population of different conformers in the electrolytes, histograms of the FSSF angles for different MD approaches and salt concentrations were calculated (Figure 3.3). Regardless of the variant of the FF used, with the growing amount of sodium salt in the solution, the peak at about 150° decreases with the simultaneous growth of the maximum near 0° . The

strongest effect is observed for NP-FF and the weakest is observed for AIMD. This tendency suggests that with addition of salt, the population of trans conformers decreases with a growing population of gauche conformations (or cis, discrimination between the two latter requires also checking the FSNS angle).

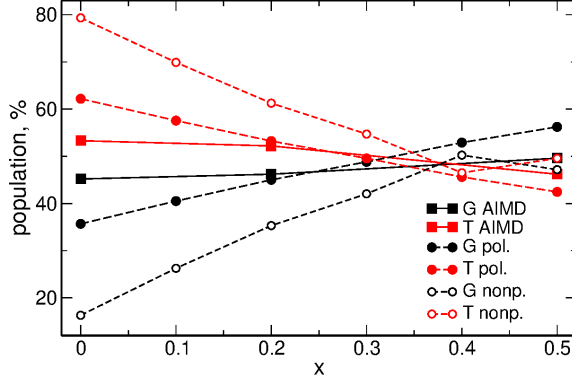


Figure 3.4: Population of different FSI^- conformers for all studied systems as a function of the sodium salt molar fraction x

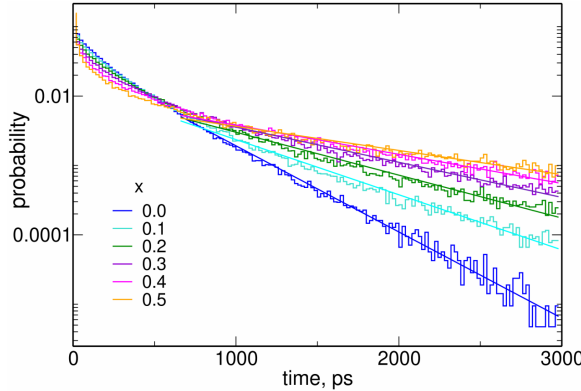


Figure 3.5: Histograms of distribution of the time between conformational changes of FSI^- anions in DP-FF MD simulations with fitted $p = Ae^{-\frac{\tau}{t}}$ curve to the long-time parts

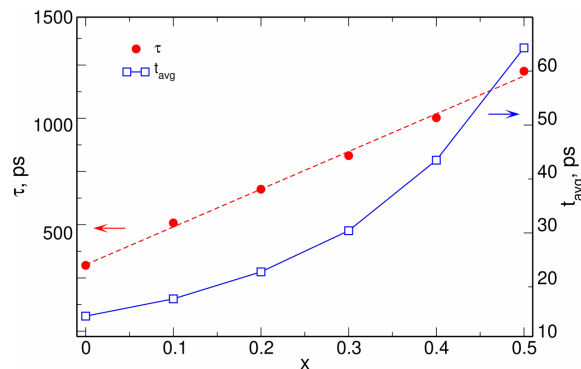


Figure 3.6: Average time between conformational changes (blue) for DP-FF MD and τ parameter (defined in Figure 3.5) dependence on the sodium salt molar fraction x

For all systems studied, the conformer population was calculated and is shown in Figure 3.4. It was observed that, as expected, cis conformations are practically absent in every case. As suspected previously, growing Na^+ concentration changes the populations of conformers, with the reverse of the gauche / trans ratio between x equal 0.3 and 0.4 for DP-FF and AIMD. For NP-FF, this ratio becomes approximately equal 1 for the most concentrated solutions. Observed changes of conformer populations with changes in NaFSI amount are smaller in AIMD. However, smaller sizes of systems studied in AIMD together with much shorter simulation times than in the FF MD give worse statistics than in the FF MD and, thus, these values have bigger error.

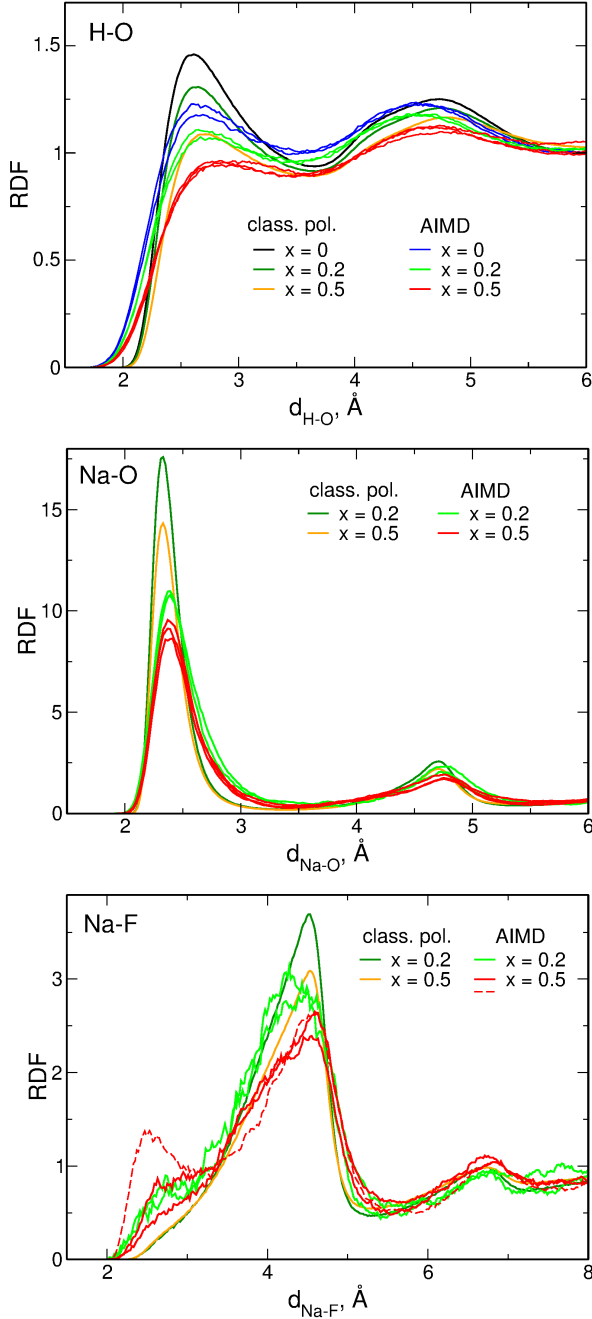


Figure 3.7: Radial distribution functions for DP-FF MD and AIMD for systems with 0, 0.2 and 0.5 NaFSI molar fractions

For systems studied by the FF MD, the dynamics of conformational changes in anions was investigated by collecting for every FSI^- how long were the intervals between moments with

changes in dihedral angles leading to changing the conformation state. Figures 3.5 and 3.6 present data obtained in DP-FF MD. It is visible, that growing sodium salt concentration slows this process with average time between conformational changes of FSI^- anions at a level of 13 ps for the neat liquid and about 60 ps for the most concentrated solution. The function $p = Ae^{-\frac{t}{\tau}}$ was fitted to the long-time part of the distribution in Figure 3.5. The τ parameter increases linearly with the salt molar fraction (Figure 3.6) as another indication of slower conformational changes in concentrated electrolytes.

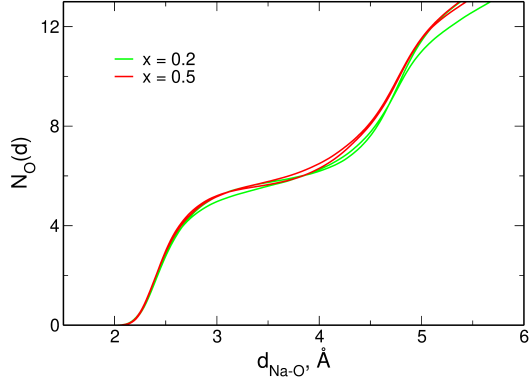


Figure 3.8: Integrated Na-O RDF for AIMD simulations

For low Na^+ concentrations, the trans conformers are more abundant, but interactions with Na^+ stabilize the gauche conformation of the FSI^- anion in concentrated salt solutions. An analogous effect of the stabilization of gauche conformer was experimentally observed from Raman spectra of EMIM-FSI liquid with LiFSI salt [317].

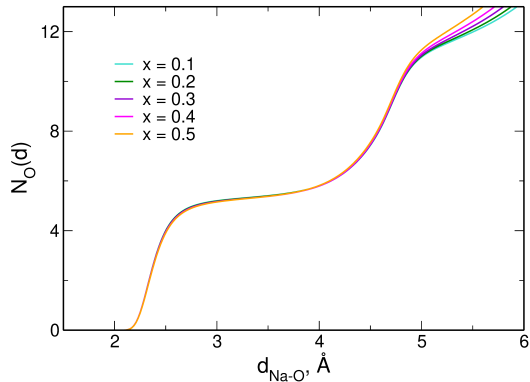


Figure 3.9: Integrated Na-O RDF for DP-FF simulations

Figure 3.7 shows the radial distribution functions (RDFs) for DP-FF MD and AIMD for systems with concentrations which were used in AIMD for H-O, Na-F and Na-O distances. In general, positions of maxima agree between these two methods, however, the peaks observed in AIMD are lower than those observed in DP-FF MD.

In the H-O RDF, the first maximum is located at 2.6-2.7 Å. For both simulation methods, its height decreases with growing concentration of the sodium salt and shifts to higher distances. It is probably related to the weakening of the hydrogen bonds between ions of the IL with the addition of sodium salt.

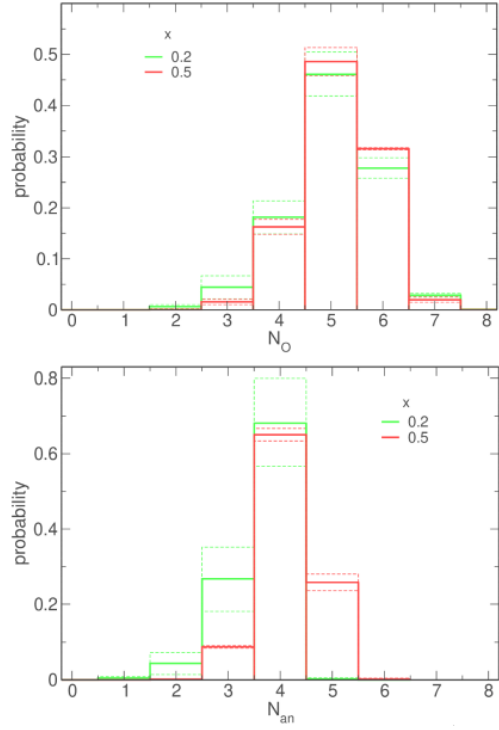


Figure 3.10: Histograms of the number of O atoms (N_O) coordinating sodium cations (upper) and number of different FSI^- anions (N_{an}) in sodium solvation shell for AIMD simulations (lower). Solid lines are average values over all studied systems at a given concentration x (shown in broken lines)

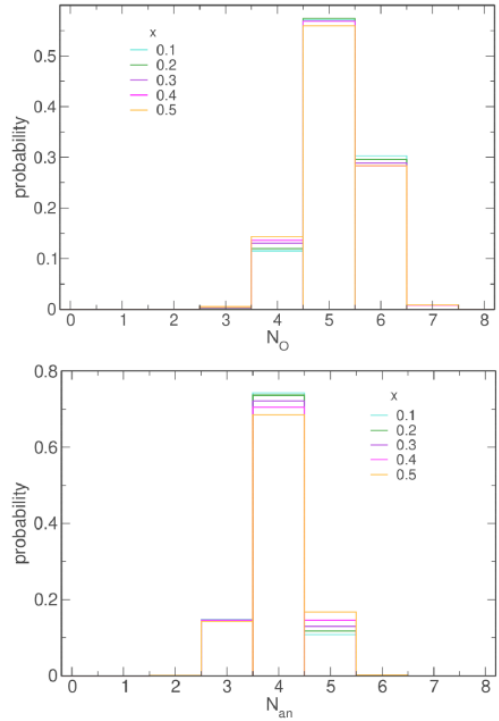


Figure 3.11: Histograms of the number of O atoms (N_O) coordinating sodium cations (upper) and number of different FSI^- anions (N_{an}) in sodium solvation shell for DP-FF simulations (lower)

Comparison of positions and heights of the first maxima in Na-O and Na-F RDFs clearly shows that Na^+ cations are mostly coordinated by oxygen atoms from FSI^- anions. It is worth noting that one of the systems with $x = 0.5$ studied in AIMD has the Na-F RDF (marked with the dashed line) differing from the others. This difference will be addressed in the further text. The position of the first maximum of Na-O RDF in the DP-FF MD is at distance smaller than in AIMD. The integrated RDFs (running coordination numbers) presented in Figures 3.8 and 3.9 show that the average number of O atoms in the first solvation shell of sodium cation is equal 5.6 for AIMD and 5.4 for DP-FF simulations.

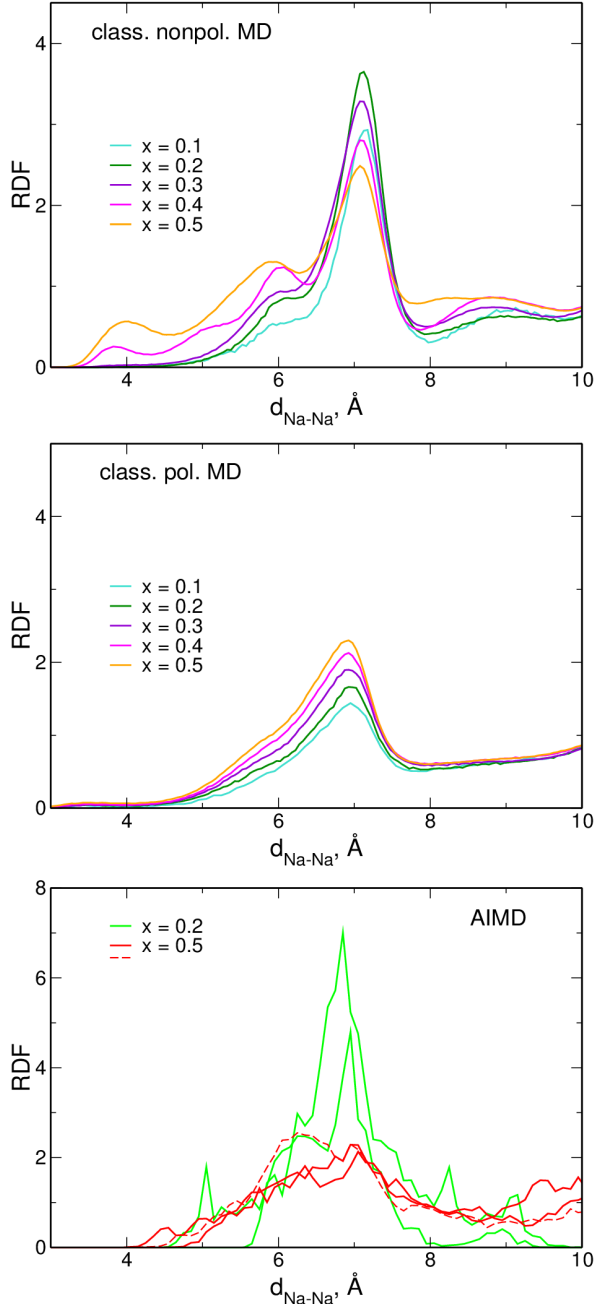


Figure 3.12: Radial distribution functions for Na-Na

Figures 3.10 and 3.11 show statistics of sodium coordination both in AIMD and DP-FF MD simulations. In both of them above 50% of Na^+ cations are coordinated by five oxygen atoms and about 30% by six. Above 60% of complexes are in the form $[\text{Na}(\text{FSI})_4]^{3-}$, what shows that in most

of them three anions are coordinated in monodentate manner and one in bidentate. Complexes with coordination number equal 6 may have two anions with monodentate coordination and two with bidentate. In AIMD results, for the system with $x = 0.5$, about 25% of sodium cations are in the form $[\text{Na}(\text{FSI})_5]^{4-}$ without significant increase in the average coordination number, thus with growing salt concentration, monodentate coordination becomes more preferred. From these plots also smaller changes in coordination patterns with changing NaFSI concentration in DP-FF MD compared to AIMD are observed. However, this difference could be an effect of worse statistics of AIMD results (smaller systems, shorter simulation times).

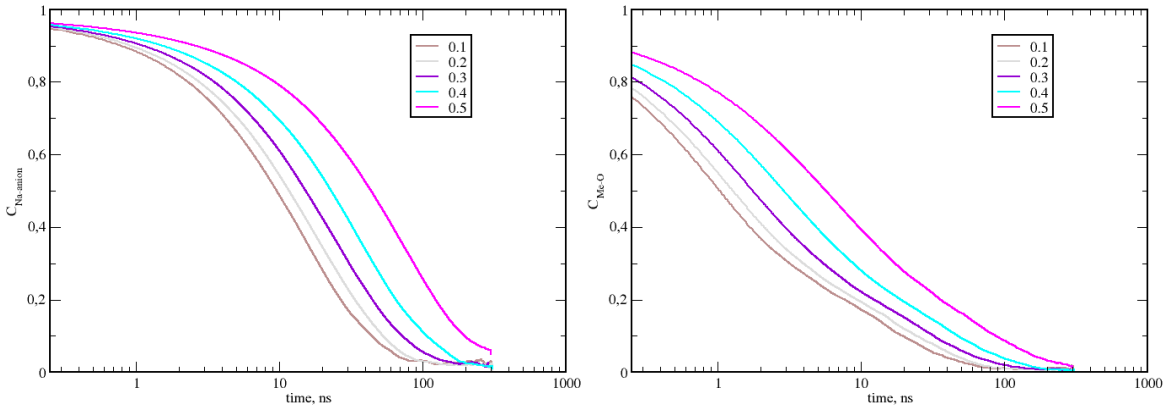


Figure 3.13: Residence time autocorrelation functions for DP-FF for Na^+ coordination by whole anions (left) and individual O atoms (right)

Figure 3.12 shows RDFs for Na-Na pairs. Due to poor statistics, the AIMD results are noisy. In FF approaches wide maximum at about 7 Å is observed and for higher concentrations in NP-FF two weaker maxima appear at lower distances; thus, some kind of weak ordering of metal ions may occur in concentrated solutions.

In Figure 3.12 dashed line marks the $x = 0.5$ system, which previously exhibited a different behavior from other $x = 0.5$ systems in Na-F RDF (Figure 3.7). Also in the case of the Na-Na RDF, its maximum is shifted toward lower values than those of replicas with this salt concentration. It suggests that this would give different results in other properties, such as IR spectra discussed in Section 4.1. In addition, it may be expected that for sufficiently long times of simulation these differences could vanish.

Figure 3.13 presents residence time autocorrelation functions (AFs) calculated for DP-FF MD simulations, both for coordination by whole anions and for individual O atoms. In both plots, it is visible that the higher the salt concentration, the slower the decay of $C(t)$. For given concentration, AF for individual O atoms decreases faster than for the whole anion. From these results, it could be deduced that for concentrated solutions, exchanges in the coordination shells are slower, and that it takes a longer time for exchange of the anion than of the single O atom. It is related to the fact that exchange of the anion requires breaking all coordination bonds to the cation.

3.2 EMIM-TFSI with NaTFSI or LiTFSI solutions

This section describes structural results obtained from classical MD for series of electrolytes based on LiTFSI or NaTFSI dissolved in EMIM-TFSI ionic liquids. This is a part of a study published in paper [II] aimed at investigating the correlations in the motions of ions in salt solutions in ILs. Such correlations can affect the conductivity of the electrolyte. They were broadly studied experimentally, for example, for lithium-based ILs [318–320], for lithium salts dissolved in glymes [321, 322] or for electrolytes with carbonates as solvents [323]. The research on this topic also involved theoretical studies with the use of MD methods [A, 324–326].

3.2.1 System details

Five systems $\text{Me}_x\text{EMIM}_{1-x}\text{TFSI}$ with $\text{Me} = \text{Li}$ or Na and x equal 0.0, 0.06, 0.12, 0.2 and 0.3 were investigated. Their compositions are listed in Table 3.2.

Table 3.2: Compositions of $\text{Me}_x\text{EMIM}_{1-x}\text{TFSI}$ systems

x	Me^+	EMIM^+	FSI^-
0	0	142	142
0.06	10	148	158
0.12	20	141	161
0.2	32	128	160
0.3	51	119	170

For classical MD pressure $p = 1$ atm and temperature $T = 333$ K were used. After 100 ns of equilibration trajectories for all systems were recorded for 1000 ns in simulations using DP-FF and NP-FF with a time step of 1.0 fs.

3.2.2 Results

The RDFs for the Me-O distances are shown in Figure 3.14. The positions of the peaks do not change significantly with salt concentration and are located at 2.0 Å and 2.1 Å for lithium in DP-FF and NP-FF respectively, while for sodium maxima appear at 2.5 Å and 2.6 Å. The longer distances for sodium as well as the fact that its maxima are lower and wider than those of lithium, are caused by the larger radius of the Na^+ ion.

Coordination numbers are determined from the integrated RDFs at the distance of 3 Å for lithium and are equal 3.96 in DP-FF and 4.76 in NP-FF and for the distance of 3.5 Å for sodium and are equal 5.34 and 5.66 respectively. The differences are related to the stronger Me-anion interactions in the polarizable simulations — maxima of the RDFs are shifted towards lower distances, so the solvation shell is tighter.

Figure 3.15 presents the abundance of the number of oxygen atoms or anions that coordinate the metal cation, respectively. Me^+ cation is treated as coordinated to the oxygen atom if its distance at a given moment is lower than threshold value: 3.0 Å for lithium and 3.5 Å for sodium. In DP-FF, most lithium ions are coordinated by 4 oxygen atoms from 2 anions,

which suggests that coordination is bidentate. For sodium cations, the most probable number of coordinating atoms are 5 and 6 from 3 anions, thus in sodium electrolytes most of metal cations are coordinated either as bidentate by two anions and as monodentate by the 3rd anion, or in bidentate manner by 3 anions. In NP-FF coordination numbers are shifted towards higher values - 5 for lithium and 6 for sodium. Both types of cation are in this case predominantly coordinated by 4 anions. Therefore, it seems that NP-FF favorizes monodentate binding in complexes. The DP-FF results agree with the structures obtained experimentally [318].

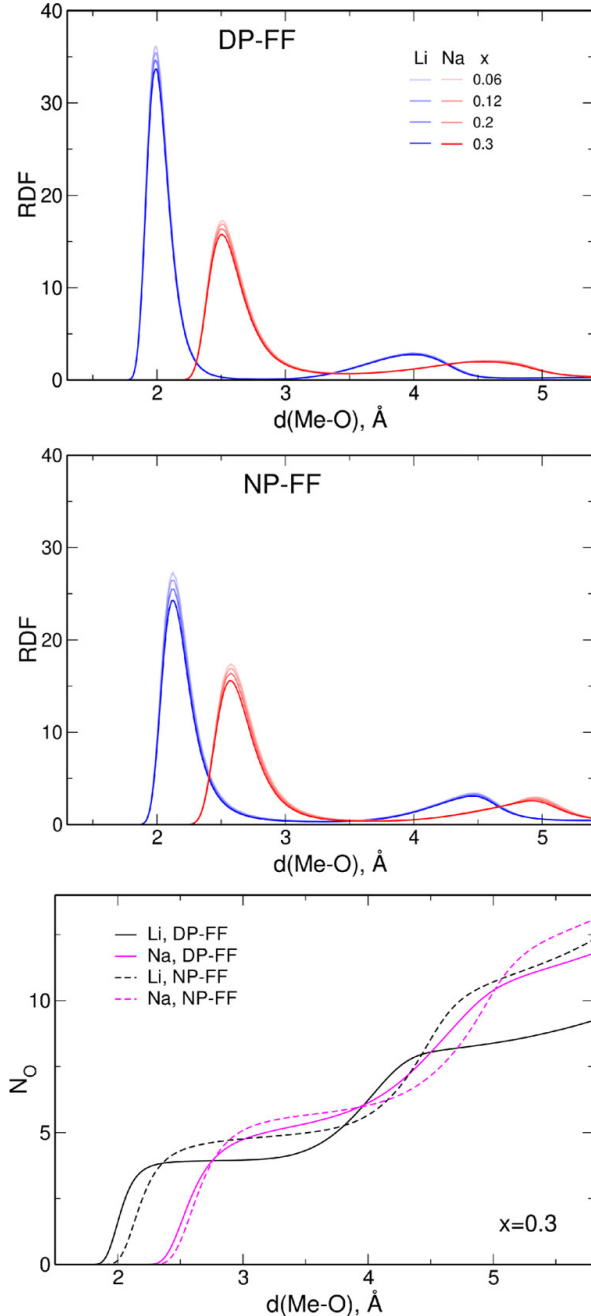


Figure 3.14: Radial distribution functions for Me-O distances in the polarizable (top) and nonpolarizable (middle) FF and the running coordination numbers for Me-O (bottom) for the system with $x = 0.3$

Residence time autocorrelation functions are plotted in Figure 3.16. The decay of this function is slower for lithium ions, which is caused by stronger interaction between the Li^+ cation

and the TFSI⁻ anion due to the smaller size of the former. Increasing salt concentration further slows the decay (except for sodium in DP-FF). For each of the data series, a stretched exponential function $e^{-\left(\frac{t}{\tau_O}\right)^\alpha}$ was fitted, the residence times obtained τ for individual oxygen atoms and for whole anions are presented at the bottom of Figure 3.16. Residence times for anions are 3-10 times larger than values for oxygen atoms, and this is due to the fact that exchange of the anion requires breaking all of the interactions from its oxygen atoms to the cation. Values for lithium are 4-8 times higher than those for sodium and are more dependent on salt concentration. These results indicate that anion exchange in the sodium solvation shell is faster than for lithium.

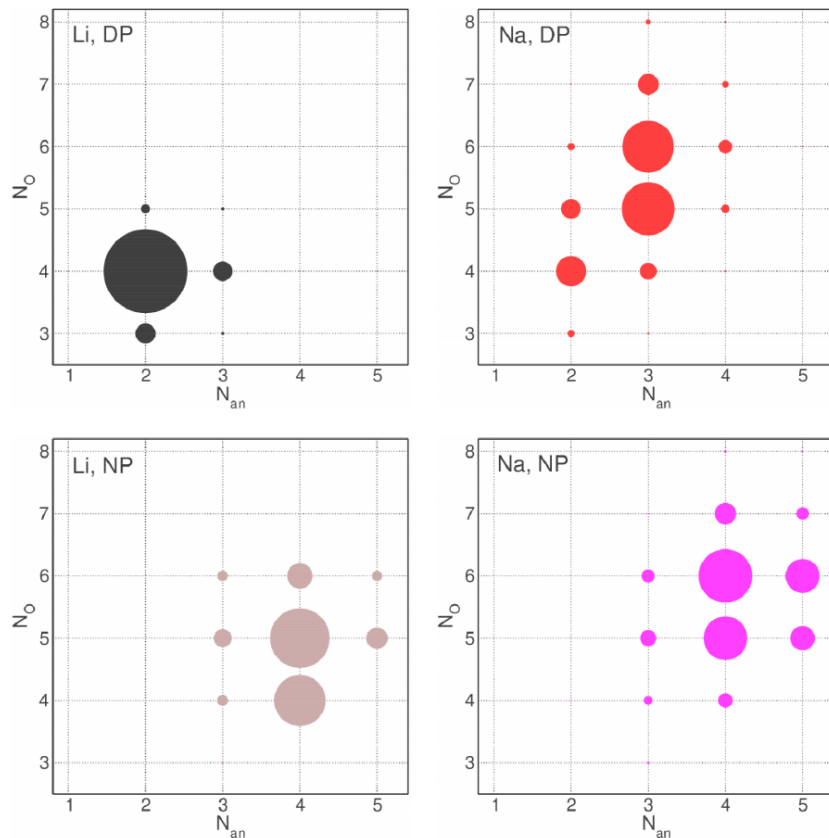


Figure 3.15: Abundance of different combinations of the number of anions N_{an} and the number of oxygen atoms N_O coordinating Me^+ ions in NP-FF and DP-FF; areas of the circles are proportional to the abundance

The structural data presented in this section show remarkable differences in the structure and dynamics of the solvation shell of Li^+ and Na^+ in EMIM-TFSI as well as the dependence of the results on the FF used in the simulations. Nevertheless, further analysis of ion transport and conductivity in [II] resulted in the conclusion that regardless of the cation or the type of FF, correlations between ion motions lead to negative Me^+ transference numbers in salt solutions in ILs.

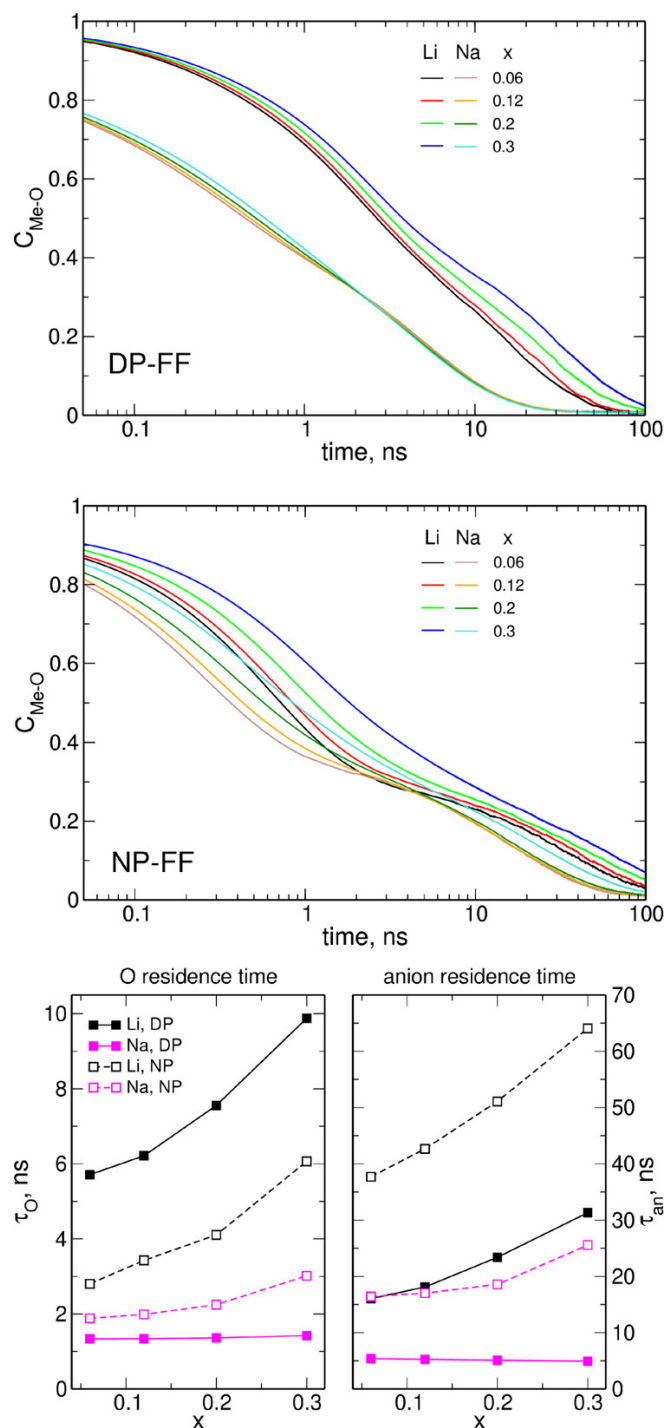


Figure 3.16: Residence time autorcorrelation functions for Me-O for DP-FF (top), NP-FF (middle) and τ parameters for O atoms and TFSI anions (bottom)

3.3 Magnesium chloride solutions in DME

Magnesium salt solutions in organic liquids, such as dimethoxyethane (DME) were studied as possible electrolytes for novel batteries [111, 327–331]. In particular, systems with $\text{Mg}(\text{TFSI})_2$ with MgCl_2 addition were experimentally investigated [332]. The data obtained shown that DME promotes aggregates formation such as $\text{Mg}_2\text{Cl}_2^{2+}$ or $\text{Mg}_3\text{Cl}_4^{2+}$. The structures of such complexes are important because they differ in electrochemical activity. The results described here were part of the study done with QC and MD methods published in the article [III].

3.3.1 System details

QC calculations were performed with use of both the PBE and the B3LYP functionals for systems in vacuum, in the implicit solvent with $\varepsilon = 7.2$ modeled by the IEFPCM method [333] and for three systems containing explicit DME molecules with structures taken from crystallographic data in [332]. The three latter structures were investigated in vacuum (explicit solvent) or embedded in the PCM solvent (hybrid solvent model).

Table 3.3: Compositions of $\text{Mg}(\text{TFSI})_2$ - MgCl_2 -DME solutions

system	classical MD			
	Mg^{2+}	TFSI^-	Cl^-	DME
I	61	82	40	500
II, IIa	86	86	86	500
III, IIIa, IIIb, IIIc	141	94	188	500

system	ab initio MD			
	Mg^{2+}	TFSI^-	Cl^-	DME
III, IIIa, IIIb, IIIc	3	2	4	30

Classical MD simulations in DP-FF were performed at pressure 1 atm and temperature 298 K with a time step of 0.5 fs for 400 ns for each system. Three types of systems with Mg salts dissolved in DME, varying in the Mg:Cl ratio, were constructed:

I — mixture of 0.5 M $\text{Mg}(\text{TFSI})_2$ and 0.25 M MgCl_2

II — mixture of 0.5 M $\text{Mg}(\text{TFSI})_2$ and 0.5 M MgCl_2

III — mixture of 0.5 M $\text{Mg}(\text{TFSI})_2$ and 1 M MgCl_2

In the initial structures of these systems ions were randomly distributed. In addition, 4 other systems were simulated: IIa with Mg^{2+} and Cl^- initially in the form of $\text{Mg}_2\text{Cl}_2^{2+}$ complex, IIIa with initial mixture of MgCl_2 and $\text{Mg}_2\text{Cl}_2^{2+}$ complexes, IIIb with form (I) and IIIc with form (II) of the complex $\text{Mg}_3\text{Cl}_4^{2+}$ (these forms are described in the next subsection).

AIMD simulations were performed in the NVT ensemble for III, IIIa, IIIb and IIIc systems with smaller number of atoms than in classical MD. The size of the periodic simulation box was

set to reproduce the densities of electrolytes obtained in classical MD simulations. Time step of 1 fs was used, and for each of the systems 35 ps of the simulation was recorded.

The compositions of the systems are listed in Table 3.3. Presented RDFs were averaged over the last 20 ns or 30 ps for classical MD and AIMD respectively.

3.3.2 Results

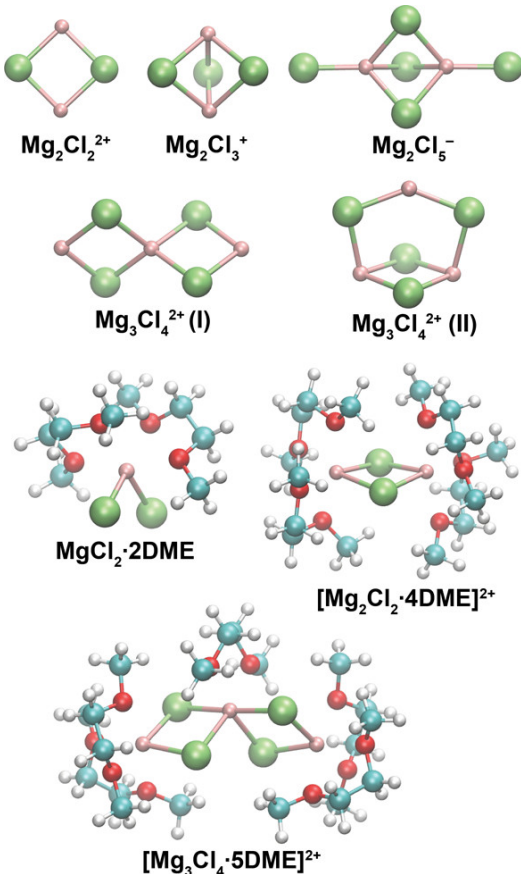


Figure 3.17: Structures of Mg:Cl complexes studied by QC methods

Figure 3.17 presents the structures of the complexes considered in QC calculations. For $\text{Mg}_3\text{Cl}_4^{2+}$ two stable geometries were found — with Mg^{2+} in linear order (form I) or triangular (form II). The results of geometry optimization in the PBE functional for selected structures are collected in Table 3.4. For the system with $\text{Mg}_3\text{Cl}_4^{2+}$ with DME molecules, only structure (I), found in the experiment, was considered. The distances between Mg^{2+} ions are in the range 3.2-3.6 Å and between Mg^{2+} and Cl^- in the range 2.2-2.5 Å. These distances increase in solvent, for Mg-Mg by 0.2 and 0.3-0.35 Å in PCM and explicit solvent, respectively, and for Mg-Cl by 0.1 and 0.15 Å. For structures containing DME molecules, there are almost no changes between vacuum and PCM, what suggests, that the explicit solvent molecules are sufficient here to describe the solvent effect on interionic distances. Cl-Cl distances are less affected by the solvent, the effect is remarkable only for MgCl_2 where presence of explicit solvent molecules change the geometry from linear to bend. In systems with explicit DME molecules, distances between Mg^{2+} ions and oxygen atoms from DME (O_E) decrease in PCM with respect to vacuum values.

Table 3.4: Interatomic distances (in Å) for chosen complexes optimized with PBE functional

Structure	vacuum			
	Mg-Mg	Mg-Cl	Cl-Cl	Mg-O _E
MgCl ₂		2 x 2.206	4.412	
[MgCl ₂ · 2E]		2.351, 2.367	3.910	2.208, 2.163 2.337, 2.339
Mg ₂ Cl ₂ ²⁺	3.175	4 x 2.358	3.486	2.140, 2.143,
[Mg ₂ Cl ₂ · 4E] ²⁺	3.534	2.467, 2.468, 2.476, 2.479	3.456	2 x 2.145, 2.146, 2.147, 2.153, 2.156
Mg ₃ Cl ₄ ²⁺ (I)	2 x 3.208, 6.415	4 x 2.298, 4 x 2.452 2 x 2.307,	2 x 3.500, 4 x 4.234	
Mg ₃ Cl ₄ ²⁺ (II)	3.145, 2 x 3.638	4 x 2.369, 2 x 2.424, 2 x 4.002, 2 x 4.380	3.486, 4 x 3.836, 4.232	
[Mg ₃ Cl ₄ · 5E] ²⁺	2 x 3.542, 6.596	2 x (2.425, 2.454, 2.489, 2.531)	2 x 3.445, 3.734, 2 x 3.742, 5.057	2 x (2.145, 2.152, 2.156, 2.180, 2.182)
PCM				
structure	Mg-Mg	Mg-Cl	Cl-Cl	Mg-O _E
MgCl ₂		2 x 2.292	4.583	
[MgCl ₂ · 2E]		2.349, 2.365	3.878	2.141, 2.180, 2.300, 2.309
Mg ₂ Cl ₂ ²⁺	3.382	4 x 2.434	3.494	2.123, 2.129, 2.141, 2.142,
[Mg ₂ Cl ₂ · 4E] ²⁺	3.539	2.473, 2.479, 2.480, 2.488	3.447	2.145, 2 x 2.152, 2.169
Mg ₃ Cl ₄ ²⁺ (I)	2 x 3.331, 6.663	4 x 2.414, 4 x 2.443 2.388, 2.396,	2 x 3.534, 4 x 4.199	
Mg ₃ Cl ₄ ²⁺ (II)	3.368, 3.705, 3.727	2 x 2.430, 2 x 2.436, 2.456, 2.463, 3.819, 3.822, 4.561, 4.594	3.508, 2 x 3.751, 3.769, 3.770, 4.424	
[Mg ₃ Cl ₄ · 5E] ²⁺	2 x 3.526, 6.578	2 x (2.433, 2.462, 2.486, 2.530)	2 x 3.462, 2 x 3.682, 3.738, 5.058	2 x (2.138, 2.146, 2.149, 2.168, 2.173)

Table 3.5: Binding energies in kcal/mol for complexes (E stands for DME)

Structure	PBE		B3LYP	
	vac	PCM	vac	PCM
MgCl ⁺	-338.5	-59.7	-336.7	-59.3
MgCl ₂	-541.2	-106.7	-539.8	-105.9
MgCl ₃ ⁻	-606.8	-132.1	-605.2	-130.4
Mg ₂ Cl ₂ ²⁺	-668.6	-135.1	-665.1	-133.3
Mg ₂ Cl ₃ ³⁺	-942.1	-186.7	-935.4	-182.0
Mg ₂ Cl ₅ ⁻	-1202.7	-260.3	-1197.0	-254.4
Mg ₃ Cl ₄ ²⁺ (I)	-1283.9	-265.0	-1277.8	-261.1
Mg ₃ Cl ₄ ²⁺ (II)	-1284.0	-266.3	-1279.4	-263.8
MgCl ₂ · 2E	-604.3	-150.6	-608.4	-155.5
[Mg ₂ Cl ₂ ·4E] ²⁺	-981.9	-268.8	-995.2	-283.0
[Mg ₃ Cl ₄ ·5E] ²⁺	-1617.9	-428.2	-1634.1	-444.2
[MgTFSI] ⁺	-338.0	-51.9	-336.9	-54.3
MgTFSI ₂	-504.3	-96.0	-508.9	-100.5

Table 3.6: Total binding effects for aggregates in kcal/mol

Aggregate	Mg/Cl ratio	PBE		B3LYP	
		vac	PCM	vac	PCM
2MgCl ⁺	1:1	-677.0	-119.3	-673.4	-118.6
Mg ₂ Cl ₂ ²⁺	1:1	-668.6	-135.1	-665.1	-133.3
2MgCl ⁺ + MgCl ₂	3:4	-1218.2	-226.0	-1213.2	-224.5
Mg ₂ Cl ₃ ³⁺ + MgCl ⁺	3:4	-1280.6	-246.4	-1272.1	-241.4
Mg ₂ Cl ₂ ²⁺ + MgCl ₂	3:4	-1209.8	-241.8	-1204.9	-239.2
Mg ₃ Cl ₄ ²⁺ (I)	3:4	-1283.9	-265.0	-1277.8	-261.1

In Table 3.5 binding energies for all complexes studied in both vacuum and implicit solvent models are shown. For Mg₃Cl₄²⁺ structures, form II has lower energy than structure I in both functionals, in PCM this effect is equal about 1-2 kcal/mol. The stabilization effect increases with the number of ions or molecules in the complex. The implicit solvent method reduces this effect by a factor 5 or 4 for complexes with or without explicit solvent molecules, respectively. The smaller reduction in the latter case is the result of screening the ions from the effective medium by explicit solvent molecules.

To compare the stabilities of systems containing different complexes, we define the total binding effect. For a system with n complexes Mg_{xn}Cl_{yn} and m complexes Mg_{xm}Cl_{ym}, the total binding effect E_b is defined as:

$$E_B = n \cdot E(\text{Mg}_{xn}\text{Cl}_{yn}) + m \cdot E(\text{Mg}_{xm}\text{Cl}_{ym}) + \\ - (n \cdot xn + m \cdot xm) \cdot E(\text{Mg}^{2+}) - (n \cdot yn + m \cdot ym) \cdot E(\text{Cl}^-), \quad (3.1)$$

where $E(Z)$ is the energy of the species Z. The calculated values E_b for the aggregates for the 1:1 or 3:4 Mg:Cl ratio are presented in Table 3.6. For the 1:1 case, the binding effect for complex Mg₂Cl₂²⁺ is about 15 kcal/mol larger than for two MgCl⁺ complexes. For the 3:4 case, the most

stable is the form $\text{Mg}_3\text{Cl}_4^{2+}$, which is by about 20 kcal/mol lower than a pair of $\text{Mg}_2\text{Cl}_2^{2+}$ and MgCl_2 complexes or a pair of MgCl^+ and Mg_2Cl_3^+ complexes and about 40 kcal/mol than MgCl_2 and two MgCl^+ complexes. The observation for $\text{Mg}_3\text{Cl}_4^{2+}$ complex could be also derived from Table 3.5 - the energy of $[\text{Mg}_3\text{Cl}_4(\text{DME})_5]^{2+}$ is about 20 kcal/mol more stabilizing than the sum of energies for $\text{MgCl}_2(\text{DME})_2$ and $[\text{Mg}_2\text{Cl}_2(\text{DME})_4]^{2+}$. These observations indicate, that $\text{Mg}_2\text{Cl}_2^{2+}$ and $\text{Mg}_3\text{Cl}_4^{2+}$ are the most preferred complexes in the solutions with Mg:Cl ratio equal 1:1 or 3:4 respectively.

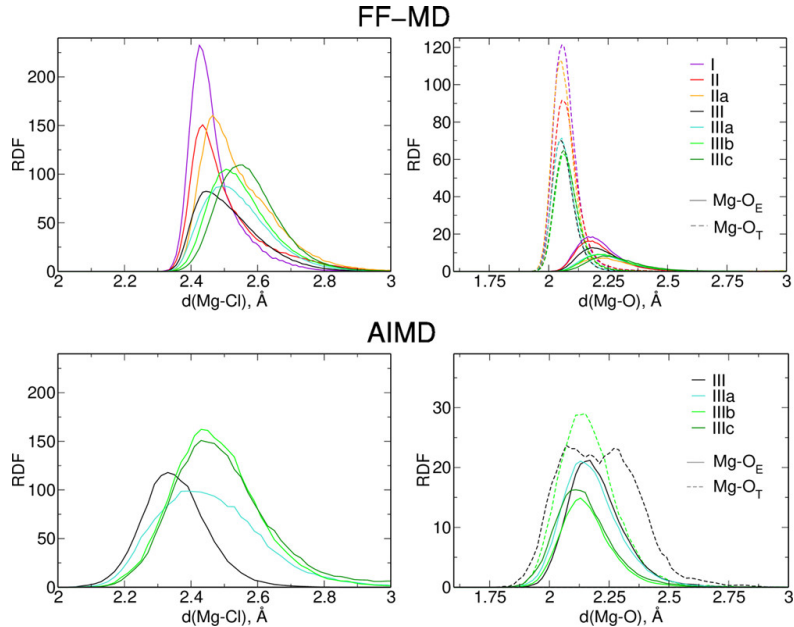


Figure 3.18: Radial distribution functions for Mg-Cl and Mg-O distances (O_E - oxygen from DME, O_T - oxygen from TFSI^-)

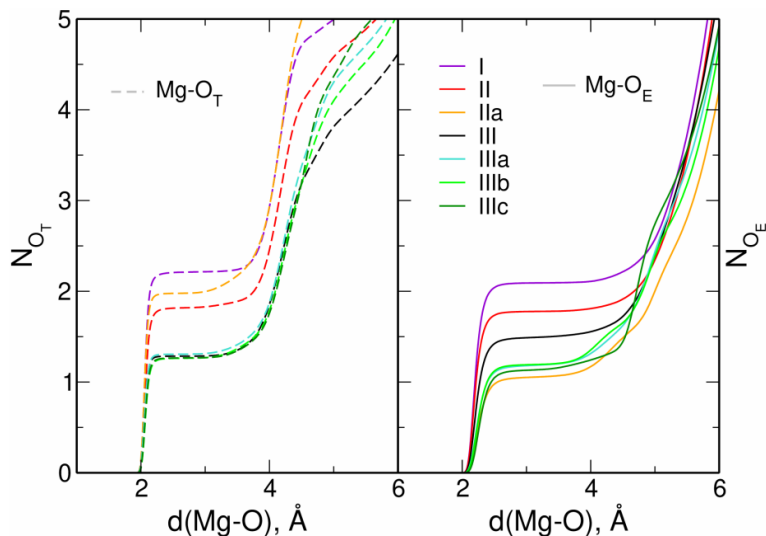


Figure 3.19: Integrated RDFs for Mg-O pairs from classical MD simulations, O_E - oxygen atoms from DME, O_T - oxygen atoms from TFSI^-

The RDFs for the Mg-Cl and Mg-O distances obtained in MD simulations are plotted in Figure 3.18. In the results of classical MD, the first maximum for Mg-Cl appears between 2.4 and

2.6 Å and is larger for systems IIIa-c, which is consistent with the results of QC calculations where Mg-Cl distance was growing with increasing number of Mg^{2+} ions in the complex. AIMD results show the same pattern, with the maxima shifted to distances shorter about 0.1 Å. Classical MD trajectories were long enough to observe the coordination of the Mg^{2+} ions by oxygen atoms both from the solvent and from the TFSI⁻ anion, with the maxima positions again in the range that is consistent with the QC results. Integrated Mg-O RDFs, presented in Figure 3.19, show that oxygen atom coordination decreases from the most diluted system I to systems IIIa-c where initially there were Mg-Cl complexes. This conclusion is confirmed by the integrated RDFs presented in Figure 3.20, where an opposite trend is observed in the plot for Mg-Cl pairs.

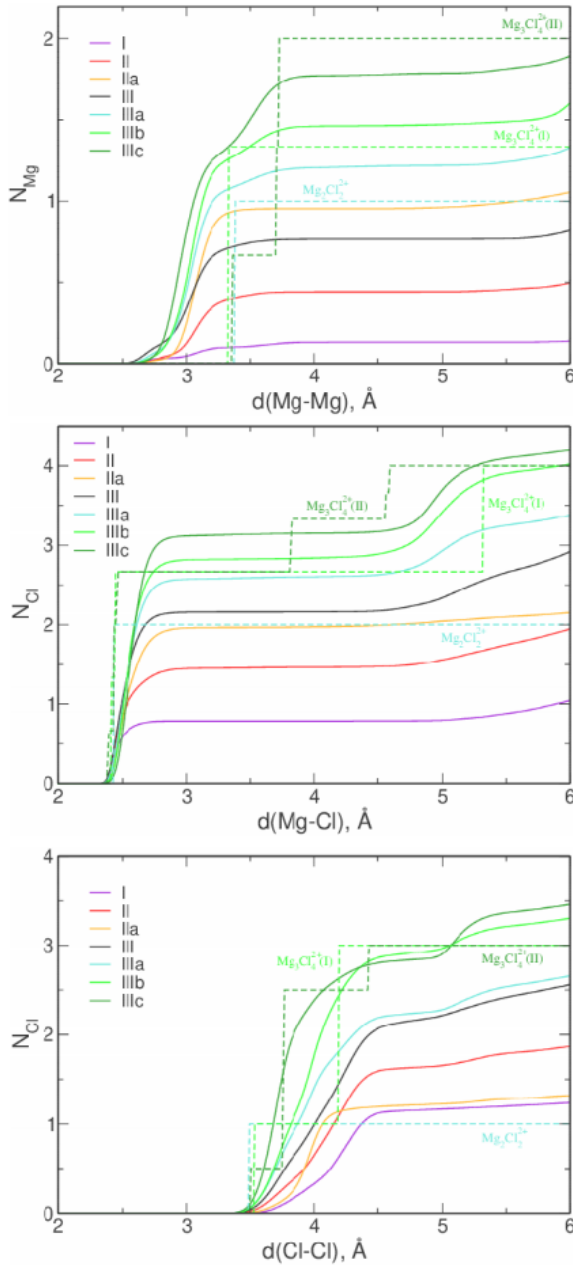


Figure 3.20: Integrated RDFs for Mg-Mg and Mg-Cl pairs from classical MD simulations. Broken lines mark RDFs for "ideal" geometries of aggregates optimized in QC calculations

In Figure 3.21 RDFs for Mg-Mg and Cl-Cl pairs are presented. The main maximum in the Cl-Cl RDF is located at distances higher for systems I and II than for IIIa-c, which may be related to

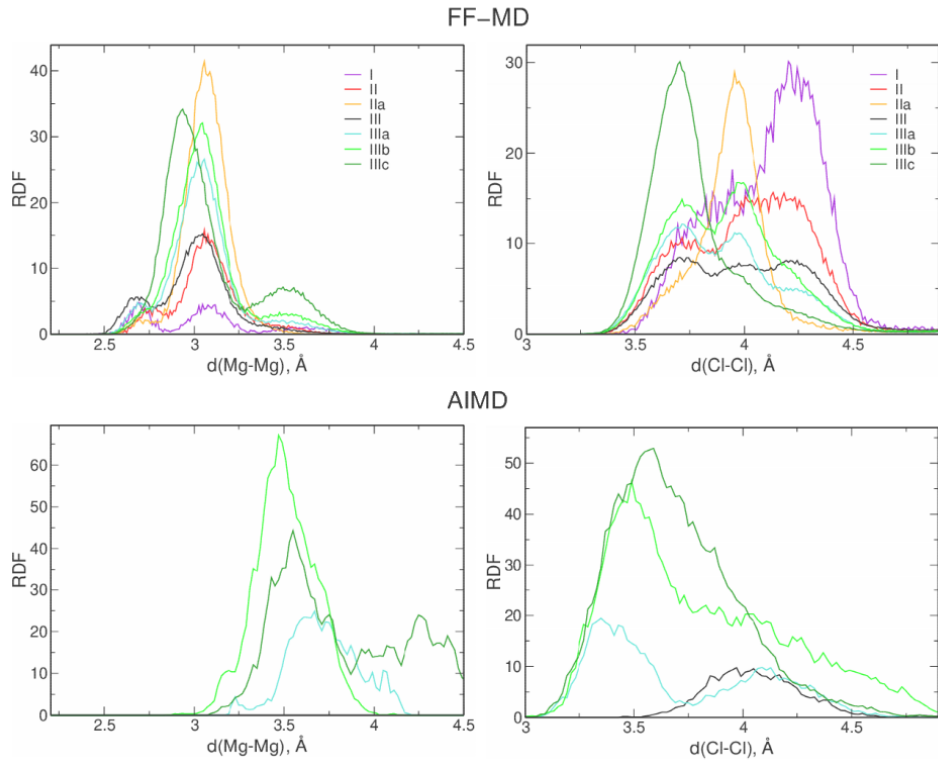


Figure 3.21: Radial distribution functions for Mg-Mg and Cl-Cl pairs

the QC results showing in $\text{Mg}_2\text{Cl}_2^{2+}$ the Cl-Cl distance longer than in the other complexes. Thus, it could be expected that in these systems the amount of this complex is significantly larger than that for IIIa-c. In AIMD, the positions of the maxima in Mg-Mg and Cl-Cl RDFs agree with the distances calculated by the QC methods. There is a difference with respect to the results from classical MD. In classical MD the Mg-Mg maximum appears at shorter distances and Cl-Cl maximum at larger distances than in AIMD. As there are no significant differences in Mg-Cl RDFs, this may be related to different shapes of $\text{Mg}_2\text{Cl}_2^{2+}$ complex in both MD approaches, with the diagonal distance Mg-Mg longer and Cl-Cl shorter in AIMD.

Systems II and IIa contain the same number of ions and solvent molecules, the same applies for systems III and IIIa-c. To check which configuration of complexation is more stable, the relative potential energies for these systems are plotted in Figure 3.22. System IIa has energy lower than the system II, what suggests that in this case ion aggregation into $\text{Mg}_2\text{Cl}_2^{2+}$ is preferred. For the second series of systems, the energy decreases in order of III > IIIa > IIIb > IIIc, what suggests that complexation into $\text{Mg}_2\text{Cl}_2^{2+}$ and $\text{Mg}_3\text{Cl}_4^{2+}$ is favorable and that the II type of the $\text{Mg}_3\text{Cl}_4^{2+}$ complex is more stable than type I.

In Figure 3.23 changes of average number of Mg^{2+} ions at the distance of 4 Å from the central Mg^{2+} cation (N_{Mg}) are plotted for each system studied by classical MD. For systems which initially contained the preferred structure of the complex (i.e. $\text{Mg}_2\text{Cl}_2^{2+}$ for the 1:1 ratio and $\text{Mg}_3\text{Cl}_4^{2+}$ (I) or (II) for the 3:4 ratio), there are only small changes of this number with no decrease, what indicates that there is no dissociation. For other systems N_{Mg} increases with time what shows that the ion aggregation process is occurring in the electrolyte. The speed of this growth decreases over time, because for larger aggregates, the mobility is decreased and it

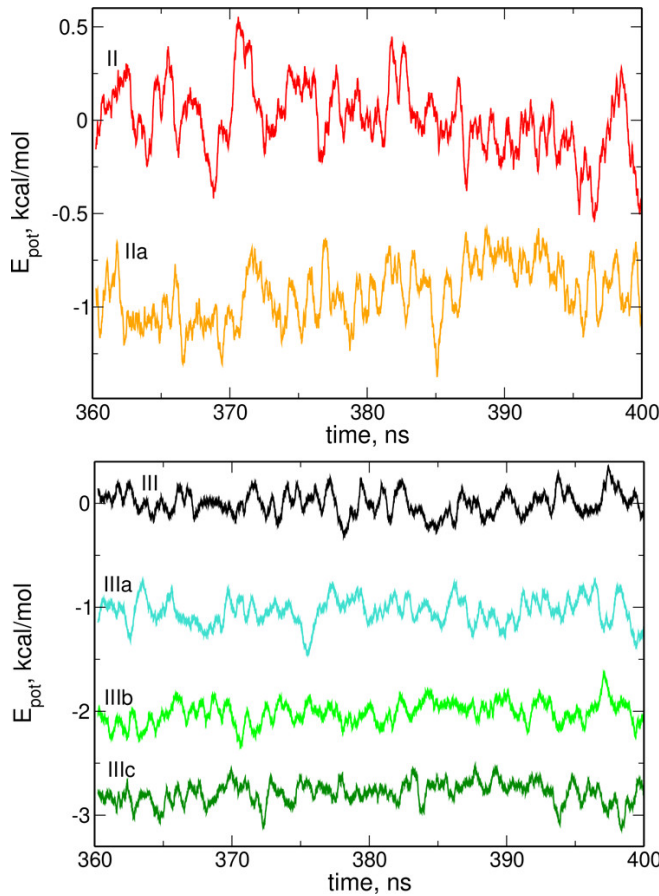


Figure 3.22: Relative potential energies E_{pot} per Mg^{2+} ion for II, IIa and III, IIIa-c systems for the last 40 ns of classical MD simulations with applied moving average over 0.5 ns.

requires larger time for the next aggregation process to occur.

For each system at 3 points of the classical trajectory - initial, after 20 ns and after 400 ns, the abundance of different forms of Mg_xCl_y complexes was determined. Results for systems I, II and IIa are in Figure 3.24 and for the other in Figure 3.25. For system I, where $\text{Mg}(\text{TFSI})_2:\text{MgCl}_2$ ratio equals 2:1, there are less Cl^- anions than metal cations, so at any time there must be some "free" magnesium ions present. This effect is observed - after 400 ns still more than 50% of cations are not coordinated to chlorine anions. Initially, some amount of MgCl^+ complex is formed and then aggregates into more complicated structures: MgCl_2 and $\text{Mg}_2\text{Cl}_y^{4-y}$ with $y > 2$.

For system II, which at the first step contained only "free" Mg^{2+} , initially MgCl^+ and MgCl_2 are produced, and after 400 ns these complexes and "free" Mg^{2+} cations are still present in the solution but MgCl^+ amount is smaller. Instead, $\text{Mg}_2\text{Cl}_y^{4-y}$ aggregates are formed. System IIa contained $\text{Mg}_2\text{Cl}_2^{2+}$ aggregate at first step, and initially within 20 ns some of them dissociated and some associated into larger aggregates, there are no significant further changes.

In systems III and IIIa-c the $\text{Mg}(\text{TFSI})_2:\text{MgCl}_2$ ratio is 1:2, so it is possible for all of the Mg^{2+} cations to form $\text{Mg}_3\text{Cl}_4^{2+}$ complexes. In systems III and IIIa aggregation processes are observed. In the former, initially within 20 ns MgCl^+ and MgCl_2 are produced and then condense into more aggregated complexes with some amount of $\text{Mg}_3\text{Cl}_4^{2+}$. In system IIIa, the amount of initially present MgCl_2 and $\text{Mg}_2\text{Cl}_2^{2+}$ decreases and both types of $\text{Mg}_3\text{Cl}_4^{2+}$ are formed. For IIIb and IIIc

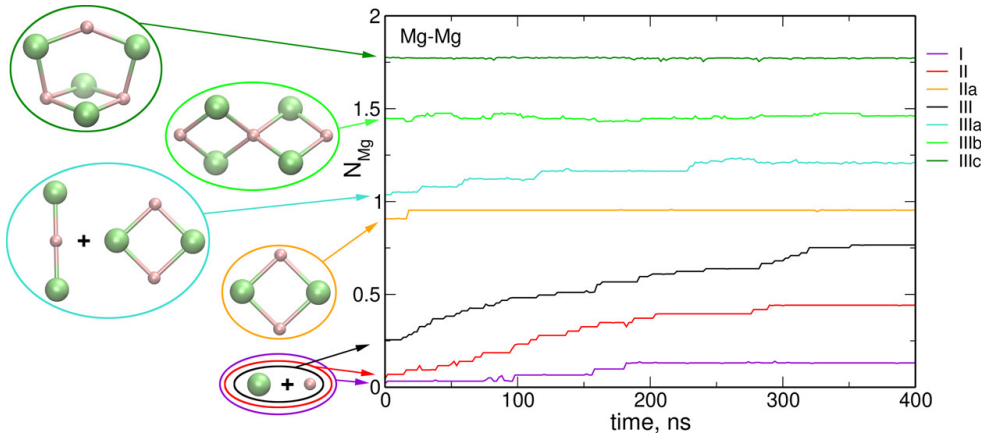


Figure 3.23: Average number of Mg^{2+} ions at the distance of 4 Å from the Mg^{2+} ion. Initial arrangements of Mg^{2+} and Cl^{-} ions are shown on the left hand side of the plot

only small number of initial complexes dissociate or associate into larger forms, and after that the amount of $\text{Mg}_3\text{Cl}_4^{2+}$ remains constant. However, in IIIb system, a conversion of type I of $\text{Mg}_3\text{Cl}_4^{2+}$ into type II is observed what remains in agreement with QC results indicating bigger stability of type II.

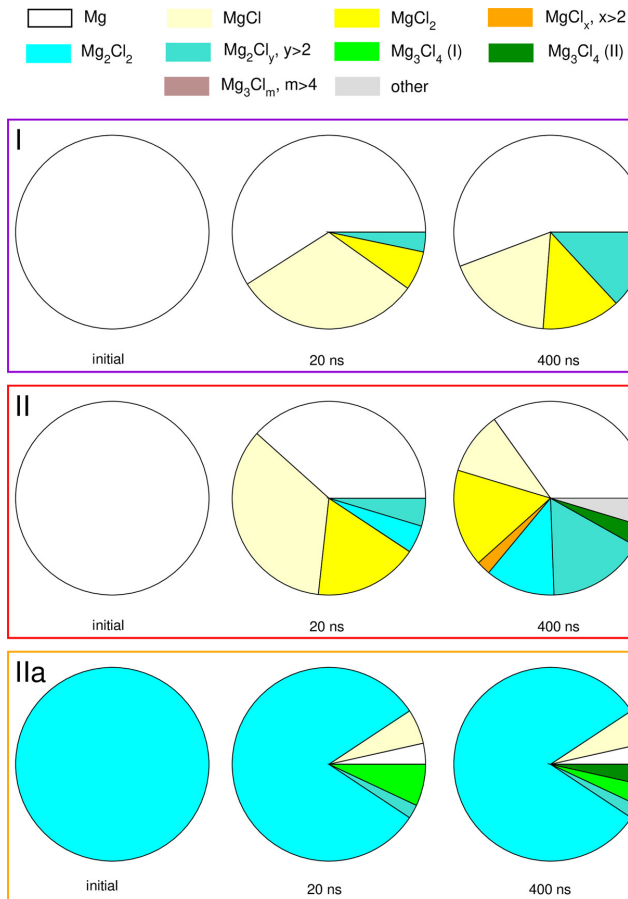


Figure 3.24: Abundance of Mg^{2+} ions in different complexes at different stages of classical MD simulations for systems I, II and IIIa

From these simulations it could be concluded that Mg^{2+} ions tend to form stable $\text{Mg}_2\text{Cl}_2^{2+}$ or $\text{Mg}_3\text{Cl}_4^{2+}$ complexes, depending on the $\text{Mg}(\text{TFSI})_2:\text{MgCl}_2$ ratio. The results support the con-

clusions of the experimental work [332] about the possible processes of ion association occurring in the electrolyte.

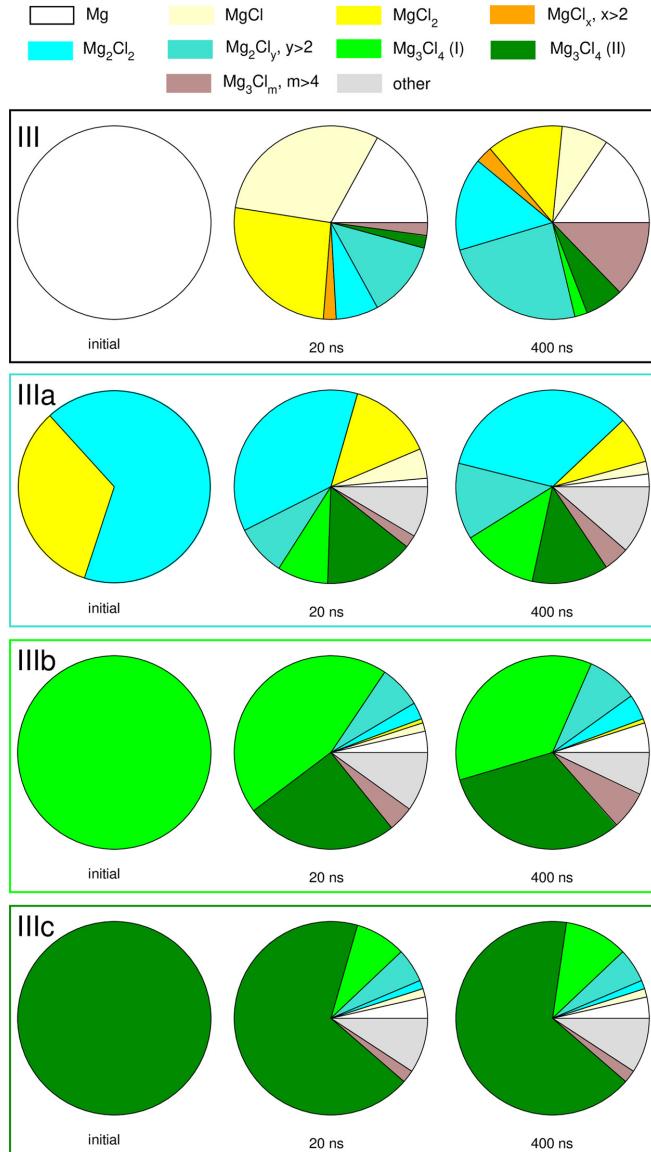


Figure 3.25: Abundance of Mg^{2+} ions in different complexes at different stages of classical MD simulations for systems III, IIIa, IIIb and IIIc

3.4 Ethylene carbonate with Na/Li TFSI salt

Ethylene carbonate (EC) is one of the most widely used solvents for ion-conducting electrolytes due to its stability [42]. To reduce the flammability, the addition of fluorinated derivatives of EC was considered and tested in lithium and sodium batteries [84–87]. This section presents results obtained for electrolytes based on LiTFSI or NaTFSI dissolved in EC or in its mono-(F1EC) and difluorinated (F2EC) derivatives, as well as for neat solvent, which were a subject of experimental work [85]. This study was published in the paper [IV].

3.4.1 System details

QC calculations were performed in vacuum using MP2 methodology to determine the Na^+ -carbonate binding energies and to obtain the IR spectra.

Table 3.7: Compositions of Li/NaTFSI - carbonate systems

system	carbonate	MeTFSI	atoms	concentration, mol/dm ³
EC	500	0	5000	0
F1EC	500	0	5000	0
F2EC	500	0	5000	0
Li-EC	474	41	5396	1.072
Li-EC	348	127	5512	2.922
Li-F1EC	466	42	5332	1.034
Li-F2EC	461	47	5362	1.065
Li-EC/F1EC	235/235	41	5356	1.041
Na-EC	474	41	5396	1.065
Na-EC	348	127	5512	2.875
Na-F1EC	466	42	5332	1.028
Na-F2EC	461	47	5362	1.055
Na-EC/F1EC	235/235	41	5356	1.034

The compositions of the systems simulated in classical MD are listed in Table 3.7. Simulations were performed under the 1 atm pressure, and in temperature of 298 K for 20 ns, and then 150 ns of trajectories were produced in the NVT ensemble, the last 100 ns was used for analysis. The time step was equal 1.0 fs.

AIMD simulations were performed for selected systems: neat solvents, Li/NaTFSI in EC and for LiTFSI in F1EC. Simulation boxes contained 50 solvent molecules (for neat solvents) or 46 solvent molecules and 4 MeTFSI ion pairs. Simulations were performed with 1.0 fs timestep for 35 ps, for analysis the last 30 ps were used.

3.4.2 Results

The binding energies calculated at the MP2 level are listed in Table 3.8. It is readily seen that the binding of Na^+ is weaker than that of Li^+ and that for both ions, the strength of the binding decreases in the order EC > F1EC > F2EC.

Table 3.8: Binding energies in kcal/mol calculated at the MP2 level, data for Li^+ are taken from [334]

cation/carbonate	EC	F1EC	F2EC
Li^+	-46.9	-42.2	-37.1
Na^+	-38.2	-34.3	-30.2

The RDFs for the $\text{Me-O}_{\text{carb}}$ pairs are presented in Figure 3.26. The positions of the first maximum do not depend on the carbonate used as a solvent and are equal 1.91 Å for lithium and 2.31-2.32 Å for sodium in 1 M solutions. The value for lithium agrees with experimentally measured 1.91 Å by neutron diffraction [112]. In AIMD, both maxima appear at higher distances, 1.95 and 1.97 Å for lithium in EC and F1EC respectively and at 2.38 Å for sodium in EC.

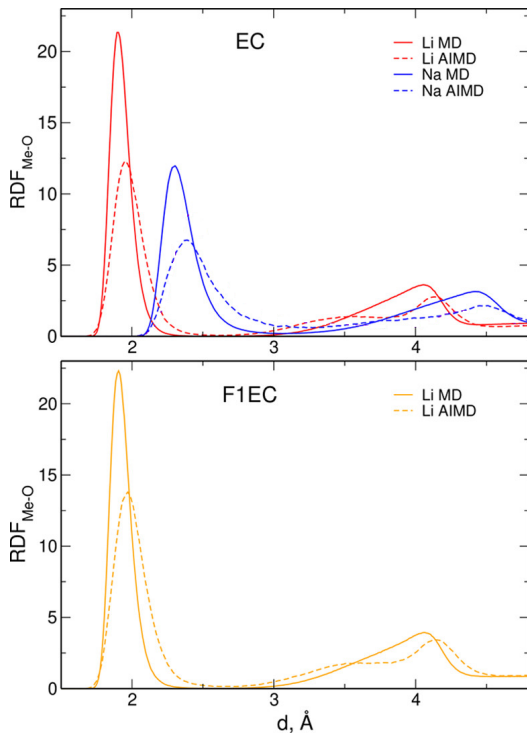


Figure 3.26: Radial distribution functions for $\text{Me-O}_{\text{carb}}$ pairs where O_{carb} is the oxygen atom from carbonate molecule

In Figure 3.27 integrated RDFs for Me-O pairs are shown. Non-negligible coordination by the TFSI^- anion is observed only in the case of F2EC or concentrated (3 M) solutions, thus only these results are presented. For lithium cations, coordination numbers in 1 M solutions are similar for EC and F1EC and equal 4. Similarly, for sodium these numbers are equal 5.3 and 5.37 respectively and are larger due to the bigger cation radius. For F2EC solutions, the number of coordinating oxygens from carbonate molecules decreases to 2.88 and 4.58 for lithium and sodium, respectively. However, in this case the average number of coordinating oxygen atoms from the TFSI^- anion are equal 1.14 and 0.91 respectively, leading to total coordination numbers equal 4.02 and 5.49 respectively. Similarly, these total values remain unaffected for 1:1 EC/F1EC solvent mixture. However, in this case, ratios of coordinating EC and F1EC are not 1:1, but are 3.18:0.81 for lithium and 3.51:1.86 for sodium, respectively. This shows that coordination

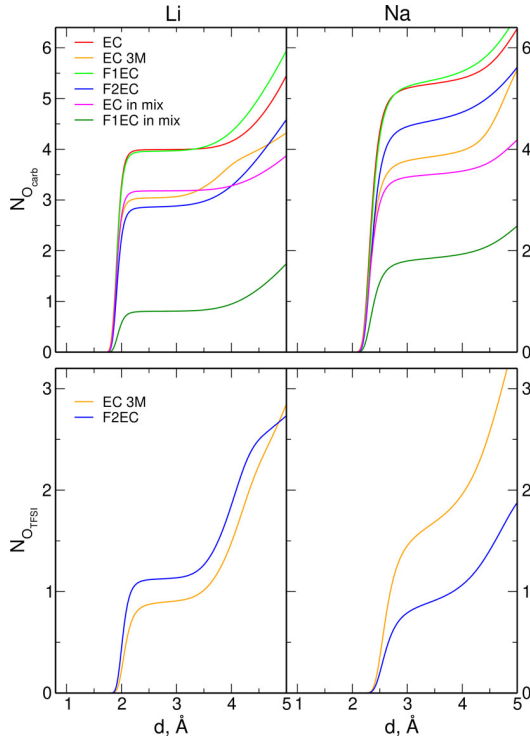


Figure 3.27: Integrated Me-O RDFs from classical MD for carbonate and TFSI oxygen atoms

to EC is preferred over F1EC and is in agreement with results of electrospray ionization mass spectroscopy experiments [204]. In 3 M solutions in EC the average number of coordinating oxygen atoms are equal 3.07 O_{carb} and 0.91 O_{TFSI} for lithium and 3.86 O_{carb} and 1.69 O_{TFSI} for sodium, respectively. Thus, here high concentration increased the probability of coordination by TFSI⁻ anions. In case of F2EC solutions non-negligible coordination by TFSI⁻ anion is caused by Me-solvent binding weaker than in EC or F1EC solutions.

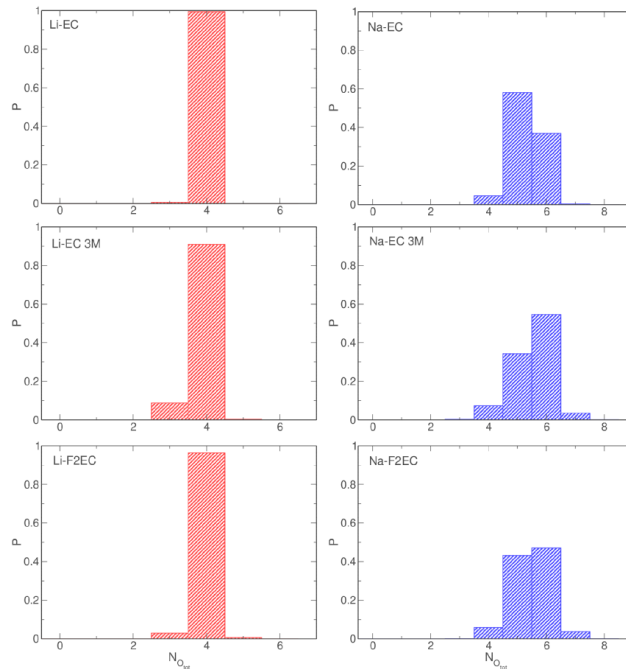


Figure 3.28: Histograms of average total numbers of oxygen atoms coordinating the Me⁺ ion

Figure 3.28 contains example histograms of total number of coordinating oxygen atoms for metal cations. For lithium, in almost all cases, the most probable number of oxygen atoms is 4, only in the 3 M solution there is about 10% of ions with coordination number equal 3. For sodium cation most probable is coordination by either 5 or 6 oxygen atoms, higher values are preferred in fluorinated solvents or in the concentrated solution. From the histograms (not shown here, but presented in [IV]) for specific oxygen atoms (from solvent or TFSI⁻ anion) it is observed that in most cases the cation is coordinated only by solvent molecules and the total coordination number is equal to the number of coordinating solvent molecules. The only exceptions are solutions in F2EC or 3 M in EC. In these systems, the possible O_{TFSI} values range from 0 to 4 for Li⁺ and from 0 to 6 for Na⁺, however 0 is the most probable number (40-55%). Even values of O_{TFSI} number seem to be favored and together with the observation that the number of coordinating TFSI⁻ anions is usually between 0 and 2, this leads to conclusion that bidentate Me⁺ coordination by the anions is preferred.

Table 3.9: Residence times in ns for oxygen atoms from solvent molecules or TFSI⁻ anions and anion residence times

system	EC	F1EC	F2EC	TFSI	
				τ_O	τ_{an}
Li-EC	7.6				
Li-EC 3 M	37.4			3.8	13.6
Li-F1EC		3.6			
Li-F2EC			1.9	3.7	12.4
Li-EC/F1EC	12.0	2.3			
Na-EC	1.5				
Na-EC 3 M	19.1			2.9	10.9
Na-F1EC		1.4			
Na-F2EC			1.0	0.7	2.4
Na-EC/F1EC	2.5	0.9			

To study the dynamics of complexation, residence time autocorrelation functions were calculated. Their plots are presented in Figures 3.29 and 3.30. For each of them stretched exponential functions $e^{-\left(\frac{t}{\tau_O}\right)^\alpha}$ were fitted yielding the residence times τ_O which are collected in Table 3.9. For every case, values for lithium are larger than for sodium and regardless of the cation they decrease in order EC > F1EC > F2EC. This implies faster exchange of solvent molecules in solvation shell for fluorinated ones what agrees with tendencies observed for binding energies from QC calculations. In concentrated electrolytes, solvent residence times increase by about an order of magnitude, which is probably caused by the bigger viscosity of such systems. In EC:F1EC mixture residence times for EC molecules are larger than those in pure EC electrolyte and the opposite effect is observed for F1EC, thus in the solvent mixture, the stronger interacting solvent remains bound to the cation for longer times and the speed of exchange of the other solvent increases. For residence times for TFSI⁻ anions and its oxygen atoms, in 3 M EC solutions values for sodium decrease about 20-30% with respect to values for lithium, in this case the dynamics is presumably limited by the viscosity. In the case of 1 M solutions in F2EC,

the decrease for sodium is about 5-fold when compared to lithium.

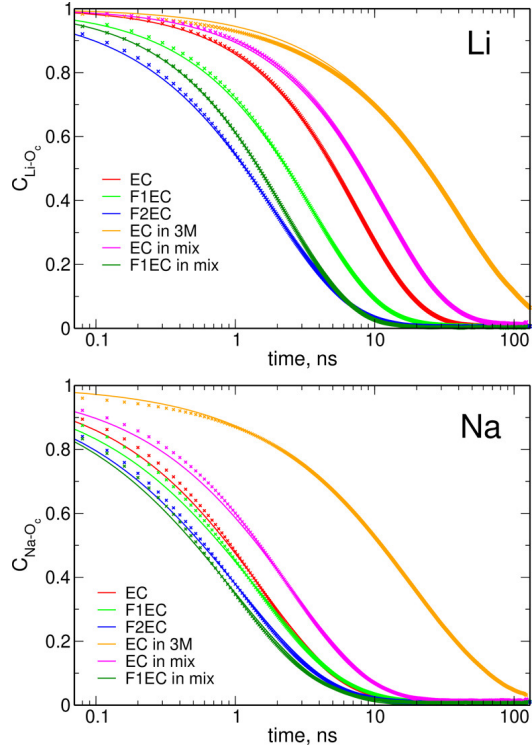


Figure 3.29: Residence time autocorrelation functions for $\text{Me-O}_{\text{carb}}$, lines are fits to the data

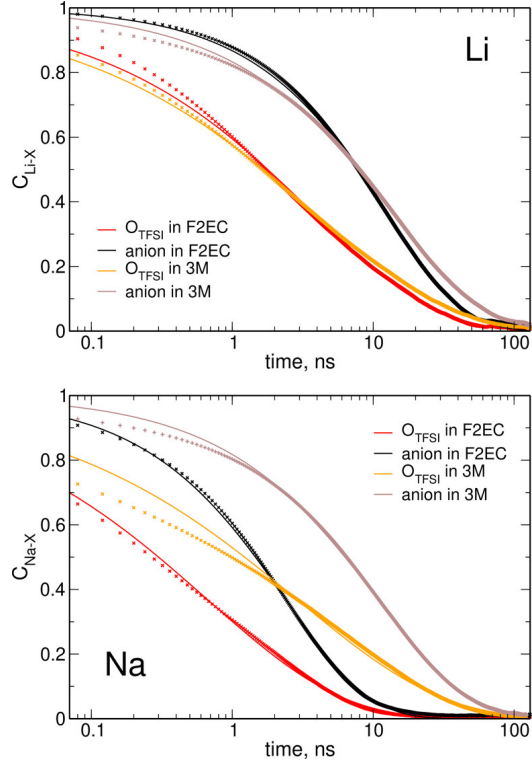


Figure 3.30: Residence time autocorrelation functions for $\text{Me-O}_{\text{TFSI}}$ and Me-anion , lines are fits to the data

Observed differences between sodium and lithium-based electrolytes in the structure and

dynamics are the effect of different strengths of cation-solvent interactions. Solutions in pure EC or F1EC do not differ significantly; however in electrolytes based on EC/F1EC mixture, cations prefer interactions with EC molecules. This trend may have an influence on the local structure and ion exchange in electrolytes with an F1EC additive, and it should be further investigated.

3.5 NaFSI/TFSI solutions in ether solvents

Among studied electrolytes for batteries are systems based on glymes. There were several works that considered diglyme [335–337] or other short glymes [39, 113, 188, 191, 206, 338–340] as a solvent. Other systems are based on polymers, mostly poly(ethylene oxide) (PEO) [37, 82, 341]. As sodium salts in such electrolytes NaFSI or NaTFSI were used [37, 82, 188, 191, 206, 338, 341]. However, published MD results had different applied methodology and typically focused on only one of these anions and either on short oligoglyme molecules or on polymer chains. Thus, the study described in this section was an attempt to compare results for both anions and for three solvents with different lengths of the ether chain: monoglyme, tetraglyme, and PEO. This study was published in the article [V].

3.5.1 System details

Electrolytes considered in this work were NaFSI or NaTFSI solutions in monoglyme, tetraglyme or short PEO chains with 100 oxygen atoms each. Systems were constructed in such a way that the total number of ether oxygens was equal 600. Thus, the number of solvent molecules was 300, 120 and 6 for monoglyme, tetraglyme and PEO respectively. For each salt, two concentrations with 30 or 100 ion pairs were simulated, leading to Na/O ratios 1:20 or 1:6. These were the ratios studied experimentally [37]. Initial structures for systems with PEO were prepared using Scigress [342].

In this work, all systems were studied by classical MD. A timestep of 1.0 fs was used. Each of the systems was equilibrated in NpT ensemble with pressure 1 atm and temperature 303 K for 50 ns (glymes) or 100 ns (PEO). Then, 150-250 ns of trajectories in the NVT ensemble, with volume reproducing the equilibrated density in NpT ensemble, were recorded. Results for a given system were averaged over 10 independent MD trajectories.

3.5.2 Results

RDFs for Na-O pairs for 1:6 electrolytes are presented in Figure 3.31. The position of the maximum for Na-O_E pair in every case is equal 2.36-2.37 Å and does not depend on the anion, solvent molecule or salt concentration. In systems with FSI⁻ anion it has a larger height than in systems with TFSI⁻. For Na-O_A pairs, the position of the maximum depends on the anion, for FSI⁻ is located at the same distance as for Na-O_E, while for TFSI⁻ it is at smaller distance - 2.3 Å. Heights of the maxima are significantly smaller for FSI⁻ anion than for TFSI⁻. This difference suggests that Na⁺ complexation by the FSI⁻ anions is weaker.

The effect of weaker complexation by FSI⁻ anion is seen in the integrated RDFs in Figure 3.32. For 1:20 systems coordination by this anion is marginal, it is non-negligible only in the system with PEO, but is still less than 1 oxygen atom per cation. For all systems, it is visible that coordination by ether oxygen is preferred over coordination by the anion; however, this effect is weaker in concentrated solutions. Only in 1:6 NaTFSI-PEO system coordination to the anion is preferred over ether oxygen atoms (average number of oxygen atoms at distance 3.5 Å equals

2.79 vs 2.64 for TFSI⁻ and PEO respectively).

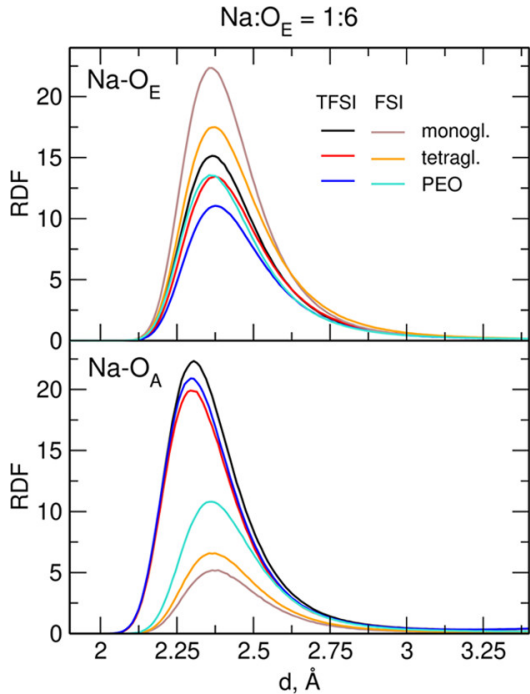


Figure 3.31: Radial distribution functions for Na-O atom pairs in 1:6 electrolytes (O_E - ether oxygen atom, O_A - oxygen atom from anion)

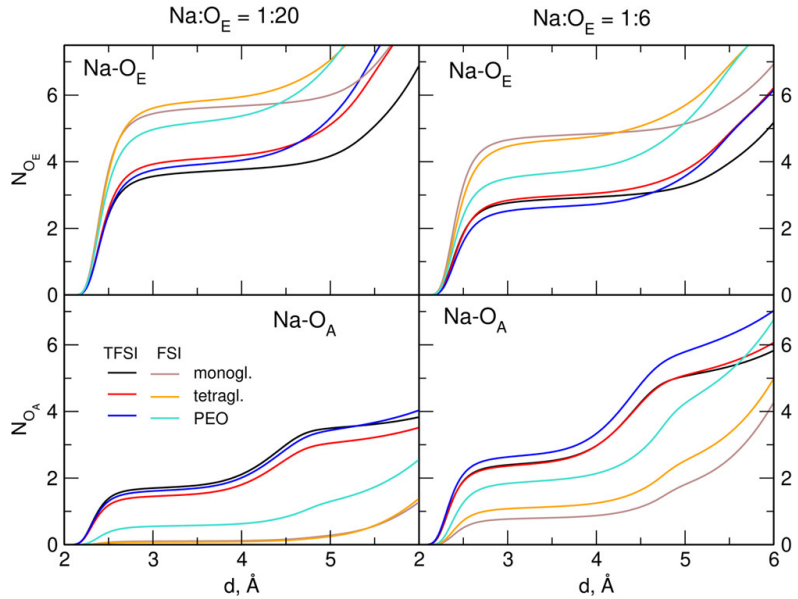


Figure 3.32: Integrated Na-O RDFs for 1:20 and 1:6 systems

To gain a better understanding of the cation-solvent or cation-anion aggregates, histograms of coordination numbers (CNs) were plotted. Selected representative examples are shown in Figure 3.33. In the 1:20 NaFSI electrolyte in tetraglyme the most probable number of ether oxygen atoms coordinating the cation is 6. At bigger concentrations, this distribution becomes wider and for PEO all values between 2 and 6 have similar probability. For NaTFSI systems,

all distributions are broad and abundance of CNs = 3, 4 or 6 is comparable. Figure 3.33(b) shows anion CNs distribution for 1:20 systems in monoglyme, here the effect of more frequent coordination by TFSI^- anions compared to FSI^- anions, as it was seen in the RDFs, is also present. For TFSI^- the most probable CNs are 2 and next 0 and 4 while for FSI^- the most probable value for more than 90% of cations is 0. Finally, Figure 3.33c shows the distribution of number of cations coordinated to PEO molecule in 1:6 system. Here, the maximum for the distribution for NaFSI electrolyte is at about 20 cations whereas for NaTFSI at about 15 cations.

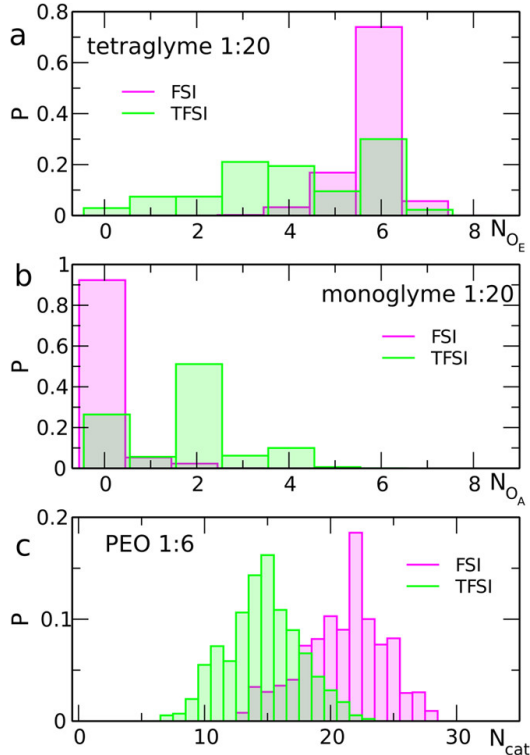


Figure 3.33: Distribution of the number of ether oxygen atoms coordinated to Na^+ (a), of the number of anion oxygen atoms coordinated to Na^+ (b), and of the number of Na^+ ions coordinated to PEO molecules (c)

For the analysis of binding pattern in mono- and tetraglyme systems, Venn diagrams were prepared showing the percentage of solvent molecules engaging specified subset of oxygen atoms in interactions with sodium cations, the graphs were symmetrized with respect to equivalent atoms. For example, for plot for monoglyme-NaFSI connections shows that 74% of monoglyme molecules interact with Na^+ cations with both oxygen atoms, and 12% with one of them, this percentage is divided equally to the two indistinguishable O atoms. Such diagrams for 1:6 systems are presented in Figure 3.34. For monoglyme in NaFSI the percentage of molecules that interact through both oxygen atoms is almost two times larger than in the NaTFSI electrolyte. In addition, in tetraglyme this ratio is about 4:1 (38% and 9% respectively). For the NaTFSI system in tetraglyme it is more probable that 3 consecutive O atoms are interacting with Na^+ (20%) while in NaFSI it is less abundant configuration (14%). In more than 80% cases, if more than one atom from tetraglyme interacts with sodium cations, the interacting atoms are consecutive oxygen atoms.

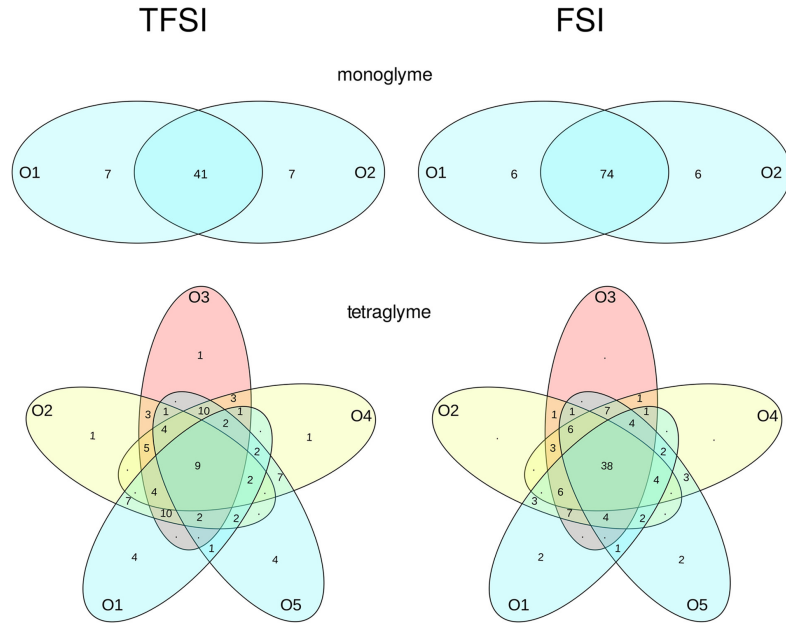


Figure 3.34: Venn diagrams showing the connectivity between Na^+ ion and oxygen atoms of the monoglyme and tetraglyme molecules in 1:6 electrolytes, values lower than 1% are displayed as dots

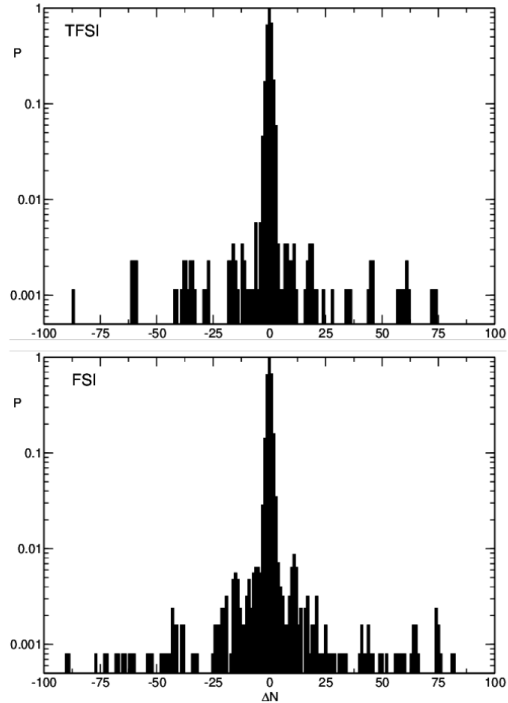


Figure 3.35: Distribution of the probability that an oxygen atom positioned at the site ΔN is coordinated to the Na^+ cation, interacting with the oxygen atom at the site $N = 0$ in the 1:6 PEO-based electrolytes

For PEO it was impossible to visualize the binding pattern using Venn diagrams, so in Figure 3.35 the probability is plotted that the same cation that interacts with the oxygen atom at position $N = 0$, simultaneously interacts with atom positioned ΔN sites apart. Significant

probability is obtained only for $|\Delta N|$ not larger than 3, but it is worth noting that there are several values with non-zero probability corresponding to $|\Delta N|$ larger than 20. These are the cases where a loop of PEO chain occurs and enables Na^+ coordination to its distant parts.

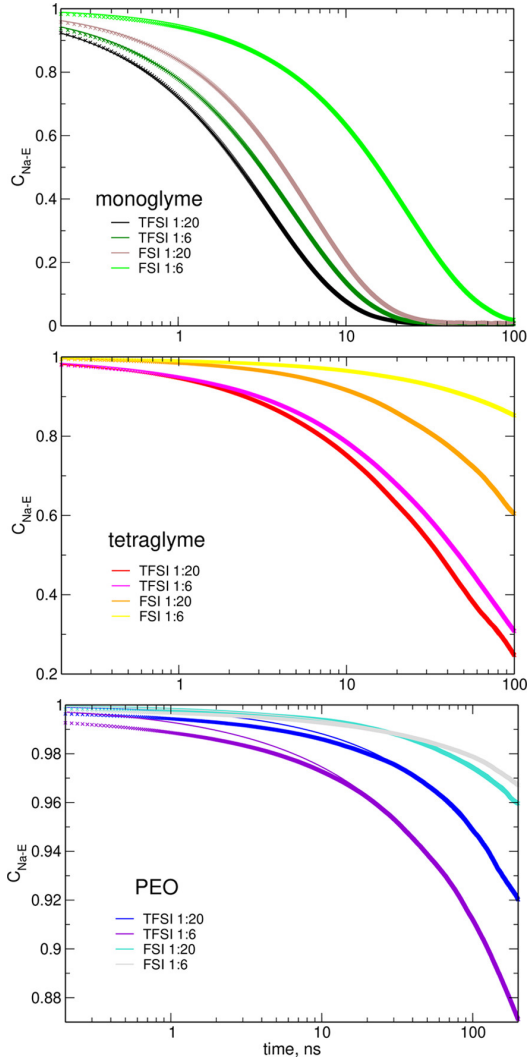


Figure 3.36: Residence time autocorrelation function for Na-ether interactions. Lines are fits to the data

As for the previously described systems, the residence time autocorrelation functions were calculated and are presented in Figure 3.36. Residence times for ether molecules τ_E were calculated by fitting stretched exponential function $e^{-(\frac{t}{\tau_E})^\alpha}$ to the obtained data. τ_E values are shown in Table 3.10. Due to larger viscosities of tetraglyme and PEO based systems, during the simulation time, only for monoglymes the autocorrelation functions reached 0. For all systems, residence times in NaFSI electrolytes are larger than in NaTFSI solutions. This suggests that NaFSI salt promotes more stable Na^+ binding to solvent molecules and thus slower exchange of ions in the solvation shell. For PEO-based electrolytes in NaFSI solutions residence times increase in 1:6 electrolyte compared to 1:20 one, while for NaTFSI the effect is opposite. A possible explanation is the different mechanism of ion transport due to larger number of cation-anion interactions in NaTFSI solutions which increases the probability of Na^+ exchange between anions.

Table 3.10: Residence times τ_E for ether molecules in nanoseconds

system	τ_E , ns
NaTFSI – monoglyme 1:20	3.5
NaTFSI – monoglyme 1:6	4.7
NaFSI – monoglyme 1:20	6.1
NaFSI – monoglyme 1:6	23
NaTFSI – tetraglyme 1:20	61
NaTFSI – tetraglyme 1:6	79
NaFSI – tetraglyme 1:20	250
NaFSI – tetraglyme 1:6	1710
NaTFSI – PEO 1:20	9090
NaTFSI – PEO 1:6	7020
NaFSI – PEO 1:20	27500
NaFSI – PEO 1:6	98100

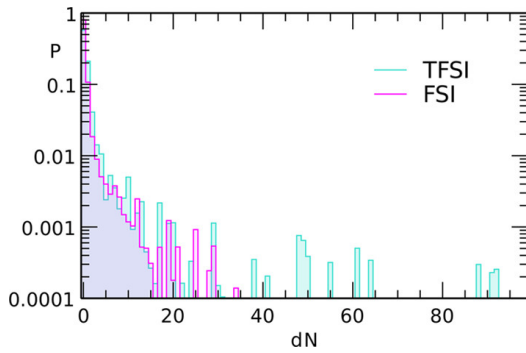


Figure 3.37: Probability of the displacement of Na^+ ion by dN sites along the PEO chain in 1:6 Na(T)FSI/PEO electrolytes after 250 ns of simulations

For the PEO-based electrolytes in addition to data about distances between coordinating oxygen atoms, the dynamics of ions movement along the chains is also interesting. Figure 3.37 presents the probability that sodium cation moved after 250 ns of simulation by dN from its original position. For the majority of cations displacements are small and do not exceed five binding sites. For dN values between 5 and 15 probabilities are below 1%. These changes of binding sites could be related to cation movements along the PEO chain. There are also less probable cases of large dN values, up to tens of sites. They may be related to breaking PEO-cation interaction at one site and association of the cation to another binding atom, which due to spatial loop of the PEO chain may be a distant one (in values of dN). These changes are more probable in the electrolyte with TFSI^- anion.

Presented results showed differences in coordination numbers and binding patterns of ether molecules between systems with FSI^- and TFSI^- anions; the latter interact more frequently with sodium cations, while the former favor sodium-ether binding.

The total number of coordinating oxygen atoms decreases with increasing salt concentration. This effect stands in agreement with coordination numbers derived from experimental Raman spectra for NaTFSI solutions in carbonate solvents [343] or mixed molecular/IL electrolytes [344]. Observed for monoglyme trend of increasing probability of cation-anion coordination for increas-

ing salt concentration is in agreement with results for polarizable MD simulations for NaTFSI solutions [340]. However, this trend observed from MD simulations for PEO differs from conclusions made from experimental Raman spectra [37], where at low salt load almost all TFSI⁻ anions are "free" while only about 2/3 of FSI⁻ anions do not interact with sodium cation. On the other side, the experimental data for diluted solutions in tetra- or pentaglyme [206] stands in an agreement with trends obtained from MD simulations. The mentioned discrepancy for PEO with simultaneous compatibility between MD and experimental results, suggest that interactions in PEO have a different character than for short glymes and would need a specifically developed FF to be correctly described in MD simulation.

3.6 EMIM-TFSI with water

ILs are, as described in Chapter 1, one of the class of possible solvents for novel electrolytes. Despite their ionic character, also short-range interactions such as hydrogen bonds (HBs) may occur if appropriate donor and acceptor groups are present [21, 345–347]. Due to their hydrophilic nature, ILs are usually contaminated by water, what increases the significance of HB formation for their properties [348–352]. One of popular ILs is EMIM-TFSI, which in pure state, was studied by MD [353]. In this section structural results obtained from EMIM-TFSI IL with differing amount of water contamination are presented. This study was described in the article [VI].

3.6.1 System details

Studied systems contained 15 pairs of EMIM-TFSI ionic pairs and an increasing number of water molecules: 0, 2, 5 and 15, corresponding to water mole fraction x equal to 0, 0.12, 0.25 and 0.5, respectively. Also, a system of neat water containing 181 molecules was modeled. In order to average results, two independent replicas for neat liquids and three for IL/water mixtures were simulated.

Initially, classical MD simulations were performed for equilibration for 100 ns in the NpT ensemble with pressure of 1 atm and temperature 298 K and then for 100 ns in the NVT ensemble. Next, structures from these simulations were used as starting points for AIMD in NVT ensemble with temperature of 298 K. 40 ps of trajectories were recorded, analysis was done for the last 30 ps. For both classical MD and AIMD a timestep of 1 fs was used.

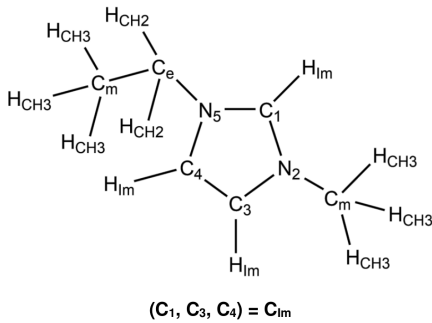


Figure 3.38: Labeling of atoms in EMIM^+ cation

Here, plots of the distribution functions were made with the use of TRAVIS [272, 273]. In the description of results O_{TFSI} means oxygen atoms from the TFSI^- anion and O_w oxygen atoms from water molecules. Labeling of atoms from EMIM^+ cation is presented in Figure 3.38.

3.6.2 Results

As a starting point for hydrogen bonding analysis, radial distribution functions are examined, plots for selected atom pairs in the system with 0.5 mole fraction of water are presented in Figure 3.39 and for neat IL in Figure 3.40. For pairs involving imidazolium ring hydrogen atoms

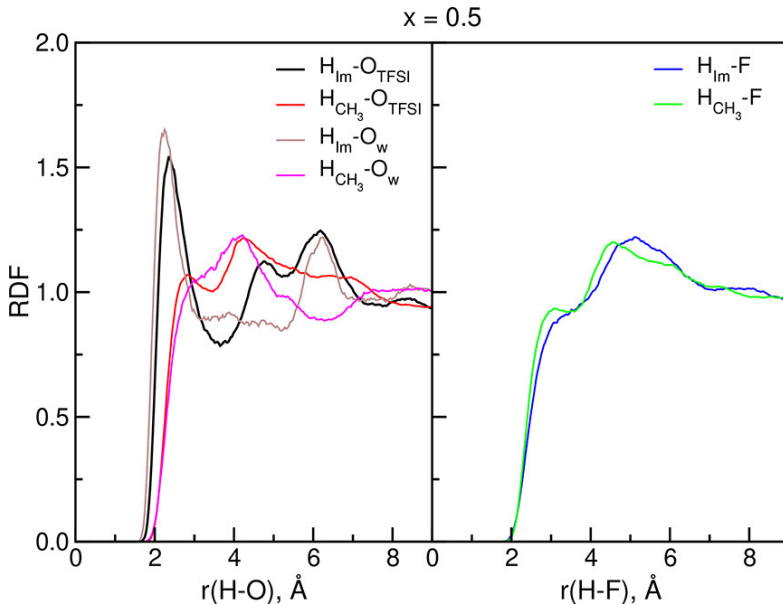


Figure 3.39: Radial distribution functions for selected atom pairs for systems with water mole fraction 0.5

(H_{Im} -O_{TFSI} or H_{Im} -O_w) the first sharp maximum appears slightly above 2 Å with smaller next maxima above 4 Å. For pairs with methyl hydrogen atoms (noted as H_{CH_3}) maxima near 2 Å are weaker and the main maxima are located at about 4 Å but still are lower than the first peak for H_{Im} atoms. At H-F RDFs the behaviour of both types of hydrogen atoms is similar with weak maxima at 3 Å and main maximum between 4.5 and 5.5 Å. Thus, from these functions it may be concluded, that EMIM⁺ will interact with oxygen atoms from anions or water molecules, mostly by the hydrogen atoms from the imidazolium ring.

To form a hydrogen bond (HB) it is also needed that the donor (D), acceptor (A) and hydrogen (H) atoms are in a sufficiently linear arrangement. Therefore, for further analysis, combined distribution functions (CDFs) were plotted. They show the relative probability of finding a configuration of atoms at a specified D-A distance and D-H-A angle. A sample plot for the system with $x = 0.5$ is presented in Figure 3.41. The preferable values for HB are D-A distance up to 350 pm and D-H-A close to 180°. There is a large probability of finding such configuration for C_{Im}-H-O_{TFSI} as well as for the C_{Im}-H-O_w. The probability of finding appropriate configurations for C_m atoms is smaller but non-negligible. Occurrences of C-H-F arrangements suitable for hydrogen bonding are infrequent.

Spatial distribution functions (SDFs) plotted in Figure 3.42 confirm previous observations - the regions of increased density of oxygen acceptors are close to hydrogen atoms from the imidazolium ring.

Figure 3.43 shows statistics of HBs for each system. The criteria of the existence of the HB were the following: D-A distance not larger than 3.5 Å and the deviation of D-H-A angle from linearity not bigger than 40°. In the neat IL, EMIM⁺ cations form 2.5 HBs per cation, 1.7 of these bonds are to oxygen atoms. About half of H-O_{TFSI} bonds are formed by hydrogen atoms from the imidazolium ring. For methyl groups the average number of bonds is 0.6, here the lower probability of bonding is compensated by the bigger number of available hydrogen atoms of this

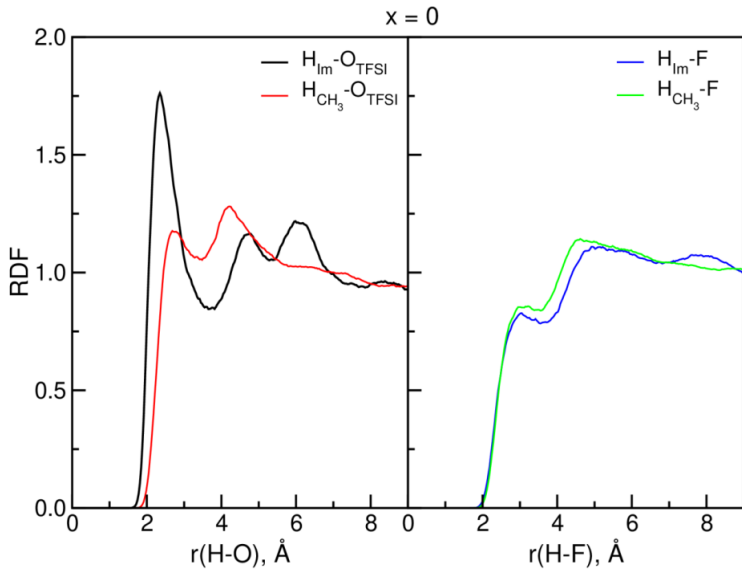


Figure 3.40: Radial distribution functions for selected atom pairs for neat IL

type. Bonds to fluorine atoms are less probable (about 0.6 bonds per cation) and to nitrogen atoms are the least probable (0.15 per cation).

In systems with water, H_2O molecules tend to form HBs with oxygen atoms from TFSI^- anions, and there is about 0.8 of HB per H_2O molecule in system with $x = 0.25$ or $x = 0.5$. The system with $x = 0.12$ is an outlier, probably because of the poor statistics when the simulation box contains only two water molecules. For EMIM^+ cations the total number of formed HBs remains approximately unaffected and is in the range of 2.45-2.56 bond/cation. However, with increase of the content of water, there appears competition between TFSI^- anions and water molecules and it leads to decrease of EMIM-TFSI HBs number.

With increasing concentration of water, also the probability of water-water HB increases, in the most concentrated mixture there are 0.7 such bonds per water molecule. For systems with $x = 0.12$ or $x = 0.25$ there is a significant number of water-N bonds, about 0.25 per H_2O molecule and it disappears at bigger concentration. The average number of total HBs formed by water molecule is smaller in IL: 1.61 in the $x = 0.5$ system while in neat water it is equal 1.91. The number of accepting hydrogen atoms is also smaller in IL and for the most concentrated mixture is equal 1.15.

For TFSI^- anions the loss of EMIM-TFSI HBs is compensated by formation of water- TFSI^- HBs, and the average number of HBs per anion increases from 2.5 in the neat IL to 3.0 in the $x = 0.5$ system.

To summarize, in a mixture of liquids, water molecules form less HBs than in the neat water. For EMIM^+ cation total number of HBs remains fairly constant, with some replacement of EMIM-TFSI HBs by EMIM -water HBs. In neat IL not all of the oxygen atoms in TFSI^- anion are used for HBs, thus it gives probability for formation of additional HBs with water and the total number of HBs per anion increases with growing concentration of water. In section 4.4 influence of changes in number of HBs on the IR spectrum of the system will be described.

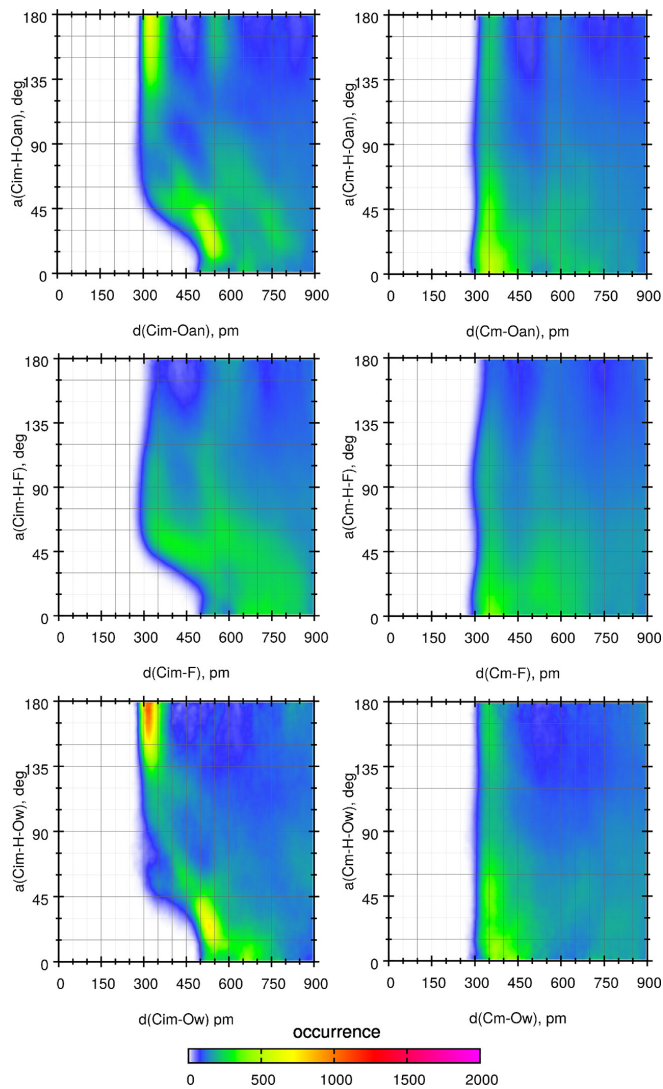


Figure 3.41: Combined distribution functions for selected donor-hydrogen-acceptor atoms in systems with water mole fraction 0.5

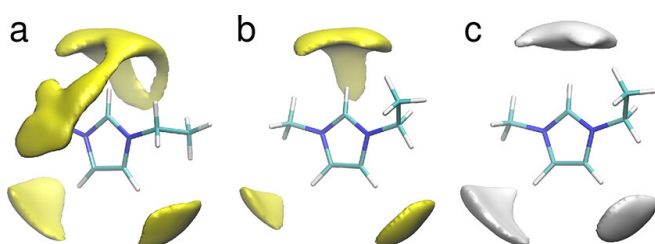


Figure 3.42: Spatial distribution functions of oxygen atoms around EMIM^+ cations: TFSI^- anions in the neat IL (a); TFSI^- anions in the $x = 0.5$ mixture (b); water molecules in the $x = 0.5$ mixture (c). Surfaces of particle isodensity of 10 atoms/ nm^3 are shown

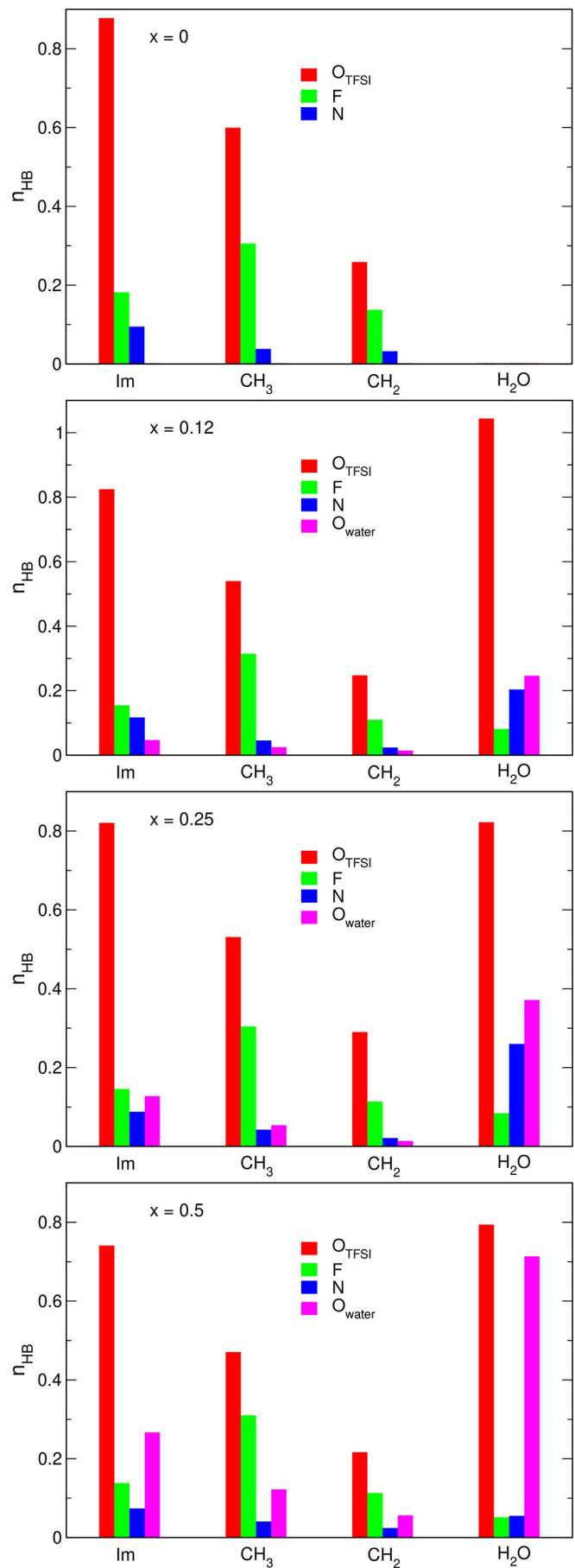


Figure 3.43: Average number of hydrogen bonds n_{HB} per donor. Donors are shown in the horizontal axis, acceptors are marked by colors

Chapter 4

IR spectra from AIMD simulations

This chapter presents the infrared spectra obtained from ab initio molecular dynamics (AIMD) simulations. Relationship between the IR spectrum and the structure of the liquid is analyzed and the results of calculations are compared to experimental data. Presented systems are some of those which structural properties were described in Chapter 3 and one with unpublished results at the moment of writing this work.

4.1 NaFSI solutions in EMIM-FSI ionic liquid

In this section spectral data for systems with NaFSI salt dissolved in EMIM-FSI ionic liquid are presented. Structural data and details of simulated systems are described in Section 3.1. The NaFSI/EMIM-FSI system was studied in the Master Thesis of the author of this work [316], therefore only new results are presented in this section, except for the top panel of Figure 4.1, which is essential for further analysis.

In experimental work [74] Raman spectra for the band at 730 cm^{-1} were obtained. However, the ab initio calculation of polarizability needed for obtaining theoretical Raman spectrum would significantly increase the computational effort of the simulation. Fortunately, the band at 730 cm^{-1} for EMIM-FSI is also active in the IR spectrum. Determination of the dipole moment does not affect the computational cost. Therefore, in this work only the IR spectrum is calculated, assuming that the shifts of the band position in IR will be a good estimate of the effect observed in Raman spectrum.

Spectra from AIMD simulations are systematically redshifted to frequencies lower about 80 cm^{-1} with respect to the experimental spectrum and are presented in Figure 4.1. The upper panel presents the mentioned region and has been discussed in the Master Thesis, here it will be only noticed that the experimentally observed blue shift of this band with increasing salt concentration was correctly reproduced. Calculated shifts: $7\text{--}8\text{ cm}^{-1}$ and 20 cm^{-1} for systems with $x = 0.2$ and $x = 0.5$, respectively, stand in a good agreement with experimental data from [74]: 7 cm^{-1} for $x = 0.2$ and 17 cm^{-1} for $x = 0.5$. One of the systems with $x = 0.5$ (shown in dashed line) is an outlier, with RDFs differing from other electrolytes with this concentration (Figures 3.7 and 3.12) and therefore it was excluded from further analysis.

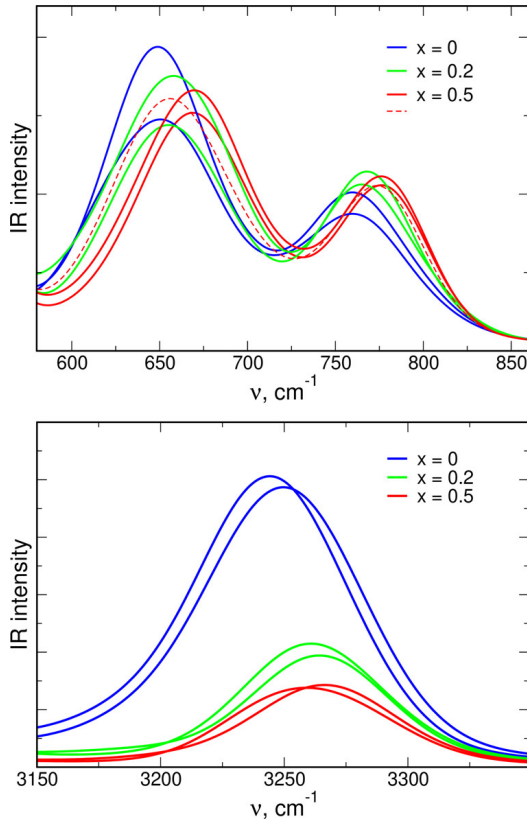


Figure 4.1: IR spectra obtained from AIMD simulations for electrolytes with different mole fractions of NaFSI

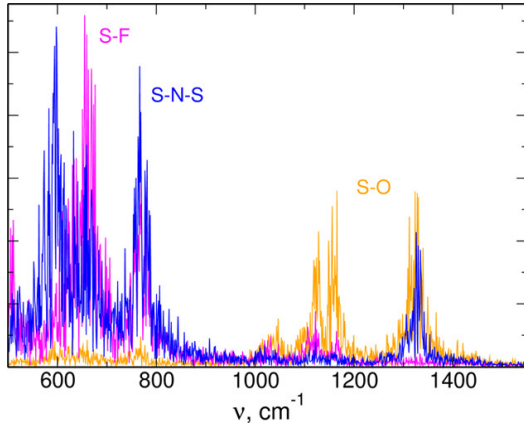


Figure 4.2: Sample Fourier transforms of S-O and S-F bond length and S-N-S angle for selected FSI^- anion

The bottom panel of Figure 4.1 presents the region of the C-H stretching band in the EMIM^+ cation. These cations do not interact directly with sodium, however a blue shift of positions for the maximum is observed. It is probably caused by changes in hydrogen bonding in the system - interactions between FSI^- anion with sodium cations are stronger than HBs. Thus with growing concentration of NaFSI less FSI^- are available for HBs and the C-H stretches are less involved in HBs. Their frequencies move towards higher values, returning to the values of "free" C-H vibrations. This result is corroborated with changes in the H-O RDF in Figure 3.7 with decreasing first maximum with NaFSI concentration increase. The effects of hydrogen

bonding on C-H vibrations in EMIM^+ cation will be addressed in section 4.4.

These results demonstrate that AIMD is able to correctly reproduce shifts observed in vibrational spectra. Oscillations in the system change periodically structural parameters such as bond lengths or angles. Thus, Fourier transforms (FTs) of these magnitudes should be able to catch the frequencies of normal nodes in which these local oscillations contribute. Therefore, to have a better insight into relation between local interactions and spectral properties, such analysis for NaFSI in EMIM-FSI IL was made. Example FTs for S-O, S-F bond lengths and S-N-S angle are presented in Figure 4.2. From this relations it is seen that the S-F stretching with some contributions of S-N-S angle bending contribute to the band at 650 cm^{-1} .

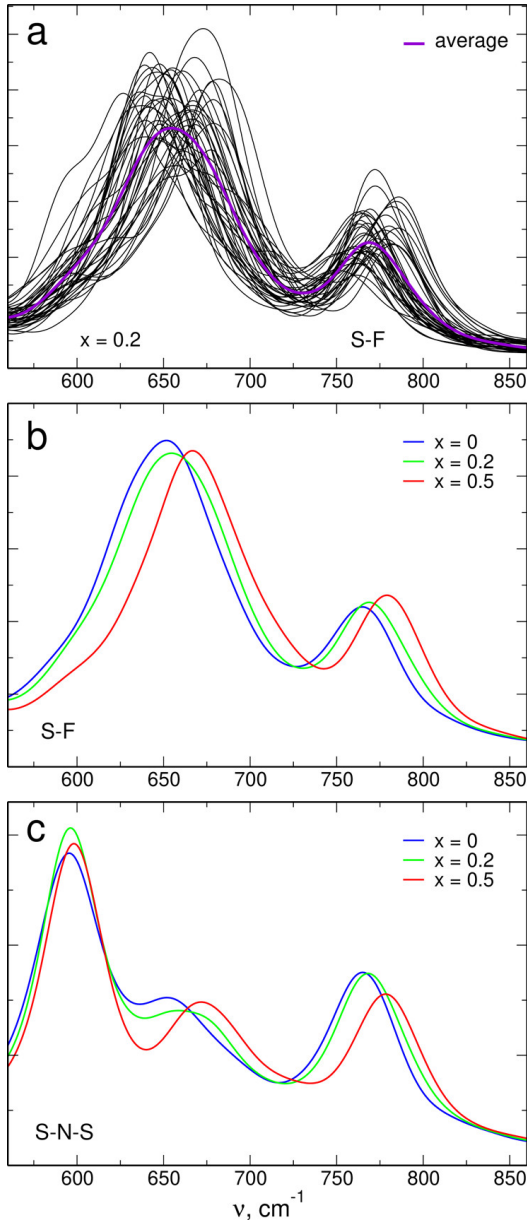


Figure 4.3: Fourier transforms of the S-F bond length for all FSI^- anions in $x = 0.2$ system (a), average values for Fourier transforms of S-F length (b) and S-N-S angles (c) for different salt concentrations

FTs for all S-F bonds in the $x = 0.2$ system are presented in Figure 4.3a. It is visible that positions of the maxima for individual bonds vary in the broad range of about 70 cm^{-1} . The

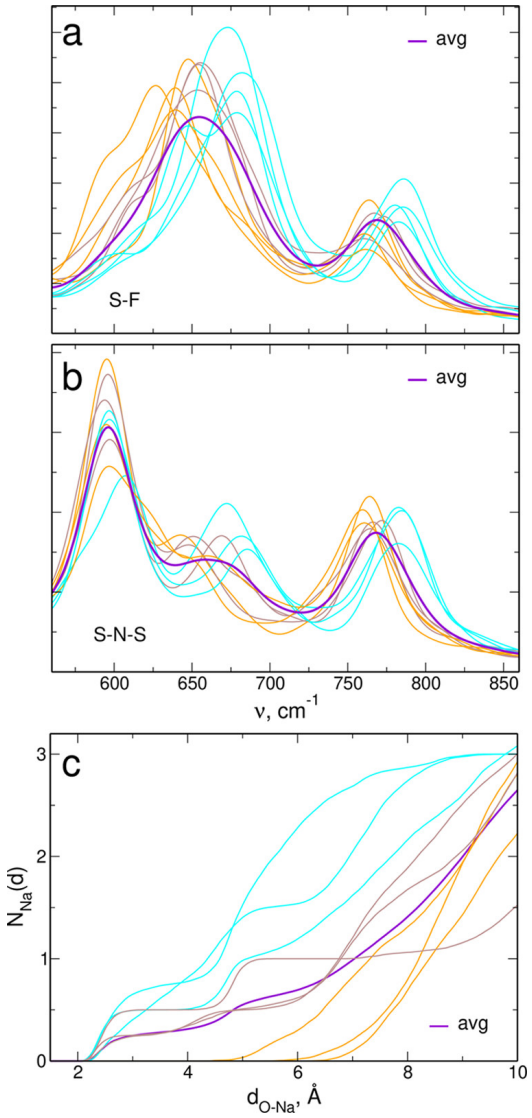


Figure 4.4: Fourier transforms of the (a) S-F bond length and (b) S-N-S angle for selected FSI^- anions in the $x = 0.2$ electrolyte and integrated (c) O-Na RDFs for selected anions

averages for S-F angles are shown in Figure 4.3b. It is clear that these FTs catch the frequencies of normal nodes, as the shifts of the maxima here are analogous to the shifts observed in the IR spectrum.

To check correlations between vibrational frequencies and the local structure, data for several selected FSI^- anions are plotted in Figure 4.4. There are three groups - anions with oscillations close to average frequency (brown lines), these blue-shifted (cyan lines) and red-shifted (orange lines) with respect to the average frequency of S-F stretching. The same colours are used for S-N-S bending in Figure 4.4b, and here the behaviour is identical, what suggests that the frequencies of S-F and S-N-S oscillations are correlated. For these selected anions in Figure 4.4c integrated RDFs for O-Na pairs are plotted. This picture shows that there is a correlation between shift of the individual frequency and the interaction with sodium cation - the anions with frequencies blue shifted with respect to the average value are interacting with more Na^+ cations while the anions with frequencies red shifted with respect to the average value do not have Na^+ cations in the first coordination shell.

Examples of mentioned anions in different environments are shown in Figure 4.5. The top panel presents an anion which has S-F stretching frequency red shifted with respect to average value (not interacting with Na^+), the middle the one with frequency close to average (weakly interacting with Na^+) and the bottom the one that has frequency blue shifted with respect to the average value (strongly interacting with Na^+). Here, weak interaction means that anion interacts with one Na^+ cation with geometry corresponding to the type III (Figure 3.2) and the strong interaction means interacting simultaneously with two Na^+ cations (right panel of bottom row of Figure 4.5) or with one cation in the stronlgy bound complex of type I (left panel).

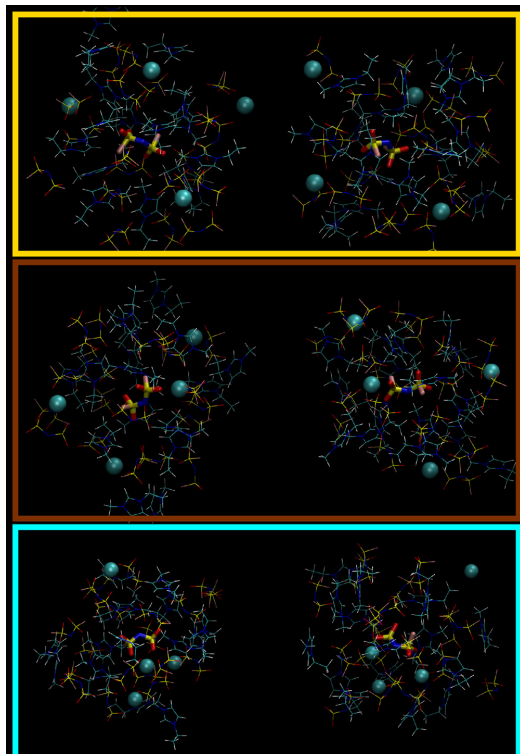


Figure 4.5: Local environment of selected FSI^- anions in the $x = 0.2$ system

Thus, here it has been shown that AIMD is able to correctly reproduce effects observed experimentally in IR spectra. What is more, as it has been seen, FTs of geometrical parameters of the system are an additional tool for analysis of vibrational spectra and looking for relations between shifts and chemical environment of molecules. It is confirmed by studying average FTs: for them, the behaviour of maximas positions is analogous to this observed in the IR spectrum.

4.2 Magnesium chloride solutions in DME

In this section, spectral data obtained from AIMD simulations for systems marked as III and IIIa-c in section 3.3 are described. It was published in the article [III].

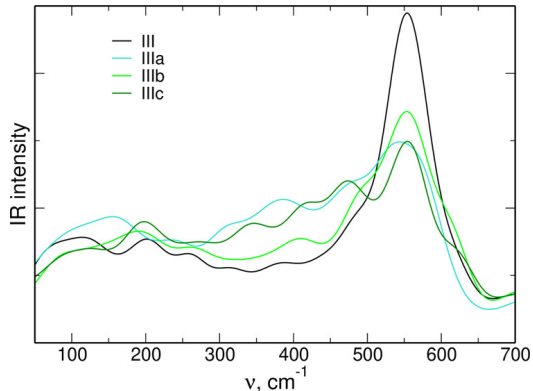


Figure 4.6: IR spectra obtained from AIMD trajectories for systems III and IIIa-c

Figure 4.6 shows IR spectra obtained from AIMD trajectories. For systems with initially aggregated ions (IIIa-c) there is an increase in intensity in the range $300\text{-}450\text{ cm}^{-1}$ with respect to system III. Based on the results of vibrational analysis from QC calculations [III] (not described here), it can be attributed to $\text{Mg}_2\text{Cl}_2^{2+}$ and $\text{Mg}_3\text{Cl}_4^{2+}$ aggregates. Additionally, the band at about 550 cm^{-1} may be assigned to TFSI^- anions.

As for the NaFSI/EMIM-FSI systems, FTs of individual structural parameters were calculated. Selected results are presented in Figure 4.7. For Mg-Mg distances observed modes have frequencies below 100 cm^{-1} but for IIIa and IIIc there are also contributions at about 350 cm^{-1} . Therefore, the observed increase in intensity in IR spectrum may be related to these displacements. For all systems containing aggregated ions in the initial structures (IIIa, IIIb and IIIc), the vibrations of Mg-Cl distances appear between 150 and 250 cm^{-1} . Comparison of these plots shows the difference between frequencies of Mg-Cl vibrations in different environments: the frequencies for MgCl_2 in IIIa are higher than for $\text{Mg}_2\text{Cl}_2^{2+}$. Similarly in IIIb system, for the linear complex $\text{Mg}_3\text{Cl}_4^{2+}$, frequencies of Mg-Cl stretching vibrations are different for inner and outer Mg^{2+} ions.

To prove the assignment of the 550 cm^{-1} band to TFSI^- anion, FTs of S-O and S-N distances and the S-N-S angles were calculated and are shown in Figure 4.8. From plots for S-N bonds and S-N-S angles it is clear that the modes at $550\text{-}600\text{ cm}^{-1}$ are related to these vibrations in every system. For the S-O stretching in system IIIb a pattern differing from the other systems is observed in the range $1000\text{-}1200\text{ cm}^{-1}$. In addition, in this case there are large differences between individual bonds within the same system.

In Figure 4.9 plots of FTs for S-O distances are presented. In each of systems IIIa-c, there were 8 S-O bonds in TFSI^- anions. It was observed that for systems IIIa and IIIc FTs of all of them are similar, so only averages over all S-O bonds for these systems are presented. It is no longer the case for IIIb system in which from eight S-O bonds, FTs for four of them are similar to those for systems IIIa and IIIc, whereas two S-O pairs are different. This effect is related

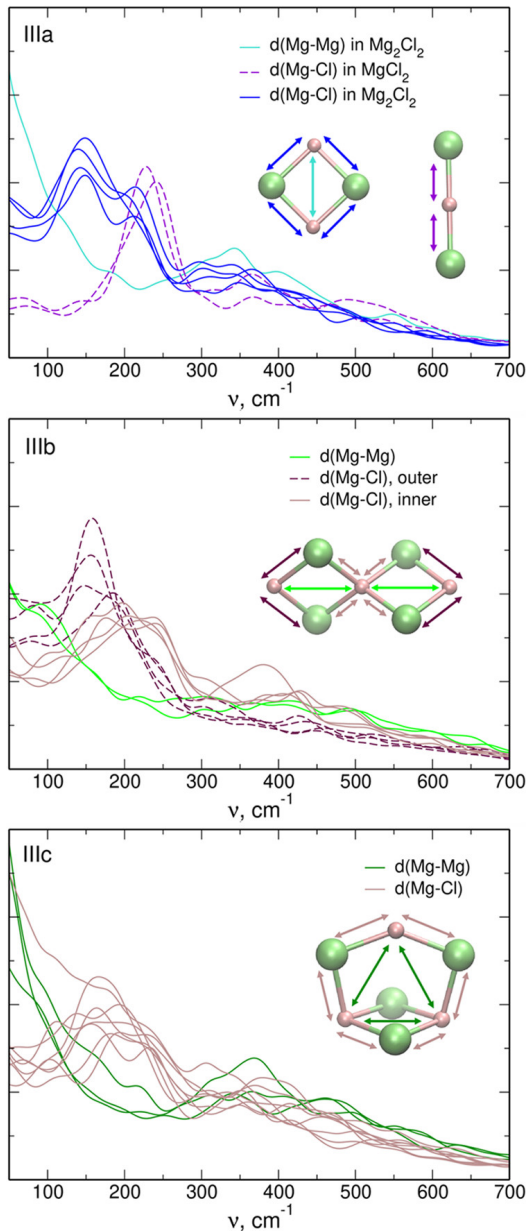


Figure 4.7: Fourier transforms of Mg-Mg and Mg-Cl distances obtained from AIMD simulations for systems IIIa-IIIc

to the fact, that IIIb system is the only one containing one TFSI^- anion coordinated to Mg^{2+} cation. Two different pairs of S-O bonds are the bonds either coordinated to Mg^{2+} cation or pointing in the opposite direction. For these bonds, positions of maxima of FT differ from those observed for "free" S-O bonds (in IIIa and IIIc systems and for four other S-O bonds in system IIIb). So, in this way it is possible to discern vibrational frequencies of "free" bonds and bonds involved in coordination during analysis of vibrational spectra of the system.

As it has been seen in Figure 4.7 and also from QC data in [III], different $\text{Mg}_x\text{Cl}_y^{(2x-y)}$ aggregates are involved in vibrations with similar frequencies, thus to differentiate them, study of changes appearing in the IR spectrum with changing composition of electrolyte (solvent, concentrations, Mg:Cl ratio) is needed.

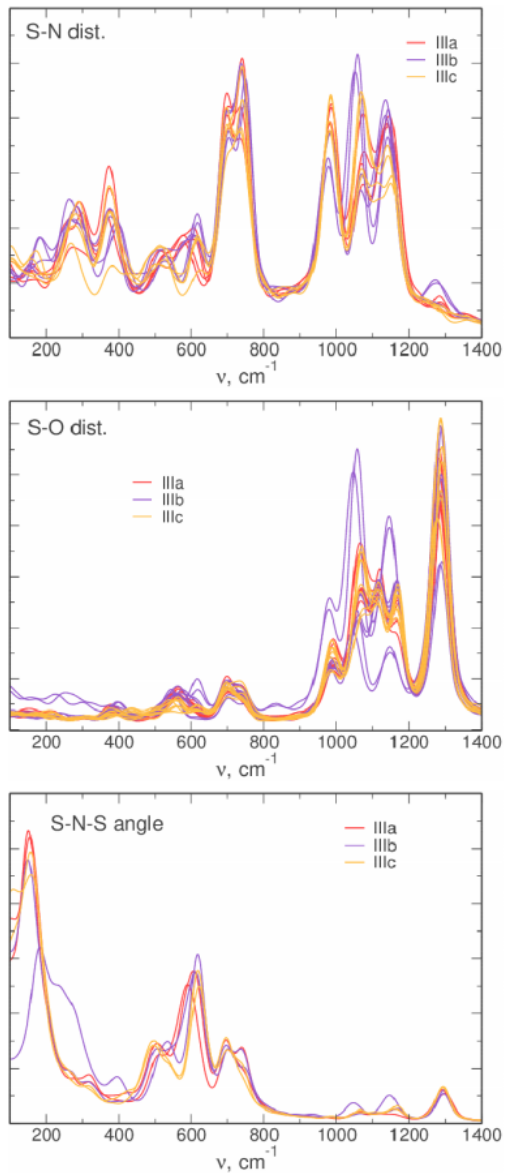


Figure 4.8: Fourier transforms of geometric parameters of TFSI^- anions from the AIMD simulations

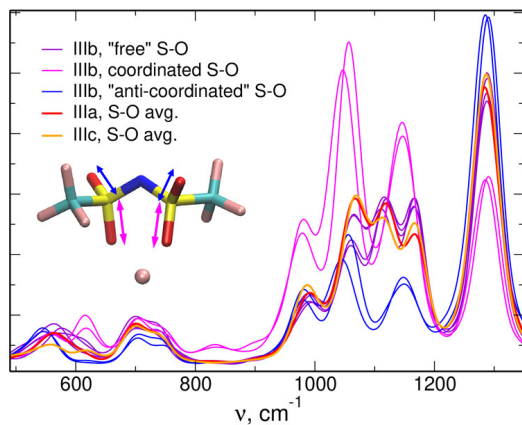


Figure 4.9: Fourier transforms of S-O bond lengths in TFSI^- anions, for systems IIIa and IIIc the averages over all bonds are presented while for system IIIb FTs for individual bonds are shown

4.3 Ethylene carbonate with Na/Li TFSI salt

In this section spectra obtained from AIMD simulations for systems based on EC and its fluorinated derivatives, structural properties of which were described in section 3.4, are presented. These results were published in the article [IV].

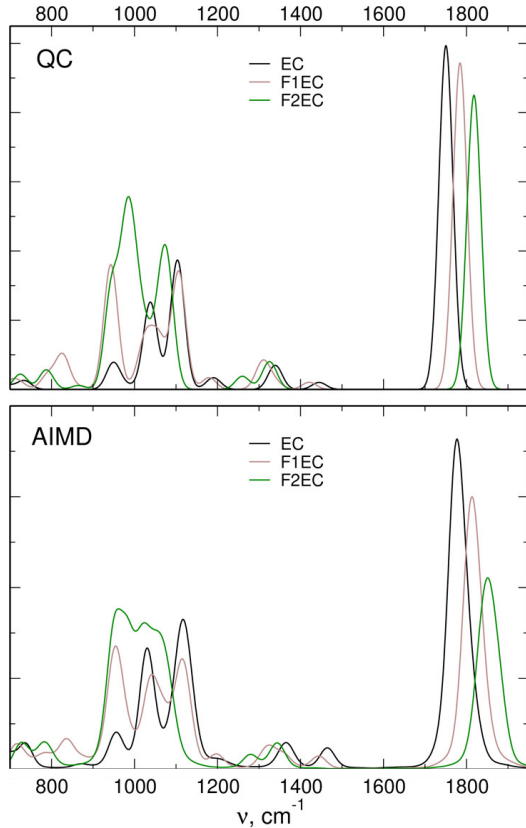


Figure 4.10: Infrared spectra for neat carbonates obtained from QC calculations or from AIMD simulations

Figure 4.10 presents IR spectra obtained for neat solvents from AIMD simulations, QC results are shown for comparison. For both cases, growing fluorination of the EC leads to increase of the C=O stretching frequency. In QC it changes from 1750 cm^{-1} for EC and 1784 cm^{-1} for F1EC to 1818 cm^{-1} for F2EC. In AIMD results higher frequency values were observed: 1777 cm^{-1} for EC, 1813 cm^{-1} for F1EC and 1851 cm^{-1} for F2EC. Despite the different positions of bands in spectra obtained in QC and AIMD, differences between carbonates with a different number of fluorine atoms are similar in both approaches.

Next, Figure 4.11 shows the spectra for electrolytes, with data for neat solvents shown for comparison. In solutions of MeTFSI salts a new peak develops near the C=O band at lower frequencies. The biggest shift of this peak is observed for the case of LiTFSI in F1EC (33 cm^{-1}), for LiTFSI in EC it is smaller (25 cm^{-1}) and the smallest effect is for NaTFSI in EC (16 cm^{-1}) but still remarkable. QC calculations identified the vibration ar 850 cm^{-1} as ring breathing mode in solvent molecule. It has very low intensity, but for lithium electrolytes a small shift towards higher frequencies could be observed, the most visible it is for LiTFSI in F1EC, the maximum is blueshifted by 17 cm^{-1} in comparison with neat F1EC. Another band identified by QC calculations is C-C stretching at about 950 cm^{-1} . For electrolytes with EC as the solvent,

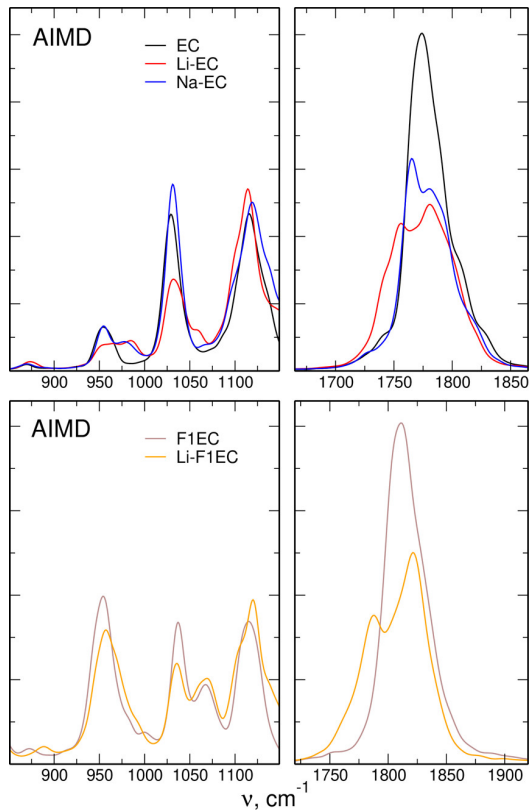


Figure 4.11: Infrared spectra of solvents and electrolyte solutions

this peak becomes broader with its barycenter shifted towards higher energies with respect to neat EC. Its intensity is bigger in the F1EC spectrum and in the LiTFSI in F1EC electrolyte a blue shift by 3 cm^{-1} is observed.

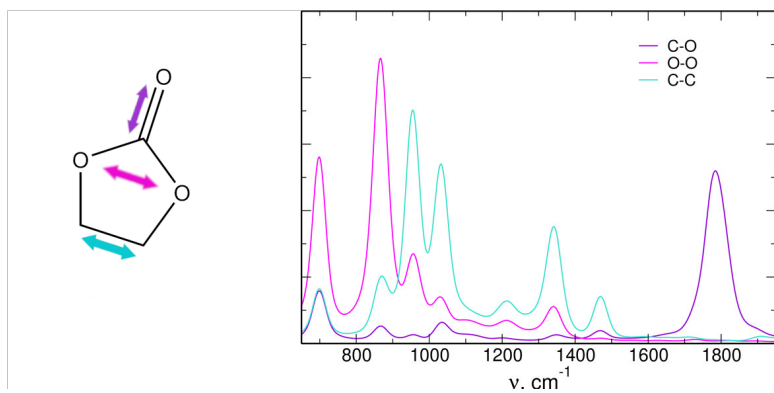


Figure 4.12: Power spectrum obtained from Fourier transforms of interatomic distances for EC (right), used atoms/bonds for calculation of these transforms (left), colors correspond to these in Fourier transforms

Appearance of new bands or shifts of existing bands in the IR spectra are attributed to interactions between carbonate molecules and Me^+ cations which affect vibrational frequencies of solvent molecules in the solvation shell of the cation. In Figure 4.12 FTs of interatomic distances averaged over all molecules for EC are presented. It is clear from this picture that $\text{C}=\text{O}$ oscillations have frequency close to 1800 cm^{-1} , $\text{O}-\text{O}$ oscillations corresponding to ring breathing

mode appear at 850 cm^{-1} and C-C bond stretch at about 950 cm^{-1} and above 1000 cm^{-1} , as expected on the basis of the QC calculations.

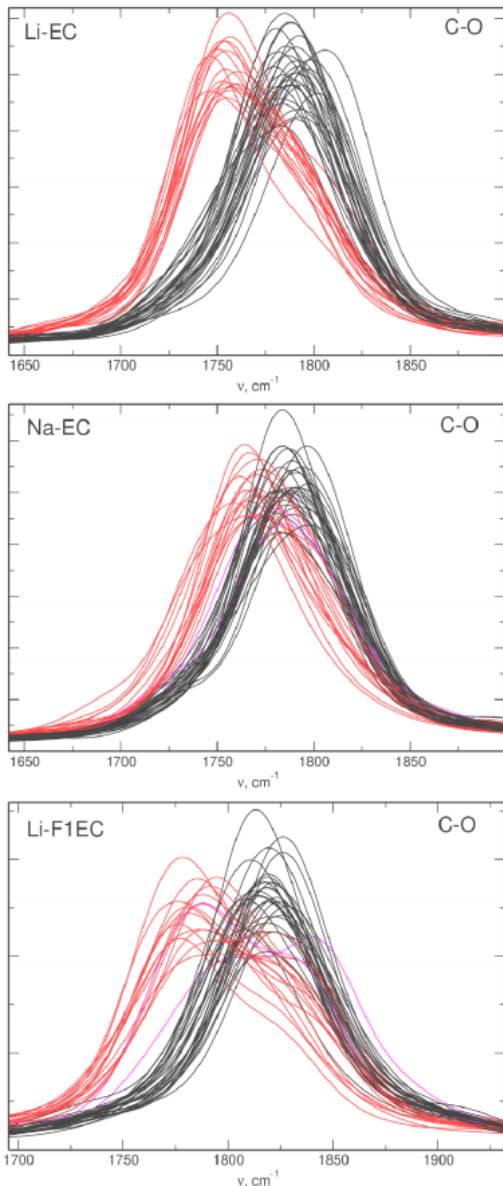


Figure 4.13: Fourier transforms of C=O bond lengths of solvent molecules. Free solvent molecules are black, molecules interacting with metal cations are red, and in magenta molecules interacting with the metal only during a part of MD trajectory are marked

As for previously described systems, FTs of geometrical parameters for individual solvent molecules were calculated. Example results for all of C=O bonds are shown in Figure 4.13. "Free" and bonded solvent molecules are distinguished with colors: black is used for "free" and red is used for bonded molecules. The difference between these two groups is clear: all bonded carbonates have maxima of FTs at higher frequencies than molecules interacting with cations. These separation of peaks could be related to appearance of the new band redshifted with respect to the original stretching C=O in the IR spectrum. Similarly as observed in Figure 4.11, the largest shifts are observed for LiTFSI in F1EC, while the smallest for NaTFSI in EC. There were also carbonate molecules, which interacted with Me^+ only within a part of the MD trajectory

and they are marked in magenta. For them shifts are also observed, but are smaller than for molecules forming complexes for the whole time of simulation.

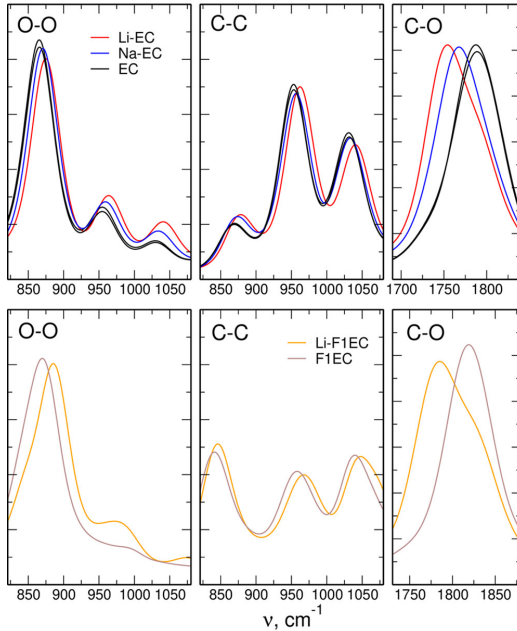


Figure 4.14: Averaged Fourier transforms of interatomic distances

Averaged FTs for geometrical parameters divided into bonded and free solvent molecules are plotted in Figure 4.14. The observed shifts are comparable with those observed in IR spectra, here for C=O in EC there are shifts by 35 cm^{-1} for lithium electrolyte (compared to 25 cm^{-1} in IR spectrum) and 21 cm^{-1} for sodium electrolyte (compared to 16 cm^{-1} in IR spectrum), respectively. For LiTFSI obtained shift equals 33 cm^{-1} (with 33 cm^{-1} observed in the IR spectrum).

These FTs help to trace changes of local oscillations, but it is important to note that the shape of the IR spectrum depends on how these local modes couple to the global modes of the whole system and whether they change the dipole moment of the whole system. If they do not have an influence on the dipole moment, they do not carry the IR intensity, thus this analysis serves as a tool to monitor the differences in the environment of different molecules, but is not able to directly reproduce the vibrational spectrum.

Table 4.1: Observed shifts of chosen bands in IR spectra compared to experimental values, references are given for each value

Electrolyte	Vibration	AIMD shift [cm^{-1}]	Experimental shift [cm^{-1}]
Li-F1EC	C=O	-33	-30 [85]
Li-EC	C=O	-25	-30 [85], -36 [204]
Na-EC	C=O	-16	-20 [204]
Li-F1EC	breathing ring mode	+17	+17 [112]

Observed shifts of the C=O band cannot be directly compared with experimental values, because this vibration in EC was not studied in the experimental work [85], but data for other

similar carbonate solvents are available and could be compared to results presented here. Shifts of the C=O band in 1 M LiTFSI solutions in diethyl carbonate and ethyl(fluoroethyl)carbonate are about 30 cm^{-1} [85]. Another work studied spectra of electrolytes based on ethyl methyl carbonate, for NaTFSI solution observed C=O shift was equal 20 cm^{-1} and for LiTFSI solution 36 cm^{-1} . In Raman spectrum for LiTFSI in F1EC, for the ring breathing mode a blue shift of 17 cm^{-1} was observed [112]. Mentioned shifts are presented with experimental values in Table 4.1. Thus, shifts observed for acyclic carbonates (as well as for ring breathing mode in cyclic carbonates) stay in an agreement of data obtained from AIMD and also the smaller size of the effect for sodium cation agrees with the size of experimentally observed changes.

4.4 EMIM-TFSI with water

This section describes infrared spectra obtained from AIMD simulations for EMIM-TFSI IL mixtures with water. Structural properties, including statistics of hydrogen bonds (HBs) are described in section 3.6. Presented results were a part of the article [VI].

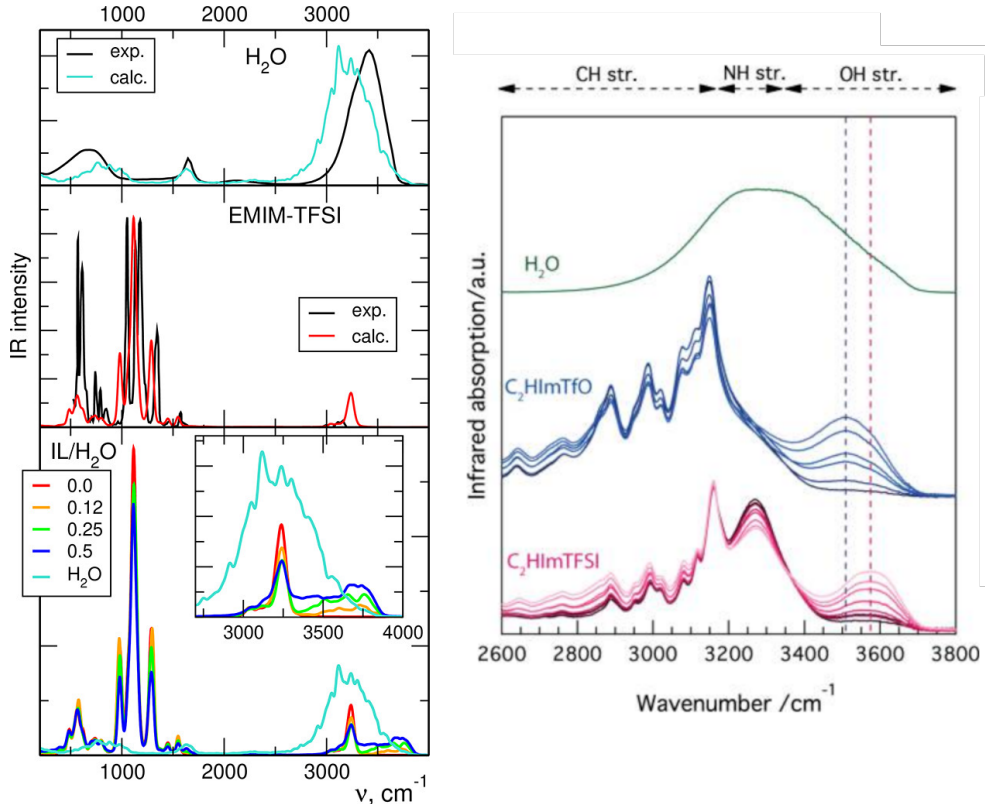


Figure 4.15: IR spectra calculated from AIMD trajectories for neat liquids and IL/water mixtures with increasing mole fraction of water, experimental spectra are from [354] for water and from [355] for IL (left); experimental spectra for H_2O and IL/ H_2O mixtures (right) [356], for EMIM-TFSI changes are shown in the bottom

IR spectra are presented as averages over all replicas in Figure 4.15. For comparison experimental spectra of water [354], EMIM-TFSI [355] and IL/ H_2O mixtures [356] are shown.

There are some differences between calculated and experimental spectra of neat liquids. While computed frequencies of the H-O-H bending mode in water at 1600 cm^{-1} agree with measured data, the O-H stretching band above 3000 cm^{-1} is shifted by $200\text{-}250 \text{ cm}^{-1}$ to lower energies with respect to the experiment. For EMIM-TFSI, the shape of the spectrum is predicted correctly, but the part below 1500 cm^{-1} is shifted to lower frequencies by about 60 cm^{-1} , the intensity of the band at 980 cm^{-1} is too low and C-H stretching bands are shifted to higher energies. However, these results are similar to benchmarking tests of applying different functionals to liquid methanol [357], so the differences with respect to measured spectra are considered as acceptable.

For mixtures, with growing amount of water the intensities of IL-related bands decrease due to decreasing concentration of ions in the solution. More significant changes are observed above 3000 cm^{-1} . At first, a small increase of intensity below C-H band at 3240 cm^{-1} is

observed. It may be attributed to shifts of the C-H vibrations in EMIM^+ cations which are in an environment different than in the neat IL. The IR intensity between 3300 and 3800 cm^{-1} increases with appearance of a new maximum at about 3700 - 3750 cm^{-1} . This could be related to O-H vibrations in H_2O molecules. The new maximum is located above the main maximum observed for neat water, so the water molecules are apparently in different environment than in a bulk water with smaller degree of water-water hydrogen bonding (what is confirmed by the analysis of structural data in section 3.6). Calculated changes agree with changes observed experimentally for $\text{EMIM-TFSI}/\text{H}_2\text{O}$ [356] (right panel of Figure 4.15) and $\text{EMIM-BF}_4/\text{H}_2\text{O}$ [358] mixtures.

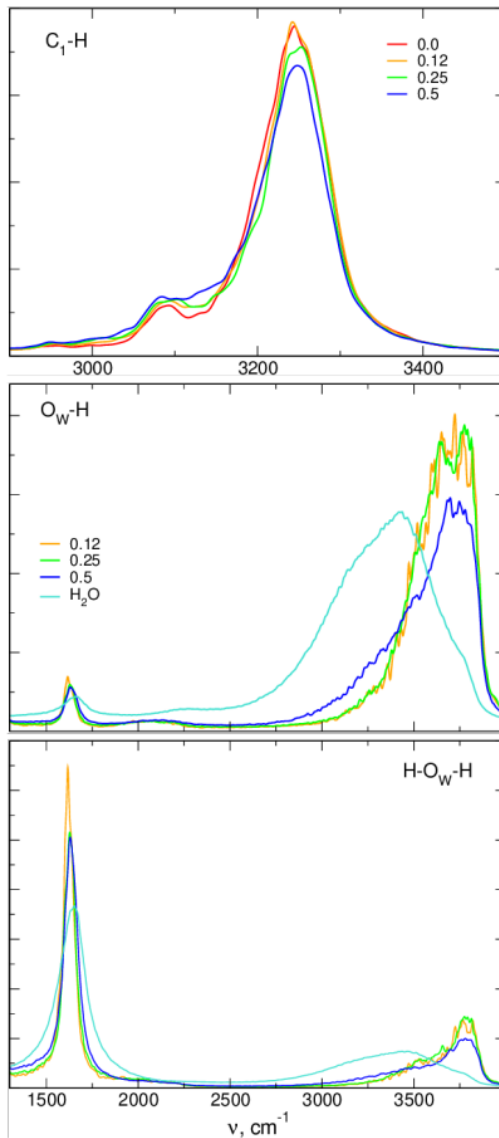


Figure 4.16: Fourier transforms of $\text{C}_1\text{-H}$, $\text{O}_w\text{-H}$ bond lengths and $\text{H-O}_w\text{-H}$ angles averaged over all ions/molecules in IL/water mixtures

As for previously described systems, Fourier transforms of selected geometrical parameters of the system were calculated to get a deeper insight into interactions. Figure 4.16 shows FTs of $\text{C}_1\text{-H}$, $\text{O}_w\text{-H}$ bond lengths and $\text{H-O}_w\text{-H}$ angles averaged over all molecules/ions (labels of atoms are the same as in Figure 3.38). Similar changes to those obtained for IR spectra in mentioned

above ranges can be observed.

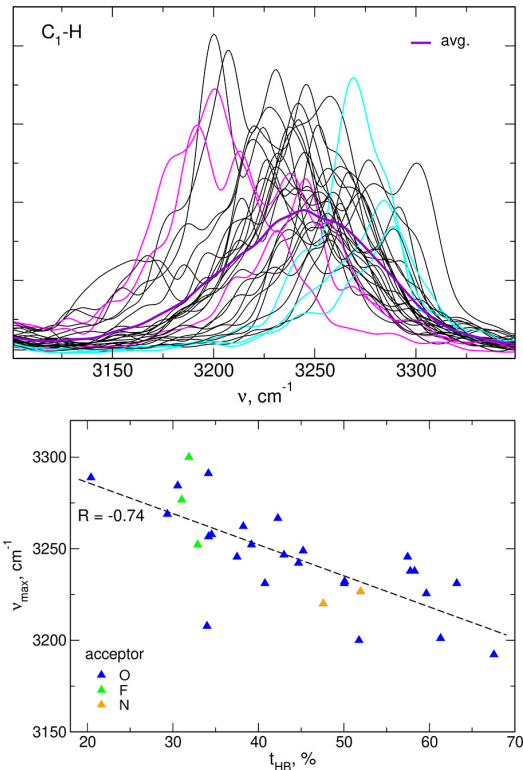


Figure 4.17: Fourier transforms of C₁-H bond lengths in neat EMIM-TFSI (top), positions of maxima in FTs of bond lengths vs the time of HB formation (bottom)

In Figure 4.17 individual Fourier transforms for all C₁-H bond lengths in neat EMIM-TFSI are presented. Positions of maxima vary in an interval of about 200 cm⁻¹ with an average at 3250 cm⁻¹ (purple line). Three EMIM⁺ ions which spent most time forming HB from C₁-H group to TFSI⁻ are shown in magenta and three ions with the shortest time of such HB formation are marked in cyan. It can be seen that, frequencies of C-H vibrations involved in HB formation are shifted below the average frequency while frequencies of "free" C-H bonds (with small times of HB formation) are shifted to higher values than average. It should be noted here, that these differences are the result of different chemical environment of particular molecules during the limited simulation time and for a sufficiently long trajectory, all of them would be on average in the same environment and differences between FTs would be small.

The bottom panel of Figure 4.17 shows the plot of position of a maximum of C₁-H FT vs average time spent on formation of HB. These two parameters are correlated, the longer is the time of HB existence the lower is the frequency of the C₁-H stretch. Majority of acceptors here are oxygen atoms, the size of the system did not allow to make a reasonable analysis for different acceptors (O, F or N). However, the plot suggests that changes for donors making HBs with fluorine acceptors are smaller than the others.

Similar analysis for systems containing water is presented in Figure 4.18. In all three systems, the observed correlation is similar to this in neat IL: HB formation decreases the frequency of a C₁-H vibration. There is no clear correlation with the type of acceptor (TFSI⁻ or water), perhaps with the exception of the system with $x = 0.5$ where the most red-shifted vibrations

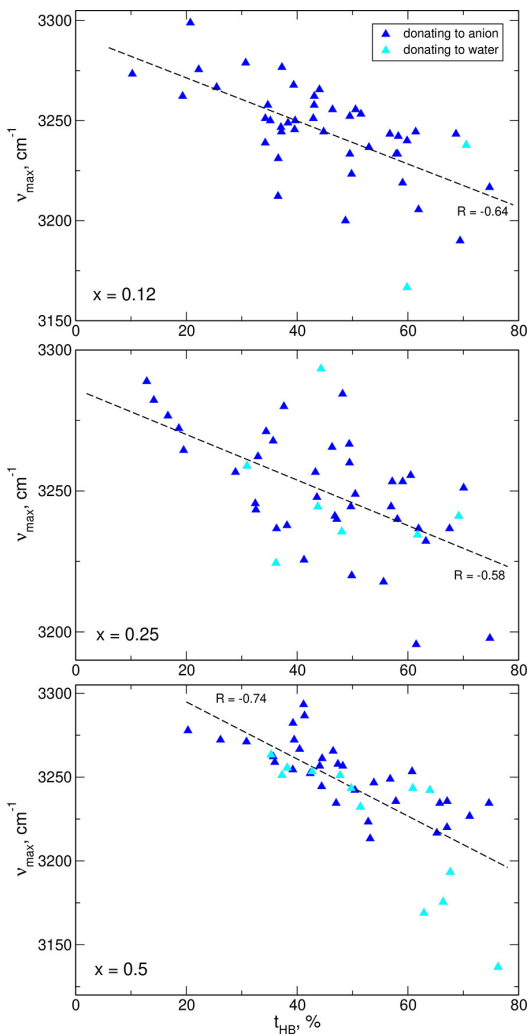


Figure 4.18: Positions of the maxima in FTs of C₁-H bond lengths vs the time of HB formation for IL/water mixtures

engage water molecules. However, again the sizes of the systems in AIMD were too small to collect more detailed data and split it by the type of the acceptor.

Results from Figures 4.17 and 4.18 confirm predictions about origins of changes observed in IR spectra. An increase of intensity observed below 3250 cm⁻¹ in water-containing samples is related to changes in HB formation of H atoms from imidazolium ring of EMIM⁺ cations. It is confirmed by statistics of increased probability of HB formation by imidazolium hydrogens with increasing water fraction (Figure 3.43).

From experimental measurements of Raman spectra for water it is known that "free" (not being a donor of a HB) O-H bonds appear at the highest frequencies (about 3600 cm⁻¹). Frequencies of O-H vibrations in water molecules involved in HBs decrease in order DDA, DA, DDAA and DAA, depending on the HB configuration of a given molecule. Here, D and A denote that the H₂O molecule serves as a donor and acceptor of a HB, respectively. For example, DDA configuration means that the molecule is an acceptor of one hydrogen atom from another molecule and simultaneously donates both hydrogen atoms to two other molecules. From deconvolution of Raman spectrum it was shown that the frequency of the DDAA configuration ("tetrahedral") is equal about 3200 cm⁻¹ and the other main contribution originates from DA

configuration (about 3400 cm^{-1}) [359].

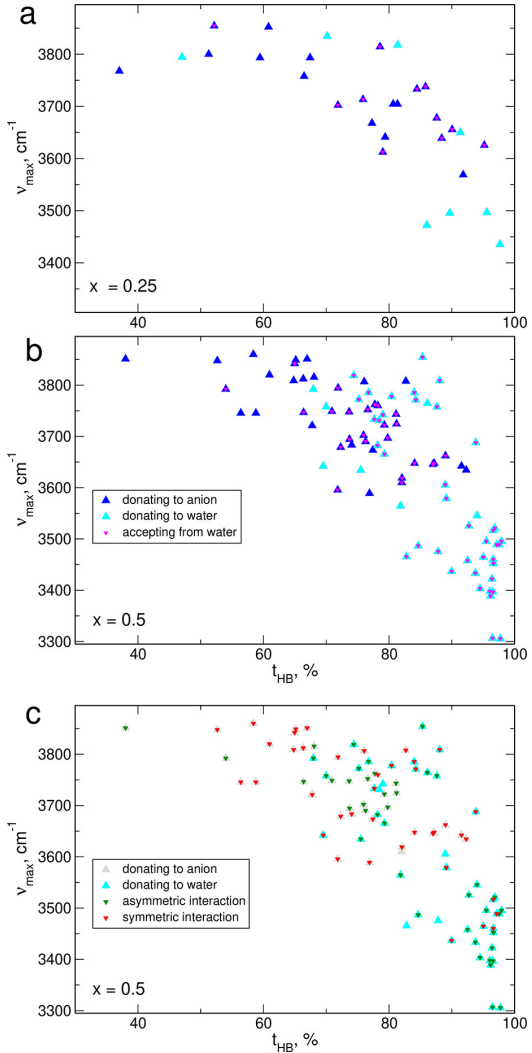


Figure 4.19: Positions of the maxima in FTs of O-H bond lengths vs the time of HB formation for IL/water mixtures with $x = 0.25$ (a), $x = 0.5$ (b) and with alternative labeling of data for $x = 0.5$ (c)

Figure 4.19a,b shows the dependence of O-H stretching frequency vs percentage of the time of HB formation for two systems with the highest water concentration. In general, the biggest the time of HB formation, the biggest red shift of related O-H stretching frequency is observed. It could be also noted, that the configuration of HBs for a given molecule is also essential, donation of H atom to TFSI^- anion results in smaller red-shifts than the donation to water molecule, and the effect is even bigger when the H_2O molecule is also an acceptor of HB from another H_2O molecule. Thus, the lowest frequencies are observed for molecules with configurations which are the most close to those in bulk water - for H_2O molecules which are simultaneously H-acceptors and H-donors from/to other water molecules. However, in studied systems the number of such water molecules is limited. Some water molecules are involved only as H-donors to TFSI^- anions, for them the O-H frequency is usually between 3850 and 3700 cm^{-1} . It is lowered to 3800 - 3600 cm^{-1} when the water molecule donating to TFSI^- anion becomes also an HB acceptor from another H_2O molecule. For molecules, which are not an acceptor of HB from water but are donors of HB to another water molecule, the frequency is in the range 3800 - 3500 cm^{-1} . All

mentioned frequencies are higher than these for bulk water, what is a result of the fact that in studied systems water molecules were in environment modified by the presence of the IL. Therefore, as it was seen in Figure 4.15, a new band with a frequency above the O-H frequency for bulk water appears (at about 3700-3750 cm⁻¹).

Figure 4.19c shows an alternative labeling for data from the system with $x = 0.5$ in agreement with symmetry of the environment of two O-H bonds in the water molecule defined in [358]. Here, there is also a color-coding of the distinction between symmetric hydrogen bonding (both O-H groups form HBs to the same type of acceptor for a similar time) and asymmetric hydrogen bonding (the acceptors for two O-H bonds are different or there is a substantial time difference of formation of HB for these bonds). According to [358], frequencies of O-H stretch depend on this symmetry as follows: $\nu_{ab} < \nu_s < \nu_{af}$ where ν_s is the frequency in symmetric environment and ν_{ab} and ν_{af} are frequencies of either "bound" or "free" O-H groups in asymmetric configuration. Therefore, the lowest frequencies are computed for O-H bonds donating to water in an asymmetric environment. It could be expected that the highest frequencies would be observed for O-H groups interacting asymmetrically with anion for short time. In studied $x = 0.5$ system only one such O-H vibration is visible, but still its frequency is among the highest calculated. So, the general trend from [358] is present in the shown data, however to be able to perform a more detailed analysis one should perform longer simulations for larger systems to obtain better statistics.

4.5 LiTFSI in water

In search for new electrolytes, superconcentrated solutions of salts in water, called "water-in-salt" electrolytes, have recently attracted significant attention [360–365]. An example of such a system are LiTFSI solutions in water, in which concentrations up to 21m can be achieved. Measured IR spectra show clear dependence on salt content [366].

In this section results for systems consisting of LiTFSI in water in different concentration are presented. As this is the subject of a recent study, at the moment of writing this thesis they are not published in any journal yet.

Table 4.2: Compositions of LiTFSI/H₂O systems

system	LiTFSI	H ₂ O
1m	4	222
5m	15	167
10m	22	122
20m	30	83

Four systems with different concentration of lithium salt were studied by AIMD: 1m, 5m, 10m and 20m. Their compositions are listed in Table 4.2. For every system two independent simulations with different initial structures were performed and for each of them 40 ps of trajectory was collected, and the last 30 ps was used for analysis. Time step of 1.0 fs was used.

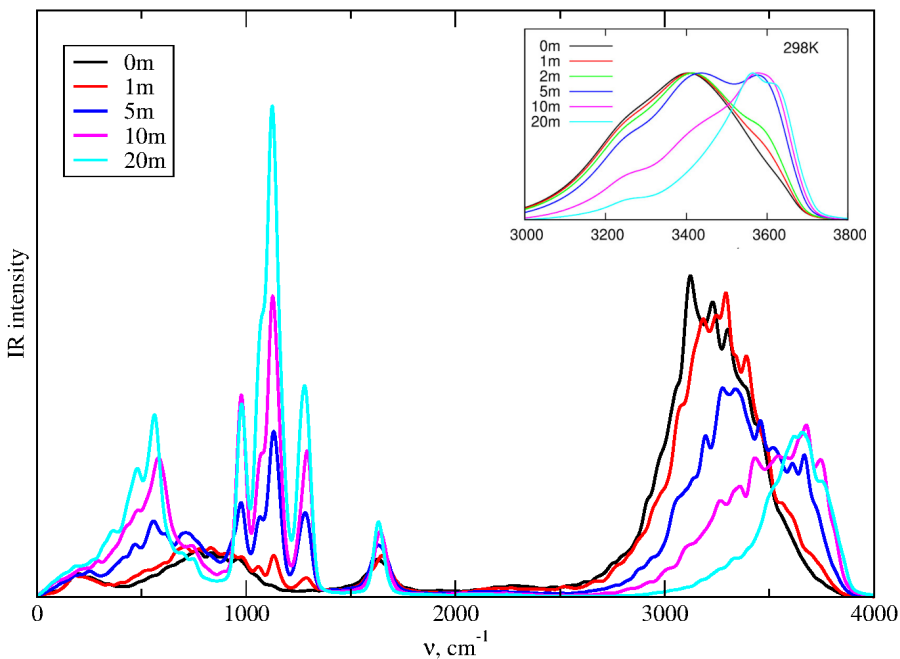


Figure 4.20: Infrared spectra obtained from AIMD for LiTFSI in H₂O systems, inset contains experimental spectra in the range of O-H vibrations from [366]

Figure 4.20 presents IR spectra averaged over replicas for each studied system. Below 2000 cm⁻¹ for every system there is a visible band at about 1650 cm⁻¹ which was present at neat water spectrum presented in Figure 4.15. Bands below this frequency have growing

intensity with growing concentration of lithium salt, for the most diluted system they are quite indistinct. Their shape is similar as for the previous system and they could be related to vibrations in TFSI⁻ anion, the growing intensity is the effect of increase of salt concentration in the system.

Above 3000 cm⁻¹ the position of the band, which may be related to O-H vibration in water molecule, is systematically shifted to higher frequencies with growing concentration of the salt, with the maximum moving from about 3150 cm⁻¹ to about 3650 cm⁻¹. It is similar to the effect observed for EMIM-TFSI with water mixtures and may be attributed to changing environment of hydrogen bonds. For the most diluted system, the most of HBs are formed between water molecules, due to low amount of salt, thus the maximum of the O-H band is the lowest among considered systems. With increasing salt amount, the water-water HBs are gradually replaced with water-TFSI⁻ HBs what changes the frequency to higher values. The observed tendency stands in an agreement with experimental results, however the maximum of the peak for bulk water and diluted solutions in AIMD spectra are shifted towards lower frequencies. For further research it is planned to analyse the local environment of water molecules in these systems, in particular to calculate average number of water-water and water-TFSI⁻ hydrogen bonds and to correlate it to the frequency of O-H vibrations.

Chapter 5

Alternatives to AIMD

In this chapter, results of calculations performed with methods computationally less expensive than AIMD are presented. They include Density Functional based Tight-Binding (DFTB) and Machine Learning (ML).

5.1 DFTB

In this section results obtained by DFTB for ethylene carbonate (EC) with NaTFSI or LiTFSI salts are presented as well as for mixtures of EMIM-TFSI ionic liquid (IL) with different amounts of water. Two approaches are shown - the standard based on Slater-Koster parameters and extended Tight Binding (xTB) GFN2 variant proposed by Grimme et. al. [299]. For both of them, all simulations were performed in NVT ensemble with temperature $T = 298$ K.

5.1.1 Ethylene carbonate with Na/Li TFSI salt

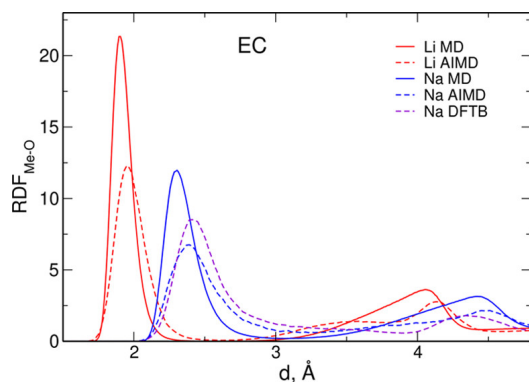


Figure 5.1: Radial distribution functions for Me-O pairs for electrolytes based on EC obtained from classical MD, AIMD and DFTB MD simulations

Results shown in this section were obtained to have comparison with AIMD results described in sections 3.4 and 4.3. Simulations were performed with the use of the DFTB+ v. 18.2 software [289] with the 3ob-3-1 parameter set [290–293]. This set does not contain parameters for lithium, so only neat solvents and NaTFSI solution in EC were studied. The compositions of

all systems were the same as for AIMD. These data were published in the article [IV]. In addition, systems studied by AIMD were simulated in DFTB+ v. 22.2 package in the xTB-GFN2 approach where it was possible to also include systems with lithium salt.

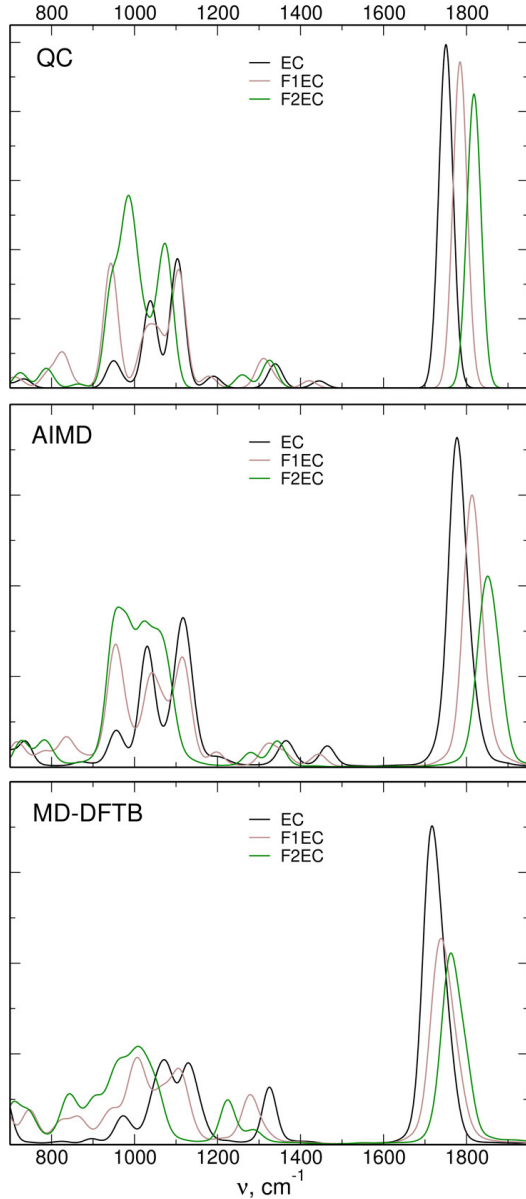


Figure 5.2: Infrared spectra of neat solvents obtained from QC calculations or from AIMD and DFTB MD simulations

Figure 5.1 presents RDFs for Me-O pairs obtained from different MD approaches. For Na-EC systems, the maximum in AIMD is located at higher distance than for classical MD (what was described previously). In DFTB it is shifted to distances longer than in AIMD (2.38 Å vs 2.40 Å) and the maximum is broader. Therefore it is expected that the interactions between sodium cation and EC are weaker in DFTB simulations than those in AIMD.

Figure 5.2 presents IR spectra for neat solvents obtained from different approaches. For DFTB, as in AIMD or QC calculations, fluorination of the solvent shifts the C=O stretching band towards higher energies, from 1717 cm⁻¹ to 1739 and 1763 cm⁻¹. However, observed frequencies are lower than in AIMD and also differences between solvents are smaller. General

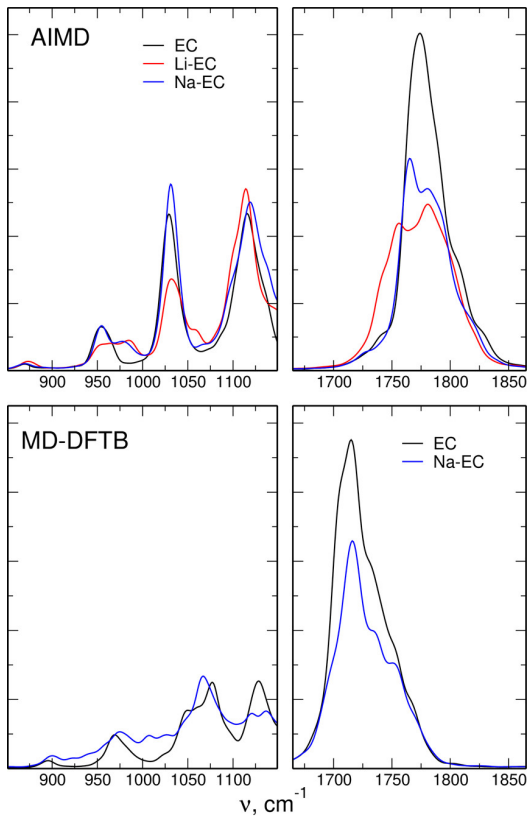


Figure 5.3: Infrared spectra of solvents and electrolyte solutions obtained from AIMD and DFTB MD simulations

features between 800 and 1200 cm^{-1} in AIMD and DFTB are similar, there are some differences in the intensity pattern.

IR spectra for electrolyte solutions are presented in Figure 5.3. The main difference which could be observed is that, in opposition to AIMD, the position of C=O band between neat solvent and the electrolyte remains unaffected. However, small blue shifts of bands between 850-950 cm^{-1} are observed as for the NaTFSI in EC in AIMD.

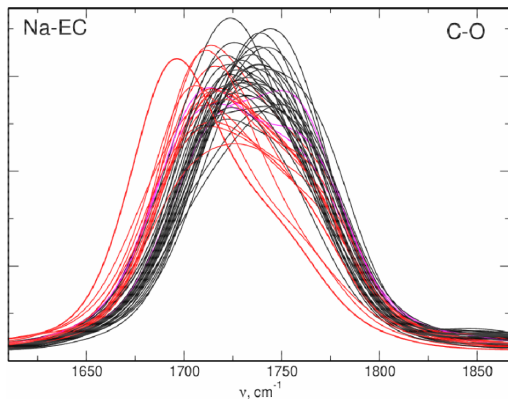


Figure 5.4: Fourier transforms of C-O distances in DFTB MD simulations. Free solvent molecules are marked in black, molecules interacting with Na^+ in red, and in magenta molecules interacting with cations for only a part of the MD trajectory. Thick red line marks the molecule interacting with 2 Na^+ ions

Similarly as in AIMD simulations, FTs of C-O distances for Na-EC system were obtained and are shown in Figure 5.4. Different colors mark free and interacting with cation solvent molecules; additionally few molecules interacting with cation only for a part of the simulation are marked. Again, interaction lowers the position of the maximum of the FT, and the effect is less visible for molecules which do not interact for the whole time of the simulation. In addition, the biggest shift is observed for the sole molecule which was interacting simultaneously with two Na^+ cations. However, differences between maximum positions are smaller than in the AIMD. This results does not agree with the IR spectrum obtained from DFTB simulation, as there the shift of C=O band position was not observed.

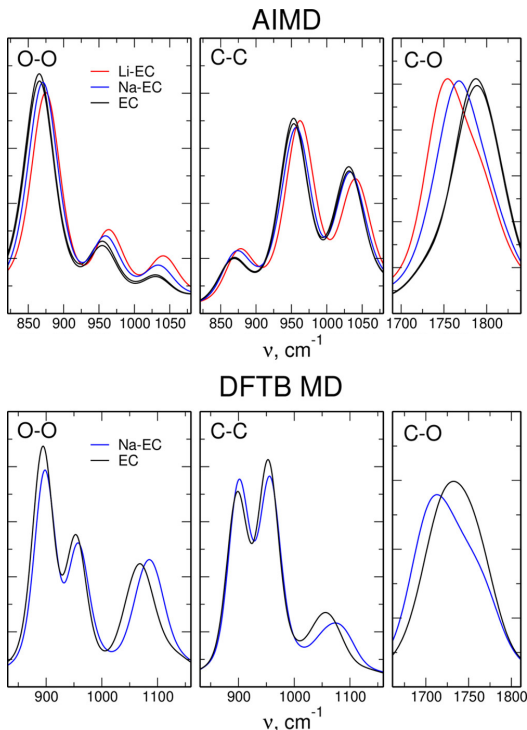


Figure 5.5: Averaged Fourier transforms of interatomic distances in AIMD and DFTB MD

In Figure 5.5 averaged FTs of interatomic distances are presented and compared with AIMD results. Here, in opposition to IR spectrum, the shift of the maximum for C=O bending is visible. It is unclear why such difference is observed. For DFTB simulations for every step of the trajectory, partial charges for each atom in the system are determined. The dipole moments are calculated based on these charges. Probably, used parametrization was not able to produce correct partial charges for sodium cation and the C and O atoms from the C=O group when they are affected by direct interaction. This led to almost unchanged positions of bands in the IR spectrum.

Figure 5.6 presents IR spectra obtained in the GFN2-xTB approach. The effect of solvent- Me^+ interactions is visible for the C=O stretching band. In the spectrum of LiTFSI in EC a shoulder appears on the low energy side of the main band, with the energy 29 cm^{-1} lower than the maximum for neat EC. There is also a small red shift of 3 cm^{-1} in the position of the maximum calculated for NaTFSI/EC electrolyte. The maximum in the LiTFSI solution in F1EC is red-shifted by 23 cm^{-1} with respect to neat F1EC. The shift for NaTFSI electrolyte is

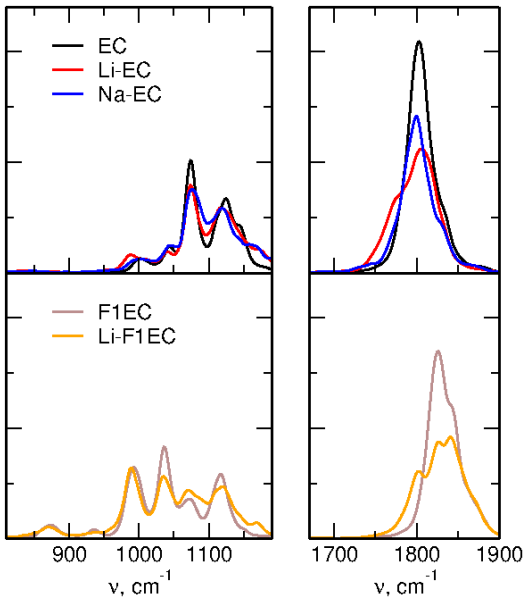


Figure 5.6: Infrared spectra obtained from GFN2-xTB MD simulations

much too small, but for LiTFSI the results are comparable to AIMD results. However, there is no blue-shift observed for the ring breathing mode. Perhaps the analysis of FTs of interatomic distances could reveal some frequency shifts not seen in the IR spectra.

In this case, DFTB simulations took shorter computational time than AIMD, however the results are worse than AIMD results with respect to experimental values. The main disadvantage of DFTB for studied systems is lack of Slater-Koster parameters for lithium and incorrect reproduction of the shift of C=O stretching band in the IR spectrum. It clearly shows the need of more appropriate parametrization, because the 3-ob-3-1 used here was mostly developed for biological systems, not electrolytes. GFN2-xTB approach is free from the limitation related to the parameters for lithium. It resulted in IR spectra more close to those obtained from AIMD than with 3-ob-3-1; the effect of red-shift of C=O band for lithium-based electrolytes was successfully reproduced. However, still results for sodium-based electrolytes are not satisfactory and the shift of the ring-breathing mode is not observed.

5.1.2 EMIM-TFSI with water

In this section results obtained with different DFTB parametrizations as well as with xTB variants: GFN1 and GFN2 are presented. Simulations were performed in DFTB+ v. 22.1 [289]. For simulations of liquid water standard DFTB parametrizations were used: 3-ob-3-1 [290–293], matsci [296], mio [295], ob2 [294] and matsci variants improved to reproduce structural parameters of bulk water, named here as water-matsci and water-matsci-uff [297]. In addition, xTB variants: GFN1 and GFN2 [298, 299] were used for such simulations. Because from parametrizations mentioned, only 3-ob-3-1 covered all elements present in the IL, only this one was used for simulations for neat EMIM-TFSI and $x = 0.5$ system. From xTB variants, GFN2 resulted in more accurate results for bulk water, so this was the only method in this approach used for ILs. The length of the trajectory and other parameters of MD simulations were the same as for the AIMD simulations, the last 30 ps were used for analysis.

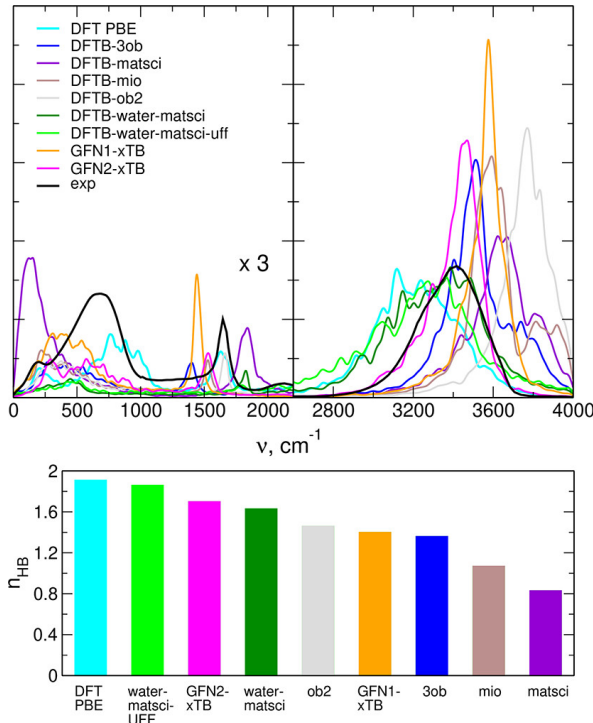


Figure 5.7: Infrared spectra calculated for bulk water in different DFTB parametrizations (top), average number of hydrogen bonds per water molecule (bottom)

Figure 5.7 shows IR spectra of bulk water obtained in different parametrizations. The low-frequency region in every case is poorly reproduced. In the O-H region the best performing were water-matsci and water-matsci-uff parametrizations, specially designed for water. Next to these two were general parameter sets: GFN2, 3ob and GFN1. In the bottom part of Figure 5.7 average numbers of HBs per water molecule are shown. The best in reproducing O-H region are the sets which predict the number of HBs close to the DFT data. However, there is no direct relation between average number of HBs to the quality of the spectrum, because 3ob which performs better than GFN1 and ob2 in reproduction of the spectrum, is worse at HBs number prediction.

A possible explanation of these differences come from SDFs presented in Figure 5.8. 3ob

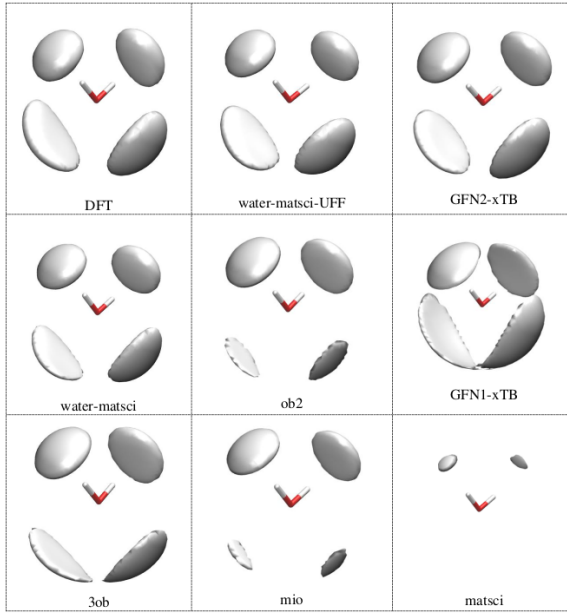


Figure 5.8: Spatial distribution functions of oxygen atoms around water molecules in bulk water obtained in DFTB simulations. Surfaces of particle density 100 atoms/nm³ are shown

parametrization gives result closer to the tetrahedral structure of water than GFN1 and ob2. To summarize this part, the best performance was obtained for parameters developed specially for description of water: water-matSci and water-matSci-uff. From general parametrizations, GFN2 was well performing.

Spectra for IL and IL mixture with water are presented in Figure 5.9. The 3ob parametrization for both cases predicts two main IR bands in the range of 1000-1300 cm⁻¹ instead of three present in DFT results. GFN2 correctly reproduces number of bands, and their frequencies are closer to DFT results. Next, in the region above 3000 cm⁻¹ in neat IL, results are similar and again GFN2 gives frequencies closer to DFT values. Significant differences are observed in the system with $x = 0.5$. In both cases an intense band at 3500 cm⁻¹ appears; in 3ob results there is also an increased IR intensity above 3700 cm⁻¹.

To explain this effect, trends in HB formation were studied. In Figure 5.10 SDFs for ILs simulated in GFN2 are presented. When compared to SDFs for DFT results in Figure 3.42 it is visible that in this case TFSI⁻ and water oxygen atoms are more evenly distributed around EMIM⁺ cations and the probability is concentrated not only close to the H_{Im} hydrogen atoms, but also near methyl groups.

Average numbers of the most abundant types of HBs are plotted in Figure 5.11. In the 3ob results, average numbers of all main types are reduced compared to DFT, so in this method the HB formation ability is smaller. It may explain the maximum at about 3800 cm⁻¹ in the IR spectrum, as this could be related to bigger number of "free" O-H bonds of water molecules in the system, contributing to this part of the spectrum. For GFN2, as it was expected from SDFs, there are more HBs involving methyl group hydrogen atoms. In HBs with water as a donor, the ratio of anion or water acceptors is changed in favor of the anions. Nevertheless, it is not clear why for both DFTB approaches the band at 3500 cm⁻¹ develops.

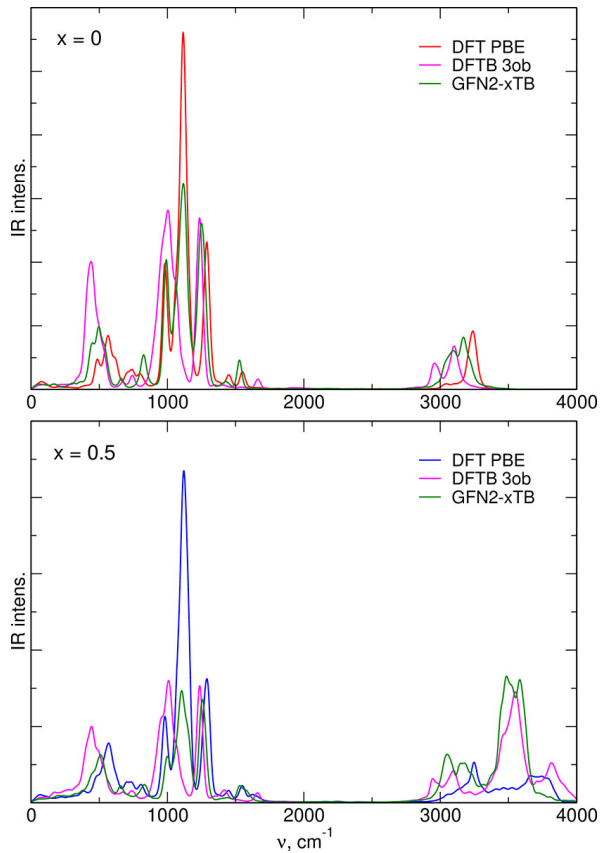


Figure 5.9: Infrared spectra of neat IL and the mixture with water obtained from MD based on PBE DFT or two DFTB parametrizations

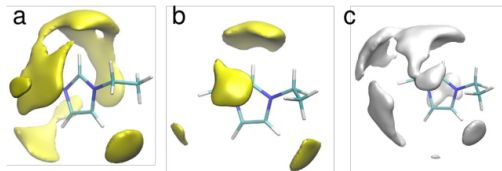


Figure 5.10: Spatial distribution functions of oxygen atoms around EMIM^+ cations in simulations from GFN2-xTB method: (a) TFSI^- anions in the neat IL, (b) TFSI^- anions in the $x = 0.5$ mixture, (c) water molecules in the $x = 0.5$ mixture. Surfaces of particle density 10 atoms/ nm^3 are shown

To summarize, for water in DFTB the specially developed parametrizations water-matsci and water-matsci-uff were the best performing, as well as the general-purpose GFN2 method. However, for IL mixtures with water neither of used parametrizations was able to correctly reproduce changes in IR spectrum caused by presence of water due to their improper description of IL-water hydrogen bonding. Therefore, for this purpose DFTB parametrizations need further corrections.

For described in this section systems, DFTB method was able to reproduce in most cases approximately the positions of bands in IR spectra. However, observed shifts were strongly dependent on the used parametrisation. From the general-purpose methods both for carbonate-based electrolytes as well as for EMIM-TFSI mixtures with water, GFN2-xTB was the best

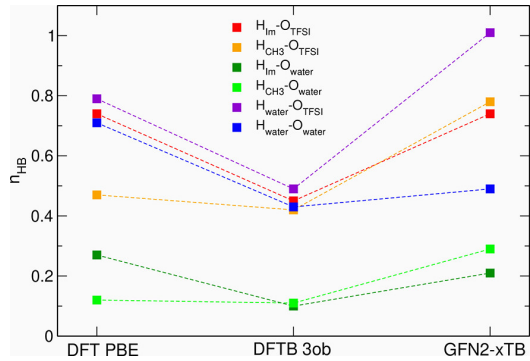


Figure 5.11: Average numbers of the most abundant hydrogen bonds obtained for $x = 0.5$ from MD simulations based on DFT or DFTB. Lines are only to guide the eye

performing. For bulk water, there was a specially developed parametrization for this purpose, and this one resulted in the closest spectrum to this obtained from AIMD. Although, still GFN2-xTB method was not able to correctly reproduce all changes observed in AIMD spectra. Thus, DFTB seems as a promising alternative to AIMD due to its reduced computational cost, however it still needs improved parametrizations to be reasonable for use in analysis of vibrational spectra.

5.2 Machine Learning

This section presents results obtained by application of neural networks (NNs) for performing MD simulations for two systems described in preceding chapters. The study was done by using NN model able to predict potential energy, forces and dipole moment for given geometry. This model was provided by Schnetpack [308]. For both systems considered here, the same parameters were used. The NN consisted of 3 interaction layers with 7.5 Å cosine cutoff with pairwise distances expanded on 20 Gaussians and 128 atomwise features layers with convolution filters. NN was trained for 200 epochs on energies, forces and dipole moments of selected frames from classical/ab initio trajectories. For evaluation of results, mean square error loss function was used with weights for every property: 0.005 for energy, 0.005 for dipole moment and 0.99 for forces. The division of the available dataset was in every case the same: 86% of frames were used as training set, 12% as validation set and 2% were left as testing set. After training, for chosen systems 35 ps of MD simulation with time step of 0.25 fs were obtained.

5.2.1 Ethylene carbonate

For neat ethylene carbonate (EC) classical MD simulations at the temperature of 400 K were performed. From these trajectories 60 000 structures containing 5 or 10 EC molecules were chosen, and for each of them energies, forces and dipole moments were calculated with PBE functional in the 6-31+G* basis set and the Grimme's dispersion correction [175] in Gaussian v09 [309]. They were used for training the NN in Schnetpack. At the end of the training the value of loss function for training set was $7.17 \cdot 10^{-5}$ and for validation set $9.08 \cdot 10^{-5}$.

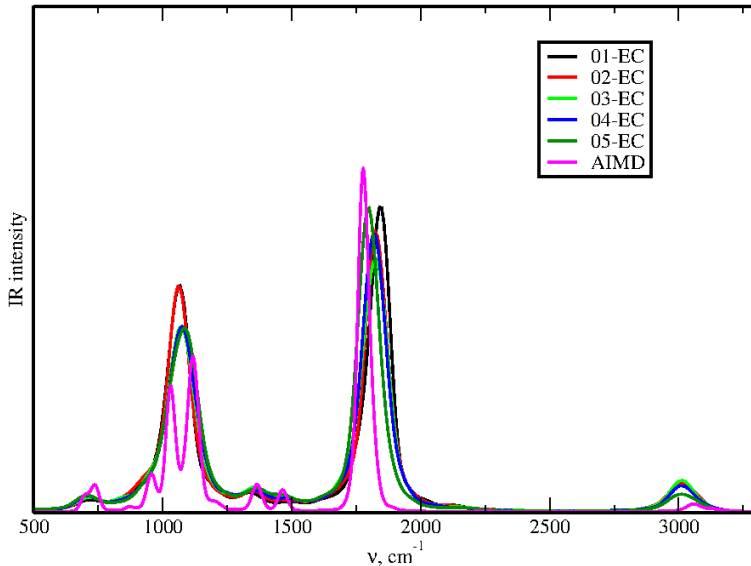


Figure 5.12: Infrared spectra obtained from MD simulation based on NN for systems containing 1 to 5 molecules of EC. Spectrum obtained from AIMD is shown for comparison

Simulations were performed for systems containing 1, 2, 3, 4 or 5 molecules of EC. For bigger number of molecules the system fell apart during the simulation. IR spectra obtained from such simulations are shown in Figure 5.12 together with AIMD result for comparison. It

could be observed that positions of bands are close to those obtained from AIMD simulation, however for vibrations with frequencies below 1800 cm^{-1} number of bands obtained from NN based MD is smaller with respect to AIMD, this is especially visible for bands between 950 and 1200 cm^{-1} . Also frequencies of C=O and C-H stretching bands (1800 cm^{-1} and about 3100 cm^{-1} respectively) are different than in AIMD, the former is blue shifted and the latter is red shifted. The probable cause may be the difference in the basis sets and in the system size — NN-based simulations included small number of EC molecules and were performed without PBC. Nevertheless, it is visible for C=O stretching band, that with growing number of EC molecules in the simulated system, the position of the maximum is moving towards the maximum observed in AIMD. Thus, probably better NN model not suffering from the disintegration of bigger systems would lead to almost identical spectrum as in AIMD.

5.2.2 Water

Structures of water systems containing 10, 20 or 30 molecules were obtained from the AIMD trajectories for neat water (section 3.6) and from the classical MD simulations in TIP3P FF [367, 368]. In the latter, additional trajectories were recorded for changed parameters of the system (density too low or too high, modified FF parameters) in order to generate some geometries distorted from the average for better training. The NN was trained on energies, forces and dipole moments calculated in Gaussian v09 [309] at the PBE/6-31+G* level with Grimme's dispersion correction [175] for 50 000 structures. At the end of the training the value of loss function for training set was $1.2 \cdot 10^{-4}$ and for validation set $1.77 \cdot 10^{-4}$.

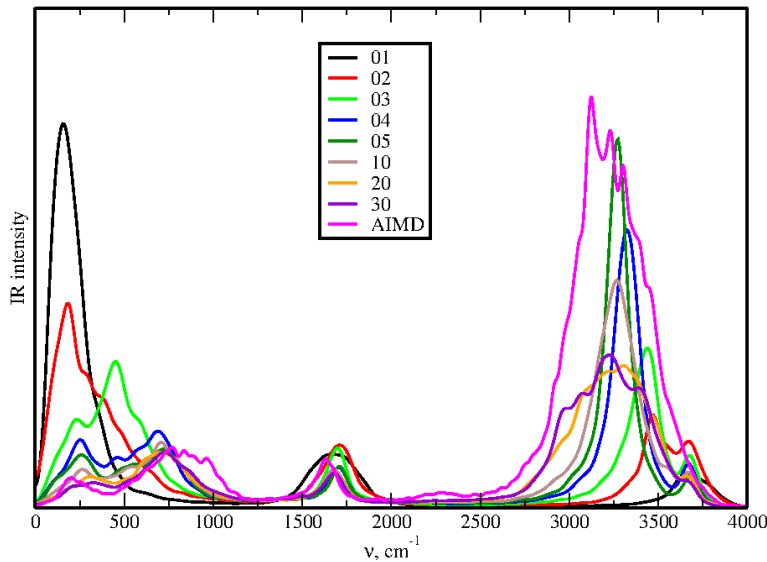


Figure 5.13: Infrared spectra obtained from MD simulation based on NN for systems containing 1 to 30 molecules of water. Spectrum obtained from AIMD is shown for comparison

After training the model, MD simulations were performed for systems containing 1, 2, 3, 4, 5, 10, 20 and 30 molecules of water. Obtained IR spectra, with AIMD spectrum for comparison, are shown in Figure 5.13. Tendencies are similar as those observed for EC: in general, positions of bands are close to those in the spectrum obtained from AIMD with shifting their frequencies

towards AIMD values with growing number of molecules used for simulation. What is more, for systems with small number of H₂O molecules, the O-H band is in the high frequency range of the spectrum (about 3800 cm⁻¹) in opposition to frequency in AIMD (about 3200 cm⁻¹). For system with 1 water molecule only the band at 3800 cm⁻¹ is present, while for systems with 2 or 3 water molecules also an additional band with lower frequency appears. With growing size of the system, the band at 3800 cm⁻¹ is disappearing. It is also visible, that the O-H band becomes broader with increasing number of water molecules. These effects are related to the formation of hydrogen bonds and are similar to those observed for ILs mixed with H₂O: "free" O-H bonds have higher frequencies of stretching and the frequency becomes lower upon formation of HBs. The systematic shift of this band with growing size of the system is therefore related to growing probability of HB formation.

For this case, not only the frequencies were in a satisfactory agreement with AIMD results, but also the effect of hydrogen bonding on the frequency of the O-H bond was reproduced.

As a test, another NN was trained, using for training only the data obtained from classical MD. The results of the simulation were approximately the same. Thus, in this case, structures extracted from classical MD are sufficient, without the need to use expensive AIMD to generate the geometries.

Methods for MD simulation based on the output of pre-trained NN seem to be a promising alternative for computationally expensive AIMD. As shown here they are capable of reproduction of HB effect on the IR spectrum. However, these methods still need further investigation, because simulations for moderately large systems were unstable: in all studied cases molecules became increasingly distorted, some bonds broke and finally the system disintegrated.

Chapter 6

Summary

This Thesis focused on liquid phase systems (ionic liquids and electrolytes) of relevance to the research on new metal-ion batteries. Special attention was paid to the changes in the properties of the solution related to the change in the concentration of the dissolved substance (salt, water) and to the effects of interactions, in particular those observable in the IR spectra. The methodology used in this work was based on molecular dynamics (MD) simulations, both classical and ab initio. Structural analysis of the results involved mostly calculations of Radial Distribution Functions (RDFs) and residence time autocorrelation functions for specific ion pairs. For chosen systems, theoretical IR spectra were obtained from MD trajectories as Fourier transforms (FTs) of the dipole moment autocorrelation functions. FTs of selected geometrical parameters (interatomic distances, angles) were used in the analysis of vibrational modes.

Structural analysis of the data revealed conformational preferences, structure of aggregates, coordination numbers for cation-anion or cation-solvent complexes, and their dependence on the concentration of the solution. Experimentally observed differences between complexation patterns for lithium and sodium cations were successfully reproduced, as well as experimental predictions about dominating forms of complexes in Mg-based electrolytes for different ratios of Mg:Cl ions were confirmed.

Residence time autocorrelation functions, determined from FF MD allowed to observe the dynamics of exchange of atoms in the coordination shell of cations. It was shown that the exchange process for Na^+ cations is faster than for Li^+ ions. When the concentration of dissolved salt increases, the dynamics of the solvation shell becomes slower.

AIMD simulations for ionic liquid-water mixtures and water-in-salt electrolytes were able to produce patterns of hydrogen bonding in agreement with experiment, which was confirmed by analysis of calculated IR spectra compared to experimental data.

A major part of this work describes the modeling of IR spectra. It was concluded that AIMD is capable of reproduction of measured changes caused by changing interactions with changing composition of the system — red/blue shifts of bands or appearance of new bands in the spectrum. Analysis of FTs of individual geometrical parameters supported the explanation of observed effects and assignment of particular vibrational modes to related bands in the IR spectrum. This approach allowed to correlate the frequency of the vibration with chemical environment of molecules, e.g. interactions with ions or hydrogen bond formation. The advantage

of this method is that it is possible to apply *a posteriori* to a recorded trajectory in opposition to Wannier function analysis, which requires determination of Wannier centers during the MD simulation.

Applicability of two approaches: DFTB and Machine Learning (ML), computationally cheaper than AIMD, was studied for reproduction of IR spectra. Although some results were close to those obtained from AIMD simulations, overall performance was not satisfactory. For DFTB there is a need of improved parametrizations; here, it was shown that specifically developed parameter sets (e.g. for water) could have much better performance. From general purpose parametrizations GFN2-xTB was the most valuable one, but still needs improvements. ML methods have problems with stability of simulated systems, which may be the effect of insufficient training sets and needs further investigation. Nevertheless, both approaches seem as promising alternatives to AIMD.

To conclude, FF MD (with some limitations) and AIMD are powerful tools for the analysis of liquid phase systems. The latter can be applied to study the vibrational spectra and their sensitivity to interactions, yielding results comparable to those obtained by experiment. Less time-consuming approaches are not yet accurate enough to replace AIMD, but after their development in the future, they may become a reasonable alternative.

6.1 Acknowledgements

The simulations performed for the purpose of this work were done with use of the PiGrid infrastructure: Prometheus and Ares clusters in the Academic Computer Centre Cyfronet AGH within computational grants plgaenael2, plgaenael3, plgaenael4, plgaenael5, plgaenael6, plgaenael7, plgaegpu3 and plgaegpu4.

This work was supported by the National Science Centre grant no. UMO-2016/21/B/St4/02110, by Jagiellonian University POB DigiWorld minigrant no. U1U/P06/DO/14.07 and by the Jagiellonian Interdisciplinary PhD Programme in the ZintegrUJ project.

List of Figures

1.1	Raman spectrum of EMIM-TFSI solution with dissolved LiTFSI [4]	19
1.2	Raman spectra of $(\text{LiTFSI})_x \text{EC}_{1-x}$ with different molar fraction x of lithium salt, with deconvoluted bands for free and coordinated EC [112]	23
1.3	Structures of diglyme-LiClO ₄ complexes calculated with DFT methods [126] . .	25
1.4	Raman spectrum of uracil calculated from AIMD simulation in gas phase and in aqueous solution [229] compared with experimental spectrum [230]	29
2.1	Example RDF (top) and integrated RDF (bottom) for Li-O pairs in LiTFSI solution in EMIM-TFSI IL with molar fraction of the salt equal 0.2 in different temperatures and pressures [A]	38
2.2	Lithium-TFSI ⁻ residence time autocorrelation functions (symbols) and exponential fits to the data (lines), in LiTFSI solution in EMIM-TFSI IL with molar fraction of the salt equal 0.2 and different temperatures and pressures [A]	39
2.3	Example of dipole moment dependence on time of the simulation (left) and obtained from it IR spectrum (right) for the system with ethylene carbonate	40
2.4	Fourier transforms of the S-F bond length and S-N-S angles of FSI ⁻ anions in the EMIM-FSI ionic liquid. Magenta line is the average [I]	41
3.1	Conformers of the FSI ⁻ anion with their relative energies in kcal/mol	52
3.2	Conformers of the Na-FSI pairs with their relative energies in kcal/mol	52
3.3	Histograms of the FSSF angle in simulated systems for classical and ab initio MD	53
3.4	Population of different FSI ⁻ conformers for all studied systems as a function of the sodium salt molar fraction x	54
3.5	Histograms of distribution of the time between conformational changes of FSI ⁻ anions in DP-FF MD simulations with fitted $p = Ae^{-\frac{\tau}{t}}$ curve to the long-time parts	54
3.6	Average time between conformational changes (blue) for DP-FF MD and τ parameter (defined in Figure 3.5) dependence on the sodium salt molar fraction x	54
3.7	Radial distribution functions for DP-FF MD and AIMD for systems with 0, 0.2 and 0.5 NaFSI molar fractions	55
3.8	Integrated Na-O RDF for AIMD simulations	56
3.9	Integrated Na-O RDF for DP-FF simulations	56
3.10	Histograms of the number of O atoms (N_O) coordinating sodium cations (upper) and number of different FSI ⁻ anions (N_{an}) in sodium solvation shell for AIMD simulations (lower). Solid lines are average values over all studied systems at a given concentration x (shown in broken lines)	57
3.11	Histograms of the number of O atoms (N_O) coordinating sodium cations (upper) and number of different FSI ⁻ anions (N_{an}) in sodium solvation shell for DP-FF simulations (lower)	57
3.12	Radial distribution functions for Na-Na	58
3.13	Residence time autocorrelation functions for DP-FF for Na ⁺ coordination by whole anions (left) and individual O atoms (right)	59

3.14 Radial distribution functions for Me-O distances in the polarizable (top) and non-polarizable (middle) FF and the running coordination numbers for Me-O (bottom) for the system with $x = 0.3$	61
3.15 Abundance of different combinations of the number of anions N_{an} and the number of oxygen atoms N_O coordinating Me^+ ions in NP-FF and DP-FF; areas of the circles are proportional to the abundance	62
3.16 Residence time autorrelation functions for Me-O for DP-FF (top), NP-FF (middle) and τ parameters for O atoms and TFSI anions (bottom)	63
3.17 Structures of Mg:Cl complexes studied by QC methods	65
3.18 Radial distribution functions for Mg-Cl and Mg-O distances (O_E - oxygen from DME, O_T - oxygen from TFSI^-)	68
3.19 Integrated RDFs for Mg-O pairs from classical MD simulations, O_E - oxygen atoms from DME, O_T - oxygen atoms from TFSI^-)	68
3.20 Integrated RDFs for Mg-Mg and Mg-Cl pairs from classical MD simulations. Broken lines mark RDFs for "ideal" geometries of aggregates optimized in QC calculations	69
3.21 Radial distribution functions for Mg-Mg and Cl-Cl pairs	70
3.22 Relative potential energies E_{pot} per Mg^{2+} ion for II, IIa and III, IIIa-c systems for the last 40 ns of classical MD simulations with applied moving average over 0.5 ns.	71
3.23 Average number of Mg^{2+} ions at the distance of 4 Å from the Mg^{2+} ion. Initial arrangements of Mg^{2+} and Cl^- ions are shown on the left hand side of the plot	72
3.24 Abundance of Mg^{2+} ions in different complexes at different stages of classical MD simulations for systems I, II and IIa	72
3.25 Abundance of Mg^{2+} ions in different complexes at different stages of classical MD simulations for systems III, IIIa, IIIb and IIIc	73
3.26 Radial distribution functions for $\text{Me}-\text{O}_{\text{carb}}$ pairs where O_{carb} is the oxygen atom from carbonate molecule	75
3.27 Integrated Me-O RDFs from classical MD for carbonate and TFSI oxygen atoms	76
3.28 Histograms of average total numbers of oxygen atoms coordinating the Me^+ ion	76
3.29 Residence time autocorrelation functions for $\text{Me}-\text{O}_{\text{carb}}$, lines are fits to the data	78
3.30 Residence time autocorrelation functions for $\text{Me}-\text{O}_{\text{TFSI}}$ and Me-anion , lines are fits to the data	78
3.31 Radial distribution functions for Na-O atom pairs in 1:6 electrolytes (O_E - ether oxygen atom, O_A - oxygen atom from anion)	81
3.32 Integrated Na-O RDFs for 1:20 and 1:6 systems	81
3.33 Distribution of the number of ether oxygen atoms coordinated to Na^+ (a), of the number of anion oxygen atoms coordinated to Na^+ (b), and of the number of Na^+ ions coordinated to PEO molecules (c)	82
3.34 Venn diagrams showing the connectivity between Na^+ ion and oxygen atoms of the monoglyme and tetraglyme molecules in 1:6 electrolytes, values lower than 1% are displayed as dots	83
3.35 Distribution of the probability that an oxygen atom positioned at the site ΔN is coordinated to the Na^+ cation, interacting with the oxygen atom at the site $N = 0$ in the 1:6 PEO-based electrolytes	83
3.36 Residence time autocorrelation function for Na-ether interactions. Lines are fits to the data	84
3.37 Probability of the displacement of Na^+ ion by dN sites along the PEO chain in 1:6 Na(T)FSI/PEO electrolytes after 250 ns of simulations	85
3.38 Labeling of atoms in EMIM ⁺ cation	87

3.39	Radial distribution functions for selected atom pairs for systems with water mole fraction 0.5	88
3.40	Radial distribution functions for selected atom pairs for neat IL	89
3.41	Combined distribution functions for selected donor-hydrogen-acceptor atoms in systems with water mole fraction 0.5	90
3.42	Spatial distribution functions of oxygen atoms around EMIM ⁺ cations: TFSI ⁻ anions in the neat IL (a); TFSI ⁻ anions in the $x = 0.5$ mixture (b); water molecules in the $x = 0.5$ mixture (c). Surfaces of particle isodensity of 10 atoms/nm ³ are shown	90
3.43	Average number of hydrogen bonds n_{HB} per donor. Donors are shown in the horizontal axis, acceptors are marked by colors	91
4.1	IR spectra obtained from AIMD simulations for electrolytes with different mole fractions of NaFSI	93
4.2	Sample Fourier transforms of S-O and S-F bond length and S-N-S angle for selected FSI ⁻ anion	93
4.3	Fourier transforms of the S-F bond length for all FSI ⁻ anions in $x = 0.2$ system (a), average values for Fourier transforms of S-F length (b) and S-N-S angles (c) for different salt concentrations	94
4.4	Fourier transforms of the (a) S-F bond length and (b) S-N-S angle for selected FSI ⁻ anions in the $x = 0.2$ electrolyte and integrated (c) O-Na RDFs for selected anions	95
4.5	Local environment of selected FSI ⁻ anions in the $x = 0.2$ system	96
4.6	IR spectra obtained from AIMD trajectories for systems III and IIIa-c	97
4.7	Fourier transforms of Mg-Mg and Mg-Cl distances obtained from AIMD simulations for systems IIIa-IIIc	98
4.8	Fourier transforms of geometric parameters of TFSI ⁻ anions from the AIMD simulations	99
4.9	Fourier transforms of S-O bond lengths in TFSI ⁻ anions, for systems IIIa and IIIc the averages over all bonds are presented while for system IIIb FTs for individual bonds are shown	99
4.10	Infrared spectra for neat carbonates obtained from QC calculations or from AIMD simulations	100
4.11	Infrared spectra of solvents and electrolyte solutions	101
4.12	Power spectrum obtained from Fourier transforms of interatomic distances for EC (right), used atoms/bonds for calculation of these transforms (left), colors correspond to these in Fourier transforms	101
4.13	Fourier transforms of C=O bond lengths of solvent molecules. Free solvent molecules are black, molecules interacting with metal cations are red, and in magenta molecules interacting with the metal only during a part of MD trajectory are marked	102
4.14	Averaged Fourier transforms of interatomic distances	103
4.15	IR spectra calculated from AIMD trajectories for neat liquids and IL/water mixtures with increasing mole fraction of water, experimental spectra are from [354] for water and from [355] for IL (left); experimental spectra for H ₂ O and IL/H ₂ O mixtures (right) [356], for EMIM-TFSI changes are shown in the bottom	105
4.16	Fourier transforms of C ₁ -H, O _w -H bond lengths and H-O _w -H angles averaged over all ions/molecules in IL/water mixtures	106
4.17	Fourier transforms of C ₁ -H bond lengths in neat EMIM-TFSI (top), positions of maxima in FTs of bond lengths vs the time of HB formation (bottom)	107

4.18 Positions of the maxima in FTs of C ₁ -H bond lengths vs the time of HB formation for IL/water mixtures	108
4.19 Positions of the maxima in FTs of O-H bond lengths vs the time of HB formation for IL/water mixtures with $x = 0.25$ (a), $x = 0.5$ (b) and with alternative labeling of data for $x = 0.5$ (c)	109
4.20 Infrared spectra obtained from AIMD for LiTFSI in H ₂ O systems, inset contains experimental spectra in the range of O-H vibrations from [366]	111
5.1 Radial distribution functions for Me-O pairs for electrolytes based on EC obtained from classical MD, AIMD and DFTB MD simulations	113
5.2 Infrared spectra of neat solvents obtained from QC calculations or from AIMD and DFTB MD simulations	114
5.3 Infrared spectra of solvents and electrolyte solutions obtained from AIMD and DFTB MD simulations	115
5.4 Fourier transforms of C-O distances in DFTB MD simulations. Free solvent molecules are marked in black, molecules interacting with Na ⁺ in red, and in magenta molecules interacting with cations for only a part of the MD trajectory. Thick red line marks the molecule interacting with 2 Na ⁺ ions	115
5.5 Averaged Fourier transforms of interatomic distances in AIMD and DFTB MD . .	116
5.6 Infrared spectra obtained from GFN2-xTB MD simulations	117
5.7 Infrared spectra calculated for bulk water in different DFTB parametrizations (top), average number of hydrogen bonds per water molecule (bottom)	118
5.8 Spatial distribution functions of oxygen atoms around water molecules in bulk water obtained in DFTB simulations. Surfaces of particle density 100 atoms/nm ³ are shown	119
5.9 Infrared spectra of neat IL and the mixture with water obtained from MD based on PBE DFT or two DFTB parametrizations	120
5.10 Spatial distribution functions of oxygen atoms around EMIM ⁺ cations in simulations from GFN2-xTB method: (a) TFSI ⁻ anions in the neat IL, (b) TFSI ⁻ anions in the $x = 0.5$ mixture, (c) water molecules in the $x = 0.5$ mixture. Surfaces of particle density 10 atoms/nm ³ are shown	120
5.11 Average numbers of the most abundant hydrogen bonds obtained for $x = 0.5$ from MD simulations based on DFT or DFTB. Lines are only to guide the eye	121
5.12 Infrared spectra obtained from MD simulation based on NN for systems containing 1 to 5 molecules of EC. Spectrum obtained from AIMD is shown for comparison	122
5.13 Infrared spectra obtained from MD simulation based on NN for systems containing 1 to 30 molecules of water. Spectrum obtained from AIMD is shown for comparison	123

List of Tables

1.1	Abundance of example elements in the earth crust [46]	21
3.1	Compositions of $(\text{NaFSI})_x(\text{EMIM-FSI})_{1-x}$ systems	51
3.2	Compositions of $\text{Me}_x\text{EMIM}_{1-x}\text{TFSI}$ systems	60
3.3	Compositions of $\text{Mg}(\text{TFSI})_2\text{-MgCl}_2\text{-DME}$ solutions	64
3.4	Interatomic distances (in Å) for chosen complexes	66
3.5	Binding energies in kcal/mol for complexes	67
3.6	Total binding effects (as defined by equation 3.1) for aggregates in kcal/mol	67
3.7	Compositions of Li/NaTFSI - carbonate systems	74
3.8	Binding energies in kcal/mol calculated at the MP2 level	75
3.9	Residence times in ns for oxygen atoms from solvent molecules or TFSI^- anions and anion residence times	77
3.10	Residence times τ_E for ether molecules in nanoseconds	85
4.1	Observed shifts of chosen bands in IR spectra compared to experimental values	103
4.2	Compositions of $\text{LiTFSI}/\text{H}_2\text{O}$ systems	111

Bibliography

- [1] Z. Kęcki. *Podstawy spektroskopii molekularnej*. PWN, 2013, pp. 11–18, 24–27, 84–101, 143–155.
- [2] J. Sadlej. *Spektroskopia molekularna*. WNT, 2002, pp. 3, 10–11, 78, 162–177, 205.
- [3] J. Clayden, N. Greeves, S. Warren, and P. Wothers. *Chemia organiczna, cz. 1*. WNT, 2009, pp. 65–72.
- [4] Y. Umebayashi, T. Mitsugi, S. Fukuda, T. Fujimori, K. Fujii, R. Kanzaki, M. Takeuchi, and S.-I. Ishiguro. “Lithium Ion Solvation in Room-Temperature Ionic Liquids Involving Bis(trifluoromethanesulfonyl) Imide Anion Studied by Raman Spectroscopy and DFT Calculations”. *J. Phys. Chem. B* 111 (2007), 13028–13032.
- [5] S. Bagchi, S. D. Fried, and S. G. Boxer. “A Solvatochromic Model Calibrates Nitriles’ Vibrational Frequencies to Electrostatic Fields”. *J. Am. Chem. Soc.* 134 (2012), 10373–10376.
- [6] L. Yu, B. S. Pizio, and T. D. Vaden. “Conductivity and Spectroscopic Investigation of Bis(trifluoromethanesulfonyl)imide Solution in Ionic Liquid 1-Butyl-3-methylimidazolium Bis(trifluoromethanesulfonyl)imide”. *J. Phys. Chem. B* 116 (2012), 6553–6560.
- [7] K. Fumino, K. Wittler, and R. Ludwig. “The Anion Dependence of the Interaction Strength between Ions in Imidazolium-Based Ionic Liquids Probed by Far-Infrared Spectroscopy”. *J. Phys. Chem. B* 116 (2012), 9507–9511.
- [8] S. Zhang, Y. Zhang, X. Ma, L. Lu, Y. He, and Y. Deng. “Benzonitrile as a Probe of Local Environment in Ionic Liquids”. *J. Phys. Chem. B* 117 (2013), 2764–2772.
- [9] L. J. G. W. van Wilderen, D. Kern-Michler, H. M. Müller-Werkmeister, and J. Bredenbeck. “Vibrational dynamics and solvatochromism of the label SCN in various solvents and hemoglobin by time dependent IR and 2D-IR spectroscopy”. *Phys. Chem. Chem. Phys.* 16 (2014), 19643–19653.
- [10] J. F. Carpenter and J. H. Crowe. “An infrared spectroscopic study of the interactions of carbohydrates with dried proteins”. *Biochemistry* 28.9 (1989), 3916–3922.
- [11] G. Lawrie, I. Keen, B. Drew, A. Chandler-Temple, L. Rintoul, P. Fredericks, and L. Grøndahl. “Interactions between Alginate and Chitosan Biopolymers Characterized Using FTIR and XPS”. *Biomacromolecules* 8 (2007), 2533–2541.
- [12] K. Yang, D. Lin, and B. Xing. “Interactions of Humic Acid with Nanosized Inorganic Oxides”. *Langmuir* 25 (2009), 3571–3576.
- [13] N. Goutev, K. Ohno, and H. Matsuura. “Raman Spectroscopic Study on the Conformation of 1,2-Dimethoxyethane in the Liquid Phase and in Aqueous Solutions”. *J. Phys. Chem. A* 104 (2000), 9226–9232.
- [14] K. Fujii, S. Seki, S. Fukuda, R. Kanzaki, T. Takamuku, Y. Umebayashi, and S.-I. Ishiguro. “Anion Conformation of Low-Viscosity Room-Temperature Ionic Liquid 1-Ethyl-3-methylimidazolium Bis(fluorosulfonyl) Imide”. *J. Phys. Chem. B* 111 (2007), 12829–12833.

- [15] P. Johansson, J. Grondin, and J.-C. Lasseègues. “Structural and Vibrational Properties of Diglyme and Longer Glymes”. *J. Phys. Chem. A* 114 (2010), 10700–10705.
- [16] N. M. Shishlov and S. L. Khursan. “Effect of ion interactions on the IR spectrum of benzenesulfonate ion. Restoration of sulfonate ion symmetry in sodium benzenesulfonate dimer”. *Journal of Molecular Structure* 1123 (2016), 360–366.
- [17] J. Zhang, Y. Duan, H. Sato, H. Tsuji, I. Noda, S. Yan, and Y. Ozaki. “Crystal Modifications and Thermal Behaviour of Poly(L-lactic acid) Revealed by Infrared Spectroscopy”. *Macromolecules* 38 (2005), 8012–8021.
- [18] V. Minaeva, A. Panchenko, N. Karaush-Karmazin, J. E. Nycz, and B. Minaev. “Manifestation of Intermolecular Interactions in the IR Spectra of 2- and 4-Methylmethcathinones Hydrochlorides: DFT Study and Hirshfeld Surfaces Analysis”. *Biointerface Research in Applied Chemistry* 13 (2023), 202.
- [19] A. D. Buckingham, J. E. Del Bene, and S. A. C. McDowell. “The hydrogen bond”. *Chem. Phys. Letters* 463 (2008), 1–10.
- [20] S. A. Katsyuba, M. V. Vener, E. E. Zvereva, Z. Fei, R. Scopelliti, G. Laurenczy, N. Yan, E. Paunescu, and P. J. Dyson. “How Strong Is Hydrogen Bonding in Ionic Liquids? Combined X-ray Crystallographic, Infrared/Raman Spectroscopic, and Density Functional Theory Study”. *J. Phys. Chem. B* 117 (2013), 9094–9105.
- [21] K. Fumino, T. Peppel, M. Geppert-Rybczyńska, D. H. Zaitsau, J. K. Lehmann, S. P. Verevkin, M. Köckerling, and R. Ludwig. “The influence of hydrogen bonding on the physical properties of ionic liquids”. *Phys. Chem. Chem. Phys.* 13 (2011), 14064–14075.
- [22] K. Fumino, A. Wulf, and R. Ludwig. “Hydrogen Bonding in Protic Ionic Liquids: Reminiscent of Water”. *Angewandte Chemie* 48 (2009), 3184–3186.
- [23] A. Kobayashi, K. Osawa, M. Terazima, and Y. Kimura. “Solute–solvent hydrogen-bonding in room temperature ionic liquids studied by Raman spectroscopy”. *Phys. Chem. Chem. Phys.* 14 (2012), 13676–13683.
- [24] R. Zhang, H. Li, Y. Lei, and S. Han. “Structures and interactions in N-methylacetamide–water mixtures studied by IR spectra and density functional theory”. *Journal of Molecular Structure* 693 (2004), 17–25.
- [25] L. Han, Y. Sun, Y. Wang, H. Fu, C. Duan, M. Wang, W. Cai, and X. Shao. “Ultra-high resolution near-infrared spectrum by wavelet packet transform revealing the hydrogen bond interactions”. *Spectrochimica Acta Part A* 289 (2023), 122233.
- [26] B. Klassen, R. Aroca, M. Nazri, and G. A. Nazri. “Raman Spectra and Transport Properties of Lithium Perchlorate in Ethylene Carbonate Based Binary Solvent Systems for Lithium Batteries”. *J. Phys. Chem. B* 102 (1998), 4795–4801.
- [27] Z. Wang, B. Huang, H. Huang, Chen. L., R. Xue, and F. Wang. “Infrared spectroscopic study of the interaction between lithium salt LiClO_4 and the plasticizer ethylene carbonate in the polyacrylonitrile-based electrolyte”. *Solid State Ionics* 85 (1996), 143–148.
- [28] M. Deepa, N. Sharma, P. Varshney, S. A. Agnihotry, and R. Chandra. “An insight into the interactions between $\text{LiN}(\text{CF}_3\text{SO}_2)_2$ - $\gamma\text{BL}/\text{DMF}$ - PMMA by FTIR spectroscopy”. *Ionics* 6 (2000), 408–414.
- [29] Y. Umebayashi, S. Mori, K. Fujii, S. Suzuki, S. Seki, K. Hayamizu, and S.-I. Ishiguro. “Raman Spectroscopic Studies and Ab Initio Calculations on Conformational Isomerism of 1-Butyl-3-methylimidazolium Bis-(trifluoromethanesulfonyl)amide Solvated to a Lithium Ion in Ionic Liquids: Effects of the Second Solvation Sphere of the Lithium Ion”. *J. Phys. Chem. B* 114 (2010), 6513–6521.

- [30] D. M. Seo, P. D. Boyle, J. L. Allen, S.-D. Han, E. Jónsson, P. Johansson, and W. A. Henderson. “Solvate Structures and Computational/Spectroscopic Characterization of LiBF₄ Electrolytes”. *J. Phys. Chem. C* 118 (2014), 18377–18386.
- [31] S.-D. Han, S.-H. Yun, O. Borodin, D. M. Seo, R. D. Sommer, V. G. Young, and W. A. Henderson. “Solvate Structures and Computational/Spectroscopic Characterization of LiPF₆ Electrolytes”. *J. Phys. Chem. C* 119 (2015), 8492–8500.
- [32] I.-D. Wu and F.-Ch. Chang. “Determination of the interaction within polyester-based solid polymer electrolyte using FTIR spectroscopy”. *Polymer* 48 (2007), 989–996.
- [33] D. M. Seo, P. D. Boyle, R. D. Sommer, J. S. Daubert, O. Borodin, and W. A. Henderson. “Solvate Structures and Spectroscopic Characterization of LiTFSI Electrolytes”. *J. Phys. Chem. B* 118 (2014), 13601–13608.
- [34] J.-C. Lasseègues, J. Grondin, C. Aupetit, and P. Johansson. “Spectroscopic Identification of the Lithium Ion Transporting Species in LiTFSI-Doped Ionic Liquids”. *J. Phys. Chem. A* 113 (2009), 305–314.
- [35] L. Aguilera, S. Xiong, J. Scheers, and A. Matic. “A structural study of LiTFSI–tetraglyme mixtures: From diluted solutions to solvated ionic liquids”. *J. Mol. Liquids* 210 (2015), 238–242.
- [36] Y. Chae, C. Lim, J. Jeon, M. Kim, K.-K. Lee, K. Kwak, and M. Cho. “Lithium-Ion Solvation Structure in Organic Carbonate Electrolytes at Low Temperatures”. *J. Phys. Chem. Lett.* 13 (2022), 7881–7888.
- [37] A. Boschin and P. Johansson. “Characterization of NaX (X: TFSI, FSI) - PEO based solid polymer electrolytes for sodium batteries”. *Electrochim. Acta* 175 (2015), 124–133.
- [38] D. Monti, E. Jónsson, M. R. Palacín, and P. Johansson. “Ionic liquid based electrolytes for sodium-ion batteries: Na⁺ solvation and ionic conductivity”. *J. Power Sources* 245 (2014), 630–636.
- [39] J. Wahlers, K. D. Fulfer, D. P. Harding, D. G. Kuroda, R. Kumar, and R. Jorn. “Solvation Structure and Concentration in Glyme-Based Sodium Electrolytes: A Combined Spectroscopic and Computational Study”. *J. Phys. Chem. C* 120 (2016), 17949–17959.
- [40] K. B. Lindberg, P. Seljom, H. Madsen, D. Fischer, and M. Korpås. “Long-term electricity load forecasting: Current and future trends”. *Utilities Policy* 58 (2019), 102–119.
- [41] M. S. Whittingham. “History, Evolution, and Future Status of Energy Storage”. *Proceedings of the IEEE* 100 (2012), 1518–1534.
- [42] K. Xu. “Nonaqueous Liquid Electrolytes for Lithium-Based Rechargeable Batteries”. *Chem. Rev.* 104 (2004), 4303–4417.
- [43] K. Xu. “Electrolytes and Interphases in Li-Ion Batteries and Beyond”. *Chem. Rev.* 114 (2014), 11503–11618.
- [44] H. J. Bergveld, W. S. Kruijt, and P. H. L. Notten. *Battery Management Systems: Design by Modelling*. Springer, 2002, pp. 107–108, 113.
- [45] Z. Xue, D. He, and X. Xie. “Poly(ethylene oxide)-based electrolytes for lithium-ion batteries”. *J. Mater. Chem. A* 3 (2015), 19218–19253.
- [46] K. H. Wedepohl. “The composition of the continental crust”. *Geochimica et Cosmochimica Acta* 59 (1995), 1217–1232.
- [47] J.-M. Tarascon. “Is lithium the new gold?” *Nature Chemistry* 5 (2010), 510.
- [48] R. E. Ciez and J. F. Whitacre. “The cost of lithium is unlikely to upend the price of Li-ion storage systems”. *J. Power Sources* 320 (2016), 310–313.

- [49] V. Palomares, P. Serras, I. Villaluenga, K. B. Hueso, Carretero-González, and T. Rojo. “Na-ion batteries, recent advances and present challenges to become low cost energy storage systems”. *Energy Environ. Sci.* 5 (2012), 5884–5901.
- [50] M. D. Slater, D. Kim, E. Lee, and C. S. Johnson. “Sodium-Ion Batteries”. *Advanced Functional Materials* 23 (2013), 947–958.
- [51] N. Yabuuchi, K. Kubota, M. Dahbi, and S. Komaba. “Research Development on Sodium-Ion Batteries”. *Chem. Rev.* 114 (2014), 11636–11682.
- [52] A. Ponrouch, D. Monti, A. Boschin, B. Steen, P. Johansson, and R. Palacín. “Non-aqueous electrolytes for sodium-ion batteries”. *J. Mater. Chem. A* 5 (2015), 22–42.
- [53] H. Pan, Y.-S. Hu, and L. Chen. “Room-temperature stationary sodium-ion batteries for large-scale electric energy storage”. *Energy Environ. Sci.* 6 (2013), 2338–2360.
- [54] H. D. Yoo, I. Shterenberg, Y. Gofer, G. Gershinsky, N. Pour, and D. Aurbach. “Mg rechargeable batteries: an on-going challenge”. *Energy Environ. Sci.* 6 (2013), 2265–2279.
- [55] J. Song, E. Sahadeo, M. Noked, and S. B. Lee. “Mapping the Challenges of Magnesium Battery”. *J. Phys. Chem. Lett.* 7 (2016), 1736–1749.
- [56] F. Tuexun, Y. Abulizi, Y. NuLi, S. Su, J. Yang, and J. Wang. “High concentration magnesium borohydride/tetraglyme electrolyte for rechargeable magnesium batteries”. *J. Power Sources* 276 (2015), 255–261.
- [57] N. S. V. Narayanan, B. V. A. Raj, and S. Sampath. “Physicochemical, spectroscopic and electrochemical characterization of magnesium ion-conducting, room temperature, ternary molten electrolytes”. *J. Power Sources* 195 (2010), 4356–4364.
- [58] T. Watkins and D. A. Buttry. “Determination of Mg²⁺ Speciation in a TFSI⁻-Based Ionic Liquid With and Without Chelating Ethers Using Raman Spectroscopy”. *J. Phys. Chem. B* 119 (2015), 7003–7014.
- [59] Y. Li, S. Guan, H. Huo, Y. Ma, Y. Gao, P. Zuo, and G. Yin. “A Review of Magnesium Aluminum Chloride Complex Electrolytes for Mg Batteries”. *Adv. Funct. Mater.* 31 (2021), 2100650.
- [60] S. He, K. V. Nielson, J. Luo, and T. L. Liu. “Recent advances on MgCl₂ based electrolytes for rechargeable batteries”. *Energy Storage Materials* 8 (2017), 184–188.
- [61] R. Mohtadi and F. Mizuno. “Magnesium batteries: Current state of the art, issues and future perspectives”. *Beilstein J. Nanotechnol.* 5 (2014), 1290–1311.
- [62] C. B. Bucur, T. Gregory, A. G. Oliver, and J. Muldoon. “Confession of a Magnesium Battery”. *J. Phys. Chem. Lett.* 6 (2015), 3578–3591.
- [63] J. Peters, D. Buchholz, S. Passerini, and M. Weil. “Life cycle assessment of sodium-ion batteries”. *Energy Environ. Sci.* 9 (2016), 1744–1751.
- [64] S. Y. Hong, Y. Kim, Y. Park, A. Choi, N.-S. Choi, and K. T. Lee. “Charge carriers in rechargeable batteries: Na ions vs. Li ions”. *Energy Environ. Sci.* 6 (2013), 2067–2081.
- [65] Z. Lu, A. Schechter, M. Moshkovich, and D. Aurbach. “One the electrochemical behavior of magnesium electrodes in polar aprotic electrolyte solutions”. 466 (1999), 203–217.
- [66] T. S. Arthur, N. Singh, and M. Matsui. “Electrodeposited Bi, Sb and Bi_{1-x}Sb_x alloys as anodes for Mg-ion batteries”. *Electrochim. Commun.* 16 (2012), 103–106.
- [67] N. Singh, T. S. Arthur, C. Ling, M. Matsui, and F. Mizuno. “A high energy-density tin anode for rechargeable magnesium-ion batteries”. *Chem. Commun.* 49 (2013), 149–151.

- [68] T. E. Sutto and T. T. Duncan. “Electrochemical and structural characterization of Mg ion intercalation into Co_3O_4 using ionic liquid electrolytes”. *Electrochim. Acta* 80 (2012), 413–417.
- [69] G. G. Amatucci, F. Badway, A. Singhal, B. Beaudoin, G. Skandan, T. Bowmer, I. Plitz, N. Pereira, T. Chapman, and R. Jaworski. “Investigation of Yttrium and Polyvalent Ion Intercalation into Nanocrystalline Vanadium Oxide”. *J. Electrochem. Soc.* 148 (2001), A940.
- [70] C. Ling and F. Mizuno. “Phase Stability of Post-spinel Compound AMn_2O_4 ($\text{A} = \text{Li}$, Na , or Mg) and Its Application as a Rechargeable Battery Cathode”. *Chem. Mater.* 25 (2013), 3062–3071.
- [71] T. E. Sutto and T. T. Duncan. “Electrochemical and structural characterization of Mg ion intercalation into RuO_2 using an ionic liquid electrolyte”. *Electrochim. Acta* 79 (2012), 170–174.
- [72] Y. Liu, L. Jiao, Q. Wu, J. Du, Y. Zhao, Y. Si, Y. Wang, and H. Yuan. “Sandwich-structured graphene-like MoS_2/C microspheres for rechargeable Mg batteries”. *J. Mater. Chem. A* 1 (2013), 5822–5826.
- [73] K. Matsumoto, T. Hosokawa, T. Nohira, R. Hagiwara, A. Fukunaga, K. Numata, E. Itani, S. Sakai, K. Nitta, and S. Inazawa. “The $\text{Na}[\text{FSA}]-[\text{C}_2\text{C}_1\text{im}][\text{FSA}](\text{C}_2\text{C}_1\text{im}^+)$: 1-ethyl-3-methylimidazolium and FSA^- : bis(fluorosulfonyl)amide) ionic liquid electrolytes for sodium secondary batteries”. *J. Power Sources* 265 (2014), 36–39.
- [74] C.-Y. Chen, T. Kiko, T. Hosokawa, K. Matsumoto, T. Nohira, and R. Hagiwara. “Ionic liquid electrolytes with high sodium ion fraction for high-rate and long-life sodium secondary batteries”. *J. Power Sources* 332 (2016), 51–59.
- [75] A. Ponrouch, E. Marchante, M. Courty, J.-M. Tarascon, and M. R. Palacín. “In search of an optimized electrolyte for Na-ion batteries”. *Energy Environ. Sci.* 5 (2012), 8572–8583.
- [76] G. H. Lane and E. Jezek. “Electrochemical studies of acetonitrile based supercapacitor electrolytes containing alkali and alkaline earth metal cations”. *Electrochim. Acta* 150 (2014), 173–187.
- [77] J. Kim, H.-D. Lim, H. Gwon, and K. Kang. “Sodium-oxygen batteries with alkyl-carbonate and ether based electrolytes”. *Phys. Chem. Chem. Phys.* 15 (2013), 3623–3629.
- [78] S. Y. Hong, Y. Kim, Y. Park, A. Choi, N.-S. Choi, and K. T. Lee. “Charge carriers in rechargeable batteries: Na ions vs. Li ions”. *Energy Environ. Sci.* 6 (2013), 2067–2081.
- [79] M. L. Aubrey, R. Ameloot, B. B. Wiers, and J. R. Long. “Metal-organic frameworks as solid magnesium electrolytes”. *Energy Environ. Sci.* 7 (2014), 667–671.
- [80] A. Bitner-Michalska, A. Krztoń-Maziopa, G. Żukowska, T. Trzeciak, W. Wieczorek, and M. Marcinek. “Liquid electrolytes containing new tailored salts for sodium-ion batteries”. *Electrochim. Acta* 222 (2016), 108–115.
- [81] M. Wiencierz and N. A. Stolwijk. “Systematics of ionic transport and pair formation in amorphous PEO–NaI polymer electrolytes”. *Solid State Ionics* 212 (2012), 88–99.
- [82] J. S. Moreno, M. Armand, M. B. Berman, S. G. Greenbaum, B. Scrosati, and S. Panero. “Composite $\text{PEO}_n:\text{NaTFSI}$ polymer electrolyte: Preparation, thermal and electrochemical characterization”. *J. Power Sources* 248 (2014), 695–702.
- [83] O. Chusid, Y. Gofer, H. Gizbar, Y. Vestfrid, E. Levi, D. Aurbach, and I. Riech. “Solid-State Rechargeable Magnesium Batteries”. *Adv. Mater.* 15 (2003), 627–630.

- [84] Y. Lee, J. Lee, H. Kim, K. Kang, and N.-S. Choi. “Highly stable linear carbonate-containing electrolytes with fluoroethylene carbonate for high-performance cathodes in sodium-ion batteries”. *J. Power Sources* 320 (2016), 49–58.
- [85] M. Bolloli, F. Alloin, J. Kalhoff, D. Bresser, S. Passerini, P. Judenstein, and J.-C. Leprêtre. “Effect of Carbonates Fluorination on the Properties of LiTFSI-based Electrolytes for Li-ion Batteries”. *Electrochim. Acta* 161 (2015), 159–170.
- [86] C. Xu, F. Lindgren, B. Philippe, M. Gorgoi, F. Björefors, K. Edström, and T. Gustafsson. “Improved Performance of the Silicon Anode for Li-Ion Batteries: Understanding the Surface Modification Mechanism of Fluoroethylene Carbonate as an Effective Electrolyte Additive”. *Chem. Mater.* 27 (2015), 2591–2599.
- [87] Z. Zhang, L. Hu, H. Wu, W. Weng, M. Koh, P. C. Redfern, L. A. Curtiss, and K. Amine. “Fluorinated electrolytes for 5 V lithium-ion battery chemistry”. *Energy Environ. Sci.* 6 (2013), 1806–1810.
- [88] A. Ponrouch, R. Dedryvère, D. Monti, A. E. Demet, J. M. A. MBA, L. Croguennec, C. Masquelier, P. Johansson, and M. R. Palacín. “Towards high energy density sodium ion batteries through electrolyte optimization”. *Energy Environ. Sci.* 6 (2013), 2361–2369.
- [89] R. Mohtadi, M. Matsui, T. S. Arthur, and S.-J. Hwang. “Magnesium Borohydride: From Hydrogen Storage to Magnesium Battery”. *Angewandte Chemie* 51 (2012), 9780–9783.
- [90] I. Shterenberg, M. Salama, H. D. Yoo, Y. Gofer, J.-B. Park, Y.-K. Sun, and D. Aurbach. “Evaluation of $(CF_3SO_2)_2N^-$ (TFSI) Based Electrolyte Solutions for Mg Batteries”. *J. Electrochem. Soc.* 162 (2015), A7118–A7128.
- [91] M. Armand, F. Endres, D. R. MacFarlane, H. Ohno, and B. Scrosati. “Ionic-liquid materials for the electrochemical challenges of the future”. *Nat. Mater.* 8 (2009), 621–629.
- [92] T. L. Greaves and C. J. Drummond. “Protic Ionic Liquids: Properties and Applications”. *Chem. Rev.* 108 (2008), 206–237.
- [93] E. W. Castner and J. F. Wishart. “Spotlight on ionic liquids”. *J. Chem. Phys.* 132 (2010), 120901.
- [94] O. Borodin, G. A. Giffin, A. Moretti, J. B. Haskins, J. W. Lawson, W. A. Henderson, and S. Passerini. “Insights into the Structure and Transport of the Lithium, Sodium, Magnesium, and Zinc Bis(trifluoromethansulfonyl)imide Salts in Ionic Liquids”. *J. Phys. Chem. C* 122 (2018), 20108–20121.
- [95] P. J. Fischer, M. P. Do, R. M. Reich, A. Nagasubramanian, M. Srinivasan, and F. E. Kühn. “Synthesis and physicochemical characterization of room temperature ionic liquids and their application in sodium ion batteries”. *Phys. Chem. Chem. Phys.* 20 (2018), 29412–29422.
- [96] G. A. Giffin. “Ionic liquid-based electrolytes for “beyond lithium” battery technologies”. *J. Matter. Chem. A* 4 (2016), 13378–13389.
- [97] S. A. M. Noor, P. C. Howlett, D. R. MacFarlane, and M. Forsyth. “Properties of sodium-based ionic liquid electrolytes for sodium secondary battery applications”. *Electrochim. Acta* 114 (2013), 766–771.
- [98] H. Yoon, H. Zhu, A. Hervault, M. Armand, D. R. MacFarlane, and M. Forsyth. “Physicochemical properties of N-propyl-N-methylpyrrolidinium bis(fluorosulfonyl)imide for sodium metal battery applications”. *Phys. Chem. Chem. Phys.* 16 (2014), 12350–12355.

- [99] C. Ding, T. Nohira, R. Hagiwara, K. Matsumoto, Y. Okamoto, A. Fukunaga, S. Sakai, K. Nitta, and S. Inazawa. “Na[FSA]-[C₃C₁pyrr][FSA] ionic liquids as electrolytes for sodium secondary batteries: Effects of Na ion concentration and operation temperature”. *J. Power Sources* 269 (2014), 124–128.
- [100] K. Matsumoto, Y. Okamoto, T. Nohira, and R. Hagiwara. “Thermal and Transport Properties of Na[N(SO₂F)₂]-[N-Methyl-N-propylpyrrolidinium][N(SO₂F)₂] Ionic Liquids for Na Secondary Batteries”. *J. Phys. Chem. C* 119 (2015), 7648–7655.
- [101] I. Hasa, S. Passerini, and J. Hassoun. “Characteristics of an ionic liquid electrolyte for sodium-ion batteries”. *J. Power Sources* 303 (2016), 203–207.
- [102] M. Forsyth, H. Yoon, F. Chen, H. Zhu, D. R. MacFarlane, M. Armand, and P. C. Howlett. “Novel Na⁺ Ion Diffusion Mechanism in Mixed Organic-Inorganic Ionic Liquid Electrolyte Leading to High Na⁺ Transference Number and Stable, High Rate Electrochemical Cycling of Sodium Cells”. *J. Phys. Chem. C* 120 (2016), 4276–4286.
- [103] D. R. MacFarlane, N. Tachikawa, M. Forsyth, J. M. Pringle, P. C. Howlett, G. D. Elliott, J. H. Davis, M. Watanabe, P. Simon, and C. A. Angell. “Energy applications of ionic liquids”. *Energy Environ. Sci.* 7 (2014), 232–250.
- [104] T. Welton. “Ionic liquids: a brief history”. *Biophysical Reviews* 10 (2018), 691–706.
- [105] C. Ma, A. Laaksonen, C. Liu, X. Lu, and X. Ji. “The peculiar effect of water on ionic liquids and deep eutectic solvents”. *Chem. Soc. Rev.* 47 (2018), 8685–8720.
- [106] J. J. Xu, H. Ye, and J. Huang. “Novel zinc ion conducting polymer gel electrolytes based on ionic liquids”. *Electrochim. Commun.* 7 (2005), 1309–1317.
- [107] M. Kar, B. Winther-Jensen, M. Forsyth, and D. R. MacFarlane. “Exploring zinc coordination in novel zinc battery electrolytes”. *Phys. Chem. Chem. Phys.* 16 (2014), 10816–10822.
- [108] E. Faegh, B. Ng, D. Hayman, and W. E. Mustain. “Practical assessment of the performance of aluminium battery technologies”. *Nature Energy* 6 (2021), 21–29.
- [109] N. Bogolowski and J.-F. Drillet. “Activity of different AlCl₃-based electrolytes for the electrically rechargeable aluminium-air battery”. *Electrochim. Acta* 274 (2018), 353–358.
- [110] Y. Nakayama, Y. Senda, H. Kawasaki, N. Koshitani, S. Hosoi, Y. Kudo, H. Morioka, and M. Nagamine. “Sulfone-based electrolytes for aluminium rechargeable batteries”. *Phys. Chem. Chem. Phys.* 17 (2015), 5758–5766.
- [111] S. H. Lapidus, N. N. Rajput, X. Qu, K. W. Chapman, K. A. Persson, and P. J. Chupas. “Solvation structure and energetics of electrolytes for multivalent energy storage”. *Phys. Chem. Chem. Phys.* 16 (2014), 21941–21945.
- [112] S. Maeda, Y. Kameda, Y. Amo, T. Usuki, K. Ikeda, T. Otomo, M. Yanagisawa, S. Seki, N. Arai, H. Watanabe, and Y. Umebayashi. “Local Structure of Li⁺ in Concentrated Ethylene Carbonate Solutions Studied by Low-Frequency Raman Scattering and Neutron Diffraction with ⁶Li/⁷Li Isotopic Substitution Methods”. *J. Phys. Chem. B* 121 (2017), 10979–10987.
- [113] P. Geysens, V. S. Rangasamy, S. Thayumanasundaram, K. Robeyns, L. V. Meervelt, J.-P. Locquet, J. Fransaer, and K. Binnemans. “Solvation Structure of Sodium Bis(fluorosulfonyl) imide-Glyme Solvate Ionic Liquids and Its Influence on Cycling of Na-MNC Cathodes”. *J. Phys. Chem. B* 122 (2018), 275–289.

- [114] M. Hilder, M. Gras, C. R. Pope, M. Kar, D. R. MacFarlane, M. Forsyth, and L. A. O'Dell. "Effect of mixed anions on the physicochemical properties of a sodium containing alkoxyammonium ionic liquid electrolyte". *Phys. Chem. Chem. Phys.* 19 (2017), 17461–17468.
- [115] M. D. Bhatt and C. O'Dwyer. "Recent progress in theoretical and computational investigations of Li-ion battery materials and electrolytes". *Phys. Chem. Chem. Phys.* 17 (2015), 4799–4844.
- [116] G. Åvall, J. Mindemark, D. Brandell, and P. Johansson. "Sodium-Ion Battery Electrolytes: Modeling and Simulations". *Adv. Energy Mater.* 8 (2018), 1703036.
- [117] M. D. Bhatt, M. Cho, and K. Cho. "Interaction of Li^+ ions with ethylene carbonate (EC): Density functional theory calculations". 257 (2010), 1463–1468.
- [118] M. D. Bhatt, M. Cho, and K. Cho. "Density functional theory calculations and ab initio molecular dynamics simulations for diffusion of Li^+ within liquid ethylene carbonate". *modelling Simul. Mater. Sci. Eng.* 20 (2012), 065004.
- [119] M. D. Bhatt, M. Cho, and K. Cho. "Conduction of Li^+ cations in ethylene carbonate (EC) and propylene carbonate (PC): comparative studies using density functional theory". *J. Solid State Electrochem.* 16 (2012), 435–441.
- [120] T. Li and P. B. Balbuena. "Theoretical Studies of Lithium Perchlorate in Ethylene Carbonate, Propylene Carbonate, and Their Mixtures". *J. Electrochem. Soc.* 146 (1999), 3613.
- [121] J. L. Allen, O. Borodin, D. M. Seo, and W. A. Henderson. "Combined quantum chemical/Raman spectroscopic analyses of Li^+ cation solvation: Cyclic carbonate solvents - Ethylene carbonate and propylene carbonate". *J. Power Sources* 267 (2014), 821–830.
- [122] M. D. Bhatt, M. Cho, and K. Cho. "Density functional theory calculations for the interaction of Li^+ cations and PF_6^- anions with nonaqueous electrolytes". *Can. J. Chem.* 89 (2011), 1525.
- [123] Y. Wang and P. B. Balbuena. "Associations of Lithium Alkyl Dicarbonates through O \cdots Li \cdots O Interactions". *J. Phys. Chem. A* 106 (2002), 9582–9594.
- [124] P. Johansson and P. Jacobsson. "Lithium salt dissociation in non-aqueous electrolytes modeled by ab initio calculations". *Solid State Ionics* 177 (2006), 2691–2697.
- [125] P. Johansson. "Electronic structure calculations on lithium battery electrolyte salts". *Phys. Chem. Chem. Phys.* 9 (2007), 1493–1498.
- [126] A. Eilmes and P. Kubisiak. "Polarizable Continuum Model Study on the Solvent Effect of Polymer Matrix in Poly(ethylene oxide)-based Solid Electrolyte". *J. Phys. Chem. A* 112 (2008), 8849–8857.
- [127] A. Eilmes and P. Kubisiak. "Relative Complexation Energies for Li^+ Ion in Solution: Molecular Level Solvation Versus Polarizable Continuum Model Study". *J. Phys. Chem. A* 114 (2010), 973–979.
- [128] A. Eilmes and P. Kubisiak. "A quantum-chemical study on the boron centers in nonaqueous electrolyte solutions and polymer electrolytes". *Electrochim. Acta* 56 (2011), 3219–3224.
- [129] E. G. Leggesse, R. T. Lin, T.-F. Teng, C.-L. Chen, and J.-C. Jiang. "Oxidative Decomposition of Propylene Carbonate in Lithium Ion Batteries: A DFT Study". *J. Phys. Chem. A* 117 (2013), 7959–7969.

- [130] Y. Wang and P. B. Balbuena. “Theoretical Insights into the Reductive Decompositions of Propylene Carbonate and Vinylene Carbonate: Density Functional Theory Studies”. *J. Phys. Chem. B* 106 (2002), 4486–4495.
- [131] K. Tasaki. “Solvent Decompositions and Physical Properties of Decomposition Compounds in Li-Ion Battery Electrolytes Studied by DFT Calculations and Molecular Dynamics Simulations”. *J. Phys. Chem. B* 109 (2005), 2920–2933.
- [132] P. Johansson, J. Tegenfeldt, and J. Lindgren. “Modelling amorphous lithium salt–PEO polymer electrolytes: ab initio calculations of lithium ion–tetra-, penta- and hexaglyme complexes”. *Polymer* 40 (1999), 4399–4406.
- [133] K. Angenendt and P. Johansson. “Ionic Liquid Structures from Large Density Functional Theory Calculations Using Mindless Configurations”. *J. Phys. Chem. C* 114 (2010), 20577–20582.
- [134] K. Angenendt and P. Johansson. “Ionic Liquid Based Lithium Battery Electrolytes: Charge Carriers and Interactions Derived by Density Functional Theory Calculations”. *J. Phys. Chem. B* 115 (2011), 7808–7813.
- [135] S. Kazemiabnavi, Z. Zhang, K. Thornton, and S. Banerjee. “Electrochemical Stability Window of Imidazolium-Based Ionic Liquids as Electrolytes for Lithium Batteries”. *J. Phys. Chem. B* 120 (2016), 5691–5702.
- [136] W. L. Jorgensen, D. S. Maxwell, and J. Tirado-Rives. “Development and Testing of the OPLS All-Atom Force Field on Conformational Energetics and Properties of Organic Liquids”. *J. Am. Chem. Soc.* 118 (1996), 11225–11236.
- [137] J. N. C. Lopes, J. Deschamps, and A. A. H. Pádua. “Modeling Ionic Liquids Using a Systematic All-Atom Force Field”. *J. Phys. Chem. B* 108 (2004), 2038–2047.
- [138] O. Borodin and G. D. Smith. “Development of Many-Body Polarizable Force Fields for Li-Battery Components: 1. Ether, Alkane, and Carbonate-Based Solvents”. *J. Phys. Chem. B* 110 (2006), 6279–6292.
- [139] O. Borodin and G. D. Smith. “Development of Many-Body Polarizable Force Fields for Li-Battery Components: 2. LiTFSI-Doped Oligoether, Polyether, and Carbonate-Based Electrolytes”. *J. Phys. Chem. B* 110 (2006), 6293–6299.
- [140] D. Bedrov, O. Borodin, Z. Li, and G. D. Smith. “Influence of Polarization on Structural, Thermodynamic, and Dynamic Properties of Ionic Liquids Obtained from Molecular Dynamics Simulations”. *J. Phys. Chem. B* 114 (2010), 4984–4997.
- [141] A. Eilmes and P. Kubisiak. “Quantum-Chemical and Molecular Dynamics Study of M⁺ [TOTO]⁻ (M = Li, Na, K) Ionic Liquids”. *J. Phys. Chem. B* 117 (2013), 12583–12592.
- [142] O. Borodin. “Polarizable Force Field Development and Molecular Dynamics Simulations of Ionic Liquids”. *J. Phys. Chem. B* 113 (2009), 11463–11478.
- [143] G. Lamoureux and B. Roux. “Modeling induced polarization with classical Drude oscillators: Theory and molecular dynamics simulation algorithm”. *J. Chem. Phys.* 119 (2003), 3025–3039.
- [144] K. Goloviznina, J. N. C. Lopes, M. C. Gomes, and A. A. H. Pádua. “Transferable, Polarizable Force Field for Ionic Liquids”. *J. Chem. Theory Comput.* 15 (2019), 5858–5871.
- [145] I. Leontyev and A. Stuchebrukhov. “Accounting for electronic polarization in non-polarizable force fields”. *Phys. Chem. Chem. Phys.* 13 (2011), 2613–2626.
- [146] A. A. Hassanali, J. Cuny, V. Verdolino, and M. Parrinello. “Aqueous solutions: state of the art in ab initio molecular dynamics”. *Phil. Trans. R. Soc. A* 372 (2014), 20120482.

- [147] E. Paquet and H. L. Viktor. “Computational Methods for Ab Initio Molecular Dynamics”. *Advances in Chemistry* 2018 (2018), 9839641.
- [148] E. Bodo. “Perspectives in the Computational Modeling of New Generation, Biocompatible Ionic Liquids”. *J. Phys. Chem. B* 126 (2022), 3–13.
- [149] O. Borodin, G. D. Smith, and P. Fan. “Molecular Dynamics Simulations of Lithium Alkyl Carbonates”. *J. Phys. Chem. B* 110 (2006), 22773–22779.
- [150] S. Shi, P. Lu, Z. Liu, Y. Qi, L. G. Hector, H. Li, and S. J. Harris. “Direct Calculation of Li-Ion Transport in the Solid Electrolyte Interphase”. *J. Am. Chem. Soc.* 134 (2012), 15476–15487.
- [151] O. Borodin and G. D. Smith. “Mechanism of Ion Transport in Amorphous Poly(ethylene oxide)/LiTFSI from Molecular Dynamics Simulations”. *Macromolecules* 39 (2006), 1620–1629.
- [152] J. Chattoraj, D. Diddens, and A. Heuer. “Effects of ionic liquids on cation dynamics in amorphous polyethylene oxide electrolytes”. *J. Chem. Phys.* 140 (2014), 024906.
- [153] L. T. Costa and M. C. C. Ribeiro. “Molecular dynamics simulation of polymer electrolytes based on poly(ethylene oxide) and ionic liquids. II. Dynamical properties”. *J. Chem. Phys.* 127 (2007), 164901.
- [154] A. Eilmes and P. Kubisiak. “Molecular Dynamics Study on the Effect of Lewis Acid Centers in Poly(ethylene oxide)/LiClO₄ Polymer Electrolyte”. *J. Phys. Chem. B* 115 (2011), 14938–14946.
- [155] O. Borodin and G. D. Smith. “Quantum Chemistry and Molecular Dynamics Simulation Study of Dimethyl Carbonate: Ethylene Carbonate Electrolytes Doped with LiPF₆”. *J. Phys. Chem. B* 113 (2009), 1763–1776.
- [156] M. T. Ong, O. Verners, E. W. Draeger, A. C. T. van Duin, V. Lordi, and J. E. Pask. “Lithium Ion Solvation and Diffusion in Bulk Organic Electrolytes from First-Principles and Classical Reactive Molecular Dynamics”. *J. Phys. Chem. B* 119 (2015), 1535–1545.
- [157] I. Skarmoutsos, V. Ponnuchamy, V. Vetere, and S. Mossa. “Li⁺ Solvation in Pure, Binary, and Ternary Mixtures of Organic Carbonate Electrolytes”. *J. Phys. Chem. C* 119 (2015), 4502–4515.
- [158] J. Vatamanu, O. Borodin, and G. D. Smith. “Molecular Dynamics Simulation Studies of the Structure of a Mixed Carbonate/LiPF₆ Electrolyte near Graphite Surface as a Function of Electrode Potential”. *J. Phys. Chem. C* 116 (2012), 1114–1121.
- [159] O. Borodin, M. Olguin, P. Ganesh, P. R. C. Kent, J. L. Allen, and W. A. Henderson. “Competitive lithium solvation of linear and cyclic carbonates from quantum chemistry”. *Phys. Chem. Chem. Phys.* 18 (2016), 164–175.
- [160] H. Liu and E. Maginn. “Effect of ion structure on conductivity in lithium-doped ionic liquid electrolytes: A molecular dynamics study”. *J. Chem. Phys.* 139 (2013), 114508.
- [161] S. V. Sambasivarao and O. Acevedo. “Development of OPLS-AA Force Field Parameters for 68 Unique Ionic Liquids”. *J. Chem. Theory Comput.* 5 (2009), 1038–1050.
- [162] O. Borodin. “Polarizable Force Field Development and Molecular Dynamics Simulations of Ionic Liquids”. *J. Phys. Chem. B* 113 (2009), 11463–11478.
- [163] K. Shimizu, D. Almantariotis, M. F. C. Gomes, A. A. H. Pádua, and J. N. C. Lopes. “Molecular Force Field for Ionic Liquids V: Hydroxyethylimidazolium, Dimethoxy-2-Methylimidazolium, and Fluoroalkylimidazolium Cations and Bis(Fluorosulfonyl)Amide, Perfluoroalkanesulfonylamide, and Fluoroalkylfluorophosphate Anions”. *J. Phys. Chem. B* 114 (2010), 3592–3600.

- [164] M. Salanne. “Simulations of room temperature ionic liquids: from polarizable to coarse-grained force fields”. *Phys. Chem. Chem. Phys.* 17 (2015), 14270–14279.
- [165] J. N. C. Lopes and A. A. H. Pádua. “CL&P: A generic and systematic force field for ionic liquids modeling”. *Theoretical Chemistry Accounts* 131 (2012), 1129.
- [166] B. D. Prince, P. Tiruppathi, R. J. Bemish, Y.-H. Chiu, and E. J. Maginn. “Molecular Dynamics Simulations of 1-Ethyl-3-methylimidazolium Bis[(trifluoromethyl)sulfonyl]imide Clusters and Nanodrops”. *J. Phys. Chem. A* 119 (2015), 352–368.
- [167] A. A. Freitas, K. Shimizu, and J. N. C. Lopes. “Complex Structure of Ionic Liquids. Molecular Dynamics Studies with Different Cation-Anion Combinations”. *J. Chem. Eng. Data* 59 (2014), 3120–3129.
- [168] D. Ruivo, J. N. C. Lopes, F. J. Deive, J. M. S. S. Esperança, L. P. N. Rebelo, A. Rodriguez, and K. Shimizu. “Molecular dynamics studies on the structure and interactions of ionic liquids containing amino-acid anions”. *Phys. Chem. Chem. Phys.* 20 (2018), 23864–23872.
- [169] S. Palchowdhury and B. L. Bhargava. “Ionic Liquids at Nonane-Water Interfaces: Molecular Dynamics Studies”. *J. Phys. Chem. B* 118 (2014), 13930–13939.
- [170] M. Brüssel, M. Brehm, T. Voigt, and B. Kirchner. “Ab initio molecular dynamics simulations of a binary system of ionic liquids”. *Phys. Chem. Chem. Phys.* 13 (2011), 13617–13620.
- [171] A. Mondal and S. Balasubramanian. “Vibrational Signatures of Cation–Anion Hydrogen Bonding in Ionic Liquids: A Periodic Density Functional Theory and Molecular Dynamics Study”. *J. Phys. Chem. B* 119 (2015), 1994–2002.
- [172] P. A. Hunt. “The simulation of imidazolium-based ionic liquids”. *Molecular Simulation* 32 (2005), 1–10.
- [173] S. Zahn, D. R. MacFarlane, and E. I. Izgorodina. “Assessment of Kohn–Sham density functional theory and Møller–Plesset perturbation theory for ionic liquids”. *Phys. Chem. Chem. Phys.* 15 (2013), 13664–13675.
- [174] E. I. Izgorodina, U. L. Bernard, and D. R. MacFarlane. “Ion-Pair Binding Energies of Ionic Liquids: Can DFT Compete with Ab Initio-Based Methods?” *J. Phys. Chem. A* 113 (2009), 7064–7072.
- [175] S. Grimme, J. Antony, S. Ehrlich, and H. Krieg. “A consistent and accurate ab initio parametrization of density functional dispersion correction (DFT-D) for the 94 elements H–Pu”. *J. Chem. Phys.* 132 (2010), 154104.
- [176] S. Grimme, W. Hujo, and B. Kirchner. “Performance of dispersion-corrected density functional theory for the interactions in ionic liquids”. *Phys. Chem. Chem. Phys.* 14 (2012), 4875–4883.
- [177] M. A. Addicoat, R. Stefanovic, G. B. Webber, R. Atkin, and A. J. Page. “Assessment of the Density Functional Tight Binding Method for Protic Ionic Liquids”. *J. Chem. Theory Comput.* 10 (2014), 4633–4643.
- [178] Q. Liu, D. Mu, B. Wu, L. Wang, L. Gai, and F. Wu. “Density Functional Theory Research into the Reduction Mechanism for the Solvent/Additive in a Sodium-Ion Battery”. *ChemSusChem* 10 (2017), 786–796.
- [179] H. Kumar, E. Detsi, D. P. Abraham, and V. B. Shenoy. “Fundamental Mechanisms of Solvent Decomposition Involved in Solid-Electrolyte Interphase Formation in Sodium Ion Batteries”. *Chem. Mater.* 28 (2016), 8930, 8941.

- [180] E. Jónsson and P. Johansson. “Modern battery electrolytes: Ion-ion interactions in Li⁺ / Na⁺ conductors from DFT calculations”. *Phys. Chem. Chem. Phys.* 14 (2012), 10774–10779.
- [181] S. Chen, J. Ishii, S. Horiuchi, M. Yoshizawa-Fujita, and E. I. Izgorodina. “Difference in chemical bonding between lithium and sodium salts: influence of covalency on their solubility”. *Phys. Chem. Chem. Phys.* 19 (2017), 17366–17372.
- [182] A. Bitner-Michalska, G. M. Nolis, G. Żukowska, A. Zalewska, M. Poterała, T. Trzeciak, M. Dranka, M. Kalita, P. Jankowski, L. Niedzicki, J. Zachara, M. Marcinek, and W. Wieczorek. “Fluorine-free electrolytes for all-solid sodium-ion batteries based on percyano-substituted organic salts”. *Scientific Reports* 7 (2017), 40036.
- [183] M. Okoshi, Y. Yamada, S. Komaba, A. Yamada, and H. Nakai. “Theoretical Analysis of Interactions between Potassium Ions and Organic Electrolyte Solvents: A Comparison with Lithium, Sodium, and Magnesium Ions”. *J. Electrochem. Soc.* 164 (2017), A54.
- [184] K. L. Browning, R. L. Sacci, and G. M. Veith. “Energetics of Na⁺ Transport through the Electrode/Cathode Interface in Single Solvent Electrolytes”. *J. Electrochem. Soc.* 164 (2017), A580.
- [185] M. Shakourian-Fard, G. Kamath, K. Smith, H. Xiong, and S. K. R. S. Sankaranarayanan. “Trends in Na-Ion Solvation with Alkyl-Carbonate Electrolytes for Sodium-Ion Batteries: Insights from First-Principles Calculations”. *J. Phys. Chem. C* 119 (2015), 22747–22759.
- [186] S. De, A. Boda, and S. M. Ali. “Preferential interaction of charged alkali metal ions (guest) within a narrow cavity of cyclic crown ethers (neutral host): A quantum chemical investigation”. *J. Molec. Struct.: THEOCHEM* 941 (2010), 90–101.
- [187] S. Terada, T. Mandai, R. Nozawa, K. Yoshida, K. Ueno, S. Tsuzuki, K. Dokko, and M. Watanabe. “Physicochemical properties of pentaglyme-sodium bis(trifluoromethanesulfonyl)amide solvate ionic liquid”. *Phys. Chem. Chem. Phys.* 16 (2014), 11737–11746.
- [188] T. Mandai, K. Yoshida, S. Tsuzuki, R. Nozawa, H. Masu, K. Ueno, K. Dokko, and M. Watanabe. “Effect of Ionic Size on Solvate Stability of Glyme-Based Solvate Ionic Liquids”. *J. Phys. Chem. B* 119 (2015), 1523–1534.
- [189] S. Terada, T. Mandai, S. Suzuki, S. Tsuzuki, K. Watanabe, Y. Kamei, K. Ueno, K. Dokko, and M. Watanabe. “Thermal and Electrochemical Stability of Tetraglyme-Magnesium Bis(trifluoromethanesulfonyl)amide Complex: Electric Field Effect of Divalent Cation on Solvate Stability”. *J. Phys. Chem. C* 120 (2016), 1353–1365.
- [190] S. Terada, H. Susa, S. Tsuzuki, T. Mandai, K. Ueno, Y. Umebayashi, K. Dokko, and M. Watanabe. “Dissociation and Diffusion of Glyme-Sodium Bis(trifluoromethanesulfonyl)amide Complexes in Hydrofluoroether-Based Electrolytes for Sodium Batteries”. *J. Phys. Chem. C* 120 (2016), 23339–23350.
- [191] S. Tsuzuki, T. Mandai, S. Suzuki, W. Shinoda, T. Nakamura, T. Morishita, K. Ueno, S. Seki, Y. Umebayashi, K. Dokko, and M. Watanabe. “Effect of the cation on the stability of cation-glyme complexes and their interactions with the [TFSA]⁻ anion”. *Phys. Chem. Chem. Phys.* 19 (2017), 18262–18272.
- [192] P. Johansson, S. P. Gejji, J. Tegenfeldt, and J. Lindgren. “Local coordination and conformation in polyether electrolytes: Geometries of M-triglyme complexes (M = Li, Na, K, Mg and Ca) from ab-initio molecular orbital calculations”. *Solid State Ionics* 86-88 (1996), 297–302.
- [193] N. R. Dhumal and S. P. Gejji. “Theoretical studies in local coordination and vibrational spectra of M⁺CH₃O(CH₂CH₂O)_nCH₃ (n = 2-7) complexes (M = Na, K, Mg and Ca)”. 323 (2006), 595–605.

- [194] A. Memboeuf, K. Vékey, and G. Lendvay. “Structure and Energetics of Poly(Ethylene Glycol) Cationized by Li⁺, Na⁺, K⁺ and Cs⁺: A First-Principles Study”. *Eur. J. Mass. Spectrom.* 17 (2011), 33–46.
- [195] N. R. Dhumal and S. P. Gejji. “Molecular interactions and vibrations in CH₃(OCH₂CH₂)₂-O-CH₃-M⁺-X⁻ (M = Li, Na, K and X = PF₆, AsF₆, SbF₆): An ab initio study”. *J. Molec. Struct.: THEOCHEM* 859 (2008), 86–92.
- [196] N. R. Dhumal and S. P. Gejji. “Theoretical studies on blue versus red shifts in diglyme-M⁺-X⁻ (M=Li, Na, K and X=BF₄, ClO₄, SCN)”. *J. Molec. Struct.: THEOCHEM* 758 (2006), 233–240.
- [197] T. V. Kaulgud, N. R. Dhumal, and S. P. Gejji. “Electronic Structure and Normal Vibrations of CH₃(OCH₂CH₂)_nOCH₃-M⁺-CF₃SO₃⁻ (n = 2-4, M = Li, Na, and K)”. *J. Phys. Chem. A* 110 (2006), 9231–9239.
- [198] N. R. Dhumal and S. P. Gejji. “Theoretical Studies on Blue versus Red Shifts in Diglyme-M⁺-X⁻ (M=Li, Na, and K and X=CF₃SO₃, PF₆ and (CF₃SO₂)₂N)”. *J. Phys. Chem. A* 110 (2006), 219–227.
- [199] P. Jankowski, J. M. G. L. Lastra, and T. Vegge. “Structure of Magnesium Chloride Complexes in Ethereal Systems: Computational Comparison of THF and Glymes as Solvents for Magnesium Battery Electrolytes”. *Batteries & Supercaps* 3 (2020), 1350–1359.
- [200] N. N. Rajput, X. Qu, N. Sa, A. K. Burrell, and K. A. Persson. “The Coupling between Stability and Ion Pair Formation in Magnesium Electrolytes from First-Principles Quantum Mechanics and Classical Molecular Dynamics”. *J. Am. Chem. Soc.* 137 (2015), 3411–3420.
- [201] T. Kimura, K. Fujii, Y. Sato, M. Morita, and N. Yoshimoto. “Solvation of Magnesium Ion in Triglyme-Based Electrolyte Solutions”. *J. Phys. Chem. C* 119 (2015), 18911–18917.
- [202] A. Baskin and D. Prendergast. “Exploration of the Detailed Conditions for Reductive Stability of Mg(TFSI)₂ in Diglyme: Implications for Multivalent Electrolytes”. *J. Phys. Chem. C* 120 (2016), 3583–3594.
- [203] X. Qu, Y. Zhang, N. N. Rajput, A. Jain, E. Maginn, and K. A. Persson. “Computational Design of New Magnesium Electrolytes with Improved Properties”. *J. Phys. Chem. C* 121 (2017), 16126–16136.
- [204] A. V. Cresce, S. M. Russell, O. Borodin, J. A. Allen, M. A. Schroeder, M. Dai, J. Peng, M. P. Gobet, S. G. Greenbaum, R. E. Rogers, and K. Xu. “Solvation behavior of carbonate-based electrolytes in sodium ion batteries”. *Phys. Chem. Chem. Phys.* 19 (2017), 574–586.
- [205] K. Mukai, T. Inoue, Y. Kato, and S. Shirai. “Superior Low-Temperature Power and Cycle Performances of Na-Ion Battery over Li-Ion Battery”. *ACS Omega* 2 (2017), 864–872.
- [206] T. Mandai, R. Nozawa, K. Tsuzuki, K. Ueno, K. Dokko, and M. Watanabe. “Phase Diagrams and Solvate Structures of Binary Mixtures of Glymes and Na Salts”. *J. Phys. Chem. B* 117 (2013), 15072–15085.
- [207] K. Fujii, M. Sogawa, N. Yoshimoto, and M. Morita. “Structural Study on Magnesium Ion Solvation in Diglyme-Based Electrolytes: IR Spectroscopy and DFT Calculations”. *J. Phys. Chem. B* 122 (2018), 8712–8717.
- [208] G. Kamath, R. W. Cutler, S. A. Deshmukh, M. Shakourian-Fard, R. Parrish, J. Huether, D. P. Butt, H. Xiong, and S. K. R. S. Sankaranarayanan. “In Silico Based Rank-Order Determination and Experiments on Nonaqueous Electrolytes for Sodium Ion Battery Applications”. *J. Phys. Chem. C* 118 (2014), 13406–13416.

- [209] E. Flores, G. Åvall, S. Jeschke, and P. Johansson. “Solvation structure in dilute to highly concentrated electrolytes for lithium-ion and sodium-ion batteries”. *Electrochim. Acta* 233 (2017), 134–141.
- [210] D. Spångberg and K. Hermansson. “The solvation of Li⁺ and Na⁺ in acetonitrile from ab initio-derived many-body solvent potentials”. *Chem. Phys.* 300 (2004), 165–176.
- [211] E. Cabaleiro-Lago and M. A. Ríos. “An intermolecular potential function for Na⁺-acetonitrile obtained from ab initio calculations.: Application to liquid simulations”. *Chem. Phys.* 236 (1998), 235–242.
- [212] L. Troxler and G. Wipff. “Conformation and Dynamics of 18-Crown-6, Cryptand 222 and Their Cation Complexes in Acetonitrile Studied by Molecular Dynamics Simulations”. *J. Am. Chem. Soc.* 116 (1994), 1468–1480.
- [213] M. He, K. C. Lau, X. Ren, N. Xiao, W. D. McCulloch, L. A. Curtiss, and Y. Wu. “Concentrated Electrolyte for the Sodium–Oxygen Battery: Solvation Structure and Improved Cycle Life”. *Angewandte Chemie* 55 (2016), 15310–15314.
- [214] Takenaka N., H. Sakai, Y. Suzuki, P. Uppula, and M. Nagaoka. “A Computational Chemical Insight into Microscopic Additive Effect on Solid Electrolyte Interphase Film Formation in Sodium-Ion Batteries: Suppression of Unstable Film Growth by Intact Fluoroethylene Carbonate”. *J. Phys. Chem. C* 119 (2015), 18046–18055.
- [215] J. M. Vicent-Luna, J. M. Ortiz-Roldan, S. Hamad, R. Tena-Zaera, S. Calero, and J. A. Anta. “Quantum and Classical Molecular Dynamics of Ionic Liquid Electrolytes for Na/Li-based Batteries: Molecular Origins of the Conductivity Behavior”. *ChemPhysChem* 17 (2016), 2473–2481.
- [216] F. Chen and M. Forsyth. “Elucidation of transport mechanism and enhanced alkali ion transference numbers in mixed alkali metal–organic ionic molten salts”. *Phys. Chem. Chem. Phys.* 18 (2016), 19336–19344.
- [217] H. Dong, J.-K. Hyun, C. P. Rhodes, R. Frech, and R. A. Wheeler. “Molecular Dynamics Simulations and Vibrational Spectroscopic Studies of Local Structure in Tetraglyme: Sodium Triflate (CH₃O(CH₂CH₂O)₄CH₃:NaCF₃SO₃) Solutions”. *J. Phys. Chem. B* 106 (2002), 4878–4885.
- [218] A. van Zon, B. Mos, P. Verkerk, and S. W. de Leeuw. “On the dynamics of PEO-NaI polymer electrolytes”. 46 (2001), 1717–1721.
- [219] A. van Zon, G.-J. Bel, B. Mos, P. Verkerk, and S. W. de Leeuw. “Structural relaxation in poly(ethylene oxide)-salt solutions”. *Comput. Mater. Sci.* 17 (2000), 265–268.
- [220] J. J. de Jonge, A. van Zon, and S. W. de Leeuw. “Molecular dynamics study of the influence of the polarizability in PEO_x-NaI polymer electrolyte systems”. 147 (2002), 349–359.
- [221] K.-J. Lin and J. K. Maranas. “Cation Coordination and Motion in a Poly(ethylene oxide)-Based Single Ion Conductor”. *Macromolecules* 45 (2012), 6230–6240.
- [222] K.-J. Lin and J. K. Maranas. “Does increasing ion-ion association improve cation mobility in single ion conductors?” *Phys. Chem. Chem. Phys.* 15 (2013), 16143–16151.
- [223] K.-J. Lin, K. Li, and J. K. Maranas. “Differences between polymer/salt and single ion conductor solid polymer electrolytes”. *RSC Adv.* 3 (2013), 1564–1571.
- [224] K.-J. Lin and J. K. Maranas. “Superionic behavior in polyethylene-oxide-based single-ion conductors”. *Phys. Rev. E* 88 (2013), 052602.

- [225] P. Kubisiak and A. Eilmes. “Solvation of Mg²⁺ Ions in Mg(TFSI)₂-Dimethoxyethane Electrolytes - A View from Molecular Dynamics Simulations”. *J. Phys. Chem. C* 122 (2018), 12615–12622.
- [226] V. Vasudevan, M. Wang, J. A. Yuwono, J. Jasieniak, N. Birbilis, and N. V. Medhekar. “Ion Agglomeration and Transport in MgCl₂-Based Electrolytes for Rechargeable Magnesium Batteries”. *J. Phys. Chem. Lett.* 10 (2019), 7856–7862.
- [227] G. Saielli. “Computational Spectroscopy of Ionic Liquids for Bulk Structure Elucidation”. *Adv. Theory Simul.* 1 (2018), 1800084.
- [228] M. Thomas, M. Brehm, R. Fligg, P. Vöhringer, and B. Kirchner. “Computing vibrational spectra from ab initio molecular dynamics”. *Phys. Chem. Chem. Phys.* 15 (2013), 6608–6622.
- [229] M. Brehm and M. Thomas. “Computing Bulk Phase Resonance Raman Spectra from ab Initio Molecular Dynamics and Real-Time TDDFT”. *J. Chem. Theory Comput.* 15 (2019), 3901–3905.
- [230] A. Aamouche, M. Ghomi, C. Coulombeau, H. Jobic, L. Grajcar, M. Baron, V. Baumruk, P. Y. Turpin, C. Henriet, and G. Berthier. “Neutron Inelastic Scattering, Optical Spectroscopies and Scaled Quantum Mechanical Force Fields for Analyzing the Vibrational Dynamics of Pyrimidine Nucleic Acid Bases. 1. Uracil”. *J. Phys. Chem.* 100 (1996), 5224–5234.
- [231] J. Kiefer, K. Noack, T. C. Penna, M. C. C. Ribeiro, H. Weber, and B. Kirchner. “Vibrational signatures of anionic cyano groups in imidazolium ionic liquids”. *Vib. Spectrosc.* 91 (2017), 141–146.
- [232] M. Brehm and D. Sebastiani. “Simulating structure and dynamics in small droplets of 1-ethyl-3-methylimidazolium acetate”. *J. Chem. Phys.* 148 (2018), 193802.
- [233] M. Campetella, A. L. Donne, M. Daniele, L. Gontrani, S. Lupi, E. Bodo, and F. Leonelli. “Hydrogen Bonding Features in Cholinium-Based Protic Ionic Liquids from Molecular Dynamics Simulations”. *J. Phys. Chem. B* 122 (2018), 2635–2645.
- [234] L. M. L. Daku. “Spin-state dependence of the structural and vibrational properties of solvated iron(II) polypyridyl complexes from AIMD simulations: aqueous [Fe(bpy)₃]Cl₂, a case study”. *Phys. Chem. Chem. Phys.* 20 (2018), 6236–6253.
- [235] S. A. Fischer, T. W. Ueltschi, P. Z. El-Khoury, A. L. Mifflin, W. P. Hess, H.-F. Wang, C. J. Cramer, and N. Govind. “Infrared and Raman Spectroscopy from Ab Initio Molecular Dynamics and Static Normal Mode Analysis: The C-H Region of DMSO as a Case Study”. *J. Phys. Chem. B* 120 (2016), 1429–1436.
- [236] F. Yan, K. Mukherjee, M. Maroncelli, and H. J. Kim. “Infrared Spectroscopy of Li⁺ Solvation in EmimBF₄ and in Propylene Carbonate: Ab Initio Molecular Dynamics and Experiment”. *J. Phys. Chem. B* 126 (2022), 9643–9662.
- [237] W. Andreoni and A. Curioni. “New advances in chemistry and materials science with CPMD and parallel computing”. *Parallel Computing* 26 (2000), 819–842.
- [238] B. L. Bhargava and S. Balasubramanian. “Insights into the Structure and Dynamics of a Room-Temperature Ionic Liquid: Ab Initio Molecular Dynamics Simulation Studies of 1-n-Butyl-3-methylimidazolium Hexafluorophosphate ([bmim][PF₆]) and the [bmim][PF₆]-CO₂ Mixture”. *J. Phys. Chem. B* 111 (2007), 4477–4487.
- [239] E. Bodo, A. Sferrazza, R. Caminiti, S. Mangialardo, and P. Postorino. “A prototypical ionic liquid explored by ab initio molecular dynamics and Raman spectroscopy”. *J. Chem. Phys.* 139 (2013), 144309.

- [240] T. Zentel, V. Overbeck, D. Michalik, O. Kühn, and R. Ludwig. “Hydrogen bonding in protic ionic liquids: structural correlations, vibrational spectroscopy, and rotational dynamics of liquid ethylammonium nitrate”. *J. Phys. B At. Mol. Opt. Phys.* 51 (2018), 034002.
- [241] A. W. Sakti, S. T. Wahyudi, F. Ahmad, N. Darmawan, H. Hardhienata, and H. Alatas. “Effects of Salt Concentration on the Water and Ion Self-Diffusion Coefficients of a Model Aqueous Sodium-Ion Battery Electrolyte”. *J. Phys. Chem. B* 126 (2022), 2256–2264.
- [242] R. F. Nalewajski. *Perspectives in Electronic Structure Theory*. Springer, 2012, pp. 125–130, 258–266, 280–284, 312–319.
- [243] F. Jensen. *Introduction to Computational Chemistry*. John Wiley & Sons, Ltd, 2007, pp. 24–62, 451–460.
- [244] A. K. Rappe, C. J. Casewit, K. S. Colwell, W. A. Goddard III, and W. M. Skiff. “UFF, a full periodic table force field for molecular mechanics and molecular dynamics simulations”. *J. Am. Chem. Soc.* 114 (1992), 10024–10035.
- [245] J. A. Rackers, M. L. Laury, C. Lu, Z. Wang, L. Lagard‘ere, J.-P. Piquemal, P. Ren, and J. W. Ponder. *TINKER 8: A Modular Software Package for Molecular Design and Simulation*. 2017.
- [246] J. C. Phillips, R. Braun, W. Wang, J. Gumbart, E. Tajkhorshid, E. Villa, C. Chipot, R. D. Skeel, L. Kale, and K. Schulten. “Scalable Molecular Dynamics with NAMD”. *J. Comp. Chem.* 26 (2005), 1781–1802.
- [247] M. J. Abraham, T. Murtola, R. Schulz, S. Páll, J. C. Smith, B. Hess, and E. Lindahl. “GROMACS: High performance molecular simulations through multi-level parallelism from laptops to supercomputers”. *SoftwareX* (2015), 19–25.
- [248] D.A. Case, H.M. Aktulga, K. Belfon, I.Y. Ben-Shalom, J.T. Berryman, S. R. Brozell, D. S. Cerutti, T. E. Cheatham III, G. A. Cisneros, V. W. D. Cruzeiro, T. A. Darden, N. Forouzesh, G. Giambaşu, T. Giese, M. K. Gilson, H. Gohlke, A. W. Goetz, J. Harris, S. Izadi, et al. *Amber 2023*. University of California, San Francisco, 2023.
- [249] B. R. Brooks, C. L. Brooks III, A. D. Mackerell Jr., L. Nilsson, R. J. Petrella, B. Roux, Y. Won, G. Archontis, C. Bartels, S. Boresch, A. Caflisch, L. Caves, Q. Cui, A. R. Dinner, M. Feig, S. Fischer, J. Gao, M. Hodoscek, W. Im, et al. “CHARMM: The biomolecular simulation program”. *J. Comp. Chem.* 30 (2009), 1545–1614.
- [250] A. P. Thompson and H. M. Aktulga. “LAMMPS - a flexible simulation tool for particle-based materials modeling at the atomic, meso, and continuum scales”. *Comp. Phys. Comm.* 271 (2022), 108171.
- [251] D. Marx and J. Hutter. *Ab Initio Molecular Dynamics*. Cambridge University Press, 2009, pp. 24–51, 85–89, 179–183.
- [252] J. Hutter and M. Iannuzzi. “CPMD: Car-Parinello molecular dynamics”. *Zeitschrift für Kristallographie - Crystalline Materials* 220 (2005), 549–551.
- [253] Thomas D. Kühne, Marcella Iannuzzi, Mauro Del Ben, Vladimir V. Rybkin, Patrick Seewald, Frederick Stein, Teodoro Laino, Rustam Z. Khalilullin, Ole Schütt, Florian Schiffmann, Dorothea Golze, Jan Wilhelm, Sergey Chulkov, Mohammad Hossein Bani-Hashemian, Valéry Weber, Urban Boršnik, Mathieu Taillefumier, Alice Shoshana Jakobovits, Alfio Lazzaro, et al. “CP2K: An electronic structure and molecular dynamics software package - Quickstep: Efficient and accurate electronic structure calculations”. *J. Chem. Phys.* 152 (2020), 194103.

- [254] P. Giannozzi, S. Baroni, N. Bonini, M. Calandra, R. Car, C. Cavazzoni, D. Ceresoli, G. L. Chiarotti, M. Cococcioni, and I. Dabo. “QUANTUM ESPRESSO: a modular and open-source software project for quantum simulations of materials”. *J. Phys.: Condens. Matter* 21 (2009), 395502.
- [255] P. Giannozzi, O. Andreussi, T. Brumme, O. Bunau, M. B. Nardelli, M. Calandra, R. Car, C. Cavazzoni, D. Ceresoli, and M. Cococcioni. “Advanced capabilities for materials modelling with Quantum ESPRESSO”. *J. Phys.: Condens. Matter* 29 (2017), 465901.
- [256] S. Goedecker, M. Terer, and J. Hutter. “Separable dual-space Gaussian pseudopotentials”. *Phys. Rev. B* 54 (1996), 1703.
- [257] C. Hartwigsen, S. Goedecker, and J. Hutter. “Relativistic separable dual-space Gaussian pseudopotentials from H to Rn”. *Phys. Rev. B* 58 (1998), 3641.
- [258] M. Krack. “Pseudopotentials for H to Kr optimized for gradient-corrected exchange-correlation functionals”. *Theor. Chem. Acc.* 114 (2005), 145–152.
- [259] J. P. Perdew, K. Burke, and M. Ernzerhof. “Generalized Gradient Approximation Made Simple”. *Phys. Rev. Lett.* 78 (1996), 1396.
- [260] J. P. Perdew, K. Burke, and Y. Wang. “Generalized gradient approximation for the exchange-correlation hole of a many-electron system”. *Phys. Rev. B* 54 (1996), 16533.
- [261] J. P. Perdew, M. Ernzerhof, and K. Burke. “Rationale for mixing exact exchange with density functional approximations”. *J. Chem. Phys.* 105 (1996), 9982–9985.
- [262] K. Burke, M. Ernzerhof, and J. P. Perdew. “The adiabatic connection method: a non-empirical hybrid”. *Chem. Phys. Lett.* 265 (1997), 115–120.
- [263] L. Piela. *Idee chemii kwantowej*. PWN, 2011, pp. 378–383.
- [264] W. G. Hoover. “Canonical dynamics: Equilibrium phase-space distributions”. *Phys. Rev. A* 31 (1985), 1695–1697.
- [265] S. Nosé. “A unified formulation of the constant temperature molecular dynamics methods”. *J. Chem. Phys.* 81 (1984), 511–519.
- [266] S. Nosé. “A molecular dynamics method for simulations in the canonical ensemble”. *Mol. Phys.* 52 (1984), 255–268.
- [267] T. Hirakawa, T. Suzuki, D. R. Bowler, and T. Miyazaki. “Canonical-ensemble extended Lagrangian Born–Oppenheimer molecular dynamics for the linear scaling density functional theory”. *J. Phys.: Condens. Matter* 29 (2017), 405901.
- [268] G. J. Martyna, M. L. Klein, and M. Tuckerman. “Nosé–Hoover chains: The canonical ensemble via continuous dynamics”. 97 (1992), 2635–2643.
- [269] G. J. Martyna, M. E. Tuckerman, D. J. Tobias, and M. L. Klein. “Explicit reversible integrators for extended systems dynamics”. *Mol. Phys.* 87 (1996), 1117–1157.
- [270] D. A. McQuarrie. *Statistical Mechanics*. Harper&Row, 1976, pp. 257–260.
- [271] B. G. Levine, J. E. Stone, and A. Kohlmeyer. “Fast analysis of molecular dynamics trajectories with graphics processing units—Radial distribution function histogramming”. *J. Comput. Phys.* 230 (2011), 3556–3569.
- [272] M. Brehm, M. Thomas, S. Gehrke, and B. Kirchner. “TRAVIS - A free analyzer for trajectories from molecular simulation”. *J. Chem. Phys.* 152 (2020), 164105.
- [273] M. Brehm and B. Kirchner. “TRAVIS - A Free Analyzer and Visualizer for Monte Carlo and Molecular Dynamics Trajectories”. *J. Chem. Inf. Model.* 51 (2011), 2007–2023.

- [274] B. Guillot. “A molecular dynamics study of the far infrared spectrum of liquid water”. *J. Chem. Phys.* 95 (1991), 1543–1551.
- [275] R. G. Gordon. “Molecular Motion in Infrared and Raman Spectra”. *J. Chem. Phys.* 43 (1965), 1307–1312.
- [276] R. Ramírez, T. López-Ciudad, P. Kumar P, and D. Marx. “Quantum corrections to classical time-correlation functions: Hydrogen bonding and anharmonic floppy modes”. *J. Chem. Phys.* 121 (2004), 3973–3983.
- [277] C. P. Lawrence, A. Nakayama, N. Makri, and J. L. Skinner. “Quantum dynamics in simple fluids”. *J. Chem. Phys.* 120 (2004), 6621–6624.
- [278] N. Marzari, A. A. Mostofi, J. R. Yates, I. Souza, and D. Vanderbilt. “Maximally localized Wannier functions: Theory and applications”. *Rev. Mod. Phys.* 84 (2012), 1419.
- [279] P. Hohenberg and W. Kohn. “Density functional theory (DFT)”. *Phys. Rev. A* 136 (1964), 864–871.
- [280] A. D. Becke. “A new mixing of Hartree–Fock and local density-functional theories”. *J. Chem. Phys.* 98 (1993), 1372–1377.
- [281] A. D. Becke. “Density-functional thermochemistry. IV. A new dynamical correlation functional and implications for exact-exchange mixing”. *J. Chem. Phys.* 104 (1996), 1040–1046.
- [282] A. D. Becke. “Density-functional thermochemistry. V. Systematic optimization of exchange-correlation functionals”. *J. Chem. Phys.* 107 (1997), 8554–8560.
- [283] M. Ernzerhof. “Construction of the adiabatic connection”. *Chem. Phys. Lett.* 263 (1996), 499–506.
- [284] P. Koskinen and V. Mäkinen. “Density-functional tight-binding for beginners”. *Comput. Mat. Sci.* 47 (2009), 237–253.
- [285] W. Matthew, C. Foulkes, and R. Haydock. “Tight-binding models and density-functional theory”. *Phys. Rev. B* 39 (1989), 12520–12536.
- [286] T. Frauenheim, G. Seifert, M. Elstner, T. Niehaus, C. Köhler, M. Amkreutz, M. Sternberg, Z. Hajnal, A. Di Carlo, and S. Suhai. “Atomistic simulations of complex materials: ground-state and excited-state properties”. *J. Phys. Condens. Matter* 14 (2002), 3015–3047.
- [287] M. Elstner, D. Porezag, G. Jungnickel, J. Elsner, M. Haugk, T. Frauenheim, S. Suhai, and G. Seifert. “Self-consistent-charge density-functional tight-binding method for simulations of complex materials properties”. *Phys. Rev. B* 58 (1998), 7260.
- [288] M. Gaus, Q. Cui, and M. Elstner. “DFTB3: Extension of the Self-Consistent-Charge Density-Functional Tight-Binding Method (SCC-DFTB)”. *J. Chem. Theory Comput.* 7 (2011), 931–948.
- [289] B. Hourahine, B. Aradi, V. Blum, F. Bonafé, A. Buccheri, C. Camacho, C. Cevallos, M. Y. Deshaye, T. Dumitrică, A. Dominguez, S. Ehlert, M. Elstner, T. van der Heide, J. Hermann, S. Irle, J. J. Kranz, C. Köhler, T. Kowalczyk, T. Kubář, et al. “DFTB+, a software package for efficient approximate density functional theory based atomistic simulations”. *J. Chem. Phys.* 152 (2020), 124101.
- [290] M. Gaus, A. Goez, and M. Elstner. “Parametrization and Benchmark of DFTB3 for Organic Molecules”. *J. Chem. Theory Comput.* 9 (2013), 338–354.
- [291] M. Gaus, X. Lu, M. Elstner, and Q. Cui. “Parameterization of DFTB3/3OB for Sulfur and Phosphorus for Chemical and Biological Applications”. *J. Chem. Theory Comput.* 10 (2014), 1518–1537.

- [292] X. Lu, M. Gaus, M. Elstner, and Q. Cui. “Parametrization of DFTB3/3OB for Magnesium and Zinc for Chemical and Biological Applications”. *J. Phys. Chem. B* 119 (2015), 1062–1082.
- [293] M. Kubillus, T. Kubař, M. Gaus, J. Řezáč, and M. Elstner. “Parameterization of the DFTB3 Method for Br, Ca, Cl, F, I, K, and Na in Organic and Biological Systems”. *J. Chem. Theory Comput.* 11 (2015), 332–342.
- [294] V. Q. Vuong, J. A. Kuriappan, M. Kubillus, J. J. Kranz, T. Mast, T. A. Niehaus, S. Irle, and M. Elstner. “Parametrization and Benchmark of Long-Range Corrected DFTB2 for Organic Molecules”. *J. Chem. Theory Comput.* 14 (2018), 115–125.
- [295] M. Elstner, D. Porezag, G. Jungnickel, J. Elsner, M. Haugk, T. Frauenheim, S. Suhai, and G. Seifert. “Self-consistent-charge density-functional tight-binding method for simulations of complex materials properties”. *Phys. Rev. B* 58 (1998), 7260–7268.
- [296] B. Lukose, A. Kuc, J. Frenzel, and T. Heine. “On the reticular construction concept of covalent organic frameworks”. *Bellstein J. Nanotechnol.* (2010), 60–70.
- [297] M. P. Lourenço, E. C. dos Santos, L. G. Pettersson, and H. A. Duarte. “Accurate SCC-DFTB Parametrization for Bulk Water”. *J. Chem. Theory Comput.* 16 (2020), 1768–1778.
- [298] S. Grimme, C. Bannwarth, and P. Shushkov. “A Robust and Accurate Tight-Binding Quantum Chemical Method for Structures, Vibrational Frequencies, and Noncovalent Interactions of Large Molecular Systems Parametrized for All spd-Block Elements ($Z = 1\text{--}86$)”. *J. Chem. Theory Comput.* 13 (2017), 1989–2009.
- [299] C. Bannwarth, S. Ehlert, and S. Grimme. “GFN2-xTB—An Accurate and Broadly Parametrized Self-Consistent Tight-Binding Quantum Chemical Method with Multipole Electrostatics and Density-Dependent Dispersion Contributions”. 15 (2019), 1652–1671.
- [300] V. Ásgeirsson, C. A. Bauer, and S. Grimme. “Quantum chemical calculation of electron ionization mass spectra for general organic and inorganic molecules”. *Chem. Sci.* 8 (2017), 4879–4895.
- [301] A. Géron. *Uczanie maszynowe z użyciem Scikit-Learn i TensorFlow*. Helion S.A., 2020, pp. 27–48, 283–372.
- [302] T. M. Mitchell. *Machine Learning*. McGraw-Hill Science/Engineering/Math, 1997, pp. 1–20.
- [303] C. M. Bishop. *Pattern Recognition and Machine Learning*. Springer, 2006, pp. 225–290.
- [304] F. Noé, A. Tkatchenko, K.-R. Müller, and C. Clementi. “Machine Learning for Molecular Simulation”. *Annu. Rev. Phys. Chem.* 71 (2020), 361–390.
- [305] I. I. Baskin, D. Winkler, and I. V. Tetko. “A renaissance of neural networks in drug discovery”. *Expert Opin. Drug Discov.* 11 (2016), 785–795.
- [306] Z. Fan, Y. Wang, P. Ying, K. Song, J. Wang, Y. Wang, Z. Zeng, K. Xu, E. Lindgren, J. M. Rahm, A. J. Gabourie, J. Liu, H. Dong, J. Wu, Y. Chen, Z. Zhong, J. Sun, P. Erhart, Y. Su, and T. Ala-Nissila. “GPUMD: A package for constructing accurate machine-learned potentials and performing highly efficient atomistic simulations”. *J. Chem. Phys.* 157 (2022), 114801.
- [307] H. Wang, L. Zhang, J. Han, and W. E. “DeePMD-kit: A deep learning package for many-body potential energy representation and molecular dynamics”. *Comput. Phys. Commun.* 228 (2018), 178–184.

- [308] K. T. Schütt, M. Gastegger, K. A. Nicoli, A. Tkatchenko, and K.-R. Müller. "SchNetPack: A Deep Learning Toolbox For Atomistic Systems". *J. Chem. Theory Comput.* 15 (2019), 448–455.
- [309] M. J. Frisch, G. W. Trucks, H. B. Schlegel, G. E. Scuseria, M. A. Robb, J. R. Cheeseman, G. Scalmani, V. Barone, B. Mennucci, and G. A. Peterson. *Gaussian 09*. Gaussian, Inc., Wallingford CT, 2009.
- [310] L. Martínez, R. Andrade, E. G. Birgin, and J. M. Martínez. "PACKMOL: A package for building initial configurations for molecular dynamics simulations". *J. Comput. Chem.* 30 (2009), 2157–2164.
- [311] T. Köddermann, D. Paschek, and R. Ludwig. "Molecular Dynamic Simulations of Ionic Liquids: A Reliable Description of Structure, Thermodynamics and Dynamics". *Chem-PhysChem* 8 (2007), 2464–2470.
- [312] T. Darden, D. York, and L. Pedersen. "Particle Mesh Ewald: An Nlog(N) Method for Ewald Sums in Large Systems". *J. Chem. Phys.* 98 (1993), 10089–10092.
- [313] S. E. Feller, Y. Zhang, R. W. Pastor, and B. R. Brooks. "Constant Pressure Molecular Dynamics Simulation: The Langevin Piston Method". 103 (1995), 4613–4621.
- [314] G. J. Martyna, D. J. Tobias, and M. L. Klein. "Constant Pressure Molecular Dynamics Algorithms". *J. Chem. Phys.* 101 (1994), 4177–4189.
- [315] H. Forbert and A. Kohlmeyer. *Fourier: Power Spectrum of Autocorrelation Function*.
- [316] P. Wróbel. "Master Thesis: Badania oddziaływań jon metalu-rozpuszczalnik w elektroli-tach dla ogniw jonowych metodami dynamiki molekularnej klasycznej i ab initio" (2018).
- [317] K. Fujii, H. Hamano, H. Doi, X. Song, S. Tsuzuki, K. Hayamizu, S. Seki, Y. Kameda, K. Dokko, M. Watanabe, and Y. Umebayashi. "Unusual Li⁺ Ion Solvation Structure in Bis(fluorosulfonyl)amide Based Ionic Liquid". *J. Phys. Chem. C* 117 (2013), 19314–19324.
- [318] M. Gouverneur, F. Schmidt, and M. Schönhoff. "Negative Effective Li Transference Numbers in Li Salt/Ionic Liquid Mixtures: Does Li Drift in the "Wrong" Direction?" *Phys. Chem. Chem. Phys.* 20 (2018), 7470–7478.
- [319] D. Dong, F. Sälzer, B. Roling, and D. Bedrov. "How Efficient is Li⁺ Ion Transport in Solvate Ionic Liquids under Anion-blocking Conditions in a Battery?" *Phys. Chem. Chem. Phys.* 20 (2018), 29174–29183.
- [320] F. Schmidt and M. Schönhoff. "Solvate Cation Migration and Ion Correlations in Solvate Ionic Liquids". *J. Phys. Chem. B* 124 (2020), 1245–1252.
- [321] K. Shigenobu, K. Dokko, M. Watanabe, and K. Ueno. "Solvent Effects on Li Ion Transference Number and Dynamic Ion Correlations in Glyme- and Sulfolane-based Molten Li Salt Solvates". *Phys. Chem. Chem. Phys.* 22 (2020), 15214–15221.
- [322] S. Pfeifer, F. Ackermann, F. Sälzer, M. Schönhoff, and B. Roling. "Quantification of Cation-Cation, Anion-Anion and Cation-Anion Correlations in Li Salt/Glyme Mixtures by Combining Very-Low-Frequency Impedance Spectroscopy with Diffusion and Elec-trophoretic NMR". *Phys. Chem. Chem. Phys.* 23 (2021), 628–640.
- [323] K. Oldiges, D. Diddens, M. Ebrahiminia, J. B. Hooper, I. Cekic-Laskovic, A. Heuer, D. Bedrov, M. Winter, and G. Brunklaus. "Understanding transport mechanisms in ionic liquid/carbonate solvent electrolyte blends". *Phys. Chem. Chem. Phys.* 20 (2018), 16579–16591.
- [324] P. Kubisiak and A. Eilmes. "Molecular Dynamics Simulations of Ionic Liquid Based Elec-trolytes for Na-Ion Batteries: Effects of Force Field". *J. Phys. Chem. B* 121 (2017), 9957–9968.

- [325] N. Molinari, J. P. Mailoa, and B. Kozinsky. “General Trend of a Negative Li Effective Charge in Ionic Liquid Electrolytes”. *J. Phys. Chem. Lett.* 10 (2019), 2313–2319.
- [326] N. Molinari, J. P. Mailoa, N. Craig, J. Christensen, and B. Kozinsky. “Transport anomalies emerging from strong correlation in ionic liquid electrolytes”. *J. Power Sources* 428 (2019), 27–36.
- [327] S.-Y. Ha, Y.-W. Lee, S. W. Woo, B. Koo, J.-S. Kim, J. Cho, K. T. Lee, and N.-S. Choi. “Magnesium(II) Bis(trifluoromethane sulfonyl) Imide-Based Electrolytes with Wide Electrochemical Windows fo Rechargeable Magnesium Batteries”. *ACS Appl. Mater. Interfaces* 6 (2014), 4063–4073.
- [328] Y. Cheng, R. M. Stolley, K. S. Han, Y. Shao, B. W. Arey, N. M. Washton, K. T. Mueller, M. L. Helm, V. L. Sprenkle, J. Liu, and G. Li. “Highly active electrolytes for rechargeable Mg batteries based on a $[\text{Mg}_2(\mu\text{-Cl})_2]^{2+}$ cation complex in dimethoxyethane”. *Phys. Chem. Chem. Phys.* 17 (2015), 13307–13314.
- [329] M. Salama, I. Shterenberg, H. Gizbar, N. N. Eliaz, M. Kosa, K. Keinan-Adamsky, M. Afir, L. J. W. Shimon, H. E. Gottlieb, D. T. Major, Y. Gofer, and D. Aurbach. “Unique Behavior of Dimethoxyethane (DME) / $\text{Mg}(\text{N}(\text{SO}_2\text{CF}_3)_2)_2$ Solutions”. *J. Phys. Chem. C* 120 (2016), 19586–19594.
- [330] S. He, J. Luo, and T. L. Liu. “ $\text{MgCl}_2/\text{AlCl}_3$ electrolytes for reversible Mg deposition/stripping: electrochemical conditioning or not?” *J. Mater. Chem. A* 5 (2017), 12718–12722.
- [331] K. Shimokawa, H. Matsumoto, and T. Ichitsubo. “Solvation-Structure Modification by Concentrating $\text{Mg}(\text{TFSA})_2$ - MgCl_2 - Triglyme Ternary Electrolyte”. *J. Phys. Chem. Lett.* 9 (2018), 4732–4737.
- [332] M. Salama, I. Shterenberg, L. J. W. Shimon, K. Keinan-Adamsky, M. Afri, Y. Gofer, and D. Aurbach. “Structural Analysis of Magnesium Chloride Complexes in Dimethoxyethane Solutions in the Context of Mg Batteries Research”. *J. Phys. Chem. C* 121 (2017), 24909–24918.
- [333] J. Tomasi, B. Mennucci, and E. Cancès. “The IEF version of the PCM solvation method: an overview of a new method addressed to study molecular solutes at the QM ab initio level”. *J. Molec. Struct.: THEOCHEM* 464 (1999), 211–226.
- [334] A. Eilmes. “ Li^+ binding to fluorinated carbonate solvents studied by ab initio quantum chemical calculations”. *J. Mol. Liq.* 224 (2016), 452–459.
- [335] T. Stattner, P. Huang, M. Goktas, P. Adelhelm, and A. Balducci. “Mixtures of glyme and aprotic-protic ionic liquids as electrolytes for energy storage devices”. *J. Chem. Phys.* 148 (2018), 193825.
- [336] K. Westman, R. Dugas, P. Jankowski, W. Wieczorek, G. Gachot, M. Morcrette, E. Irisarri, A. Ponrouch, M. R. Palacín, J.-M. Tarascon, and P. Johansson. “Diglyme Based Electrolytes for Sodium-Ion Batteries”. *ACS Appl. Energy Mater.* 1 (2018), 2671–2680.
- [337] M. Goktas, C. Bolli, J. Buchheim, E. J. Berg, P. Novák, F. Bonilla, T. Rojo, S. Komaba, K. Kubota, and P. Adelhelm. “Stable and Unstable Diglyme-Based Electrolytes for Batteries with Sodium or Graphite as Electrode”. *ACS Appl. Mater. Interfaces* 11 (2019), 32844–32855.
- [338] S. Terada, H. Susa, S. Tsuzuki, T. Mandai, K. Ueno, K. Dokko, and M. Watanabe. “Glyme-Sodium Bis(fluorosulfonyl)amide Complex Electrolytes for Sodium Ion Batteries”. *J. Phys. Chem. C* 122 (2018), 16589–16599.
- [339] S. R. G. Kankanamge, K. Li, K. D. Fulfer, P. Du, R. Jorn, R. Kumar, and D. G. Kuroda. “Mechanism behind the Unusually High Conductivities of High Concentrated Sodium Ion Glyme-Based Electrolytes”. *J. Phys. Chem. C* 122 (2018), 25237–25246.

- [340] T. P. Liyana-Arachchi, J. B. Haskins, C. M. Burke, K. M. Diederichsen, B. D. McCloskey, and J. W. Lawson. “Polarizable Molecular Dynamics and Experiments of 1,2-Dimethoxyethane Electrolytes with Lithium and Sodium Salts: Structure and Transport Properties”. *J. Phys. Chem. B* 122 (2018), 8548–8559.
- [341] A. Boschin and P. Johansson. “Plasticization of NaX-PEO solid polymer electrolytes by Pyr₁₃X ionic liquids”. *Electrochim. Acta* 211 (2016), 1006–1015.
- [342] Poland FQS Poland Ltd.: Kraków. *SCIGRESS*. URL: <https://www.fqs.pl/en/chemistry/products/scigress>.
- [343] D. Monti, E. Jónsson, A. Boschin, M. R. Palacín, A. Ponrouch, and P. Johansson. “Towards Standard Electrolytes for Sodium-Ion Batteries: Physical Properties, Ion Solvation and Ion-Pairing in Alkyl Carbonate Solvents”. *Phys. Chem. Chem. Phys.* 22 (2020), 22768–22777.
- [344] D. Monti, A. Ponrouch, M. R. Palacín, and P. Johansson. “Towards Safer Sodoum-Ion Batteries via Organic Solvent/Ionic Liquid Based Hybrid Electrolytes”. *J. Power Sources* 324 (2016), 712–721.
- [345] P. A. Hunt, C. R. Ashworth, and R. P. Matthews. “Hydrogen Bonding in Ionic Liquids”. *Chem. Soc. Rev.* 44 (2015), 1257–1288.
- [346] Y.-L. Wang, B. Li, S. Sarman, F. Mocci, Z.-Y. Lu, J. Yuan, A. Laaksonen, and M. D. Fayer. “Microstructural and Dynamical Heterogeneities in Ionic Liquids”. *Chem. Rev.* 120 (2020), 5798–5877.
- [347] H. Abe. “Phase Variety in Ionic Liquids: Hydrogen Bonding and Molecular Conformations”. *J. Mol. Liq.* 332 (2021), 115189.
- [348] K. R. Seddon, A. Stark, and M. J. Torres. “Influence of Chloride, Water and Organic Solvents on the Physical Properties of Ionic Liquids”. *Pure Appl. Chem.* 72 (2000), 2275–2287.
- [349] M. Moreno, F. Castiglione, A. Mele, C. Pasqui, and G. Raos. “Interaction of Water with the Model Ionic Liquid [bmim][BF₄]: Molecular Dynamics Simulations and Comparison with NMR Data”. *J. Phys. Chem. B* 112 (2008), 7826–7836.
- [350] X. Zhong, Z. Fan, Z. Liu, and D. Cao. “ocal Structure Evolution and its Connection to Thermodynamic and Transport Properties of 1- Butyl-3-methylimidazolium Tetrafluoroborate and Water Mixtures by Molecular Dynamics Simulations”. *J. Phys. Chem. B* 116 (2012), 3249–3263.
- [351] V. L. Martins, B. G. Nicolau, S. M. Urahata, M. C. C. Ribeiro, and R. M. Torresi. “Influence of the Water Content on the Structure and Physicochemical Properties of an Ionic Liquid and Its Li⁺ Mixture”. *J. Phys. Chem. B* 117 (2013), 8782–8792.
- [352] K. Dziubinska-Kühn, J. Croese, M. Pupier, J. Matysik, J. Viger-Gravel, B. Karg, and M. Kowalska. “Structural Analysis of Water in Ionic Liquid Domains - A Low Pressure Study”. *J. Mol. Liq.* 334 (2021), 116447.
- [353] M. Z. Brela, P. Kubisiak, and A. Eilmes. “Understanding the Structure of the Hydrogen Bond Network and Its Influence on Vibrational Spectra in a Prototypical Aprotic Ionic Liquid”. *J. Phys. Chem. B* 122 (2018), 9527–9537.
- [354] J. E. Bertie and Z. Lan. “Infrared Intensities of Liquids XX: The Intensity of the OH Stretching Band of Liquid Water Revisited, and the Best Current Values of the Optical Constants of H₂O(l) at 25°C between 15,000 and 1 cm⁻¹”. *Appl. Spectrosc.* 50 (1996), 1047–1057.

- [355] N. R. Dhumal, K. Noack, J. Kiefer, and H. J. Kim. “Molecular Structure and Interactions in the Ionic Liquid 1-Ethyl-3-methylimidazolium Bis(Trifluoromethylsulfonyl)imide”. *J. Phys. Chem. A* 118 (2014), 2547–2557.
- [356] N. Yaghini, J. Pitawala, A. Matic, and A. Martinelli. “Effect of Water on the Local Structure and Phase Behavior of Imidazolium-Based Protic Ionic Liquids”. *J. Phys. Chem. B* 119 (2015), 1611–1622.
- [357] S. Taherivardanjani, R. Elfgen, W. Reckien, E. Suarez, E. Perlt, and B. Kirchner. “Benchmarking the Computational Costs and Quality of Vibrational Spectra from Ab Initio Simulations”. *Adv. Theory Simul.* 5 (2022), 2100293.
- [358] K. Mukherjee, S. Palchowdhury, and M. Maroncelli. “OH Stretching and Libration Bands of Solitary Water in Ionic Liquids and Dipolar Solvents Share a Single Dependence on Solvent Polarity”. *J. Phys. Chem. B* 126 (2022), 4584–4598.
- [359] Q. Sun. “The Raman OH stretching bands of liquid water”. *Vib. Spectrosc.* 51 (2009), 213–217.
- [360] L. Suo, O. Borodin, T. Gao, M. Olguin, J. Ho, X. Fan, C. Luo, C. Wang, and K. Xu. “Water-in-salt electrolyte enables high-voltage aqueous lithium-ion chemistries”. *Science* 350 (2015), 938–943.
- [361] S. Han. “Dynamic features of water molecules in superconcentrated aqueous electrolytes”. *Sci. Rep.* 8 (2018), 9347.
- [362] Z. Li, R. Bouchal, T. Mendez-Morales, A.-L. Rollet, C. Rizzi, S. Le Vot, F. Favier, B. Rotenberg, O. Borodin, O. Fontaine, and M. Salanne. “Transport Properties of Li-TFSI Water-in-Salt Electrolytes”. *J. Phys. Chem. B* 123 (2019), 10514–10521.
- [363] T. R. Kartha and B. S. Mallik. “Ionic conductance and viscous drag in water-in-salt electrolytes for lithium and sodium ion batteries and supercapacitors”. *Mater. Today Commun.* 25 (2020), 101588.
- [364] M. Zhang, H. Hao, D. Zhou, Y. Duan, Y. Wang, and H. Bian. “Understanding the Microscopic Structure of a “Water-in-Salt” Lithium Ion Battery Electrolyte Probed with Ultrafast IR Spectroscopy”. *J. Phys. Chem. C* 124 (2020), 8594–8604.
- [365] K. S. Han, Z. Yu, H. Wang, P. C. Redfern, L. Ma, L. Cheng, Y. Chen, J. Z. Hu, L. A. Curtiss, K. Xu, V. Murugesan, and K. T. Mueller. “Origin of Unusual Acidity and Li⁺ Diffusivity in a Series of Water-in-Salt Electrolytes”. *J. Phys. Chem. B* 124 (2020), 5284–5291.
- [366] Y. Zhang, N. H. C. Lewis, J. Mars, G. Wan, N. J. Weadock, C. J. Takacs, M. R. Lukatskaya, H.-G. Steinrück, M. F. Toney, A. Tokmakoff, and E. J. Maginn. “Water-in-Salt LiTFSI Aqueous Electrolytes. 1. Liquid Structure from Combined Molecular Dynamics Simulation and Experimental Studies”. *J. Phys. Chem. B* 125 (2021), 4501–4513.
- [367] D. J. Price and C. L. Brooks. “A modified TIP3P water potential for simulation with Ewald summation”. *J. Chem. Phys.* 121 (2004), 10096–10103.
- [368] W. L. Jorgensen, J. Chandrasekhar, J. D. Madura, R. W. Impey, and M. L. Klein. “Comparison of simple potential functions for simulating liquid water”. *J. Chem. Phys.* 79 (1983), 926–935.